
Free standing Cu nanowire networks as catalyst for electrochemical CO₂ reduction

Kupfer Nanodrahtnetzwerke als Katalysator für elektrochemische CO₂ Reduktionsreaktionen

Zur Erlangung des Grades eines Doktors der Naturwissenschaften (Dr. rer. nat.)

genehmigte Dissertation von M.Sc. Nils Ulrich

Tag der Einreichung: 17.07.2024

Darmstadt 2024 — D 17

1. Gutachten: Prof. Dr. Maria Eugenia Toimil-Molares
2. Gutachten: Prof. Dr. Bastian J.M. Etzold



TECHNISCHE
UNIVERSITÄT
DARMSTADT

**Fachbereich Material und
Geowissenschaften
Ionenstrahlmodifizierte
Materialien**

Free standing Cu nanowire networks as catalyst for electrochemical CO₂ reduction
Kupfer Nanodrahtnetzwerke als Katalysator für die elektrochemische CO₂ Reduktion

Genehmigte Dissertation von M.Sc. Nils Ulrich

1. Gutachten: Prof. Dr. Maria Eugenia Toimil-Molares
2. Gutachten: Prof. Dr. Bastian J.M. Etzold

Tag der Einreichung: 17.07.2024

Tag der Prüfung: 18.10.2024

Darmstadt 2024 — D 17

Darmstadt, Technische Universität Darmstadt
Jahr der Veröffentlichung auf TUprints: 2024

Bitte zitieren Sie dieses Dokument als:
URN: urn:nbn:de:tuda-tuprints-287901
URL: <http://tuprints.ulb.tu-darmstadt.de/28790>

Dieses Dokument wird bereitgestellt von tuprints,
E-Publishing-Service der TU Darmstadt
<http://tuprints.ulb.tu-darmstadt.de>
tuprints@ulb.tu-darmstadt.de



Die Veröffentlichung steht unter folgender Creative Commons Lizenz: CC BY 4.0 International
<https://creativecommons.org/licenses/by/4.0/>

Erklärung zur Dissertation

Hiermit versichere ich, die vorliegende Dissertation ohne Hilfe Dritter nur mit den angegebenen Quellen und Hilfsmitteln angefertigt zu haben. Alle Stellen, die aus Quellen entnommen wurden, sind als solche kenntlich gemacht. Diese Arbeit hat in gleicher oder ähnlicher Form noch keiner Prüfungsbehörde vorgelegen.

Salach, den 15.07.2024

(N. Ulrich)

Abstract

To tackle the threats of global warming, finding effective ways to decrease the CO₂ emissions caused by the human population must advance with utmost priority. Thus, efficient progress is necessary regarding decarbonization, carbon sequestration and carbon recycling. Among these approaches, carbon recycling is most promising as it offers a path towards a carbon-neutral circular economy. Through electrochemical CO₂ reduction reactions for carbon neutral electrosynthesis processes, CO₂ can be converted into value-added chemicals.

This thesis focuses on the fabrication of three-dimensional, highly interconnected copper (Cu) nanowire networks and their application as catalysts for electrochemical CO₂ reduction reactions. The networks are grown by electrodeposition of Cu in porous polycarbonate membranes which are produced by means of ion-track nanotechnology. The geometrical parameters of the networks are varied with respect to length, diameter and number density of the nanowires. Compared to a 1 cm² planar sample area, the fabricated Cu nanowire networks surfaces reach up to 300 cm². The characterization of the nanowire networks involves techniques such as scanning electron microscopy (SEM), X-ray diffraction (XRD) and transmission electron microscopy (TEM), both before and after the CO₂ reduction reaction.

The electrochemically active surface area of the nanowire networks is determined by evaluating the double layer capacitance via cyclic voltammetry. In all cases, the experimentally measured electrochemically active surface surpasses the calculated values based on the geometrical wire surface, most probably due to surface roughness resulting from the chemical treatment in the pre-cleaning process.

A variety of Cu nanowire networks are tested as catalysts for electrochemical CO₂ reduction. The conversion efficiency and selectivity of CO₂ reduction towards liquid- and gas-phase products are studied at different applied potentials. The networks exhibit structural stability and conversion efficiencies up to 30% for the reaction of CO₂ to its reduction products within a potential range between -0.5 V and -0.93 V vs. RHE. At higher potentials, cathodic corrosion causes nanowire degradation. This directly leads to changes in surface structure and wire morphology due to material dissolution and redeposition processes.

To assess the long-term performance, the CO₂ reduction reaction at the nanowire networks is operated for 8 h at different potentials. No significant trends for the current density and gas-phase reaction products are observed within this time frame. However, under operation, the Cu nanowire networks undergo gradual degradation as indicated by a loss in cell resistance and increased surface roughness.

Overall, this thesis offers valuable insights into the design, fabrication, and characterization of highly interconnected copper nanowire networks and their application and performance as catalysts for electrochemical CO₂ reduction. It also highlights the challenges associated with cell design, catalyst stability and product analysis during the CO₂ reduction reaction and proposes new approaches for future experiments.

Zusammenfassung

Um den Gefahren durch globale Erderwärmung entgegenzuwirken, müssen die von der menschlichen Bevölkerung verursachten CO₂ Emissionen rasch gesenkt werden. Dafür sind effiziente Fortschritte in den Bereichen Dekarbonisierung, Kohlenstoffspeicherung und Kohlenstoffrecycling durch die Umwandlung von CO₂ in höherwertige Chemikalien, unter Anwendung kohlenstoffneutraler Elektrosyntheseprozesse durch CO₂ Reduktionsreaktionen, erforderlich.

Diese Arbeit konzentriert sich auf die Herstellung und Prüfung dreidimensionaler, stark vernetzter Kupfer (Cu) Nanodrahtnetzwerke mit genau definierten geometrischen Parametern, welche mittels galvanischer Kupferabscheidung, in durch Ionenspur-Nanotechnologie hergestellten Polymertemplaten, synthetisiert werden. Bevor die Nanodrahtnetzwerke als Katalysatoren für die elektrochemische CO₂-Reduktion in einem wässrigen Elektrolyten eingesetzt werden, werden sie einem sauren Vorreinigungsverfahren unterzogen, welches die katalytische Effizienz von Kupfer erhöht. Die Nanodrahtnetzwerke werden vor und nach der CO₂-Reduktion mit Rasterelektronenmikroskopie (REM), Röntgenbeugung (XRD) und Transmissionselektronenmikroskopie (TEM) charakterisiert.

Die elektrochemisch aktive Oberfläche von Nanodrahtnetzwerken mit systematischen Variationen in Drahtlänge, Drahtdurchmesser und Nanodrahtdichte wird durch Bestimmung der Doppelschichtkapazität mittels zyklischer Voltammetrie ermittelt und beträgt bei den hergestellten Cu Nanodrahtnetzwerken bis zu 300 cm² auf einer planaren Probenfläche von 1 cm². Die gemessenen elektrochemisch aktiven Oberflächen sind aufgrund der Oberflächenrauheit durch die chemische Vorbehandlung größer als die Modellwerte der geometrischen Oberfläche.

Cu-Nanodrahtnetzwerke werden als Katalysator für die elektrochemische CO₂-Reduktion getestet. Die Umwandlungseffizienzen und Selektivitäten der CO₂-Reduktion zu Flüssig- und Gasphasenprodukten werden als Funktion der angelegten Spannung untersucht. Die Netzwerke weisen strukturelle Stabilität und CO₂-Umwandlungseffizienzen von bis zu 30 % in einem Potentialbereich zwischen -0,5 V und -0,93 V vs. RHE auf. Bei höheren Potentialen führt kathodische Korrosion zu Änderungen in Struktur und Morphologie der Nanodrähte durch Ablösungs- und Redepositionsprozesse.

Um die Langzeitstabilität zu beurteilen, wird die CO₂-Reduktion für 8 Stunden bei verschiedenen Potentialen durchgeführt. Für die Stromdichte und Gasphasenprodukte sind im Laufe der Zeit keine signifikanten Trends zu beobachten, jedoch zeigen die Cu-Nanodrahtnetzwerke leichte Degradation.

Insgesamt liefert diese Arbeit wertvolle Einblicke in das Design, die Herstellung und die Charakterisierung hochgradig vernetzter Kupfer-Nanodrahtnetzwerke, sowie ihre Anwendung als Katalysatoren für die elektrochemische CO₂-Reduktion. Zudem werden die Herausforderungen hinsichtlich Versuchsaufbau, Katalysatorstabilität und Produktanalyse während der Reduktionsreaktion hervorgehoben.

Contents

Abstract	2
Zusammenfassung	3
Contents	4
1 Introduction	6
2 Synthesis and characterization of Cu nanowire networks	12
2.1 Swift heavy ion irradiation of polymer foils	12
2.2 Selective ion-track etching	15
2.3 Electrodeposition of Cu nanowire networks	18
2.4 Preparation of Cu nanowire networks for catalysis: Cleaning and anodization	24
3 Determination of the electrochemically active surface area of Cu nanowire networks	28
3.1 Theoretical calculations regarding the nanowire network geometry	28
3.2 ECSA determination using the electrical double layer capacitance (C_{DL})	33
3.2.1 ECSA reference measurements on a flat Cu plate	36
3.2.2 ECSA determination of Cu nanowire networks	39
3.2.3 ECSA of Cu nanowire networks with different network heights	40
3.2.4 ECSA of Cu nanowire networks with different nanowire diameter	42
3.2.5 ECSA of Cu nanowire networks with different nanowire number density	43
4 Cu nanowire networks as catalyst for electrochemical CO ₂ reduction	46
4.1 Electrochemical CO ₂ reduction	46
4.2 CO ₂ reduction reaction products for different Cu structures: planar, nanowire array and nanowire network	61
4.3 Determining the suitable potential region for CO ₂ reduction experiments at Cu nanowire networks	68
4.4 Product selectivity of the CO ₂ reduction reaction at different potentials	70
4.4.1 Structural characterization of the nanowire networks by XRD before and after the CO ₂ reduction	75
4.4.2 Structural characterization of the nanowire networks by STEM before and after the CO ₂ reduction	80

4.5	Effect of pre-cleaning and anodization of the Cu nanowire network on the product selectivity of the CO ₂ reduction	83
4.6	Failed CO ₂ reduction at Cu nanowire networks with in-situ IR-drop correction	87
4.7	Studies on cathodic corrosion effects and timeframe at high applied potentials	91
4.8	Test of long term stability of Cu nanowire networks during CO ₂ reduction	94
4.9	Evaluation of the product selectivity during long-term CO ₂ reduction at Cu nanowire networks	97
4.10	Tests of reachable potentials during CO ₂ reduction with different electrolyte concentrations	103
5	Conclusions and Outlook	109
	Bibliography	i
	List of abbreviations	xx
	List of figures	xxii
	List of tables	xxx
	Publications	xxxii
	Acknowledgements	xxxiv

1 Introduction

The human population on earth is growing rapidly with rising living standards, demanding more mobility and industrial economy [1,2]. The saturation of the resulting massive increase in energy demand is still based on the exploitation of earth's carbon-based fossil resources, leading to a high-level emission of the greenhouse gas CO₂. This ongoing development has already yielded an imbalance to the planets natural carbon circle and resulted in global warming [1,3].

It was discovered already more than a century ago by the pioneer work of Arrhenius that the concentration of CO₂ in the earth atmosphere is directly having an influence on the ground temperature [4]. In 1938 a first connection was drawn between an increasing average atmospheric temperature from the beginning of the industrial age and the huge release of CO₂ into the atmosphere by the fossil fuel consumption of the human population [5]. This conclusion was affirmed and strengthened by atmospheric temperature observations in the following decades. In 1967 a computer model was established, which was the first proper computation of global warming and stratospheric cooling, allowing predictions about future climate development with regard to greenhouse gas concentrations in the atmosphere [6]. Additionally, a strong rise of the CO₂ concentration in atmosphere was documented at the Mauna Loa observatory in Hawaii around that time and was once more connected to the combustion of petroleum, carbon and natural gas [7]. The Mauna Loa measurements continue until today, providing the so-called "Keeling curve" (Figure 1 a)) as the longest continuous record of atmospheric CO₂ concentration in the world, showing an everlasting increase since 1960, which correlates to the increasing average surface temperature on earth that is shown in Figure 1 b) [8,9].

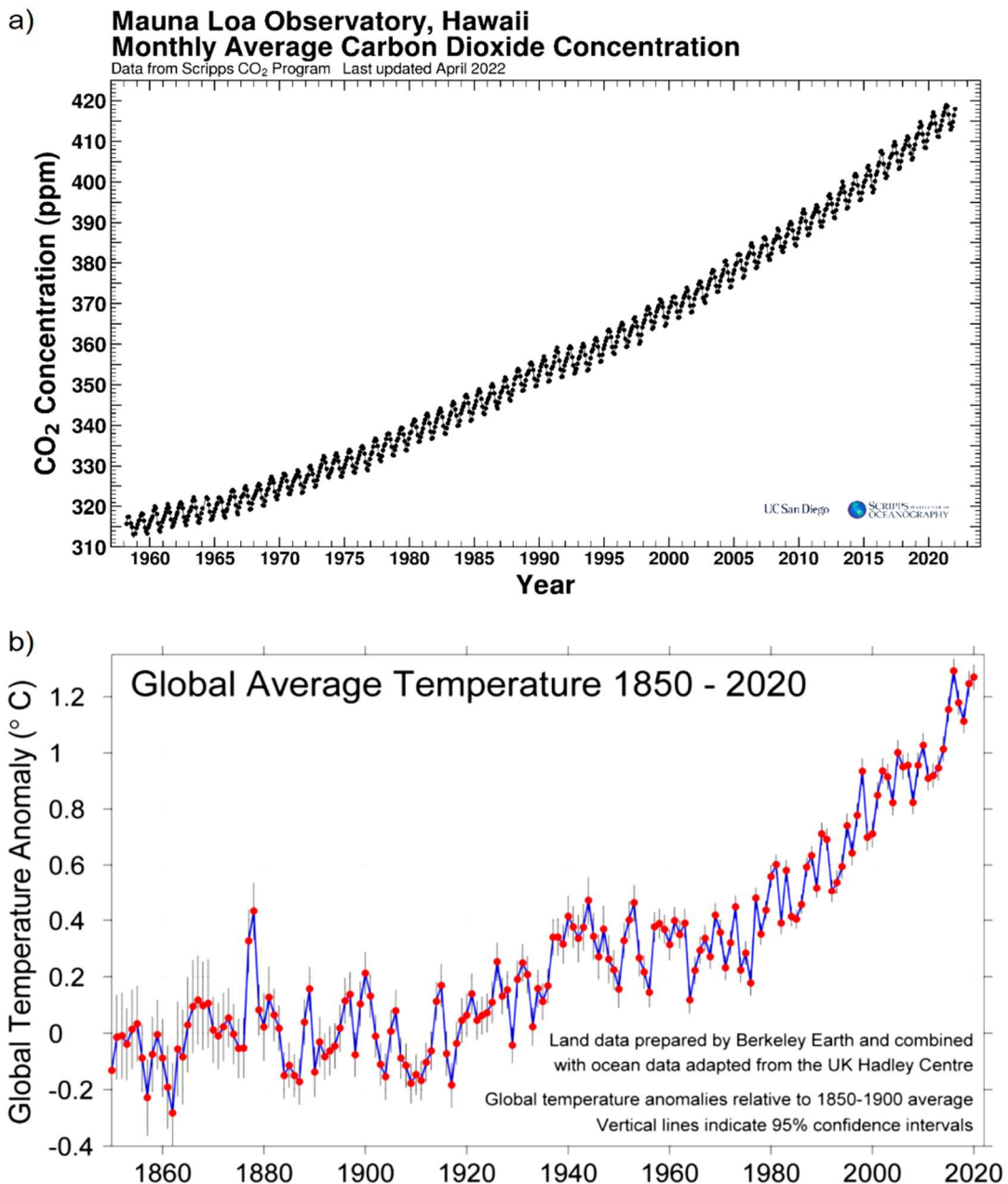


Figure 1: a) Atmospheric CO₂ concentration from 1958-2022 observed at the Mauna Loa observatory in Hawaii, showing a strong increase of ~25 % over the past 60 years [8] and b) global average temperature on land and ocean recorded from 1850 on. Published with permission from Dr. Pieter Tans, NOAA/GML (gml.noaa.gov/ccgg/trends/) and Dr. Ralph Keeling, Scripps Institution of Oceanography (scrippsco2.ucsd.edu/).

Due to the clear link between the burning of fossil resources by humans, atmospheric CO₂ concentration and global warming, scientists largely agree that the current climate change is caused by the human population, a fact that is more and more coming to the attention of the general public [10]. The average global temperature nowadays is already 0.7 °C higher than in pre-industrial times. Thus, in 1997 the Kyoto protocol was established where the industrial nations agreed to reduce their greenhouse gas emissions until 2012 by 5.2 % in comparison to the year 1990. In 2009, the Copenhagen Accord pledged to limit the global temperature increase to 2 °C. However, the Kyoto protocol did not succeed in reducing the global CO₂ emissions significantly [11].

Since the problem of global warming is still urgent, limiting the global temperature increase to a maximum value of 1.5 °C above pre-industrial levels was set as new target during the Paris climate agreement of 195 states in 2015. To achieve this goal, the global CO₂ emissions need to decrease rapidly and reach a level of zero latest by 2050 [12,13].

As the CO₂ concentration in the atmosphere nowadays reaches values around 400 ppm, the climate change is already irreversible for at least 1000 years. This is because the CO₂ removal from the atmosphere is mainly done by the oceans which takes time and ends in an equilibrium state with a higher level of CO₂ concentration in the atmosphere [14]. Moreover, a sudden stop of CO₂ emission by mankind cannot be expected. The emissions can only be reduced as much as possible by developing sustainable techniques for all processes that are based on fossil resources [15].

The effects of global warming on regional precipitation, based on a robust physical understanding of the atmosphere are simply explained by the “wet-gets-wetter, dry-gets-drier” paradigm [16,17]. The precipitation and its distribution around the globe are linked to the atmospheric temperature, since warm air can take up more humidity, which is not coming down as rain. Thus, more droughts in warm regions are a consequence of global warming and a long-term decrease of rainfall has already been observed for the Mediterranean, southern Africa and southwest North America [12,18–22]. This is directly related to an intensity increase of rainfall events in the northern hemisphere [15], which is showing the whole range of impacts on ecosystems, agriculture and desertification [21,23–25].

Another main consequence of global warming is the rise of the sea level. Warming firstly causes water to expand, which is the dominant part of temperature induced changes in sea levels, leading to a sea level increase of up to 0.5 m already in the coming 100 years for a continuous increase in temperature [26]. Secondly, the melting of ice, e.g. land ice and polar ice shields can contribute additional 1-2 m of sea level rise already until the year 2100 [27].

The changes in precipitation and temperature distribution, as well as the rising sea level, can make some areas of the world uninhabitable and thus lead to social and economic disturbances, accompanied by migration movements and changes in lifestyle across the whole planet [28,29].

Global warming can only be tackled by efficient scientific and technologic progress in the following three areas: Decarbonization, carbon sequestration and carbon recycling. Since full decarbonization and carbon sequestration need tremendous measures that overstrain the worldwide economy, enormous research efforts are being devoted to carbon recycling [3].

To prevent a worst-case scenario, every effort must be made to minimize the impact of the negative effects caused by anthropogenic CO₂ emission. This requires new sustainable approaches in all CO₂ emitting processes based on fossil resources like power generation from coal or gas, cement and steel production, or the synthesis of chemicals like e.g. ethylene or ammonia, which release megatons of CO₂ into the atmosphere every year [30,31]. The chemical industry is responsible for 20 % of the total CO₂ emission

from all industrial processes and thus green electrosynthesis provides a certain impact on reducing CO₂ releases [32].

By recycling CO₂ into value-added products, a circular carbon neutral economy with the potential to decouple economic growth from CO₂ emission [33] can be established [34–37]. One pathway for CO₂ recycling is the use of electrochemical CO₂ reduction reactions towards value-added chemicals, involving H₂O as proton donor and electrical energy coming from renewables as input.

Over the years, many catalyst materials have been studied regarding their effect on the CO₂ reduction reaction. Since this reaction is always in competition with the hydrogen evolution in aqueous media, only few materials have proven usable to catalyze CO₂ reduction more than hydrogen evolution. A key result of these studies was that different materials catalyze the CO₂ reduction towards different products, for example CO or formate for noble metal catalysts like Au, Ag, Pd [38–44].

As early as 1989, Cu has been shown to possess the unique property to transform CO₂ electrochemically into a mixture of advanced hydrocarbons [45], a chemical reaction that has already been proposed to be economically viable [46–48].

It has been demonstrated that the product selectivity of CO₂ reduction reactions at Cu catalysts depends on many factors [49–51]. The surface and crystallographic structure is obviously a key factor that has also been used as valuable tool to gain further insight into the selectivity towards specific products [52–55], and to clarify reaction mechanisms [56–59]. Thus, nanoporous structures are of great interest in a variety of scientific and technological fields such as biology, chemistry and materials science since they provide a huge surface to volume ratio, which has proven to be beneficial for electrochemical reactions as well.

One of the available methods widely applied to tailor the geometric parameter of nanostructures is the template method, where the synthesized material adopts the size and shape of a hosting matrix [60]. In particular, this method has been widely applied to fabricate nanowires by depositing material into a nanoporous template. The hosting porous templates are made of a variety of materials, for example anodic aluminium oxide (AAO) [61–63] or etched ion track membranes, which are usually polymers but also silica or mica [64–70].

AAO templates are synthesized by the anodic oxidation of aluminium in acidic solutions [71,72], forming nanochannels inside the template with controllable diameter and a channel density that is defined by their arrangement [73]. An advantage of AAO templates is the possibility of hexagonal channel arrangement, achieved by double anodization, allowing high channel densities up to 10¹² channels/cm² [74]. However, the flexibility to adjust the shape and arrangement of the channels is rather limited [75].

In contrast, etched ion track polymer templates offer the huge advantage, that their geometrical parameter like nanochannel diameter, length, number density, shape and arrangement (parallel or interconnected channels) can be tailored independently by the irradiation and etching parameters [76–78]. Their

fabrication is based on the irradiation of an insulating polymer foil with swift heavy ions having an energy high enough to penetrate the entire material thickness up to several tens of μm . While passing the material, each ion loses its energy and creates an individual track with broken bonds and other defects along its path [70,76,79–82]. In a subsequent step, the irradiated foil is subjected to selective etching which converts these ion tracks into nanochannels with well-defined shape. Cylindrical, conical, biconical or cigar-like shapes and diameter from ~ 10 nm up to a few μm are possible [68,76–78,83–86].

The templates used in this work are generated by swift heavy ion irradiation of polycarbonate (PC) foils at the accelerator facility of the GSI Helmholtzzentrum (Darmstadt, Germany). The standard irradiation is performed normal to the surface using fluences between one single ion and $\sim 10^{10}$ ions/ cm^2 . Since each individual ion creates a track, the applied fluence determines the resulting nanochannel density, with the upper limit being defined by the materials stability after the etching process. The ion tracks are stochastically distributed, which may create overlapping tracks/pores at high fluences. Ordered track patterns can be produced with a microprobe which places ion after ion onto a predefined position. The operation is at 1 kHz, therefore this technique has a low production efficiency and is not suitable for large samples or high throughput production [87–89]. Sequential ion-irradiation under various tilted angles leads to templates with crossing ion tracks. Thus, the etching process finally yields a template with an equivalent nanochannel network structure [78,90].

Etched ion-track templates with tailored nanochannels have been applied in many ways, i.e. as nanoporous membranes for filtration and biotechnological applications [91] or for studies as battery separators [92]. Membranes with a single nanopore are suitable model systems for measuring ionic transport properties in analogy to biological ion channels [93–102]. Furthermore, they serve as templates for the synthesis of nanotubes by atomic layer deposition (ALD) [103–106]. Nanowire arrays or networks can be achieved by electroless [107,108] and electrodeposition of a variety of materials including Cu [86,109–114], Ni [115–117], Au [113,118], Pt [90,119–121], Bi [122], Sb [123,124], Cu_2O [125,126] or ZnO [110,127]. Recently it was demonstrated that Cu and Cu_2O nanowires can be transformed into metal organic frameworks (MOF) with promising properties for catalytic applications [126,128]. Nanowire networks synthesized by electrodeposition in interconnected nanochannel membranes have been studied for thermoelectric applications regarding Bi nanowire networks [122] or as electrode for photoelectrochemical water splitting in the case of Cu_2O or ZnO nanowire networks [125,127] as well as for catalytic methanol oxidation in the case of Au nanowire networks [118].

This thesis focusses on the application of free-standing three-dimensional Cu nanowire networks as catalyst for the electrochemical CO_2 reduction reaction. Such nanowire networks are promising catalysts because of their large surface area which directly influences the reaction efficiency. The synthesis of Cu nanowire networks by the template method allows to tailor the nanowire parameters including wire diameter and number density as well as their crystalline structure, which should have an impact on the product selectivity. [51,129,130]. So far, the most commonly used Cu nanostructure catalysts consist of Cu

nanoparticles [131–133] or Cu nanowire arrays [134,135] that have random geometric arrangements, a certain size distribution and little flexibility to control their parameters. The product selectivity at different reaction potentials and the long-term stability of the networks was investigated in this thesis as well.

Since the surface area is a key parameter for the catalyst performance, a process to determine the electrochemically active surface area (ECSA) of Cu nanowire networks was developed.

Before and after their application as catalyst for electrochemical CO₂ reduction, the Cu nanowire networks were characterized regarding their morphology and crystalline structure with scanning electron microscopy (SEM), energy dispersive X-ray spectroscopy (EDX), X-ray diffraction (XRD) and scanning transmission electron microscopy (STEM).

2 Synthesis and characterization of Cu nanowire networks

2.1 Swift heavy ion irradiation of polymer foils

The interaction of energetic ions with matter depends on the energy of the projectile ion. At small energies, typically up to a few hundred keV that are reached shortly before the stopping of an ion during its passage through the material, the process is dominated by nuclear stopping where the ion transfers its energy by elastic collisions with the target atoms [77,136]. At higher ion energies, the energy is mainly transferred by excitation and ionization of the target atoms. This process is called electronic stopping [137] and leads to an electron cascade. This electron cascade finally transfers the energy from the electronic system onto the atoms of the target material and thus a straight cylindrical damaged track along the ion path is formed [86]. The energy loss $\left(\frac{dE}{dx}\right)_e$ in the electronic stopping regime is described by the Bethe-Bloch equation (1) [76,137–139].

$$\left(\frac{dE}{dx}\right)_e = \frac{4\pi e^4 * (Z_{eff})^2 * Z_t * N_t}{m_e v_p^2} * \left[\ln\left(\frac{2m_e * c^2 * \beta^2}{I}\right) - \beta^2 - \delta - U \right] \quad (1)$$

In this formula, e is the elementary charge, m_e the electron mass, v_p the ion velocity, Z_{eff} the equilibrium effective charge of the projectile ion, Z_t the atomic number of the target material, N_t the target atoms density, I the ionization energy of the target atoms, and β the velocity of the ions relative to the speed of light c . δ and U are correction factors taking into account relativistic effects and contributions from inner shell electrons, respectively.

Currently, there are two theories describing the energy transfer from the electronic system of the target material atoms into its lattice structure. One is the Coulomb Explosion or ion spike model, assuming that positively charged atomic cores resume in the center of the ion path, causing repelling coulomb forces that lead to bond breaking and defect creation with vacancies and interstitials, which finally results in the formation of an ion track [140].

The other theory is the thermal spike model, assuming a direct energy transfer from the electronic subsystem into the lattice, which generates high temperatures along the ion path, leading to local melting and track formation [141].

In both cases, the processes occur in very short timescales after the ion-impact. The initial ionization process happens in the first $10^{-17} - 10^{-16}$ s and the electron cascade spreads within $10^{-15} - 10^{-14}$ s. The energy within the electron subsystem is transferred to the lattice by electron-phonon coupling directly after $10^{-13} - 10^{-12}$ s and heats the atomic system around the ion path [80,142]. The subsequent cooling in the thermal spike model occurs within $\sim 10^{-10}$ s freezing the structure in the molten zone. In most insulators, the resulting track has a diameter of up to 10 nm [79,80,82,141,143,144].

In the past, numerous studies tried to clarify and characterize the damage induced when irradiating polymers with swift heavy ions. For high energies in the range of several MeV per nucleon (MeV/u) as used in this work, the most important parameter is the electronic energy loss according to the Bethe-Bloch formula [81].

For the irradiation of ion-track templates, the thickness of the irradiated material has to be chosen in such a way, that it is smaller than the ions penetration depth described by equation (2) [145].

$$R_p = \int_{E_0}^0 \left(\frac{dE}{dx} \right)_e^{-1} dE \quad (2)$$

$\left(\frac{dE}{dx} \right)_e$ describes the energy loss due to electronic stopping. The irradiations in this thesis were performed with 5 –11 MeV/u ions providing a constant energy loss along the whole ion trajectory through the target and leading to a homogeneous material damage along the track. The nuclear and electronic energy loss of Au ions as a function of the specific ion energy in a polycarbonate target and the corresponding ion range is presented in Figure 2 a) and b). Both curves were obtained by simulations using the SRIM2003 code [146].

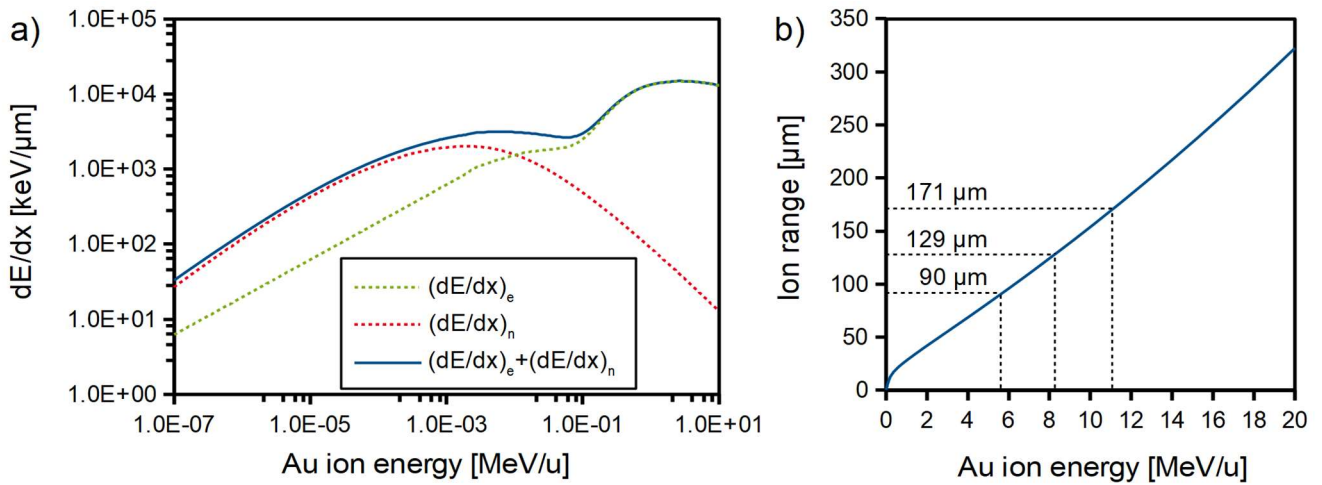


Figure 2: The electronic energy loss (dashed green line), the nuclear energy loss (dashed red line) and the resulting total energy loss as sum (blue line) as a function of the specific energy of Au ions a) and the projected range b) in polycarbonate according to simulations using the SRIM2003 code [146]. The ranges for the irradiation energies of 5.6 MeV/u, 8.3 MeV/u and 11.1 MeV/u used in this work are marked with dashed black lines.

Circular foils with a diameter of 30 mm were cut out of a 30 μm thick polycarbonate roll (Makrofol N, Bayer AG, Leverkusen, Germany) and irradiated with swift heavy ions. The irradiations were performed at the X0 beamline of the UNILAC linear accelerator of GSI Helmholtz Zentrum with Au ions accelerated to specific energies of 11.4 MeV/u, 8.6 MeV/u and 5.9 MeV/u.

For recording the ion flux during sample irradiation, a secondary-electron transmission monitor (SEETRAM) measures the secondary-electron emission induced by the ion beam when passing through

three 1- μm thick aluminum foils. The ions deposit about 0.3 MeV/u on their way through these three foils, reaching the polymer foils with a specific energy of 11.1 MeV/u, 8.3 MeV/u and 5.6 MeV/u, respectively. For these three energies, SRIM 2003 code simulations predict a penetration depth of the ions in polycarbonate (density 1.24 g/cm³) of $\sim 171\ \mu\text{m}$, $\sim 133\ \mu\text{m}$ and $\sim 91\ \mu\text{m}$, respectively [146] as shown in Figure 2. For efficient irradiation, the polymer films were mounted in stacks. The stack thickness was in all cases less than the ion range to guarantee homogeneous track formation in all polymer foils. Depending on the beam energy, the stacks consisted of 4, 3, or 2 foils of 30 μm Makrofol N.

For the fabrication of parallel nanowire arrays, the foils were irradiated under normal beam incidence as presented in Figure 3 a) with an ion-fluence of $\sim 10^9\ \text{i}/\text{cm}^2$. For the fabrication of interconnected nanowire networks, the foils were irradiated sequentially under four different incidence angles of 45° with respect to the polymer surface normal, as shown in Figure 3 b). For most samples, the beam fluence was adjusted to $\sim 2 \times 10^8\ \text{i}/\text{cm}^2$ for each direction, which is in sum a total fluence of $\sim 8 \times 10^8\ \text{i}/\text{cm}^2$. In cases where lower or higher values were applied, the total fluence is explicitly stated.

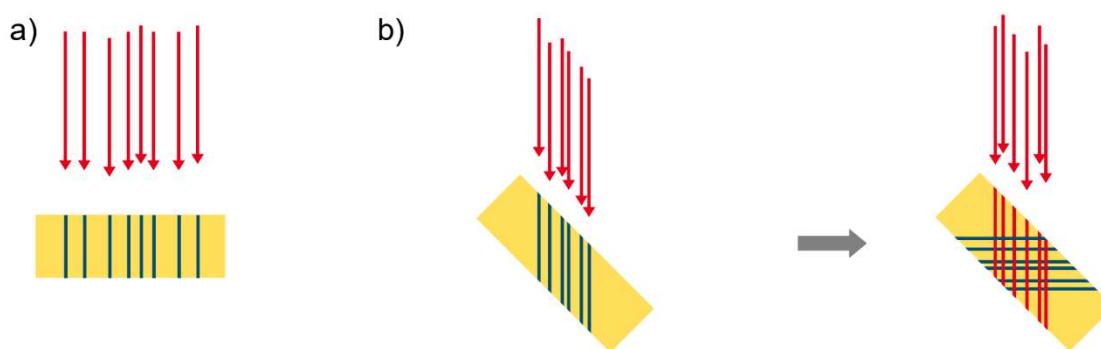


Figure 3: Schematics of the irradiation of polymer foils a) perpendicular to the polymer surface and b) under 45° tilt combined with a rotation of 90° around the surface normal between irradiation steps.

After irradiation, the polymer foils were stored in air for at least half a year. Aging is known to improve the track etchability, resulting in a narrower diameter distribution during the subsequent ion-track etching process [69,79,147].

Prior to chemical etching, the irradiated membranes were exposed to ultraviolet (UV) light (30 W Vilber Lourmat T-30 M UV fluorescent lamp) with wavelengths between 280 nm and 400 nm for 1 h from each side. Similar as the aging effect, this UV treatment increases the track etching rate by polarizing and sensitizing new end groups along the ion-track [79,148]. Additionally, it has been shown that UV radiation reduces the size distribution of the nanopores obtained in the subsequent etching step to a standard deviation of $\sim 3\%$ [79,148,149].

2.2 Selective ion-track etching

To transform the irradiated polymer foil into a template with nanopores, the damaged material along the ion tracks is selectively removed in a suitable etchant. The geometry of the resulting nanochannel is determined by the employed etching conditions. The etching process is described by a combination of two etching rates as illustrated in Figure 4 a), where v_t is the anisotropic fast etching rate along the ion-track and v_b is the isotropic bulk etching rate of the pristine polymer material.

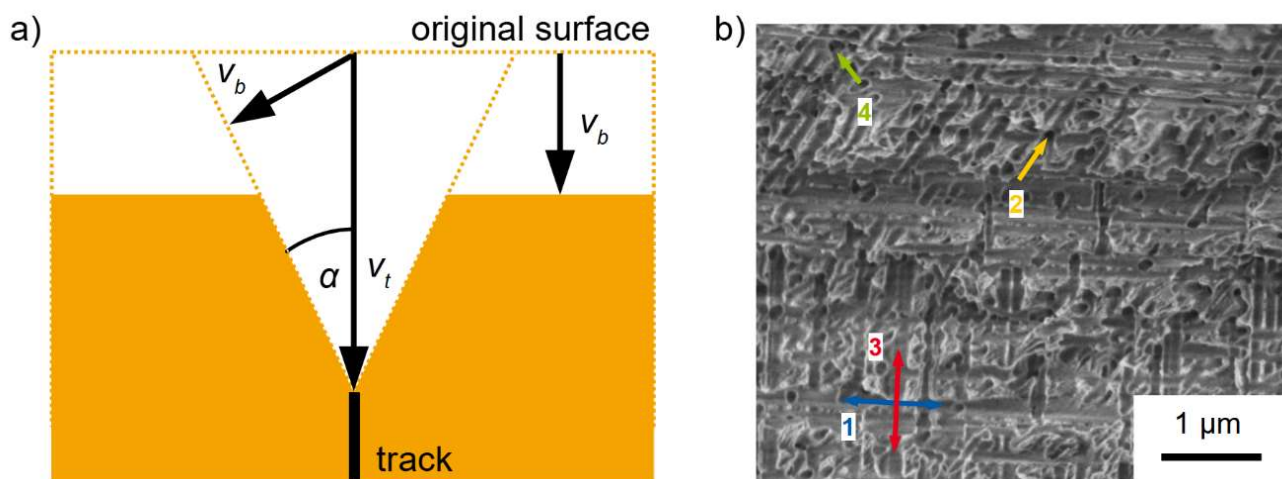


Figure 4: a) Schematic of the initial stages of etching of the ion-track. The pore opening angle α depends on the ratio of the track etching rate v_t and bulk etching rate v_b . b) For $v_t \gg v_b$ cylindrical nanochannels are achieved as visible in the cross section of the nanopore network template that was sequentially irradiated from four directions under an angle of 45° to the surface normal.

The nanochannel geometry is defined by the ratio of v_t and v_b as well as by symmetric or asymmetric etching conditions, i.e. the etchant being applied from both sides or to only one side. The size of the resulting nanochannels is adjusted by the concentration and temperature of the etchant as well as by the etching time [79,150–152]. The half opening angle of a pore is defined by $\sin \alpha = \frac{v_b}{v_t}$. If $v_t \gg v_b$, the resulting pore can be regarded as cylindrical [151], whereas for v_t only slightly larger than v_b biconical pores are obtained [153]. In this work, membranes with interconnected cylindrical nanochannels, were synthesized by employing symmetric etching conditions via immersion of the whole template in the etching solution as shown in Figure 5.

The selective etching process was performed by immersing four PC foils at a time in 6 M NaOH solution, tempered to 50°C [148]. To prevent the sample foils from touching each other, they were placed in a custom-made holder as shown schematically in Figure 5. The etching solution was prepared by dissolving 120 g of NaOH pellets ($\geq 98\%$, Carl-Roth, Karlsruhe, Germany) in deionized water (Millipore Direct Q-5) to form 500 ml of solution. The etching bath was put in a tempered pot and constantly stirred at ~ 250 rpm with a magnetic stirrer to secure a constant heat distribution and homogeneous etchant concentration in the whole bath and thus around each polymer foil [79,151].

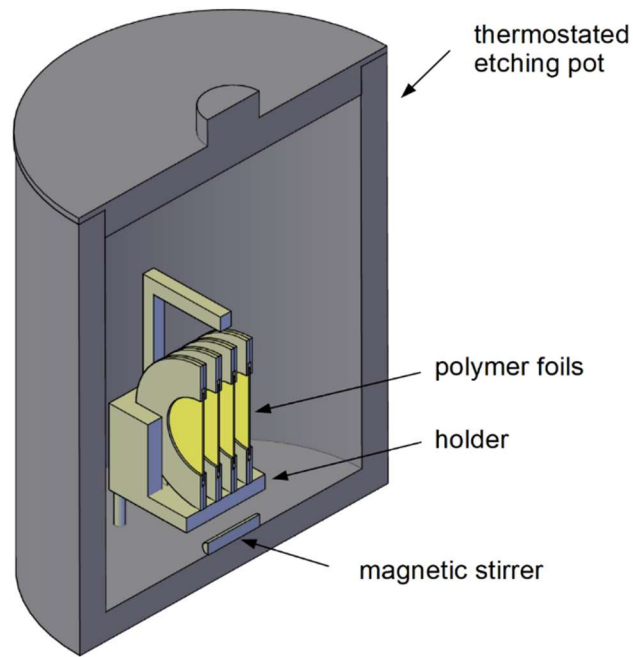


Figure 5: Cross section of the thermostatic pot and the sample holders used for selective ion-track etching of the irradiated polymer foils. For etching, the pot temperature is controlled to $50 \pm 2 \text{ }^\circ\text{C}$ and a magnetic stirrer is situated under the sample holder.

The etching process was stopped after the desired time, assuming a diameter growth rate of 25 nm/min [79,154] by removing the membranes from the etching solution and immediately immersing them into deionized water. To remove all possible etchant residues and small amounts of dissolved polymer material, the membranes were immersed for 10 minutes each in two more pots filled with fresh deionized water.

This etching process transforms the irradiated polymer into a membrane with nanochannels whose diameter is precisely controlled by the etching time [76,78,86,155]. Under the applied conditions the growth rate of the pore radius is $\sim 12 \text{ nm/min}$.

Etched polymer membranes were inspected by scanning electron microscopy (SEM) using a low acceleration voltage of 0.5 kV to avoid electric charging effects. The working distance was set to 3 mm . To determine the pore number density precisely, SEM-images (magnification $\times 5000$) were analyzed at four different positions distributed over the whole membrane. Pore counting was performed in a square region of $20 \times 15 \text{ }\mu\text{m}$ at each position. Finally, the number densities determined at the various positions were averaged and are given as effective pore number density.

To image the cross-sections of the pores by SEM, the polymer membranes were immersed in liquid nitrogen. This leads to embrittlement and facilitates breaking them without distorting the pores. Cross-section images allow the visualization of channels along their entire length. Fractured membrane sections were fixed with a carbon tape on a special SEM holder that allows obtaining a 90° cut vertical surface. Such samples were sputter coated with Au before analysis to reduce charging effects from the electron beam.

Figure 6 presents two representative SEM images of polymer membranes irradiated with different fluences of a) $1 \times 10^8 \text{ cm}^{-2}$ and b) $2.5 \times 10^8 \text{ cm}^{-2}$ from four directions each.

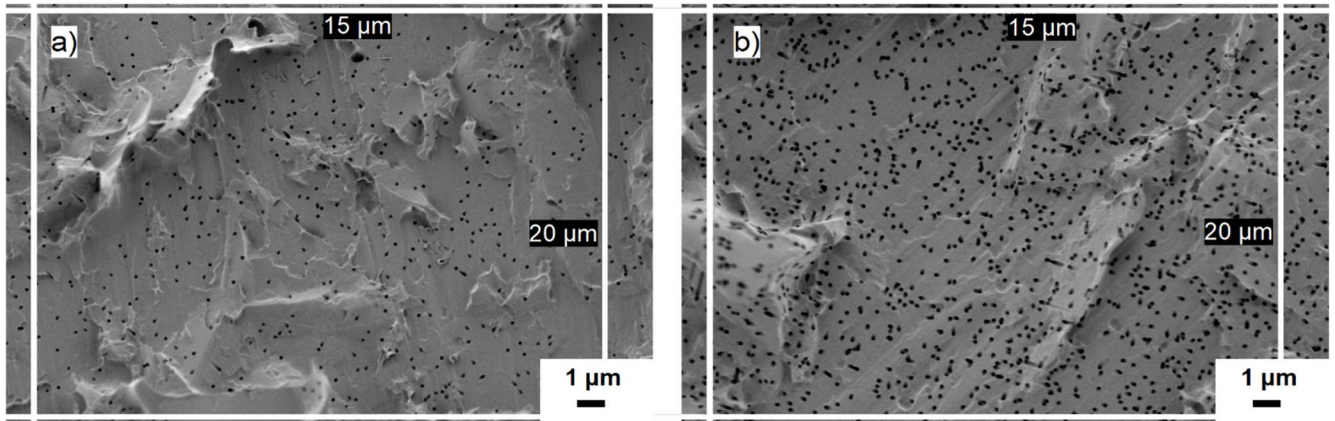


Figure 6: SEM images of polymer membranes with interconnected nanopores of 150 nm diameter. Both samples were irradiated under a tilting angle of 45° from four directions with fluences of a) $1 \times 10^8 \text{ cm}^{-2}$ and b) $2.5 \times 10^8 \text{ cm}^{-2}$, each. The frame marks the region of $20 \times 15 \mu\text{m}$ in which the pores are counted for fluence determination.

For selected samples and specific etching times, the diameter of the nanopores was determined from top view as well as cross-section SEM images as shown in Figure 7 a) and b), respectively. The cross-section image clearly illustrates the interconnected nanopore network structure.

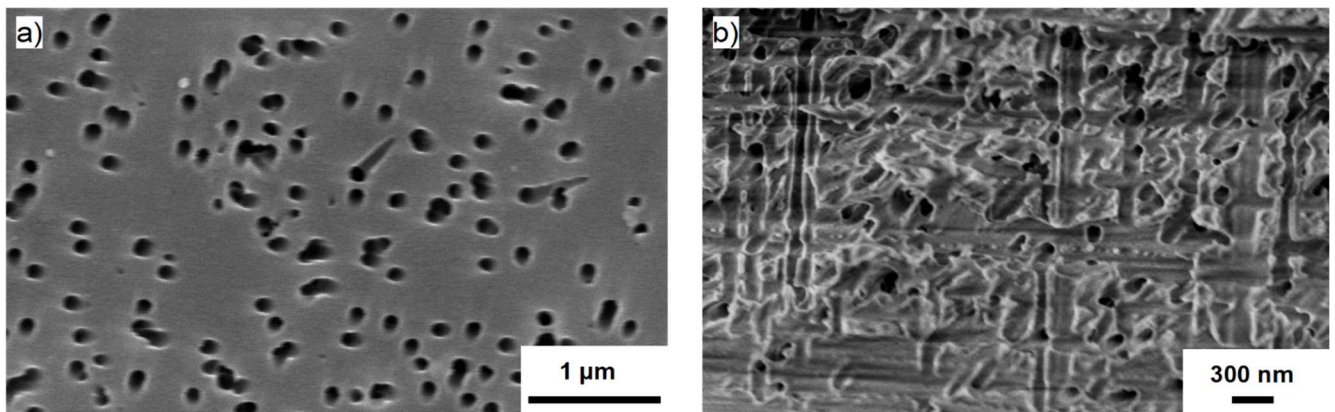


Figure 7: Representative SEM images of etched ion-track membranes with interconnected nanopore network structure, a) top-view and b) cross-section view.

Determining the precise nanopore number density is important to later know the geometrical surface area of the nanowire networks grown in these templates. By analyzing top-view and cross-section SEM images, the nanopore diameter for the used track-etching conditions as a function of time yields an etching rate of the radius of $12.1 \pm 0.4 \text{ nm/min}$. The etching rate is calculated from the pore sizes of three different etched ion-track membranes each for etching times of 2, 4, 6 and 8 minutes as presented in Figure 8.

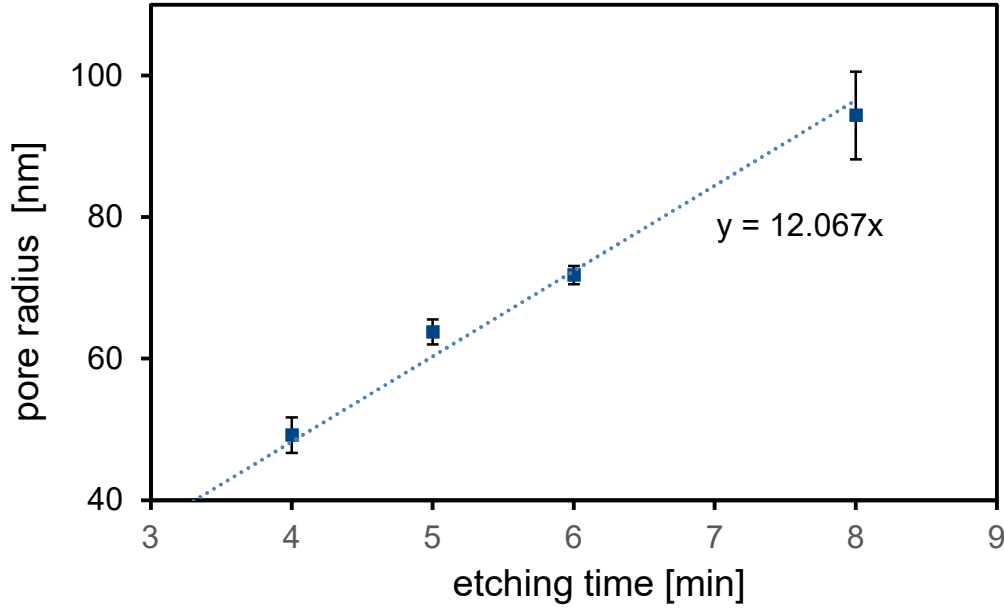
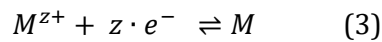


Figure 8: Average pore radius as a function of etching time in 6 M NaOH solution at 50 °C. Each data point represents a mean value from all pores placed in a square region of 20 x 15 μm on three independently etched membranes.

2.3 Electrodeposition of Cu nanowire networks

The nanowire networks are synthesized by electrodeposition of Cu into the etched ion track nanopores. Electrodeposition is a common galvanic process. Here, some of the basic principles are explained.

When a metal electrode M is immersed into an electrolyte containing its ions and no external force (i.e. current or potential) is applied, a dynamic equilibrium between metal dissolution (oxidation) and ion deposition on the electrode (reduction) is established at the metal-electrolyte interface, described by equation (3).



The reaction from left to right, which is the reduction of a positively charged metal ion M^{z+} to the metal M is consuming z electrons e^{-} , whereas the oxidation in the reverse direction is releasing electrons. In dynamic equilibrium, oxidation and reduction are occurring at the same rate, thus the interface is not polarized and the anodic and cathodic currents are equalizing each other. This equilibrium potential E_{eq} depends on the metal and the electrolyte parameters and is described by the Nernst-equation (4) [156].

$$E_{eq} = E^0 + \frac{RT}{zF} \cdot \ln \frac{a_{M^{z+}}}{a_M} \quad (4)$$

E^0 defines the standard potential, R the gas constant, T the absolute temperature, z the number of transferred electrons and F the Faraday constant. $a_{M^{z+}}$ and a_M denote the activities of the metal ions in solution and electrode respectively. In a pure metal electrode, the ion activity has a value of 1, whereas for

highly diluted electrolytes the ion activity is equivalent to the concentration c_{M^+} , neglecting ion-ion interactions. Thus, in this case, the Nernst-equation results in equation (5).

$$E_{eq} = E^0 + \frac{RT}{zF} \cdot \ln c_{M^+} \quad (5)$$

To measure and control the electrode potentials in a reliable way, a reference electrode with a constant well-known equilibrium potential, needs to be inserted into the electrolyte as well. A standard reference is the standard hydrogen electrode (SHE), whose standard electrode potential is defined as zero at all temperatures or its subtype the reversible hydrogen electrode (RHE), having a pH dependent standard potential. Other widely used reference electrodes are saturated calomel electrodes (SCE) and silver chloride electrodes (Ag/AgCl).

An electrochemical process occurs between two electrodes that are removed from their equilibrium potential by an external potential E generating a current flow I between the two electrodes. In such a two-electrode setup, the electrochemical cell consists of two half cells with their own half-cell potentials. The cell potential is equivalent to the sum of the two half-cell potentials plus the potential drop ($I \cdot R$) resulting from the electrolyte resistance R (IR -drop) as described in formula (6).

$$E = \eta_c - \eta_a + I \cdot R \quad (6)$$

with η_c being the cathodic overpotential and η_a being the anodic overpotential. For measuring the half-cell overpotentials, a reference electrode is inserted into the setup, leading to a so called three-electrode setup. If the reference electrode is placed close to the working electrode and the electrolyte conductivity is high, as it is usually the case in electrodeposition processes, the IR -drop can be neglected.

For electrodeposition, the setup is pushed out of its equilibrium by an applied potential, leading to the dissolution of ions at the anode, if it is a sacrificial anode made of the material that is to be deposited. These ions are then transferred through the electrolyte as current and deposited at the negatively polarized cathode. Electrodeposition can be carried out in different ways, either potentiostatically by applying a constant potential over a period of time or galvanostatically with a constant current, as well as by more advanced methods like pulsed plating, where a potential is switched between potentials with different deposition rates to give the system time to equalize between each deposition step [157]. The mass m of the material deposited in a certain time t is described by Faraday's law (formula (7)) and is directly proportional to the current I . M is the molar mass of the metal with an ionic valence z , and F is the Faraday constant.

$$m = \frac{M}{zF} \cdot \int_0^t I dt \quad (7)$$

The magnitude of the generated ionic current depends on the reaction rate upon potential application, defined by a multitude of parameters like temperature, electrolyte composition and concentration, sample geometry and many more [156].

The electrochemical reaction during electrodeposition is a sequence of reaction steps, with the necessary overpotential being directly defined by the thresholds of each partial reaction step. The overpotentials are given by the charge transfer across the electrochemical double layer, which is formed as soon as a metal is in contact with an electrolyte. Also, the diffusion limits for mass transfer of the ions through the electrolyte and the chemical reaction and material crystallization on the cathode play a role. The slowest of these processes is limiting the whole reaction speed and thus considered as the rate determining step (RDS).

If the charge transfer is the rate determining step, the current density j flowing through the cell is described by the Butler-Volmer equation (8), where α is the charge transfer coefficient and j_0 the exchange current density, R the gas constant and T the temperature.

$$j = j_0 \left(e^{\frac{(1-\alpha)zF\eta}{RT}} - e^{\frac{-\alpha zF\eta}{RT}} \right) \quad (8)$$

The two exponential terms describe the current densities for the anodic and cathodic partial reactions.

At very high cell overpotentials, the ions directly get reduced at the electrolyte-metal interface, which becomes ion depleted. In this case, the mass transport $J_i(X)$ of a species i with charge z_i , described by the Nernst-Planck equation (formula (9)) is the rate determining step.

$$J_i(X) = J_{i,d}(X) + J_{i,m}(X) + J_{i,c}(X) = -D_i \cdot \nabla c_i - \frac{zF}{RT} D_i c_i \nabla \phi + c_i \cdot v(x) \quad (9)$$

Here, $J_{i,d}$ describes the diffusion induced flux, $J_{i,m}$ the flux due to migration, $J_{i,c}$ the convection induced mass transport and ∇c_i and $\nabla \phi$ are the concentration and potential gradients, respectively, with D_i as diffusion coefficient. If the species i is charged to a value of z , the flux J_i corresponds to a current density j_i according to equation (10).

$$j_i = zFJ_i \quad (10)$$

When the electrolyte is not stirred and a highly conductive electrolyte is applied, as it is the case for electrodeposition, the terms for migration and convection can be neglected.

For the electrodeposition of Cu nanowires into the channels of the track etched PC templates, two preparation steps were necessary. First, to make the polymer foil electrically conductive, the rough side of the membrane was sputter coated with a ~200 nm thick Cu layer. In a second step, the sputtered Cu layer was reinforced by electrodepositing a ~10 μm thick Cu layer. This extra layer was electrodeposited potentiostatically for 20 minutes at room temperature in a two-electrode setup at $U = -0.5$ V vs. Ag/AgCl

employing a 238 g/l CuSO_4 (99.995 %, Sigma-Aldrich, Taufkirchen, Germany) + 21 g/l H_2SO_4 (99.999 %, Sigma-Aldrich, Taufkirchen, Germany) electrolyte in an electrochemical cell setup, schematically presented in Figure 9 a) [112]. The sputtered Cu layer in this case was acting as cathode, being electrically contacted with a Cu ring, whereas a Cu-rod (99.95 %, Goodfellow, Huntingdon, UK) was applied as sacrificial anode. The resulting layer is thick enough to close the nanochannels of the track-etched membrane and serves as a solid backelectrode for the next electrodeposition process inside the pores.

For the second step, the electrodeposition of Cu into the nanochannels, the membrane was placed between two Teflon compartments of the electrochemical cell, with the previously deposited Cu backelectrode layer being contacted from the back side with a Cu plate, thus serving as working electrode. The compartment towards the open pores was filled with an electrolyte composed of 238 g/l CuSO_4 (99.995%, Sigma-Aldrich, Taufkirchen, Germany) + 21 g/l H_2SO_4 (99.999%, Sigma-Aldrich, Taufkirchen, Germany) + 0.5 ‰ DOWFAX 2A1 surfactant. The addition of the surfactant improves the wettability of the membrane, which is in particular essential for homogeneous electrodeposition of interconnected nanochannels [158]. Before starting the electrodeposition, the electrolyte was tempered for 45 minutes at the deposition temperature of 60 °C. This ensures a uniform temperature distribution in the electrolyte bath and thus homogeneous filling of all pores. Deposition was performed in a three-electrode setup at a constant potential of $U = -20$ mV vs. Ag/AgCl controlled by an Interface 1000 (Gamry Instruments, Warminster, PA, USA) potentiostat, as presented in Figure 9 b).

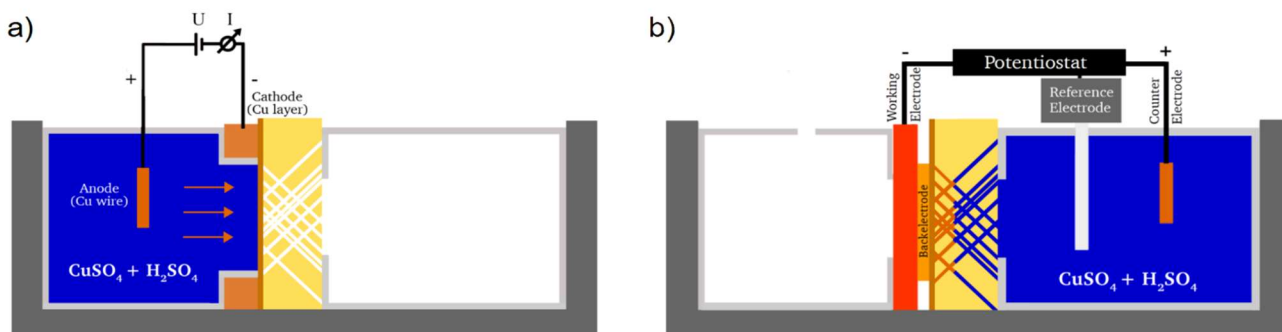


Figure 9: a) Scheme of the electrochemical two-electrode setup, applied for electrodeposition of the Cu backelectrode onto the Cu-sputtered rough side of the PC membrane. The arrows indicate the deposition direction of the Cu ions from anode to cathode. b) scheme of the electrochemical three-electrode setup, applied for electrodeposition of Cu nanowires into the interconnected nanochannels of the PC membrane.

The Cu-electrodeposition process was monitored by recording current-time ($I-t$) curves as shown exemplarily in Figure 10.

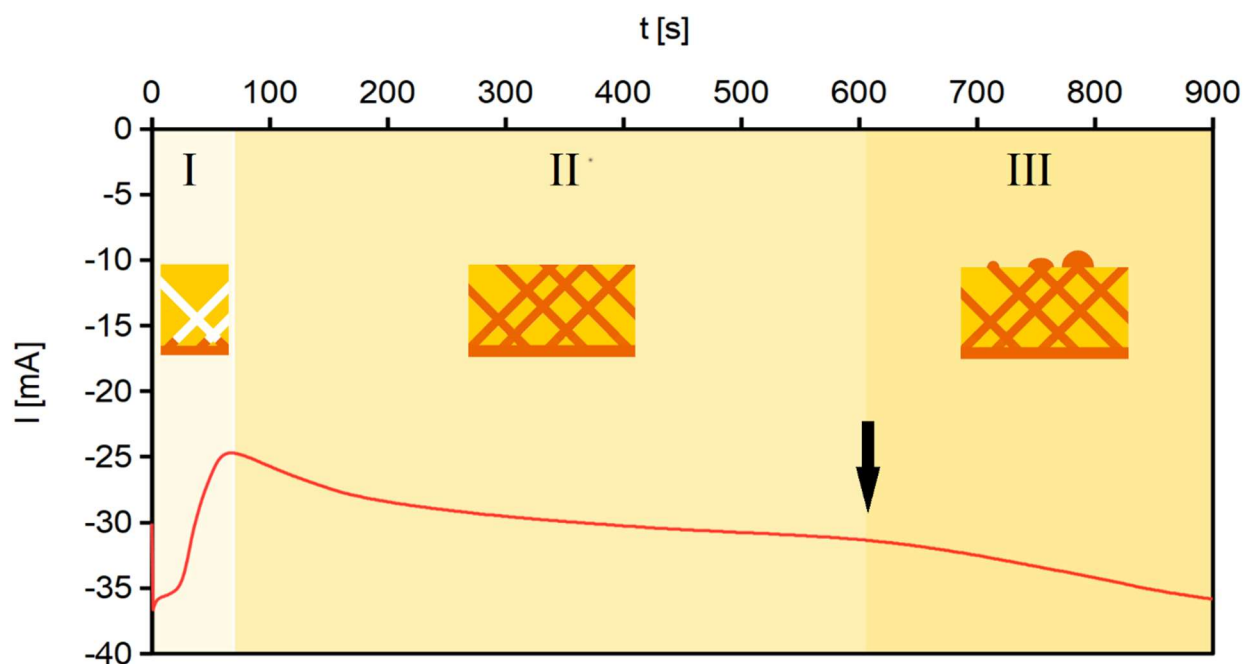


Figure 10: Representative $I-t$ curve recorded during the electrodeposition of Cu at an applied potential of $U = -20$ mV vs. Ag/AgCl into a track-etched membrane with interconnected nanochannels. As schematically indicated, three different regimes can be distinguished during the deposition process. The arrow is indicating the beginning of cap growth when the pores are completely filled.

During the Cu electrodeposition into the pores, three different stages can be distinguished due to the fact that the current density is rather constant. In section I, double layer charging at the working electrode and first nucleation processes occur and lead to a current increase directly after the potential is applied, and a subsequent decrease during the formation and stabilization of the diffusion layer. In section II, during the electrodeposition of material from the bottom of the channels towards the upper side of the membrane, the current slightly increases ($\sim 15\%$) during 5 – 6 min. This rise of the current is attributed to the decrease in remaining channel length, which facilitates the diffusion of the electrolyte inside the channels. In section III, the pores are completely filled and caps start to grow on top of the membrane leading to a current increase due to the larger area of the effective working electrode on which the deposition occurs. In this work, the Cu electrodeposition process was usually stopped when the pores were fully filled, i.e., as soon as the current increase due to cap growth was identified (see arrow in Figure 10). The deposition time of a nanowire network until the beginning of cap growth, is depending on the amount of material that needs to be deposited with a constant deposition rate. Thus, this time is depending on membrane height, nanopore diameter and nanopore number density [159].

To release the nanowire network from the membrane, the sample was fixed on an aluminum holder and immersed into dichloromethane (CH_2Cl_2 , purity $>99.5\%$, Carl Roth GmbH & Co.KG, Karlsruhe, Germany). The solution was exchanged regularly for at least 48 h to ensure complete removal of the dissolved polymer residues.

Analysis of the nanowire networks was performed by scanning electron (SEM) imaging and energy dispersive X-ray spectroscopy (EDX) as well as X-ray diffractometry (XRD) and scanning transmission electron microscopy (STEM). For SEM imaging, usually an acceleration voltage of 1 kV and a working distance of 3 mm were used. For top-view imaging, the free-standing network was mounted on a pin-holder fixed with a ring-shaped holder. For cross-section SEM imaging, the nanowire network was cut into two pieces and placed vertically in a holder, fixing the sample from both sides. The length and the diameter of the wires as well as the height of the network were measured using the internal, calibrated length measurement tool of the Zeiss Gemini SEM software.

To ensure the elemental purity of the networks and identify possible contaminations, EDX analysis available in our SEM was applied. When the electron beam hits a sample, X-rays are emitted whose energy is specific for a given element. The technique thus provides information on the elemental composition of the sample [160,161].

EDX multipoint spectra and EDX mappings were recorded with a Bruker XFlash 5030 detector and using an acceleration voltages of 20 kV and a working distance of 8.2 mm. The spectra and qualitative mapping images, giving the spatial distribution of the detected elements along the nanowire network, were analyzed with the Quantax software from Bruker, belonging to the EDX detector. The acquisition time for the EDX spectra was ~ 15 minutes.

Figure 11 shows SEM images for a) top view and b) cross section view of a Cu nanowire network deposited at a potential of -0.02 V vs. Ag/AgCl. The height of the network is 30 ± 2 μm , the nanowire diameter is 136 ± 6 nm and the measured nanowire number density is 8.0×10^8 wires/ cm^2 . Complete and homogeneous pore filling is indicated by charge calculations from the $I-t$ curve recorded during electrodeposition similar to the example shown in Figure 10. The deposited charge until the beginning of cap growth amounts to 19 ± 2 C and thus a deposited Cu mass of 6.3 ± 0.5 mg which corresponds to a material volume of 0.7 ± 0.1 mm^3 . Taking into account the total number of pores, this value gives a filling rate of 96 ± 7 % with regard to the calculated volume of all pores. Since all nanowire networks in this work were homogeneously deposited into the pores until the beginning of cap growth, pore filling rates of ~ 100 % are typical for all networks studied in this thesis. Details on calculating the volume of a nanopore network are described below in section 3.1.

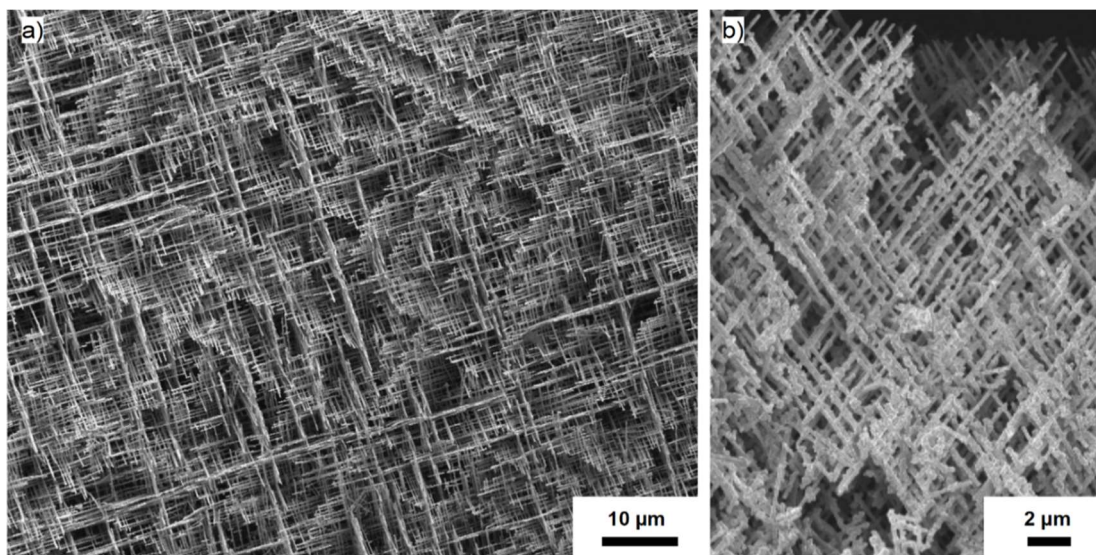


Figure 11: SEM images of a Cu nanowire network electrodeposited for 15 minutes at -20 mV vs. Ag/AgCl with a clearly visible network structure in a) top view and b) cross sectional view.

2.4 Preparation of Cu nanowire networks for catalysis: Cleaning and anodization

For a successful and fully comprehensible CO₂ reduction reaction, the cleanliness of the surface of the Cu wire as catalyst is of significant importance. Contaminations of other metal atoms need to be ruled out, since they favor the hydrogen evolution reaction (HER), which competes with the CO₂ reduction reaction [162–165]. Therefore, an acidic pre-cleaning and anodization procedure, leading to an increased CO₂ reduction efficiency [166,167] had been previously developed [50] and successfully applied to other Cu structures [53,168].

Due to the reduced diameter of the nanowires, the pre-cleaning process parameters needed to be adjusted with the goal to yield clean pure nanowire surfaces while maintaining the geometry and morphology of the nanowires and the network. As shown in section 4.5, the adjusted pre-cleaning process resulted in increased CO₂ reduction efficiencies on the Cu nanowire networks as well and thus has shown to be beneficial.

The adjusted pre-cleaning procedure consists of: (i) 5 min immersion in 0.1 M H₂SO₄. For this, a polyether ether ketone (PEEK) holder is used. (ii) cleaning for 10 min in deionized H₂O. (iii) immersion for 5 min in 0.1 M H₃PO₄, and (iv) 10 min immersion into deionized H₂O.

The following anodization of the sample took place at $U = 1$ V for 1 min in a two-electrode configuration with the Cu nanowire network as working electrode and a platinum wire as counter electrode. This anodization process forms a thin surface film of copper oxide on the nanowires, which is later removed directly before the CO₂ reduction procedure, leading to a clean Cu surface. The positive oxidative potential was applied with a Gamry Interface 1000 potentiostat. The anodization configuration is shown schematically in Figure 12.

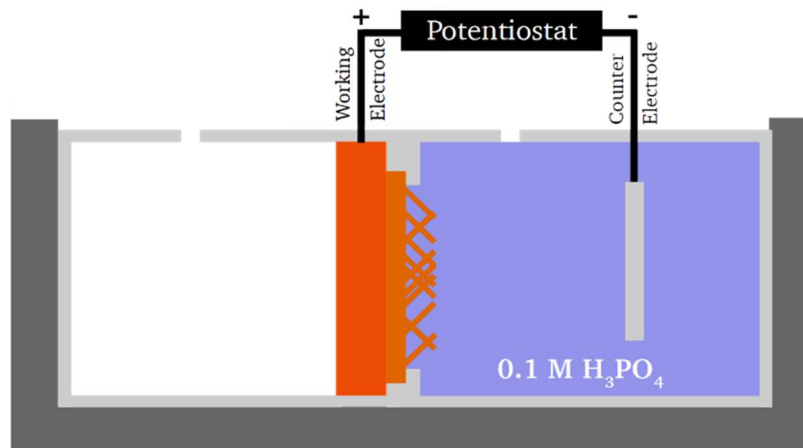


Figure 12: Setup for the anodization of the Cu nanowire network with 0.1 M H_3PO_4 in an electrochemical cell. The network serves as working electrode and is contacted from the back side with a Cu plate, whereas a Pt wire serves as counter electrode for the potential application in a two-electrode setup.

The sequence of SEM images shown in Figure 13 demonstrates that the adapted procedure only slightly increases the surface roughness without influencing the general nanowire network structure, i.e. without causing changes in the nanowire diameter.

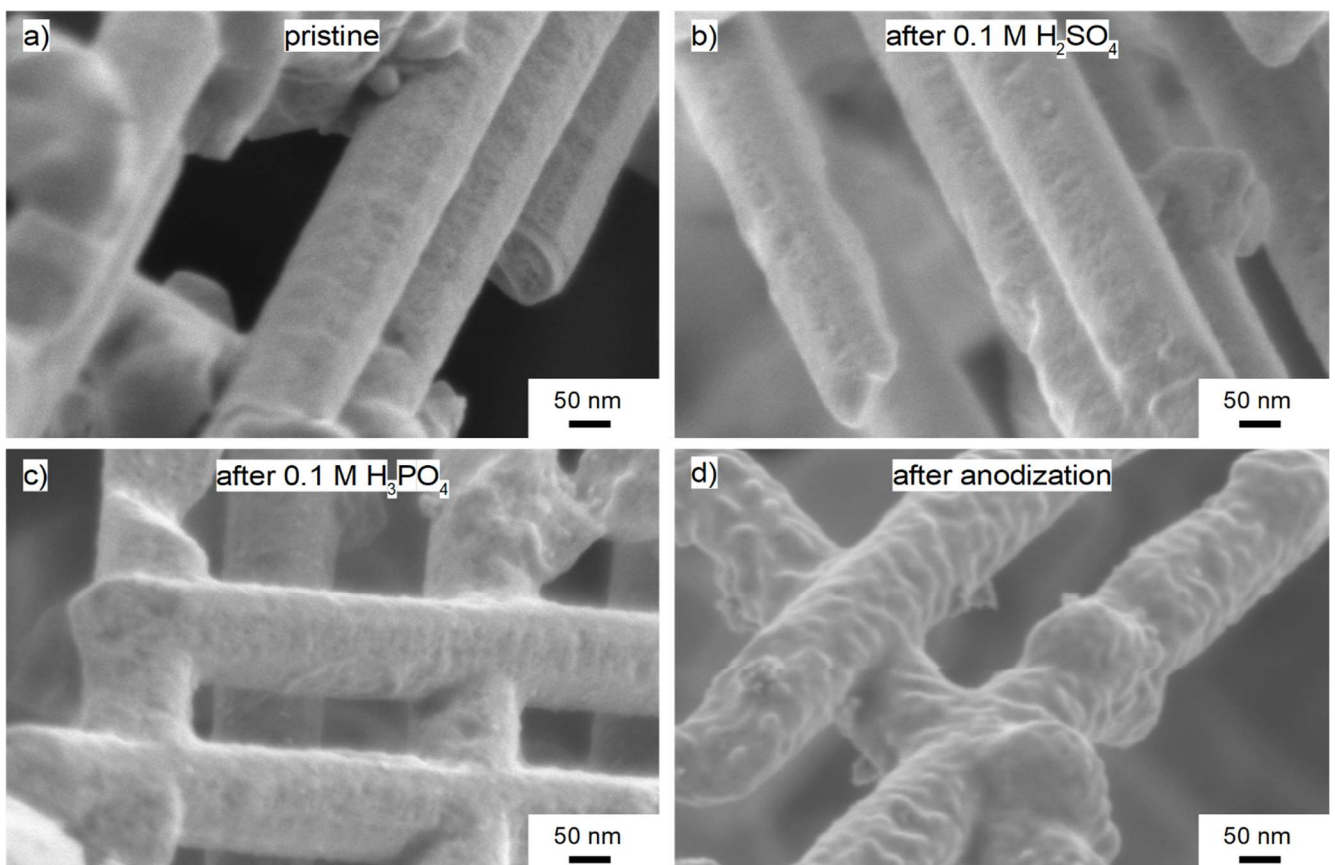


Figure 13: SEM images of the Cu nanowire network before and after consecutive pre-cleaning and anodization steps. a) pristine state b) after immersion in 0.1 M H_2SO_4 , c) after immersion in 0.1 M H_3PO_4 and d) after anodization.

The images reveal that the overall 3D network structure of the Cu nanowire network is maintained during all pre-cleaning and anodization steps. After the first pre-cleaning step in H_2SO_4 (b)) the Cu nanowire

surface does not exhibit any changes. After the pre-cleaning procedure in H_3PO_4 (c)) the images show a very slight increase in surface roughness. Phosphoric acid is known to reduce the native surface copper oxide, which is probably responsible for the slightly rougher surface [169,170]. The anodization procedure oxidizes the Cu nanowire surface resulting in a further and more significant increase of the surface roughness as clearly evident from the SEM images shown in Figure 13 d). Just before the CO_2 reduction, this surface oxide is later removed by surface reduction CV scans in a reductive potential region and together with the increased roughness this explains a more active surface of the catalyst structure as described in section 4.5.

To verify that this pre-cleaning procedure is not contaminating the nanowire network surface, the composition of the wires was analyzed afterwards by EDX and compared to a pristine Cu nanowire network. The EDX spectra of the pristine and the pre-cleaned Cu nanowire networks are presented in Figure 14 a) and b), respectively, with the peaks of the detected elements marked in red and the positions of the possible sulfur and phosphor contaminations marked in green [171].

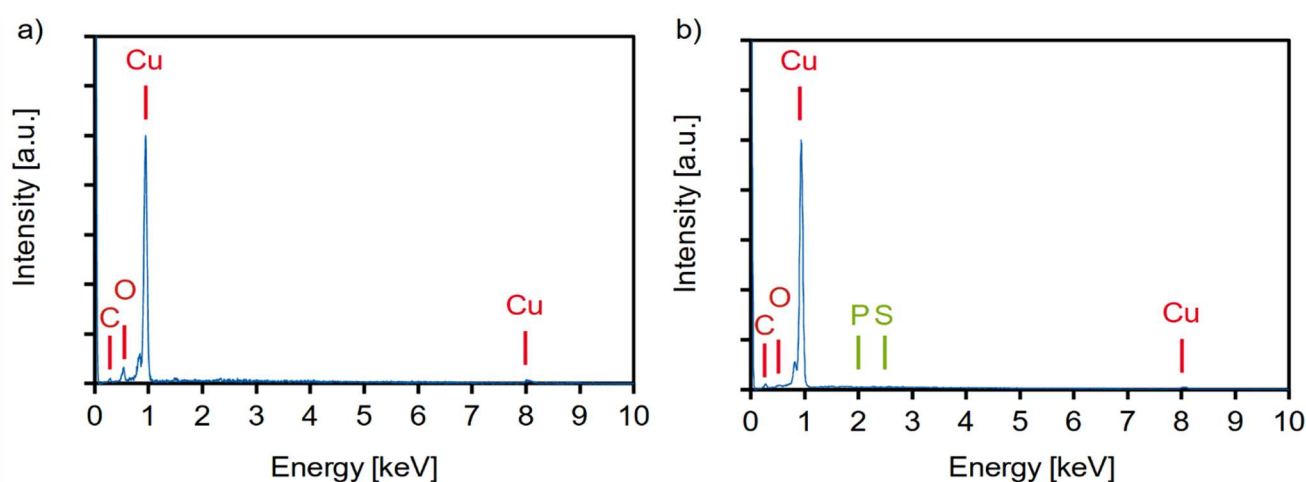


Figure 14: EDX spectra of Cu nanowire networks, synthesized on a Cu backelectrode. a) before (pristine) and b) after pre-cleaning. The position of the copper signals are marked in red and the positions of possible contaminations of sulfur and phosphor are marked in green [171].

The EDX spectrum of the pristine Cu nanowire network (Figure 14 a)) exhibits, as expected, the main Cu peaks together with a small oxygen peak, attributed to the native surface oxide layer on the Cu nanowires and a very small carbon peak attributed to a slight C contamination, which could either belong to a very small amount of polymer residue, or electron-beam induced effects. Otherwise, no additional peaks from contaminating elements are identified, leading to the conclusion, that the Cu nanowire networks are quite pure structures.

The EDX spectrum of the Cu nanowire network after the acidic pre-cleaning procedure is shown in Figure 14 b). Besides the main Cu peak an O peak appears, which is smaller than the one of the pristine sample, indicating the dissolution of copper oxide during the acidic pre-cleaning treatments. The slight carbon signal is ascribed to a contamination. No additional peaks due to contaminating material are observed, and

no signals are found at the expected positions of sulfur and phosphor. The electrodeposition of Cu wires from high purity CuSO_4 electrolyte in combination with a special cleaning procedure, obviously provides nanowire networks with surfaces of high purity as necessary for CO_2 reduction application with the Cu nanowire network as catalyst.

3 Determination of the electrochemically active surface area of Cu nanowire networks

3.1 Theoretical calculations regarding the nanowire network geometry

The geometrical parameters (length, diameter, number density) of Cu nanowire networks synthesized by electrodeposition in etched ion track membranes can be varied in a defined way during the synthesis process. The nanowire diameter corresponds to the diameter of the nanochannels in the template, which is adjusted by controlling the duration of the track etching process. The nanowire number density is the same as the nanochannel density and is controlled by the ion irradiation fluence since each ion produces an individual track that is converted into an open channel [79,86,88,90]. The network height is adjusted by the thickness of the polymer and the electrodeposition time.

A two-dimensional scheme of the network structure is depicted in Figure 15 a) with nanowires being interconnected under an angle of 90° . The irregular distances of the nanowire crossings are illustrated in the representative SEM image in Figure 15 b), and are due to the random distribution of the ion-tracks on the sample, as well as the resulting random distribution of the nanochannels as displayed in Figure 6. The yellow circles mark interconnections of two wires. The stochastic distribution of the wires in each of the four directions results in a highly complex geometry, for which the estimated surface area cannot be readily calculated. We thus applied a simplified model that includes the wire length L (resulting directly from network height h), the wire diameter d and the total number of wires n to estimate the surface of such a nanowire network, and that does not consider the stochastic wire distribution resulting in pore overlaps and wires passing each other closely instead of ordered crossings.

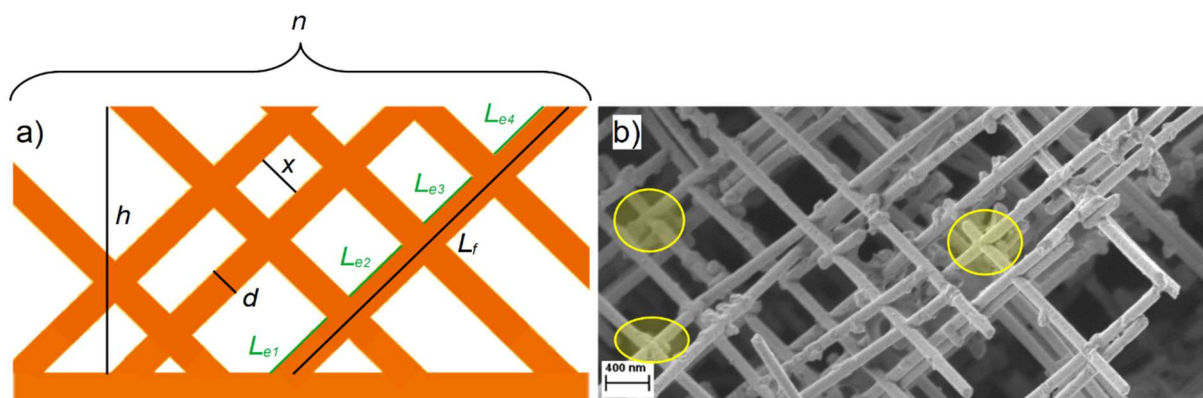


Figure 15: a) Two-dimensional scheme of the nanowire network of height h , full wire length L_f , effective length L_e of wire segments with accessible surface, nanowire diameter d , total number of nanowires n and spacing x between adjacent wires. b) SEM image of a nanowire network with examples of intersecting nanowires marked by yellow circles

Due to the irradiation under 45° , the nanowire length L_f is larger than the network height h as described by equation (11).

$$L_f = \frac{h}{\sin(45^\circ)} \quad (11)$$

The geometric surface A of the network depends on the effective wire length, wire diameter d and the total nanowire number n of the sample. Regarding the wire length, it needs to be considered that the nanowire crossings reduce the accessible surface as well as the volume and mass of the network compared to the integrated surface of all individual wires. For a given nanowire, the crossings reduce the full wire length L_f to the effective length L_e which is considered as the sum of all wire segments L_{ei} between the crossings ($L_e = L_{e1} + L_{e2} + L_{e3} + L_{e4}$ in Figure 15 a)). The model calculation considers two limit cases as a function of two nanowire categories: N_x wires of full length L_f and $(1-N_x)$ wires of maximum reduced length L_e ($L_e = L_f - (\sqrt{n} \cdot L_f \cdot d)$). The total surface A and volume V of the network is composed of the contribution of wires of category N_x and $1-N_x$ given by equation (12) and (13), respectively.

$$A = \left(N_x * 2\pi \frac{d}{2} L_f * F \right) + \left((1 - N_x) * 2\pi \frac{d}{2} L_e * F \right) \quad (12)$$

$$V = \left(N_x * \pi \left(\frac{d}{2} \right)^2 L_f * F \right) + \left((1 - N_x) * \pi \left(\frac{d}{2} \right)^2 L_e * F \right) \quad (13)$$

By multiplying the network volume with the mass density of the material, the estimated mass m of the nanowire network is obtained ($m = V \times \rho$). The two limit cases correspond to (i) all wires having the full length without any crossings, which is equivalent to a nanowire array and (ii) all nanowires have an effective length reduced to the minimum value by a maximum number of possible crossings defined by the number of nanowires n , which is equivalent to a totally regular arranged nanowire network structure.

Figure 16 presents a) the calculated surface area A_{theo} , b) volume V , c) mass m and d) specific surface area ($SSA = \frac{A_{theo}}{m}$) for Cu nanowire networks ($\rho = 8.92 \text{ g/cm}^3$) as a function of network height for a planar sample area of 1.8 cm^2 . The nanowire diameter is 150 nm and the nanowire number density $8 \times 10^8 \text{ cm}^{-2}$ (corresponding to the sum of the four sequential irradiations with an ion beam fluence of $2 \times 10^8 \text{ i/cm}^2$ each). The graphs represent the upper limit when all wires have the full length L_f (blue), the lower limit when all wires have a reduced length L_e (red), and a more realistic situation, were 50 % of the wires have the full length and 50 % have a reduced length (green). These calculations illustrate the dependence of the surface and volume of the network on the wire length.

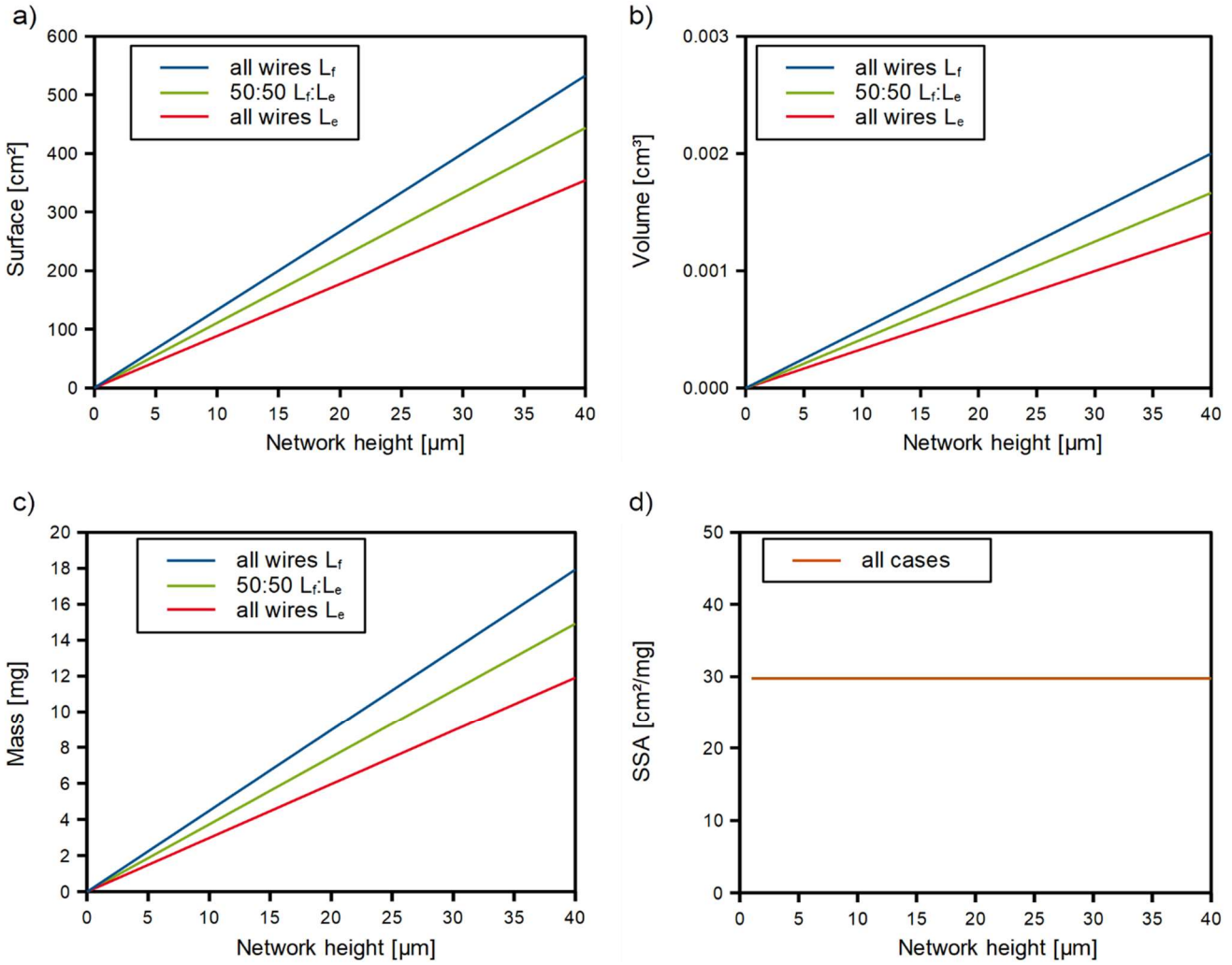


Figure 16: Model calculation of a) surface area, b) volume, c) mass and d) specific surface area as a function of network height for fixed nanowire diameter (150 nm) and number density ($8 \times 10^8 \text{ cm}^{-2}$) on a planar sample of 1.8 cm^2 size.

The surface area, volume and mass increase linearly with increasing network height. This is not surprising, considering that an increase in network height corresponds to longer wires, which is a linear factor in both parts of the surface area calculation given in formula (12) and (13). In these calculations the percentage of wires considered without crossings, that are not counting for surface, mass or volume, is a linear factor. Thus, the slope of the boundary conditions curve for 100 % of the wires having no crossings is higher than for the realistic consideration of 50:50 wire length distribution or even all wires having a reduced wire length by the full number of crossings. The specific surface area of all cases is identical with a value of $29.76 \text{ cm}^2/\text{mg}$, since the slope of surface and mass is equal for each case, thus the division causes a fixed value.

Figure 17 presents a) the calculated surface area A , b) volume V , c) mass m and d) specific surface area ($SSA = \frac{A_{theo}}{m}$) for Cu nanowire networks as a function of nanowire diameter at a constant network height of 30 μm and a fixed nanowire number density of $8 \times 10^8 \text{ wires}/\text{cm}^2$. The graphs represent the upper limit of all wires considered with full length L_f (blue), the lower limit of all wires with reduced length L_e (red), and a realistic value, were 50 % of the wires can be considered as full length and 50 % as effective length (green).

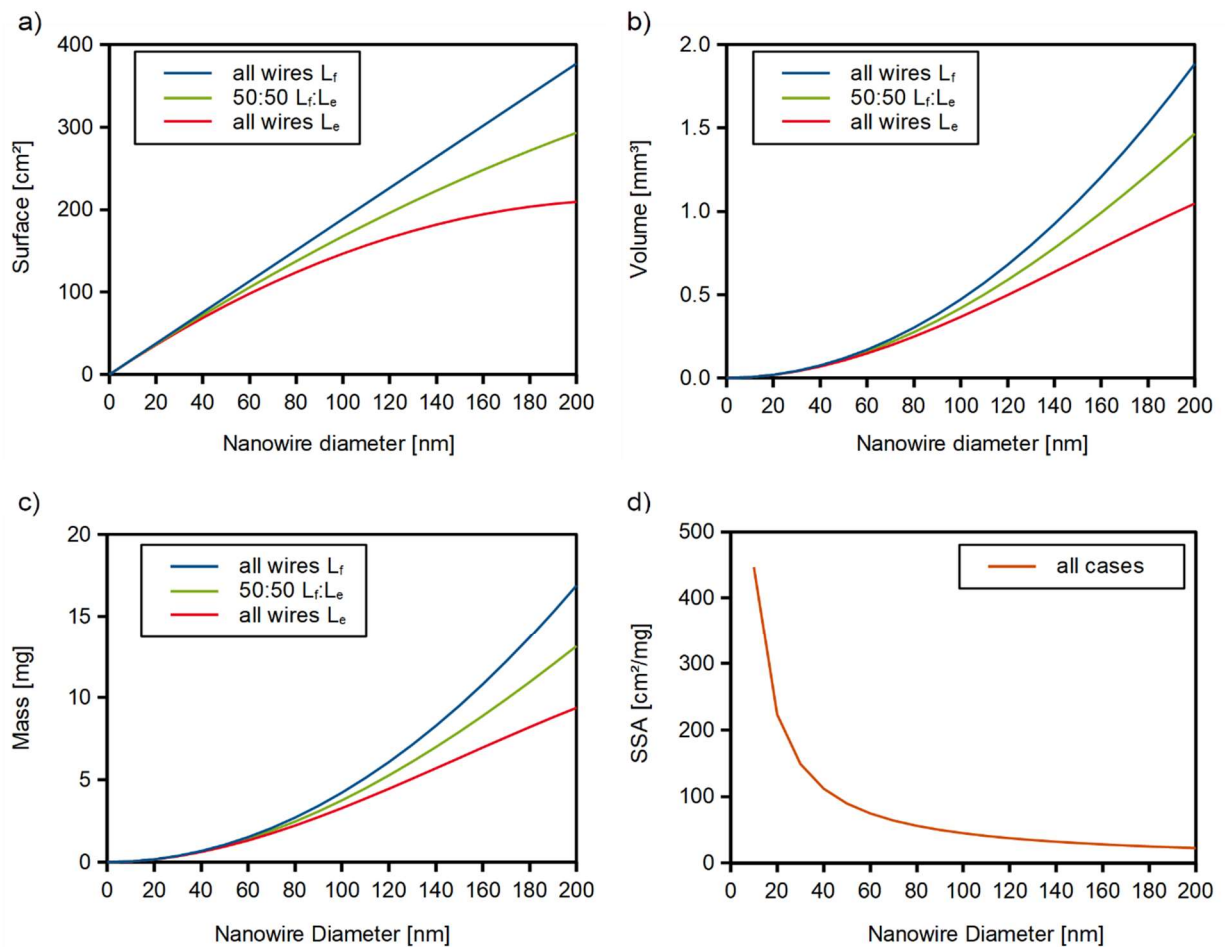


Figure 17: Model calculation for a) surface area A , b) volume V , c) mass m and d) *specific surface area* as a function of nanowire diameter for a nanowire network with a constant network height of 30 μm and a fixed nanowire number density of 8×10^8 wires/ cm^2 on a planar area of 1.8 cm^2 .

Considering all nanowires as full-length wires, the surface area of the network increases linearly with wire diameter. However, as soon as crossings come into play, the increase is sublinear due to the more prominent impact of the surface reduction by crossings between adjacent nanowires with increasing wire diameter. This sublinear increase is even more pronounced for the lower boundary condition when all wires are assumed to have the maximum possible number of crossings. The same effect is observable for the volume and mass model calculations. Here, for the boundary condition of all nanowires considered with maximum length, the curve shows a parabolic behavior, as expected from formula (13). The evolution of the SSA is identical for all three cases, since the considerations regarding the crossings apply equally for mass and surface.

Figure 18 displays the graphs for a) the calculated surface area A , b) volume V , c) mass m and d) specific surface area (SSA) for Cu nanowire networks as a function of nanowire number densities, but constant nanowire diameter of 150 nm and a constant network height of 30 μm .

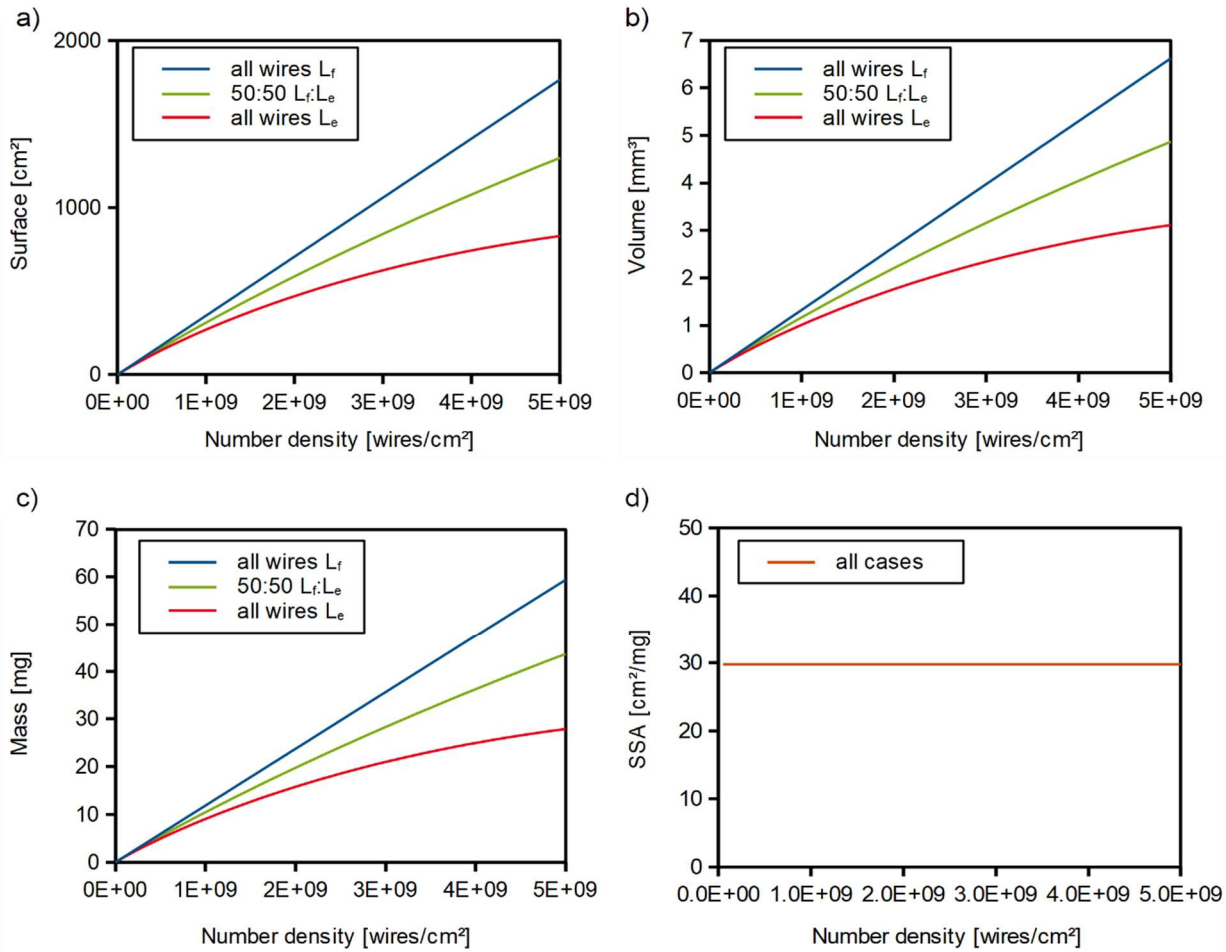


Figure 18: Model calculation of the Cu nanowire networks a) surface area A , b) volume V , c) mass m and d) specific surface area as a function of nanowire number density with constant network height and nanowire diameter of 30 μm and 150 nm, respectively, on a planar area of 1.8 cm^2 .

For changes in the nanowire number density, the curves of surface area, volume and mass follow the same trend for each model case of different wire length distribution. For the boundary condition of all wires having the full length, they increase linearly with the nanowire number density. However, the curves are sublinear, when crossings are considered. Additionally, at high irradiation fluences and large pore diameters, pore overlap occurs in the ion track membranes, which also contributes to this sublinear behavior.

The specific surface area of all networks with different nanowire number densities is identical with a value of 29.76 cm^2/mg , since the curve shapes of surface and mass are equal for each case, thus the division causes a fixed value.

3.2 ECSA determination using the electrical double layer capacitance (C_{DL})

To date, no standardized procedure exists for evaluating catalyst activities. Reported results have thus to be checked carefully regarding their acquisition procedure and especially their normalization to a certain surface area, when comparing different catalyst efficiencies for electrochemical CO₂ reduction [172].

Mainly three methods are used to normalize the activity of an electrocatalyst. One is the mass activity defined as reaction current per catalyst loading. However, this method is not separating the bulk of the catalyst, which is not contributing to catalytic activity. Thus, a normalization to the real surface area provides a better approach. Such a normalization considers the geometric surface activity described by the reaction current normalized to the geometric electrode area. This straightforward method is used for the normalization of the CO₂ reduction activities in this thesis. Another method allowing deeper insight by taking into account also the catalyst structure is the normalization of the catalyst activity regarding the real surface area participating in the reaction, which can be determined as electrochemically active surface area (ECSA) by electrochemical methods such as hydrogen adsorption, surface oxide reduction, CO stripping, metal underpotential deposition, nitrous oxide reactive frontal chromatography [173–176] or determination of the electrical double layer capacitance [177].

The ECSA determination via measurements of the electrical double layer capacitance (C_{DL}) by cyclic voltammetry scans offers the advantage that it takes place in the non-Faradaic region. It thus does not alter the catalyst surface and can be performed in basically every electrolyte [173–175,177,178].

When a metal is inserted into a liquid electrolyte, an electrical double layer (EDL) is formed at its surface, caused by the surface charges. For a given material-solution combination, the surface charges of the metal are defined by number and type of acidic and basic groups of the solution due to protonation or deprotonation [179,180]. The electrical double layer is directly depending on the pH value of the electrolyte with a specific pH value. The situation when the surface charge is neutralized, is called the point of zero charge (pzc). The electrical double layer is formed by ions being bound to the surface by van der Waals forces acting at short distances, as well as by electrostatic interaction of electrolyte ions with the materials surface charge. Those interactions are described by Derjaguin, Landau, Verwey, and Overbeek in the DLVO theory [181], which assumes an infinite flat surface exhibiting a uniform surface charge density. In contrast to those electrostatic forces, van der Waals forces are very insensitive to the electrolyte concentration and pH value [182].

As soon as the pH value of the liquid deviates from the point of zero charge, the surface charges at the liquid-solid interface result in the formation of the EDL as screening layer of oppositely charged counterions to secure charge equalization [156,183,184] and is described as homogeneous layer in the DLVO theory. The Gouy-Chapman-Stern model divides the EDL more precisely in three regions as shown in Figure 19 [182].

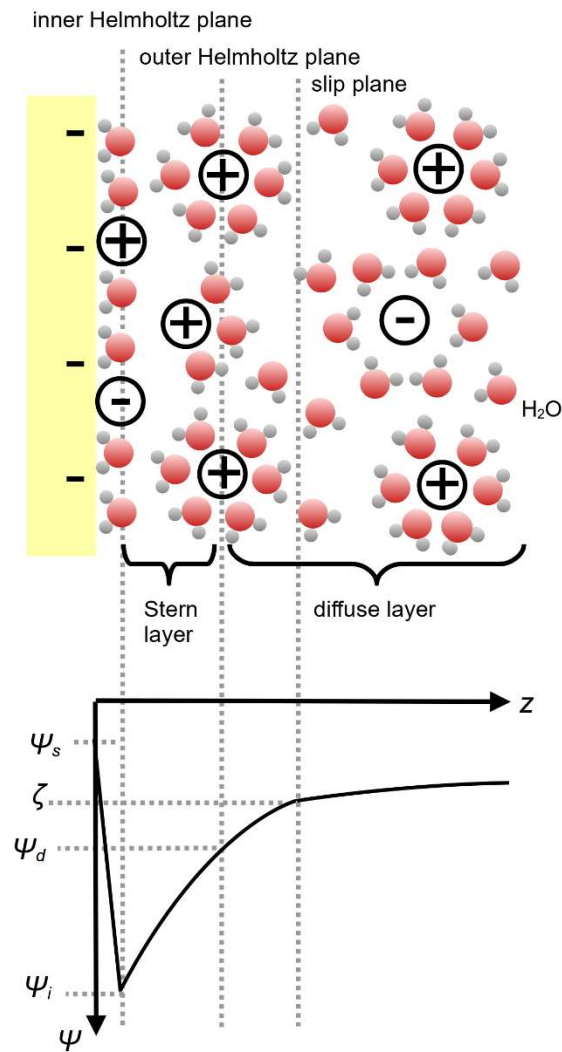


Figure 19: Gouy-Chapman-Stern model of the electrical double layer at the solid-electrolyte interface, with the corresponding potential distribution as a function of distance from the material [182].

The first intermediate layer is called inner Helmholtz plane and consists of co- and counterions, which are non-hydrated and specifically adsorbed on the surface. The second layer is the outer Helmholtz plane and is formed by hydrated and partially hydrated counterions. Between inner and outer Helmholtz plane, the Stern layer is placed, in which charge and potential gradient are assumed to be linear. In the third layer, mobile co- and counterions are present and thus it is called diffuse layer, containing the slip plane. The EDL thickness is directly depending on pH and ionic strength of the liquid [185,186]. Physically the EDL can be treated as capacitor, with its capacitance being dependent on its area and thus directly proportional to the metal surface area [178,187,188].

The application of a potential on a metal electrode immersed in an electrolyte leads to different behaviors in different potential regions, which can be studied by cyclic voltammetry (CV). For certain applied potentials different chemical reactions occur due to charge transfer processes through the electrode/electrolyte interface such as e.g. conversion reactions like surface oxidation and reduction, corrosion reactions like catalyst dissolution, and catalytic reactions like hydrogen or oxygen evolution or

CO₂ reduction reactions. These reactions occur in the so-called Faradaic regions of the CVs and affect the electrical double layer. Therefore, to deduce the electrochemically active surface area from the measurement of the double layer capacitance, a potential window in the CV is chosen where no reaction occurs. These potential windows are called non-Faradaic regions [173]. In the non-Faradaic region, the application of the potential results in a constant current flow related only to the charging and discharging of the EDL.

In the non-Faradaic regions, the differential double layer capacitance C_{DL} is described by formula (14) and (15).

$$C_{DL} = \frac{dQ}{dU} \quad (14)$$

$$I = \frac{dQ(U)}{dt} \quad (15)$$

The measured current I depends directly on a charge Q over time t for an applied potential U , leading to the relation between double layer capacitance C_{DL} and current I as presented in formula (16).

$$I = C_{DL} \cdot \frac{dU}{dt} \quad (16)$$

Consequently, the double layer capacitance C_{DL} is obtained by plotting a set of CV scans with different scan rates around a specific potential in the non-Faradaic region. Taking the current difference ΔI from the distance of the two CV branches and plotting it for various scan rates v , a linear regression is obtained whose slope is C_{DL} according to formula (17) [174,189].

$$C_{DL} = \frac{\Delta I}{v} \quad (17)$$

Finally, the ECSA is obtained by the ratio of the measured C_{DL} of the electrode (here the nanowire network) to the specific double layer capacitance of a sample of well-known surface area A_s of the same material C_s measured in the same electrolyte and setup (equation (18)).

$$ECSA = \frac{C_{DL} * A_s}{C_s} \quad (18)$$

To determine the ECSA by double layer capacitance measurements, a modified polyether ether ketone (PEEK) cell (adapted from the cell proposed by Kuhl et al. [50]), was constructed and employed (Figure 20).

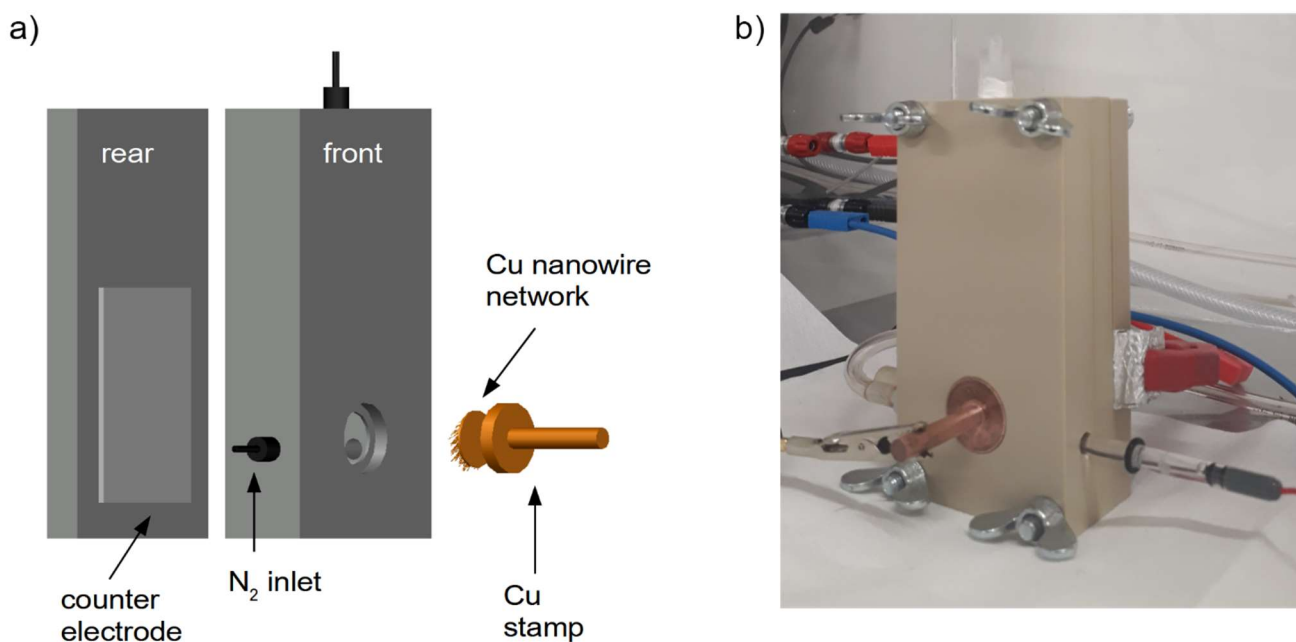


Figure 20: a) Schematics and b) photograph of components of the PEEK electrochemical cell used for double layer capacitance measurements. The nanowire network mounted on a Cu stamp is inserted from the front side. Both front and rear cell parts are screwed together. The counter electrode is electrically contacted from the rear side with an Al foil.

This electrochemical cell (Figure 20) consists of two components: First, the rear part on which a Ti plate is placed as counter electrode that is electrically contacted from the back via an aluminum foil and second, the front part, which has a free space of 13 ml inside, with a N_2 inlet from one side and the Ag/AgCl reference electrode inserted from the other side. The Cu nanowire network is inserted into a circular opening at the front-side plate and kept in place by a Cu stamp, which also contacts it electrically. Thus, the Cu nanowire network is the working electrode. On the top side, this compartment has an exhaust port for the N_2 gas to exit. For the CV measurements, the cell was filled with 13 ml 0.1 M $KHCO_3$ (99 %, Santa Cruz Biotechnology, Dallas, Texas, United States) electrolyte (pH = 7), which is the same one as later used for CO_2 reduction experiments. To ensure that every measured charge can be attributed only to the electrochemical double layer formation and to avoid surface oxidation, the electrolyte was saturated with N_2 by constant purging to remove gas phase hydrogen and oxygen directly from the system.

All CV scans for ECSA determination were performed in this three-electrode setup controlled by a Gamry Interface 1000 potentiostat.

3.2.1 ECSA reference measurements on a flat Cu plate

According to equation (19), the determination of the electrochemically active surface area of the nanowire networks, requires the measurement of the double layer capacitance values of a flat reference plate with a well-known geometrical surface area A_{plate} . $C_{DL_{network}}$ and $C_{DL_{plate}}$ denotes the double layer capacitance values measured for the nanowire network and for the flat reference plate, respectively.

$$ECSA = \frac{C_{DL_network} * A_{plate}}{C_{DL_plate}} \quad (19)$$

A test of the surface area determination by measuring C_{DL} with CV scans in the non-Faradaic region was performed on a pristine Cu plate, which was measured firstly over a surface area of $1.8 \pm 0.1 \text{ cm}^2$ and secondly on a reduced area of $1.1 \pm 0.1 \text{ cm}^2$ obtained by covering parts of the surface with Kapton tape. The results for the C_{DL} deduced from CV scans are presented in Table 1.

Table 1: Geometrical surface areas and C_{DL} of the full Cu plate and the same plate with a surface area reduced with Kapton tape.

	Full size	Reduced size	Relation
Geometrical surface [cm^2]	$1.8 \pm 0.1 \text{ cm}^2$	$1.1 \pm 0.1 \text{ cm}^2$	1.6
C_{DL} [μF]	20.1 ± 0.5	13.7 ± 0.7	1.5

The deviation of the two relations is 6 %, possibly due to surface scratches not being fully equally distributed along the whole plate surface.

This control experiment performed at the Cu plate shows that the ECSA of Cu electrodes can be determined using the double layer capacitance method. These experiments served also to select the appropriate scan rates and potential windows in the non-Faradaic region for further experiments.

To eliminate uncertainties in the surface area, caused by scratches and surface roughness, we used a flat Cu plate with a well-defined lapped and polished surface, prepared at the target laboratory of GSI Helmholtzzentrum, Darmstadt, Germany, as reference for further experiments. The smoothness of the surface was controlled by optical microscopy and profilometry mapping (Veeco Instruments, DEKTAK 8). Analyzing three profilometry maps on an area of $2 \times 2 \text{ mm}^2$ yielded a roughness factor of 1.01, i.e. a flat surface.

For the ECSA determination via C_{DL} of the lapped and polished Cu-plate, first, three CV scans were performed in a region from -0.5 to 0.5 V vs. Ag/AgCl with a scan rate of 10 mV/s in a 0.1 M KHCO_3 electrolyte that are shown in Figure 21 with the non-Faradaic region being indicated.

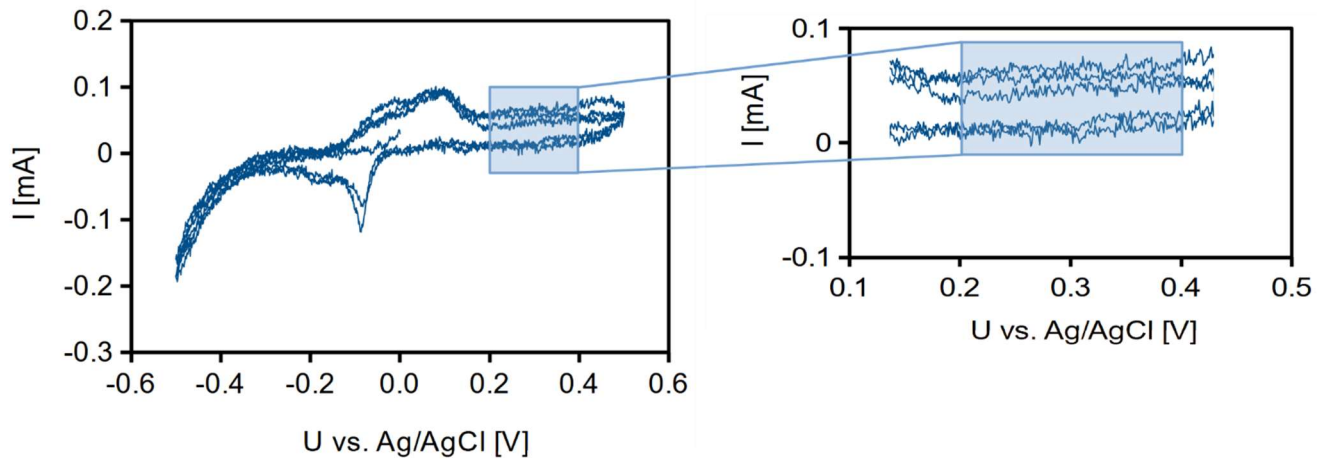


Figure 21: CV scans recorded for a lapped and polished Cu reference plate in 0.1 M KHCO_3 . The blue box shows the non-Faradaic region between 0.2 and 0.4 V.

Figure 22 shows the CV scans for ECSA determination, which were performed around 280 ± 10 mV, 320 ± 10 mV and 360 ± 10 mV using three different scan rates (30 mV/s (blue), 40 mV/s (red) and 50 mV/s (yellow)).

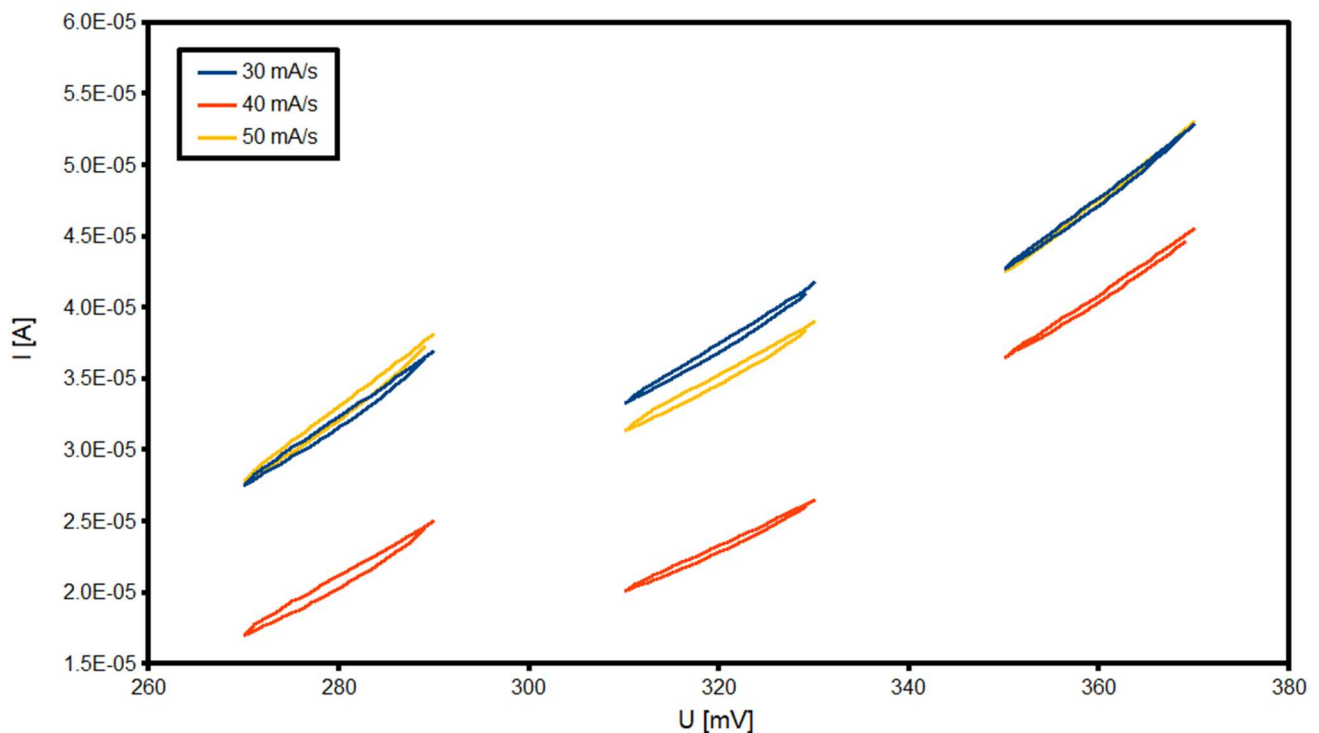


Figure 22: CV scans performed on the 1.8 cm^2 lapped and polished Cu plate with scan rates of 30 (blue), 40 (red) and 50 mV/s (red) at potentials of 280 ± 10 mV, 320 ± 10 mV and 360 ± 10 mV.

The CV scans show an increase in current difference (ΔI) of the two branches of the CV scans with increasing scan rates as given by the definition for the double layer capacitance (equation (17)). The CV scans performed at 40 mV/s are found at slightly different absolute current positions, which might be attributed to a disturbance in the cell setup, probably some increased resistance by dirt or gas bubbles on the counter electrode or reference electrode.

For the calculation of C_{DL} the values obtained by three scans with different scan rates at each potential were averaged. Due to the low roughness factor of the lapped and polished Cu plate, its geometrical area of $1.8 \text{ cm}^2 \pm 0.1 \text{ cm}^2$ is assumed to be the actual surface area. Thus, the measured double layer capacitance $C_{DL} = 14.3 \pm 2.4 \text{ } \mu\text{F}$ provides the reference double layer capacitance $C_{ref} = 8.1 \pm 1.4 \text{ } \mu\text{F}/\text{cm}^2$.

3.2.2 ECSA determination of Cu nanowire networks

Figure 23 shows three consecutively measured CVs of a Cu nanowire network with a base area of 1.8 cm^2 , height $30 \text{ } \mu\text{m}$, wire diameter 150 nm , and nanowire number density $2 \times 10^9 \text{ cm}^{-2}$. The CVs were recorded with a scanning rate of 10 mV/s from $U = -0.5 \text{ V}$ to $U = 0.5 \text{ V}$ vs. Ag/AgCl, to determine the non-Faradaic region.

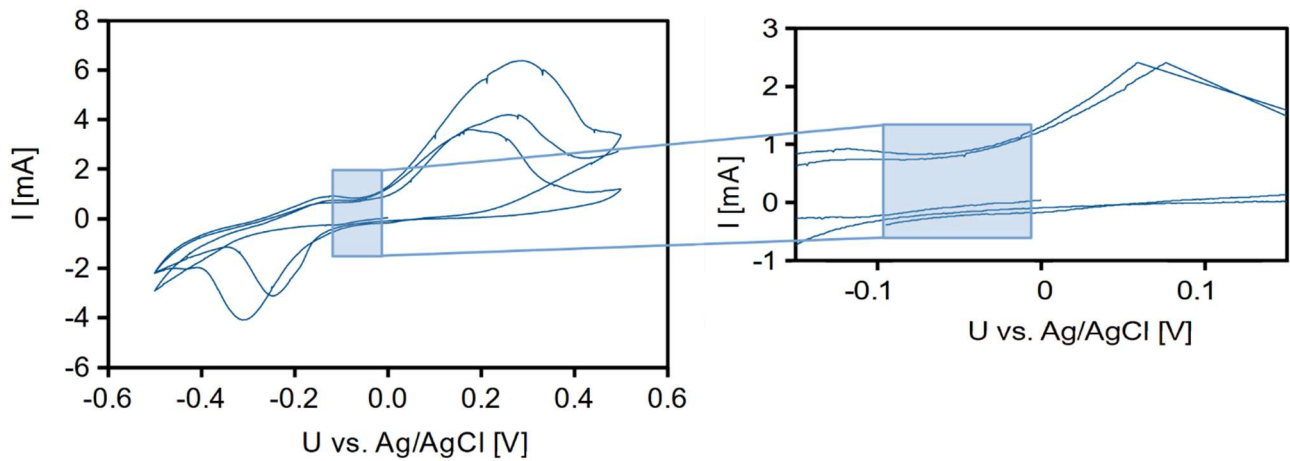


Figure 23: Three CV scans for a representative Cu nanowire network (1.8 cm^2 area, $30 \text{ } \mu\text{m}$ height, 150 nm nanowire diameter, $2 \times 10^9 \text{ cm}^{-2}$ nanowire number density) recorded between $U = -0.5 \text{ V}$ and $U = 0.5 \text{ V}$ (vs. Ag/AgCl) at a scan rate of 10 mV/s . The non-Faradaic region is highlighted in the light blue box.

The CVs display an oxidation peak at $\sim 0.3 \text{ V}$ and a reduction peak at $\sim -0.3 \text{ V}$, as well as a non-Faradaic region from -0.1 V to 0 V vs. Ag/AgCl. To provide a clean surface for the following measurements, each CV was stopped at 0 V at the end of a branch coming from the reductive potential region.

In the next step, additional CV scans in a region of $\pm 10 \text{ mV}$ around -90 mV , -70 mV , -50 mV and -20 mV were performed with different scan rates of 30 mV/s , 40 mV/s and 50 mV/s each to determine the C_{DL} of the nanowire networks as shown exemplary in Figure 24 for a Cu nanowire network with $h = 30 \text{ } \mu\text{m}$, $d = 150 \text{ nm}$ and number density $= 4 \cdot 5 \times 10^8 \text{ cm}^{-2}$.

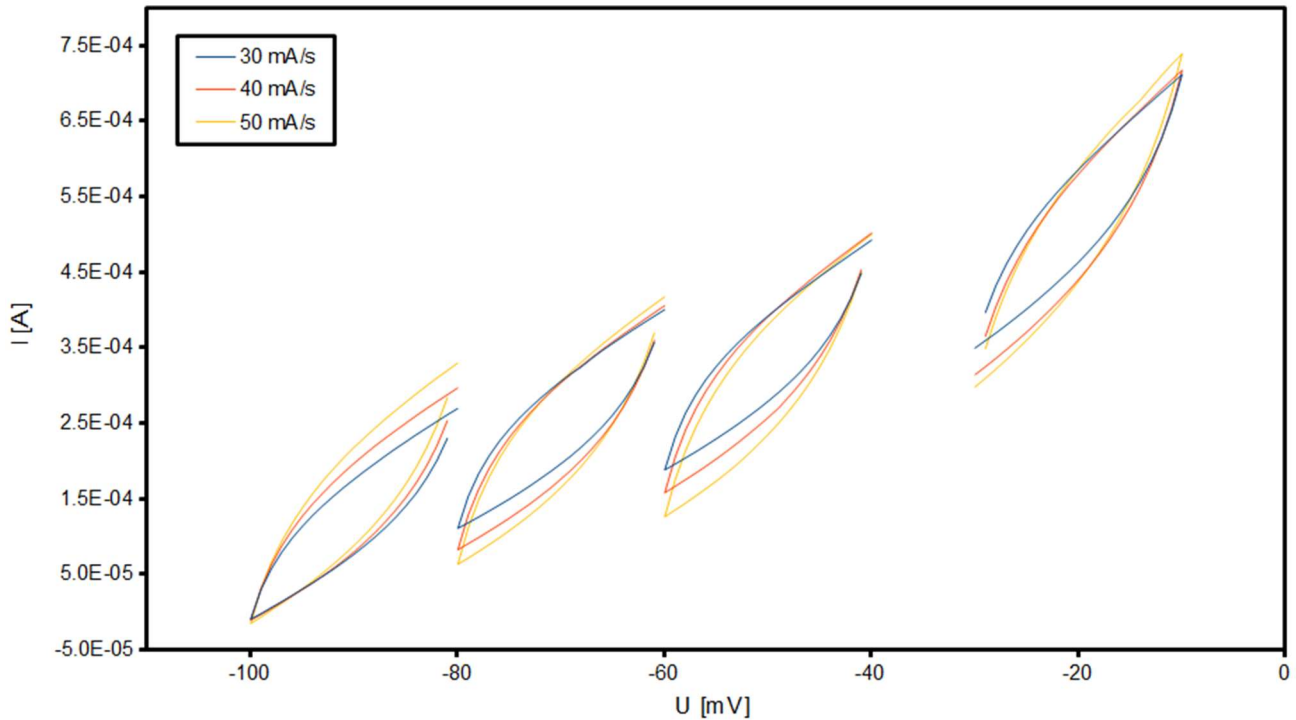


Figure 24: CV scans with scan rates of 30 mV/s, 40 mV/s and 50 mV/s at potentials of -90 ± 10 mV, -70 ± 10 mV, -50 ± 10 mV and -20 ± 10 mV.

The values for ΔI and thus also for C_{DL} deduced from these CV scans are larger than the ones for the lapped and polished Cu plate due to the larger ECSA of the nanowire networks. At each potential, ΔI strongly increases for larger scan rates as expected from the C_{DL} definition. Additionally, the CV scans slightly shift for the different scan rates at each potential, but this does not influence the resulting ΔI values.

3.2.3 ECSA of Cu nanowire networks with different network heights

A measurement series was conducted for nanowire networks with different heights. The C_{DL} determined by CV scans in the non-Faradaic region was then divided by the reference C_{DL} (C_{ref}) of the lapped and polished Cu plate to get the ECSA of the nanowire network. Figure 25 compares the measured ECSA values (black) with the geometrical surface area of the model calculation for the realistic case with an equidistribution of the nanowires with full and with reduced length (red line) adapted to the same geometrical network parameter, i.e. planar sample area, nanowire diameter, nanowire number density and network height. All nanowire networks of this series had a wire diameter of 150 ± 5 nm and a nanowire number density of $8 \times 10^8 \pm 8 \times 10^7$ cm⁻² on a planar sample area of 1.8 cm² determined by pore counting on SEM images. The analysis of the respective SEM images was conducted on five areas of 300 μ m² each, distributed regularly over the whole membrane to average beam inhomogeneities. The nanowire diameter was measured on SEM images of the nanowire networks, while the network height was determined by SEM cross section imaging after the ECSA determination measurements.

Due to the random nanowire arrangement, the precise number of intersections cannot be determined. The calculated surface S_{theo} values therefore have an uncertainty, which is represented in Figure 25 by the shaded areas around the solid lines.

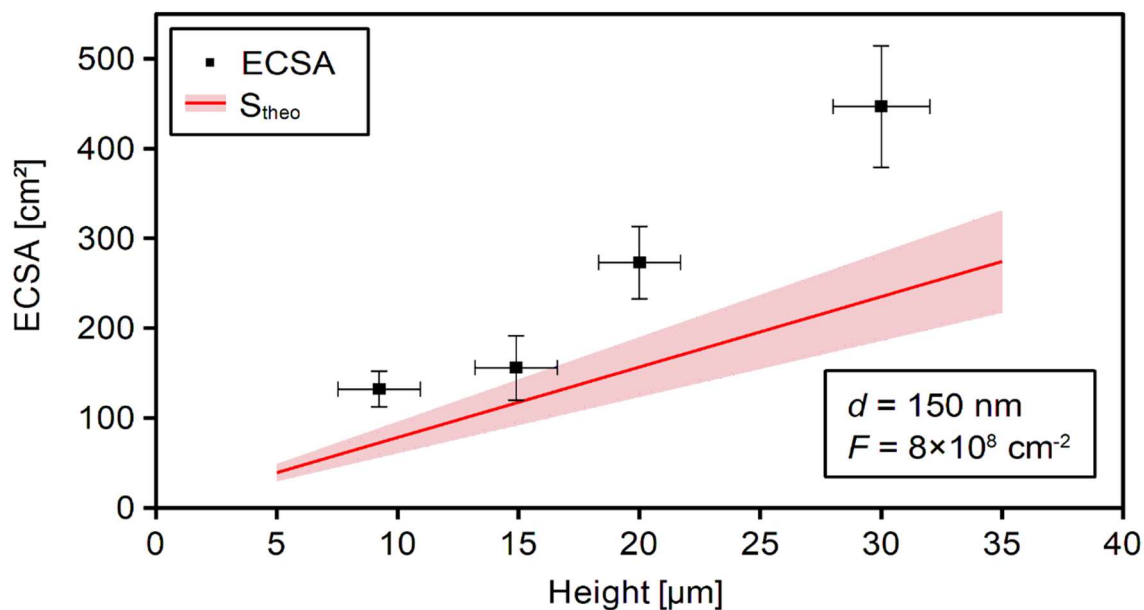


Figure 25: Experimentally determined ECSA values (black squares) and calculated theoretical surface areas (red line) (shaded areas indicate uncertainties in the model due to the stochastic nanowire arrangement) of Cu nanowire networks with systematic variations of the network height h . The inset displays the fixed wire parameters of this series.

The measured ECSA values increase from $133 \pm 20 \text{ cm}^2$ to $447 \pm 68 \text{ cm}^2$ with increasing network heights from $9 \pm 1 \text{ }\mu\text{m}$ to $30 \pm 1 \text{ }\mu\text{m}$. Considering the error bars, this increase could be regarded as rather linear as expected due to the linear influence of the network height on the surface area.

ECSA values smaller than the theoretical surface area for individual networks could be expected due to the presence of contaminations (e.g. polymer residues) on the nanowire surface, diminishing the contact area with the electrolyte. But surprisingly, this is not the case here. All our experimentally determined ECSA values are higher than the theoretical surface area by almost a factor of 1.8. These higher values are attributed to the surface roughness of the nanowires, which increases significantly during the acidic pre-cleaning treatment, as shown exemplarily for a network of $30 \text{ }\mu\text{m}$ height in Figure 26. The calculations of the geometrical surface area presented in section 3.1 do not take the nanowire roughness into account but assume smooth cylinders.

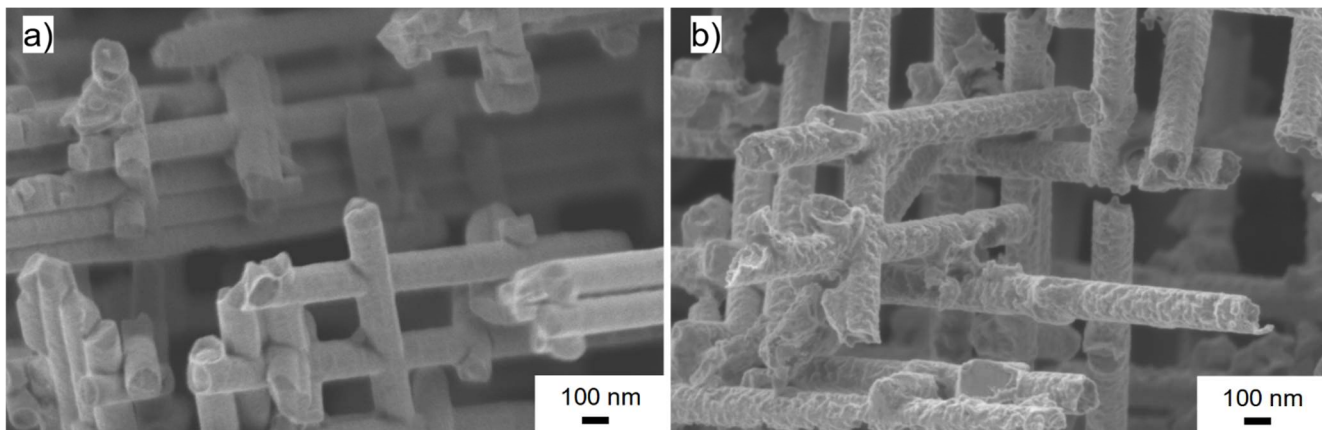


Figure 26: Nanowire network a) before and b) after the acidic pre-cleaning process. The as-synthesized networks have a smooth surface while acidic cleaning obviously roughens the wire surface.

3.2.4 ECSA of Cu nanowire networks with different nanowire diameter

In a second series, the ECSA of nanowire networks with different nanowire diameter was determined via the double layer capacitance method. Figure 27 shows the measured ECSA values for the nanowire networks with average wire diameter of 113 ± 4 nm, 142 ± 4 nm and 171 ± 4 nm (black) together with the theoretical values from the model calculation (red line) taking into account a realistic wire length distribution regarding the number of crossings. The respective SEM images of these networks are shown in

Figure 28. All other geometrical parameters of the network were kept the same i.e. a height of 30 ± 1 μm , a nanowire number density of $8 \times 10^8 \pm 8 \times 10^7$ cm^{-2} and a planar sample area of 1.8 cm^2 .

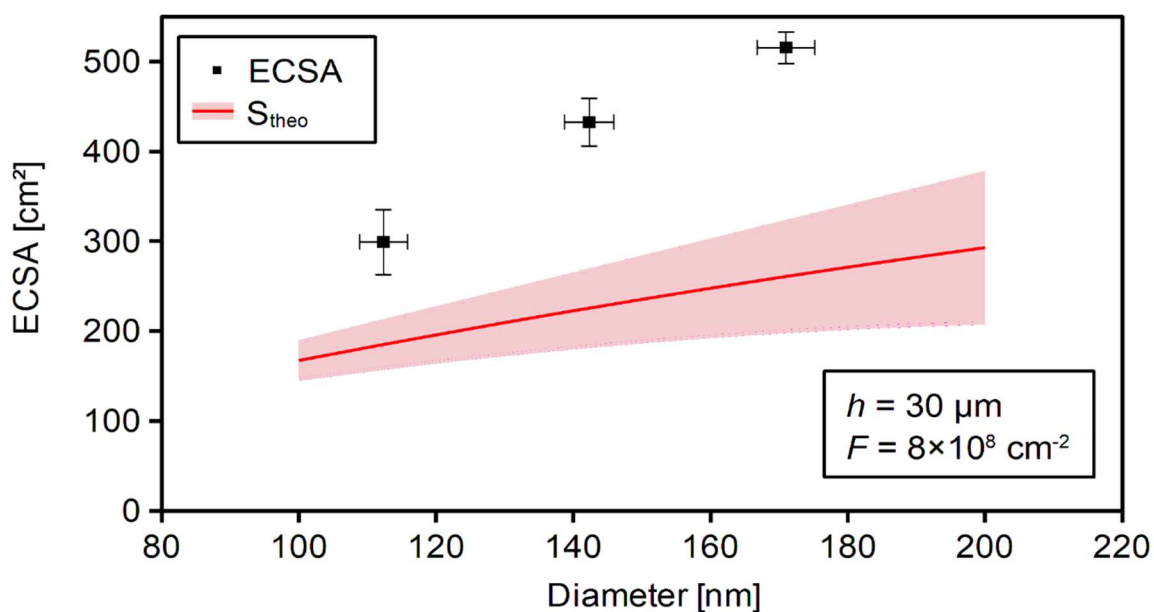


Figure 27: Experimentally determined ECSA values (black squares) and calculated theoretical surface areas (red line) (shaded areas indicate uncertainties due to the stochastic nanowire arrangement) of Cu nanowire networks with systematic variations of the nanowire diameter d . The inset displays the fixed parameters for this series.

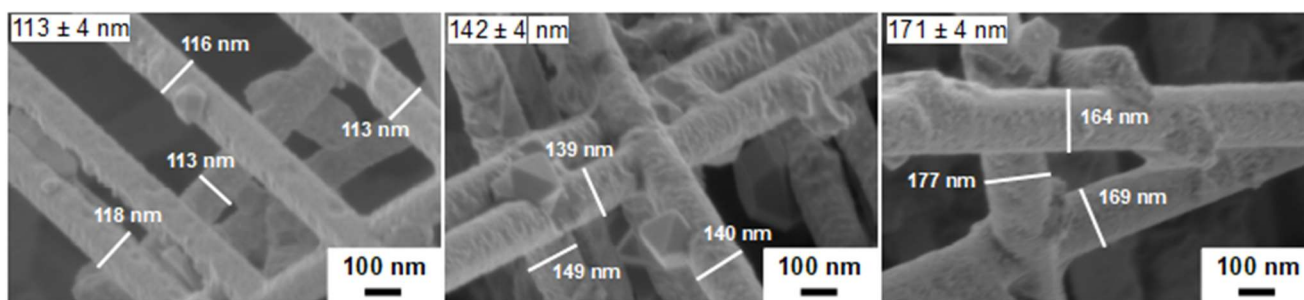


Figure 28: SEM images of Cu nanowire networks with different wire diameter used for ECSA determination. The images were taken after the acidic pre-cleaning, but before the ECSA measurement. The inset displays the average nanowire diameter calculated from 10-20 nanowires measured as shown exemplarily in the images.

The measured ECSA values increase with nanowire diameter, as expected from the theoretical model calculation. In the experimental values, as well as in the model calculation this increase is slightly sublinear, due to the more prominent impact of the surface reduction by crossings for larger wire diameters. Thus, the behavior of the measured ECSA values correlates well with the theoretical calculations.

However, all measured ECSA values are again up to a factor of 1.8 larger than the theoretical values. This effect is again ascribed to the surface roughness, which is observable in

Figure 28 and caused by the acidic pre-cleaning treatment.

3.2.5 ECSA of Cu nanowire networks with different nanowire number density

In a third series, the ECSA of nanowire networks with different nanowire number density was determined. The nanowire number density for the networks was determined by pore counting on SEM images of the corresponding etched ion-track membrane before electrodeposition of the Cu nanowires, as described in section 2.2. A comparison of the measured ECSA values of networks with nanowire number densities of $1.8 \times 10^8 \text{ cm}^{-2}$, $4.2 \times 10^8 \text{ cm}^{-2}$, $8 \times 10^8 \text{ cm}^{-2}$ and $1.1 \times 10^9 \text{ cm}^{-2}$ (black) with the model calculations for the realistic crossing number (red line) is shown in Figure 29. All other geometrical parameters were kept the same for the nanowire networks, with a network height of $30 \pm 1 \mu\text{m}$, a nanowire diameter of $150 \pm 5 \text{ nm}$ and a planar sample area of 1.8 cm^2 .

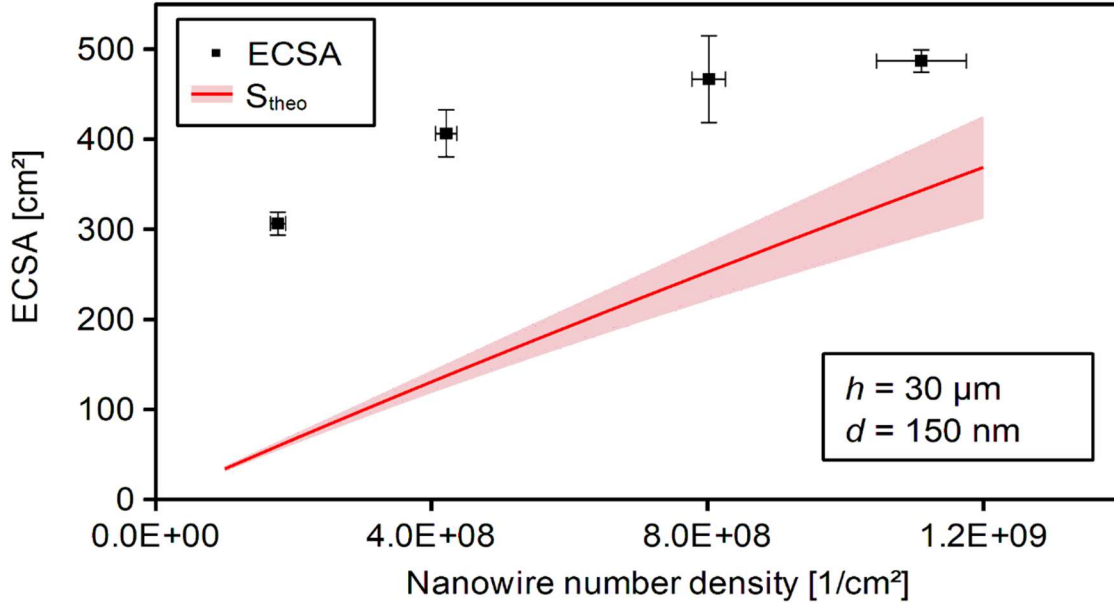


Figure 29: Experimentally determined ECSA values (black squares) and calculated theoretical surface areas (red line) (shaded areas indicate uncertainties due to the stochastic nanowire arrangement) of Cu nanowire networks with systematic variations of the nanowire number density F . The inset displays the fixed parameters for this series.

As presented in Figure 29, the measured ECSA of the Cu nanowire networks, as well as the geometrical surface area from the model calculation does not increase linearly with nanowire number density. This behavior is again due to the increasing amount of nanowire crossings with increasing nanowire number density, which reduces the effective nanowire length with the exposed nanowire surface, coinciding with the model calculation presented in chapter 3.1.

Due to the nanowire roughening caused by the pre-cleaning treatment, the measured values are again larger than the ones predicted by the theoretical model calculation. For the nanowire networks with a nanowire number density of $1.8 \times 10^8 \text{ cm}^{-2}$ the ECSA is by a factor of 5.2 higher than the geometrical surface area (S_{geo}). The factor of this increase gets smaller with increasing nanowire number density, via values of 2.9 for $4.2 \times 10^8 \text{ cm}^{-2}$, 1.7 for $8 \times 10^8 \text{ cm}^{-2}$ towards 1.4 for $1.1 \times 10^9 \text{ cm}^{-2}$. This decrease in influence of the surface roughness with increasing nanowire number density is also coming from the increase in the number of crossings, which is reducing the exposed surface area of the nanowires between them. Thus, the surface area on which the roughness has an influence gets smaller, decreasing the impact of the roughness, which causes a smaller difference to the model calculation. This decreasing influence in roughness effect also explains the decrease of the curve slope for the measured ECSA values with increasing number density.

In all cases the measured ECSA values are higher than the corresponding geometrical surface areas from the model calculations. For the series with different network height and different nanowire diameter, this surface area increase caused by roughness is relatively constant by a factor of 1.8. For the series with varying nanowire number density, this increase factor decreases with increasing nanowire number density, which is explainable by the larger number of crossings. Overall, the data follow an expected

behavior without inconsistencies which demonstrates that the whole surface area of the nanowire network is electrochemically active and thus available for chemical reactions.

All nanowire networks presented ECSA values up to 500 cm² on a flat sample area of only 1.8 cm² which is an increase by a factor of almost 300.

In each of the above series, one nanowire network had identical geometrical parameter, their respective ECSA and capacity values are summarized in Table 2. They show excellent agreement within the experimental uncertainties.

Table 2: Double layer capacity C_{DL} and ECSA values for different samples with identical geometrical parameters (30 μm network height, 150 nm wire diameter and a nanowire number density of $8 \times 10^8 \text{ cm}^{-2}$ on a planar sample area of 1.8 cm²) from independent ECSA determination measurements.

	C_{DL} [mF]	ECSA [cm²]
From series with different height	3.6 ± 0.5	447 ± 68
From series with different diameter	3.5 ± 0.2	433 ± 27
From series with different number density	3.6 ± 0.3	450 ± 37

Nanowire networks with these geometrical parameters of 30 μm network height, 150 nm nanowire diameter and a nanowire number density of $8 \times 10^8 \text{ cm}^{-2}$ were used as catalyst for the CO₂ reduction experiments in this thesis since they provide an ECSA of $\sim 440 \text{ cm}^2$ on a planar sample area of only 1.8 cm², which is a surface area increase by a factor of almost 250. Additionally, they obtain excellent mechanical stability by still providing enough porosity between the wires to allow sufficient gas and liquid transport. On the other hand, as stated in chapter 4.2 the nanowire interspace is small enough to limit release and diffusion of the intermediate products to promote C-C coupling for C₂+ product formation.

4 Cu nanowire networks as catalyst for electrochemical CO₂ reduction

4.1 Electrochemical CO₂ reduction

The application of CO₂ as feedstock for the electrochemical synthesis of value-added chemicals is already used industrially for the synthesis of urea [190], salicylic acid [191], cyclic carbonates [192,193] and polyols [194]. Currently a lot of research is progressing, evaluating the necessary processes and catalysts to economically convert CO₂ into other more advanced chemicals [34–37], especially methane or methanol that can be used as synthetic fuels [195–202]. These processes offer the opportunity to include CO₂ reduction reactions into a sustainable carbon cycle as shown in Figure 30 [203].

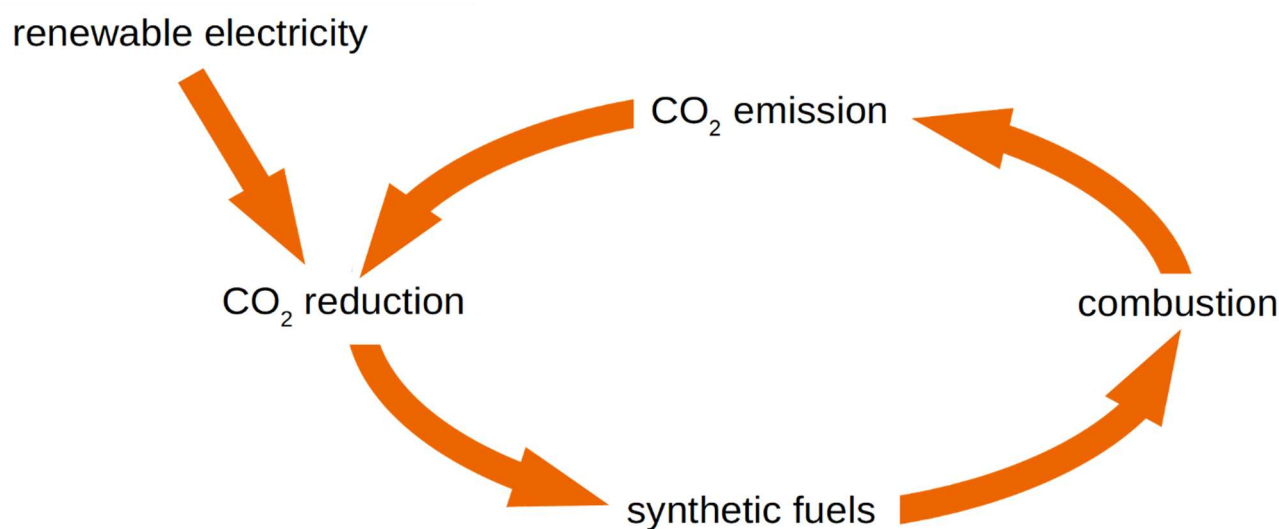


Figure 30: Scheme of a sustainable carbon cycle based on the transfer of CO₂ into synthetic fuels by electrochemical CO₂ reduction reactions [203].

Since CO₂ is one of the most stable molecules, energy has to be applied to transform it into other chemicals by reduction reactions. Usually this energy is provided by the application of an electric potential, which delivers electrons that are consumed in the reduction reactions [204]. The thermodynamic standard electrode potential E^0 at standard conditions for the CO₂ reduction reaction is defined by formula (20).

$$E^0 = -\frac{\Delta G^0}{nF} = -\frac{\Delta H^0 - T \cdot \Delta S^0}{nF} \quad (20)$$

With ΔG^0 being the change of Gibbs free-energy, ΔH^0 the enthalpy change, T the reaction temperature, ΔS^0 the entropy change, n the amount of transferred electrons per atom and F the Faraday constant [156,178,205].

The resulting thermodynamic equilibrium potentials versus reversible hydrogen electrode (RHE) at pH = 7 for half-cell reactions of CO₂ to several value-added chemicals are provided in Table 3.

Table 3: Half-cell reactions and standard equilibrium potentials for CO₂ reduction reactions to value added chemicals in aqueous solution at pH = 7 [50,206,207].

Product	Half-cell reaction	E ⁰ vs. RHE [V]
carbon monoxide	$\text{CO}_2 + \text{H}_2\text{O} + 2 \text{e}^- \rightleftharpoons \text{CO} + 2 \text{OH}^-$	-0.10
formate	$\text{CO}_2 + \text{H}_2\text{O} + 2 \text{e}^- \rightleftharpoons \text{HCOO}^- + \text{OH}^-$	-0.02
methanol	$\text{CO}_2 + 5 \text{H}_2\text{O} + 6 \text{e}^- \rightleftharpoons \text{CH}_3\text{OH} + 6 \text{OH}^-$	0.03
methane	$\text{CO}_2 + 6 \text{H}_2\text{O} + 8 \text{e}^- \rightleftharpoons \text{CH}_4 + 8 \text{OH}^-$	0.17
ethylene glycol	$2 \text{CO}_2 + 8 \text{H}_2\text{O} + 10 \text{e}^- \rightleftharpoons \text{C}_2\text{H}_6\text{O}_2 + 10 \text{OH}^-$	0.20
ethylene	$2 \text{CO}_2 + 8 \text{H}_2\text{O} + 12 \text{e}^- \rightleftharpoons \text{C}_2\text{H}_4 + 12 \text{OH}^-$	0.08
ethanol	$2 \text{CO}_2 + 9 \text{H}_2\text{O} + 12 \text{e}^- \rightleftharpoons \text{C}_2\text{H}_5\text{OH} + 12 \text{OH}^-$	0.09
n-propanol	$3 \text{CO}_2 + 13 \text{H}_2\text{O} + 18 \text{e}^- \rightleftharpoons \text{C}_3\text{H}_7\text{OH} + 18 \text{OH}^-$	0.21

Each of these CO₂ reduction reactions is a multi-step reaction. Thus, kinetic barriers have to be overcome and more energy than suggested by the equilibrium potential is necessary for a successful reaction. This more negative potential that needs to be applied for a certain reduction reaction to happen is called overpotential. Overpotentials can be reduced tremendously by suitable catalysts that either lower the energy that is needed for the formation of intermediates or open new reaction pathways leading to an increased product formation rate and thus a higher reaction efficiency [178,208].

The ratio of the different products resulting from a CO₂ reduction reaction is called selectivity and since the standard equilibrium potentials are all relatively close together, a good catalyst has to reduce the overpotential of only one reaction significantly to enhance the selectivity. Additionally, the CO₂ reduction reaction in aqueous electrolyte is always competing with the hydrogen evolution reaction (HER), which occurs at a similar equilibrium potential (0 V vs. SHE). Thus, a good catalyst to enhance CO₂ reduction efficiency should also suppress or minimize the HER [209–211].

The electrochemical CO₂ reduction reaction products in heterogeneous catalysis, i.e. when inserting a metal as not consumed catalyst electrode into the electrolyte, strongly depend on the type of material used as catalyst [56,162–164,212]. While Hg, Cd, Pb, Ti, Sn or In reduce CO₂ primarily to formate (HCOO⁻) at high overpotentials [165] and Au, Ag, Zn mainly generate carbon monoxide (CO) [165,213], Cu is the only metal that possesses the ability to transform CO₂ electrochemically into a mixture of advanced hydrocarbons [3,45,50]. Additionally, CO₂ reduction at Cu benefits from less favorable HER compared to other metals.

The selectivity towards certain products during the CO₂ reduction is described by the Faradaic efficiency (FE), which is the yield of electrons for the reaction towards one certain product. The CO₂ reduction on Cu is currently widely studied, since especially a tuning of the selectivity into the direction of multi-carbon C₂₊ products is still desired [37,214]. It is known that the product selectivity of CO₂ reduction reactions at Cu surfaces is influenced by the electrolyte type, concentration and pH-value [49,57,215], the applied reduction potential [50] and the topology and crystallographic surface orientation of the Cu catalyst

[51,129,130]. By the comparison of crystalline Cu nanoparticles to spherical Cu nanoparticles it was shown that (100) facets support the formation of ethylene (C_2H_4) and (111) facets support the formation of methane (CH_4) [216]. Cu single-crystals with a (110) surface orientation promote C_2 -binding, leading to a higher selectivity towards C_2+ products [217].

To understand selectivity trends and to successfully tune catalyst structures, it is of key importance to know the CO_2 reduction reaction mechanisms towards a certain product. Thus, this has been a major topic of research in the community. As shown in Figure 31, all CO_2 reduction reaction mechanisms start with the reduction of CO_2 towards a simple intermediate such as carbon monoxide (CO) or formate ($HCOO^-$) and its binding as adsorbate on an active center of the Cu catalyst surface [218]. The latter is an energy intensive step as it includes a change of the atomic arrangement in the molecule from a linear towards a bent structure. Due to this required high energy, this step is always considered as the first rate-determining step (RDS) [219].

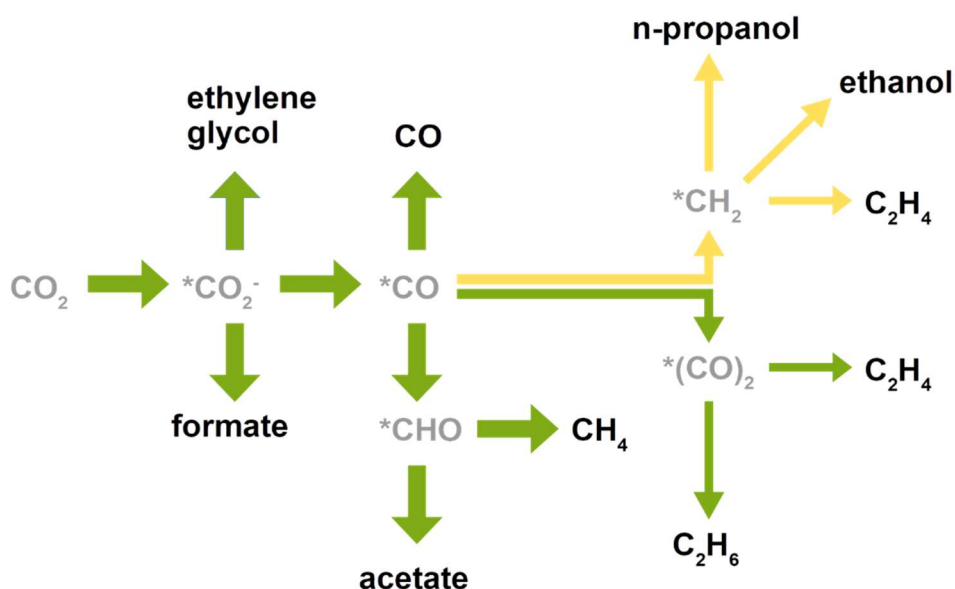


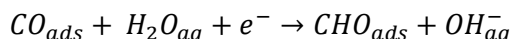
Figure 31: Proposed CO_2 reduction reaction pathways for hydrocarbon products (black) via intermediates (grey) on Cu catalysts, as indicated by studies with dendritic Cu foam catalysts modified by ionic liquids. The carbene pathways are marked with yellow arrows, the dimerization pathways in green [53].

Two binding arrangements of the CO_2 molecule on the surface are possible during this first reduction step. On the one hand, one or two oxygen atoms can bind to the surface, forming an $*OCHO$ intermediate that is reduced further on and desorbed as $HCOOH$ or $HCOO^-$. On the other hand, the carbon atom can bind to the catalyst as $*COOH$, and then be further reduced by releasing an OH^- ion. In this latter case, further reduction to $*CO$ occurs, which can either be released as product or reacts onwards by coupled electron-proton transfers to $*CH_2OH$ and finally methanol (CH_3OH). There are more reaction possibilities for this adsorbed $*CO$, which are, e.g. (i) oxygen loss and reduction towards $*CH_3$ and then desorption as CH_4 or (ii) pairing

of neighboring adsorbates in different hydrogenation states and further reaction towards more advanced C2 and C3 products [162,219–221]. The hydrogenation of the adsorbed *CO intermediate can proceed via two reaction pathways. One of them is the Tafel-process, where adsorbed *CO and adsorbed *H react to adsorbed *CHO [222].



Another possibility is the hydrogenation occurring via a Heyrovsky process where the adsorbed *CO reduces and reacts with water from the electrolyte [222].



This *CHO intermediate is formed as only type of hydrogenated intermediate at Au and Ag surfaces, whereas another hydrogenated form in the shape of *COH occurs as sole intermediate on Co, Ni, Rh, Pd, Ir and Pt catalysts. Cu is the only metal allowing the formation of both hydrogenated *CO intermediate forms [58].

Various pathways are proposed for the reaction of intermediates towards C2+ products. For the first C-C bond formation step of two adsorbed intermediates, two possibilities exist, which were shown by density functional theory (DFT) to depend on the applied overpotential. At low overpotentials dimerization of adsorbed *CO molecules is the preferred process, whereas at high overpotentials an adsorbed *CO reacts with an adsorbed, hydrogenated *CHO molecule [222].

The formation of ethylene glycol (C₂H₆O₂) is proposed to occur via dimerization of two adsorbed *CO accompanied by a protonation [3,50]. However, recent studies using ionic liquids suppressing the *CO₂- showed less efficiency for C₂H₆O₂ formation. This finding leads to the conclusion that its formation more likely occurs via the dimerization of two adsorbed *CO₂- molecules [53] forming an oxalate species that reacts on to C₂H₆O₂ which was proposed earlier as possible pathway [223]. The dimerization of two adjacent adsorbed *CO molecules with further reduction and protonation also leads to C₂H₄ product formation. In the course of this process, one adsorbed *CO needs to be transferred into an adsorbed *OCH intermediate [53].

Ethane (C₂H₆) results from the reduction product of C₂H₄ after two more protonation steps. Significant Faradaic efficiencies were only observed in nanoporous Cu catalysts, the formation of C₂H₆ is therefore attributed to re-adsorption and reduction of C₂H₄ [3,224,225]. Newer studies using ionic liquids for suppressing the C₂H₄ formation have shown no influence of the ionic liquid on the C₂H₆ formation efficiency [53]. Thus, a CO dimerization pathway via an ethoxy intermediate is proposed for the C₂H₆ formation [134,226].

Ethanol (C₂H₆O) is considered to follow similar reaction pathways as C₂H₄ [227,228]. However, studies with ionic liquids revealed suppressed C₂H₄ formation, thus this pathway is ruled out [53].

The same applies to the synthesis of n-propanol (C_3H_8O), which, as generally accepted, undergoes intramolecular C-C coupling between adsorbed CO and adsorbed carbene intermediates to form propionaldehyde (C_3H_6O), which is further reduced to C_3H_8O [227–229]. Thus C_3H_8O is also only formed via the carbene pathway [53].

The other family of reaction pathways for C_2+ product formation is predominant at higher overpotentials. They are called carbene pathways and include the direct hydrogenation of adsorbed $*CO$ into either $*CHO$ or $*COH$. The latter is directly reduced to $*CH_2$ and then transferred by C-C coupling between two $*CH_2$ or CO insertion into ethylene [230].

Additionally, the formation of acetate ($C_2H_3O_2^-$) is proposed to occur via CO_2 addition to an adsorbed $*CH_3$ molecule, which is formed previously from dehydrogenization of $*CH_2OH$ coming from two times hydrogenation of an adsorbed $*CO$ [53].

Porous structures have shown to tune the product selectivity into a certain direction, by being energetically favorable for a specific reaction mechanism. Thus, systematic variations of the surface structure have been a valuable tool to gather further insights into the reaction selectivity towards certain products [52–55] and to clarify the proposed reaction mechanisms [56–59].

However, the electrochemical CO_2 reduction reaction at porous electrodes is a highly complex process, influenced by many factors. The electrochemical reaction conditions like local reactant concentration and pH value, as well as temperature and applied potential directly play a role. Furthermore, the mass transport of gaseous and liquid reactants and products along the porous electrode structure are crucial factors for the reaction selectivity and efficiency. They are influenced by convection, diffusion and migration as well as the wettability of the porous electrode. Finally, the reactions are also influenced by phase transitions of molecules during the reaction. For the CO_2 reduction reaction, the gaseous CO_2 needs to be dissolved in the electrolyte and to be reduced towards a product, which can be released as gaseous bubbles, or remain dissolved in the liquid electrolyte as well. Not only do these phase transitions consume energy, but also evaporation or trapping of reactants and products by the catalyst structure must be considered, since they can favor the reaction mechanism in a certain direction [52].

Recently, numerous Cu nanostructures, as shown exemplary in Figure 32, have been studied regarding their CO_2 reduction efficiency and product selectivity.

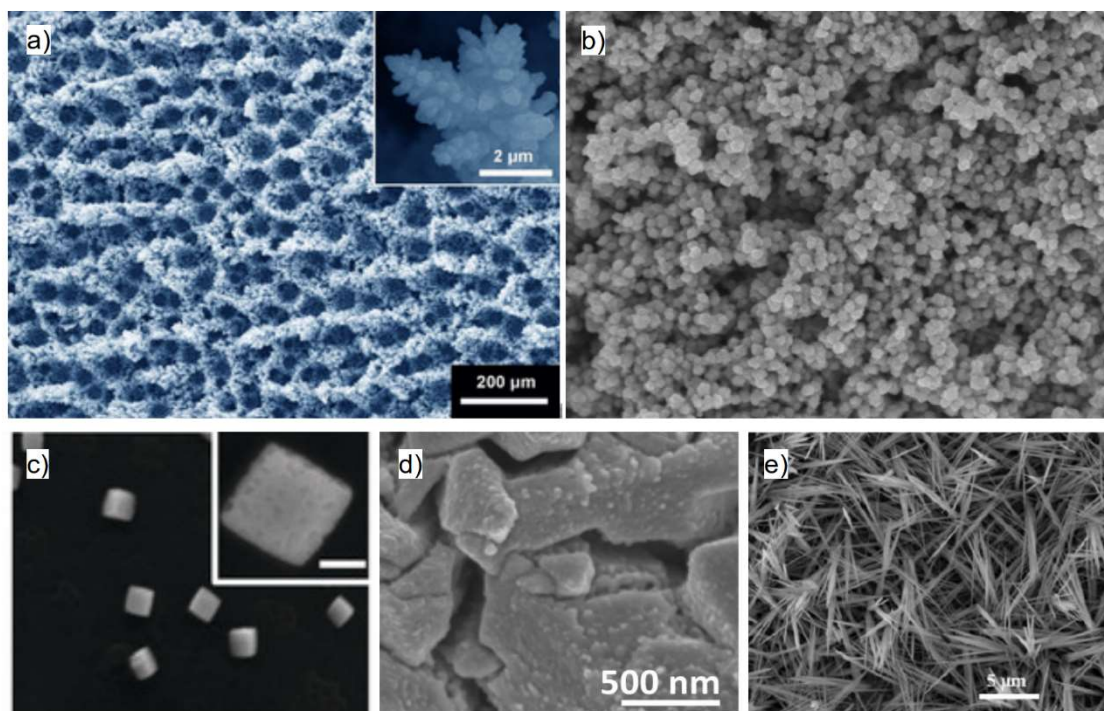


Figure 32: Examples of Cu nanostructures that are presented in literature as activity enhanced catalysts for CO₂ reduction reactions, such as a) dendritic Cu foams [53], b) spherical nanoparticles [231], c) nanocubes [232], d) nanoparticles on a polycrystalline Cu film [233] and e) nanowire arrays derived by the reduction of CuO nanowires [134].

Dendritic mesoporous Cu foams with large surface area (Figure 32 a)) are synthesized by an HER-assisted electrodeposition process of Cu under acidic conditions, where the hydrogen gas bubbles introduce the porosity [234]. Such Cu nanofoams show a lower onset potential for electrochemical CO₂ reduction as well as a different product distribution and yield in comparison to flat Cu surfaces [235]. Their product selectivity is increased for ethylene (C₂H₄) and further C₂+ products (up to 55 % Faradaic efficiency). This effect is assigned to trapping of the intermediate reaction products carbon monoxide (CO) and formic acid (HCOOH) in the porous foam structure leading to enhanced C-C coupling [54,55,235,236]. Due to this outstanding CO₂ reduction behavior, these dendritic Cu foams were used as catalyst for CO₂ reduction reaction in an ionic liquid modified electrolyte to clarify reaction pathways. This was achieved by checking the product distribution when suppressing an intermediate reaction step with the ionic liquid [53] and applying the ionic liquids suppression power to tune the reaction selectivity towards one specific product. Thus, a formation efficiency for formic acid (HCOOH) of 85 % [237] was achieved.

While foams are formed by nanostructures and pores with a large size distribution, Cu nanoparticles of well-defined dimensions, offer the chance to study the influence of size effects on the CO₂ reduction reactions, current density, and product selectivity. First studies on spherical Cu nanoparticles (Figure 32 b)) showed that the current density increases with decreasing particle size. However, the nanoparticles did not exhibit reaction selectivity towards advanced hydrocarbons, since small nanoparticles with diameter below 10 nm show Faradaic efficiencies for hydrogen evolution and carbon monoxide (CO) formation of ~65 % and ~25 %, respectively [131]. Additionally, it was shown that a decrease in interparticle distance

leads to an increase in Faradaic efficiencies for hydrocarbon formation with a decrease in hydrogen evolution, indicating an increase in CO intermediate re-adsorption and further reaction to hydrocarbons in smaller interparticle spaces [133].

Another distinctively shaped Cu nanoparticle type allowing inference on the catalyst size and shape properties on the CO₂ reduction reaction are Cu-nanocubes (Figure 32 c)). Using these nanocubes, it was shown that larger particles have higher reaction efficiencies and higher selectivity towards ethylene (C₂H₄) formation up to 41 % [238]. Density functional theory indicated that edge sites are key sites for the adsorption and stabilization of CO₂ reduction intermediates and thus lead to an inhibition of the HER. For the C-C coupling towards C₂ products, an optimal ratio of edge sites over plane-sites is crucial. A nanocube edge length of 44 nm showed best performance for CO₂ reduction towards ethylene (C₂H₄) [238]. In addition, nanocubes have proven to be most beneficial towards ethylene (C₂H₄) synthesis since they exhibit (100) surfaces, which have already been shown on single crystals to favor ethylene (C₂H₄) formation [232,238–240].

Nanoparticles with no distinct shape and diameters between 2 and 15 nm, placed on a carbon support were studied as CO₂ reduction catalyst as well and showed strong selectivity by generating only methane (CH₄) and ethylene (C₂H₄) as reaction products with Faradaic efficiencies of ~40 % for C₂H₄ and ~10 % for CH₄, respectively. The HER was suppressed to a great amount by only taking ~20 % of the applied charge at -1.1 V vs. RHE. A decrease of particle size showed a decrease in C₂H₄ efficiency, which is in agreement with the studies of spherical Cu nanoparticles and can be attributed to an increase of the number of low-coordination sites as edges and corners [132]. In accordance, Cu nanoparticles (Figure 32 d)) on a polycrystalline Cu support showed relatively high Faradaic efficiencies of 32 % for C₂H₄ as well and additionally 16 % efficiency for the formation of ethane (C₂H₆) at -1.0 V vs. RHE [233]. Several works show that the type of support for the nanoparticles also influences the product selectivity of the CO₂ reduction reaction. It has been stated that the interface of a carbon base structure and the metal catalyst influences the CO₂ reduction reaction by enhanced electrical conductivity and exposure of the interfacial catalytic sites [241]. Thus, the leading Cu catalyst structures regarding the Faradaic efficiency for C₂H₄ formation are Cu nanoparticles on a carbon support in a flow electrolyzer setup [242,243].

In further studies, randomly arranged Cu(OH)₂ nanowire arrays (Figure 32 e)) were synthesized on a Cu foil or Cu mesh [135] by a wet-chemical method and then transformed into CuO nanowires by thermal annealing. For CO₂ reduction they were transformed into Cu nanowire arrays by application of a reductive potential. In first studies, those nanowire arrays showed a Faradaic efficiency for the CO₂ reduction towards carbon monoxide (CO) of 50 % at a low applied overpotential of only -0.49 V vs. RHE, which was ascribed to a higher stabilization of the adsorbed CO₂- intermediate at the large surface area of the nanowire array [244]. In further studies, the nanowire length and number density were varied and the effect on the selectivity towards different hydrocarbons investigated. It was shown that the selectivity towards certain hydrocarbons could be tuned by geometrical variations. Longer nanowires lead to higher formation

efficiencies for hydrocarbons in general and C₂+ molecules in particular. This effect was linked to an increased local pH value in the nanowire array structure leading to a favoring of the dimerization of adsorbed CO molecules [134]. Research on these nanowire array structures led to a deeper insight into the mass-transfer process that has a significant influence on the reaction efficiency and selectivity at the surface of Cu nanostructures and plays an important role in the electrocatalytic performance at high overpotentials by placing an upper limit on the CO₂ conversion rate [245,246].

Advanced computational modelling studies propose densely-arranged Cu nanopyramids with ~25 nm height and width as efficient catalysts for the CO₂ reduction towards diols such as ethylene glycol C₂H₆O₂. The simulations propose that the pyramids are able to retain two oxygen atoms for hydroxyl formation by decreasing the reaction barrier due to their spatial alignment. For pyramids exhibiting Cu (111) facets, three aspects promote the diol formation: improved adsorption of the CO intermediate, geometrically preferable sites for C–C coupling arranged close to each other, and a boosted surface electron transfer due to interatomic bonds [247,248]. However, the synthesis of such Cu nanopyramids to experimentally proof these computational prospects is still a challenge.

Most of the Cu nanostructures investigated so far exhibit random geometrical arrangements and a certain range of size dispersity. They usually served as model system to provide insight on the influence of size and porosity on the electrochemical CO₂ reduction reaction as well as on the reaction pathways. Ordered assemblies and monodispersed nanostructures like the nanowire networks with well-defined geometrical parameters synthesized by electrodeposition in etched ion-track membranes, in turn, offer new opportunities to investigate not only reaction mechanisms but also the influence of 3D structure and porosity on the transport of gaseous reactants, electrolyte access, and reaction product dynamics.

The CO₂ reduction reaction on Cu produces a mixture of liquid and gas phase products. Thus, for the analysis several methods that allow the qualitative and quantitative detection of these products need to be combined. Gas products are usually analyzed online by electrochemical mass spectroscopy [249–252] or online gas chromatography (GC) [40,50,253,254]. For the analysis of the liquid phase products, high-performance liquid chromatography (HPLC) [40,253–255] or nuclear magnetic resonance (NMR) [50,254,256–259] have proven to be valuable. In this work, the combination of online GC and NMR analysis of the electrolyte after the CO₂ reduction reactions was chosen.

Chromatography is a separation technique based on two phases. One is the mobile phase, i.e. the mixture to be separated that moves in a definite direction along a stationary phase, which adsorbs the components of the mixture with different affinities, leading to the separation [260]. Chromatography can be applied with suitable tools and techniques for liquid mixtures as well as for mixtures of gases. In GC the gas mixture is transported as volatile phase along a stationary phase that can either be a liquid [261,262] or a solid component in a separation column. The gas sample is first introduced into the apparatus either with a syringe or by a sampling valve. Then it is transported by an inert carrier gas through the narrow analytical

column which contains the stationary phase inside on the walls and is heated inside an oven, The different mixture components are thus separated by being adsorbed for different times inside the column. Finally, they exit the column into a detector at different retention times. Thus, the signal of the detector giving the amount of chemical components leaving the column can be directly attributed to a specific gas [263].

NMR proves advantageous for quantitative analysis of liquid phase CO₂ reduction reaction products due to its ability to detect smallest amounts of organic molecules [264]. NMR is based on magnetic resonance, a phenomenon that interacts with the atomic nuclei when applying a suitable radiofrequency radiation [265–267]. Each atom possesses a specific frequency at which a change of the orientation of the nuclear spin can occur. The resonance frequency is specific for the element. In ¹H-NMR as used in these studies, the magnetic excitation of the hydrogen atoms is used for sample analysis. The resonant frequency of the molecules, also known as chemical shift, is defined by the number and binding of hydrogen atoms in the molecules of the analyzed liquids. E.g. the three protons of the methyl group (CH₃) are magnetically equivalent and have the same chemical shift. Thus, the signals of these atoms generate one reflex at the same position. The chemical shift positions and intensity relations of NMR signals are specific for each substance. For example, ethanol (CH₃CH₂OH) generates signals at three specific chemical shifts, i.e. one for the CH₃ group around 1 ppm, one for the CH₂ group 4 ppm and one for the OH group between 2–6 ppm. The strength of this reflexes is detected by a magnetic recording coil. Comparison of the signal to the intensities of a calibrated reference allows qualitative and quantitative inference on the composition of the analyzed liquid mixture. The number of H atoms in such a specific group defines whether its NMR reflex is either a singlet, doublet, triplet or quadruplet. The combination of these reflexes finally provides the spectrum of the molecule under study [268].

The electrochemical CO₂ reduction applying the Cu nanowire network as catalyst was performed in an electrochemical cell made of the inert polymer PEEK, as shown in Figure 33. The cell design is based on the cell reported by Kuhl et al [50].

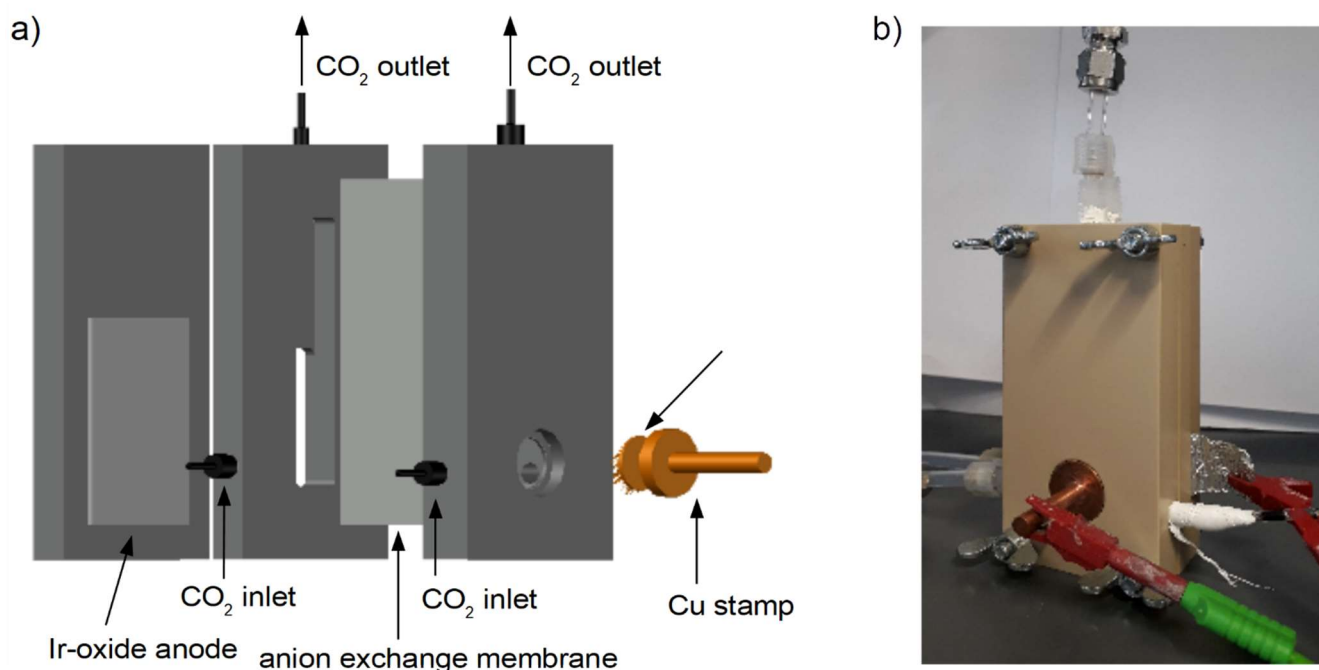


Figure 33: a) Schematics and b) photograph of the electrochemical cell used for CO₂ reduction experiments. The nanowire network is inserted in the corresponding front opening of the cell by a Cu stamp, all cell parts are screwed together and the counter electrode is electrically contacted from the back side by an Al foil.

In this cell the Cu nanowire network is inserted in the front opening of the cathode compartment and electrically contacted by a Cu stamp as working electrode with a nanowire network of a planar area of 1.8 cm². The cell is composed of two compartments separated by an anion exchange membrane (Selemion AMV, AGC Inc., Amagasaki, Japan). This membrane is suitable for catholyte and anolyte separation in aqueous CO₂ electroreduction. It suppresses further oxidation of the CO₂ reduction products, but does not fully prevent the passage of formate and acetate into the anode compartment [50,269]. For activation, i.e. swelling and exposure of the anion-conducting molecule groups [270,271], the membrane was stored in deionized water before usage. Each compartment has a CO₂ inlet from the side at its bottom part and an outlet on the top side, which on the cathode side is directly connected to the injection valve of the gas chromatograph by a plastic tube. For the electrochemical CO₂ reduction measurements all cell parts shown in Figure 33 are screwed together and sealed with Viton rings to prevent electrolyte leakage. 5 ml of 0.1 M KHCO₃ electrolyte, which is CO₂ saturated by constant purging for at least 1 h, was filled into the cathode compartment of the cell and 8 ml into the anode compartment. The pH value of the CO₂ saturated 0.1 M KHCO₃ electrolyte was measured to be pH = 6.8. During the reaction, a constant CO₂ gas flow of 30 ml/min through the cathode compartment and 7 ml/min through the anode compartment was applied to prevent a strong effect of pressure difference. The gas flow was regulated by two mass flow controllers (MFC) (Bronkhorst FG-201CV, Wagner Mess- und Regeltechnik, Offenbach, Germany), which were calibrated in a range from 0-200 ml/min for CO₂ flow. The volume flux of these MFC is directly adjusted by a digital controller set next to them. The CO₂ streamed from the bottom of the cell compartments towards the top, maintaining the saturation of the electrolyte. An Ag/AgCl (3 M KCl) reference electrode was inserted into

the cathode compartment as well. An Ir-mixed oxide coated Ti plate (Metakem, Usingen, Germany) was used as anode at the back of the anode compartment and was contacted with an aluminum stripe from its back side in a way that it cannot get in contact with the electrolyte. The electrochemical process was carried out with a PARSTAT (Ametek, Berwyn, Pennsylvania, US) multichannel potentiostat. The gas output of the cathode led to a gas chromatograph (GC2030, Shimadzu, Kyoto, Japan), for analysis of the gas phase reaction products. During the CO₂ reduction, the GC triggered an injection into the capillary column every 12 minutes with a ball valve. After the reaction experiment, the catholyte was collected and analyzed ex-situ by nuclear magnetic resonance (NMR) for detection of liquid phase reaction products.

The CO₂ reduction measurements were performed in six steps. First, the solution resistance (R_u) was measured by electrochemical impedance spectroscopy (EIS) in a frequency range of 1000-0.01 Hz at -0.9 V vs. Ag/AgCl. However, due to the oxidized nanowire network surface, this check yielded unprecise R_u values and thus was only used to check the validity of setup and electrical contacts. In a second step, all oxide layers at the nanowire surface were removed by applying ten cyclic voltammetry scans in a reductive potential range from -0.5 V vs. Ag/AgCl to -1.8 V vs. Ag/AgCl. with a scan rate of 200 mV/s. The CVs were repeated until they stabilized, indicating the complete removal of the oxide layer. Figure 34 presents 10 CV scans applied for the surface reduction of a 3D Cu nanowire network with $d = 150$ nm, $h = 30$ μ m and $F = 8 \times 10^8$ cm⁻². The arrow indicates the movement of the position of following CV curves until they remain at one position, when all surface oxide is removed.

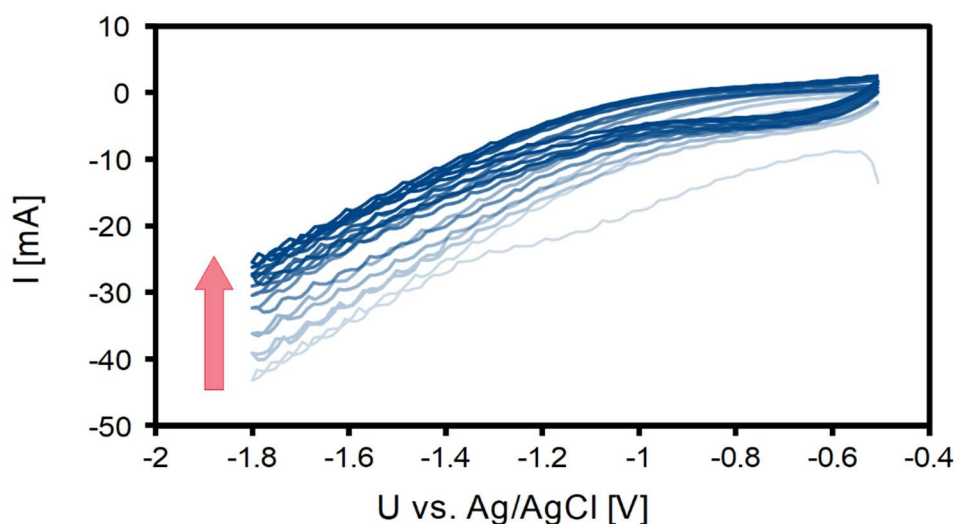


Figure 34: Exemplary CV scans from -0.5 V vs. Ag/AgCl to -1.8 V vs. Ag/AgCl recorded during the surface reduction of a Cu nanowire network with $d = 150$ nm, $h = 30$ μ m, $F = 8 \times 10^8$ cm⁻².

To study possible changes of the network morphology during the surface reduction step, the morphology of a pre-cleaned and anodized Cu nanowire network ($d = 150$ nm, $h = 30$ μ m, $F = 8 \times 10^8$ cm⁻²) was analyzed before and after its exposure to a certain number of CV scans (namely 5, 10, 20, 50, 100, 150, 200 CV scans).

In addition, electrochemical impedance spectroscopy was performed to determine the resistance R_u , which is shown in Figure 35.

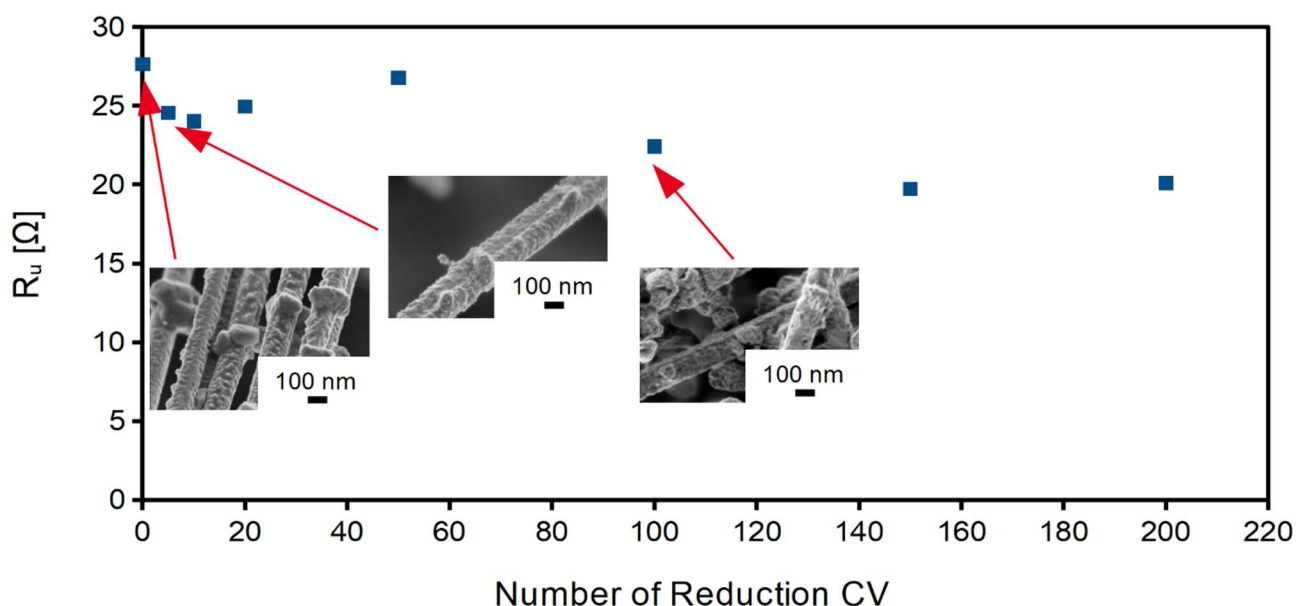


Figure 35: Resistance R_u of a Cu nanowire network after a certain number of CV scans for surface reduction.

Before any surface reduction CV, a R_u value of 27.6Ω was measured, which decreased to 24.6Ω after the first 5 CV scans, indicating the removal of surface oxide. The value decreased further to 24Ω during the next 5 scans and after 10 CV scans the first minimum resistance is reached, indicating a full removal of surface oxide after 10 CV scans without further change in the surface structure as observed in the SEM images presented in Figure 35. When continuing with further CV scans, the resistance staid stable with only slight changes until decreasing down to values of 22.4Ω after 100 CV scans on to values $\sim 20 \Omega$ after 150 and 200 scans. As observed in the SEM images in Figure 35, already for the network exposed to 100 reduction CV, cathodic corrosion occurred, leading to surface roughening and the formation of pinholes. Thus, a larger surface area is in contact with the electrolyte, leading to more charge transfer with decreasing resistance. This corrosive impact of a large number of surface reduction CV is not beneficial for the Cu nanowire network, but does not play a role for the CO_2 reduction reaction protocol applied in this thesis, since in this work, we consistently applied only 10 CV scans to attain a full removal of surface oxide without sample degradation.

In a third step, R_u of the setup and sample was precisely determined with potentiostatic EIS at a potential of $-0.9 \text{ V vs. Ag/AgCl}$ which is a potential where no significant reaction falsifying the impedance measurement is to be expected. EIS was started at a frequency of 10 kHz which has shown to be appropriate for determining R_u , a value that is necessary later for transforming the applied potential vs. Ag/AgCl reference electrode into a potential vs. reference hydrogen electrode (RHE) that is compensated by the IR-drop of the setup. The Nyquist plot in Figure 36 shows the imaginary impedance Z_{im} over the real

impedance Z_{re} of such an exemplary EIS measurement performed after the surface oxide reduction. R_u is defined by the crossing of the Nyquist plot with the X-axis leading in this case to a resistance of $R_u = 26.4 \Omega$.

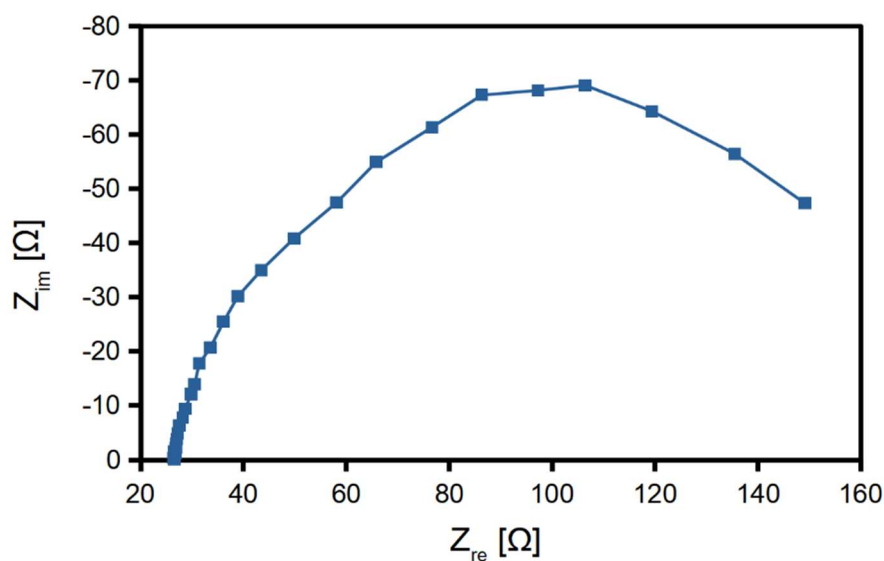


Figure 36: Electrochemical impedance spectroscopy measurement for a Cu nanowire network ($d = 150 \text{ nm}$, $h = 30 \text{ }\mu\text{m}$, $F = 8 \times 10^8 \text{ cm}^{-2}$), performed after the electrochemical surface reduction.

Finally, electrochemical CO_2 reduction was performed at a constant potential for one hour. After three minutes of entry time, the first injection of the exit gas mixture into the GC was performed, which was repeated for four more times in 12-minute intervals. An exemplary chronoamperometry curve of such a potentiostatic CO_2 reduction for one hour is presented in Figure 37 for the same Cu nanowire network characterized in Figure 34 and Figure 36. The electrode potential is $U_{el} = -0.75 \text{ V}$ vs. RHE, resulting from the applied potential of $U_{appl} = -1.66 \text{ V}$ vs. Ag/AgCl. The red arrows indicate the times of injection of the collected gas into the GC analysis column.

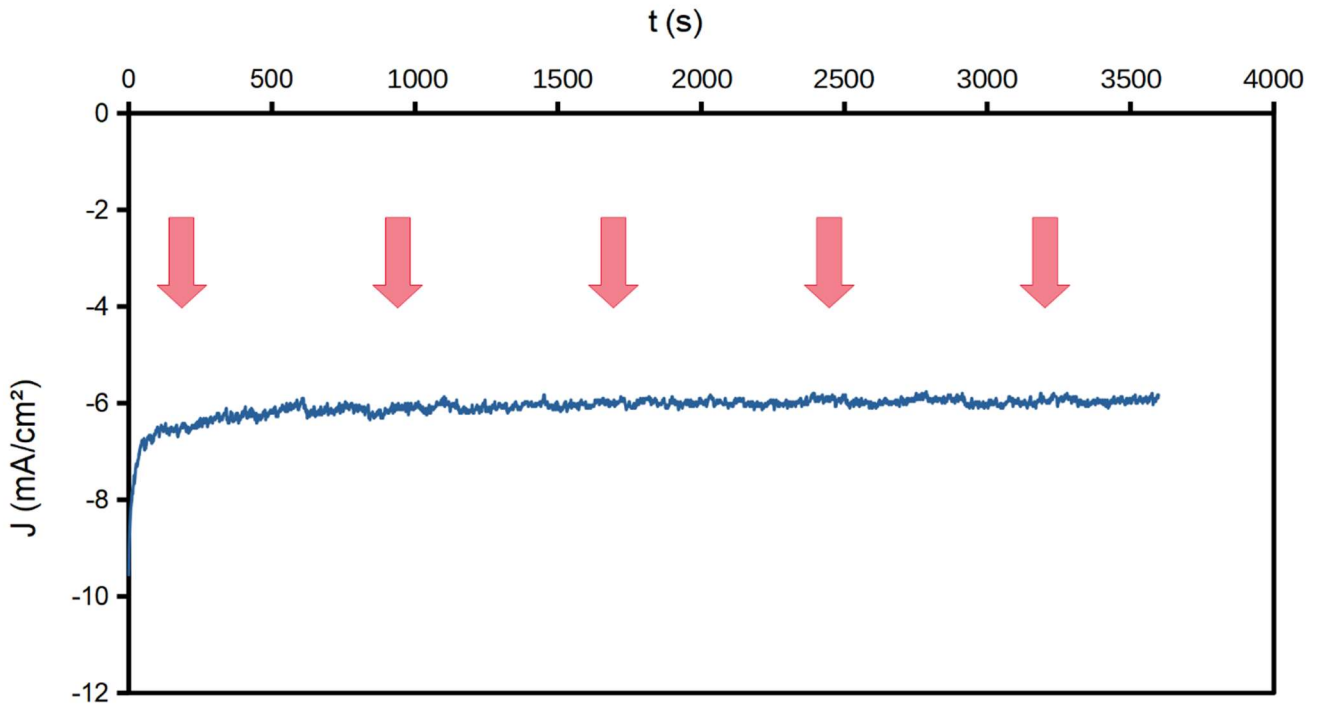


Figure 37: Exemplary chronoamperometric current density over time ($J-t$) for one-hour potentiostatic CO_2 reduction at a Cu nanowire network at an electrode potential U_{el} of -0.75 V vs. RHE.

After injection into the GC, the collected gas phase products are transported by the carrier gas N_2 into the ShinCarbon ST Packed analysis column (Restek, #19043) of 500 μL volume. After passing through the column, the gas stream is separated by a splitter into a field ionization detector (FID) for the identification of methane (CH_4), ethylene (C_2H_4), ethane (C_2H_6), formic acid (HCOOH), acetic acid (CH_3COOH), ethanol ($\text{C}_2\text{H}_6\text{O}$), n-propanol ($\text{C}_3\text{H}_8\text{O}$) and ethylene glycol ($\text{C}_2\text{H}_6\text{O}_2$). A thermal conductivity detector (TCD) provides the detection of hydrogen (H_2) and carbon monoxide (CO).

The mole fraction χ_p of a specific product is calculated using the GC response factors that were determined by calibration with sample gases of known concentration. The Faradaic efficiency FE [%] is calculated by equation (21)

$$FE [\%] = \frac{I_p}{I_{avg}} = \frac{\chi_p \cdot z \cdot F \cdot \dot{n}(\text{CO}_2)}{I_{avg}} \quad (21)$$

where I_p denotes the partial current assigned to the specific product and I_{avg} is the total current of the CO_2 reduction reaction. I_p is defined by the mole fraction χ_p of the product, the number of transferred electrons z by the chemical reaction of CO_2 to this product and F is the Faraday constant. The molar CO_2 gas flow $\dot{n}(\text{CO}_2)$ is deduced from the ideal gas law (equation (22)).

$$\dot{n}(\text{CO}_2) = \frac{p\dot{V}(\text{CO}_2)}{RT} \quad (22)$$

with the operating pressure $p = 10^5$ Pa, the CO_2 volume flow $\dot{V}(\text{CO}_2) = 2 \times 10^{-5}$ mol/s, the universal gas constant R and the operating temperature $T = 298.15$ K.

For the NMR analysis of the electrolyte after the CO_2 reduction reaction, 0.5 g of the catholyte was mixed with 25 μg of 0.01 M maleic acid (99 %, Acros Organics, Geel, Belgium) as reference for the quantitative analysis, and D_2O (99.9 %, Sigma-Aldrich, St. Louis, Missouri, US) as solvent. H-NMR was performed with a Bruker 500 MHz DRX 500 NMR spectrometer including a water suppression mode [272]. For quantitative analysis, the proton normalized area of the maleic acid standard was compared to the proton normalized area of a significant functional group of the product molecule.

After this chronoamperometric CO_2 reduction, another EIS was performed to detect changes in R_u , which would indicate a change of the catalyst structure. Such an exemplary Nyquist plot is shown in Figure 38.

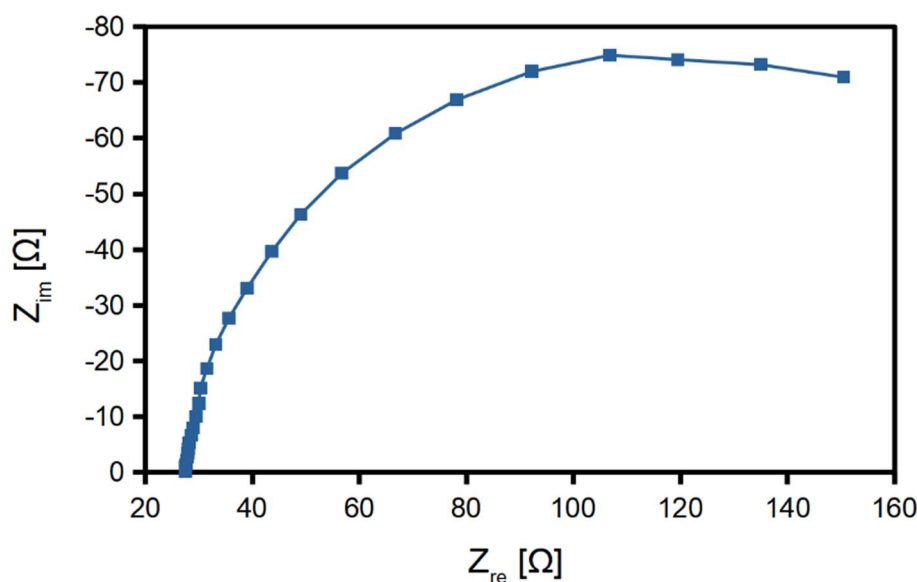


Figure 38: EIS measurement for the same Cu nanowire network, measured after potentiostatic CO_2 reduction for one hour at -0.75 V vs. RHE.

The impedance measurement after the reduction reaction for this network shows a resistance of 25.3Ω , at the crossing of the plot with the Z_{re} axis. Thus, compared to the R_u determined before the CO_2 reduction (see Figure 36), a resistance loss of only 1Ω occurred at the nanowire network. Such a small value, as well as the stability of the current density during the 1 h of CO_2 reduction is an indication for a good stability of the network.

4.2 CO₂ reduction reaction products for different Cu structures: planar, nanowire array and nanowire network

To evaluate whether the Cu NWNWs are suitable catalysts for CO₂ reduction, we first compared the performance, in particular the product selectivity, of four types of Cu samples with different geometries, namely, (i) an as-purchased high purity 1 mm thick Cu-plate (99.99 %, Alfa Aesar, Haverhill, Massachusetts, US), (ii) a flat electrodeposited Cu backelectrode, prepared under identical conditions as the substrate for the Cu nanowire networks (details in section 2.3), (iii) an array of Cu nanowires with 150 ± 3 nm diameter and an average wire length of 3.9 ± 0.5 μm (determined from wire length measurements on 30 nanowires in cross-section SEM images) and $2 \times 10^9 \pm 1 \times 10^8$ cm^{-2} nanowire number density, and (iv) a Cu nanowire network with 30 ± 0.5 μm height, 150 ± 4 nm wire diameter and $2 \times 10^9 \pm 1 \times 10^8$ cm^{-2} nanowire number density. SEM images of these four different structures are presented in

Figure 39.

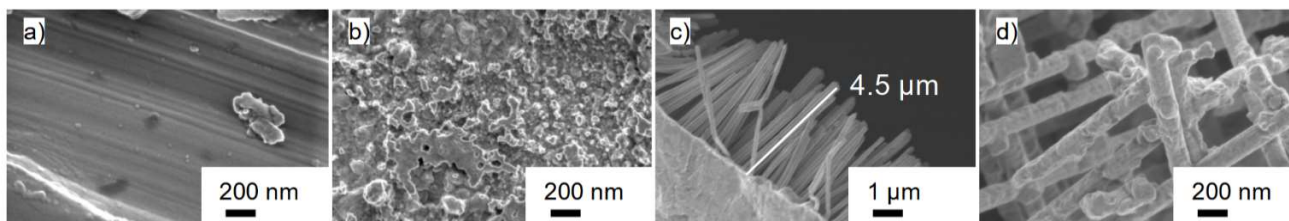


Figure 39: High magnification SEM images of the a) as purchased Cu plate, b) electrodeposited fine-grained Cu film, c) Cu nanowire array (cross-section image) and d) Cu nanowire network, all before the CO₂ reduction experiments.

For every sample geometry, the CO₂ reduction reaction was performed at $U_{el} = -0.66$ V vs. RHE, -0.7 V vs. RHE and -0.83 V vs. RHE. The potentials were applied sequentially from lower to higher for one hour each. In between each voltage step, the catholyte was removed for NMR liquid phase product analysis, the anolyte was also removed and new electrolyte was inserted in both cell compartments. Then, EIS was performed with the electrolyte for R_u determination, which is necessary for correct adjustment of the electrode potential. Before the measurement, all samples were pre-cleaned with 0.1 M H₂SO₄ and 0.1 M H₃PO₄ and oxidatively anodized in 0.1 M H₃PO₄ as described in chapter 2.4. When placed into the electrochemical cell, the surface oxide was removed by ten reductive CV scans for all samples. To test the reproducibility, three identical samples of each type were studied and their values for IR-compensated potential, current density and Faradaic efficiencies were averaged. Figure 40 shows the averaged $J-t$ curves for these CO₂ reduction reactions at the different electrode structures.

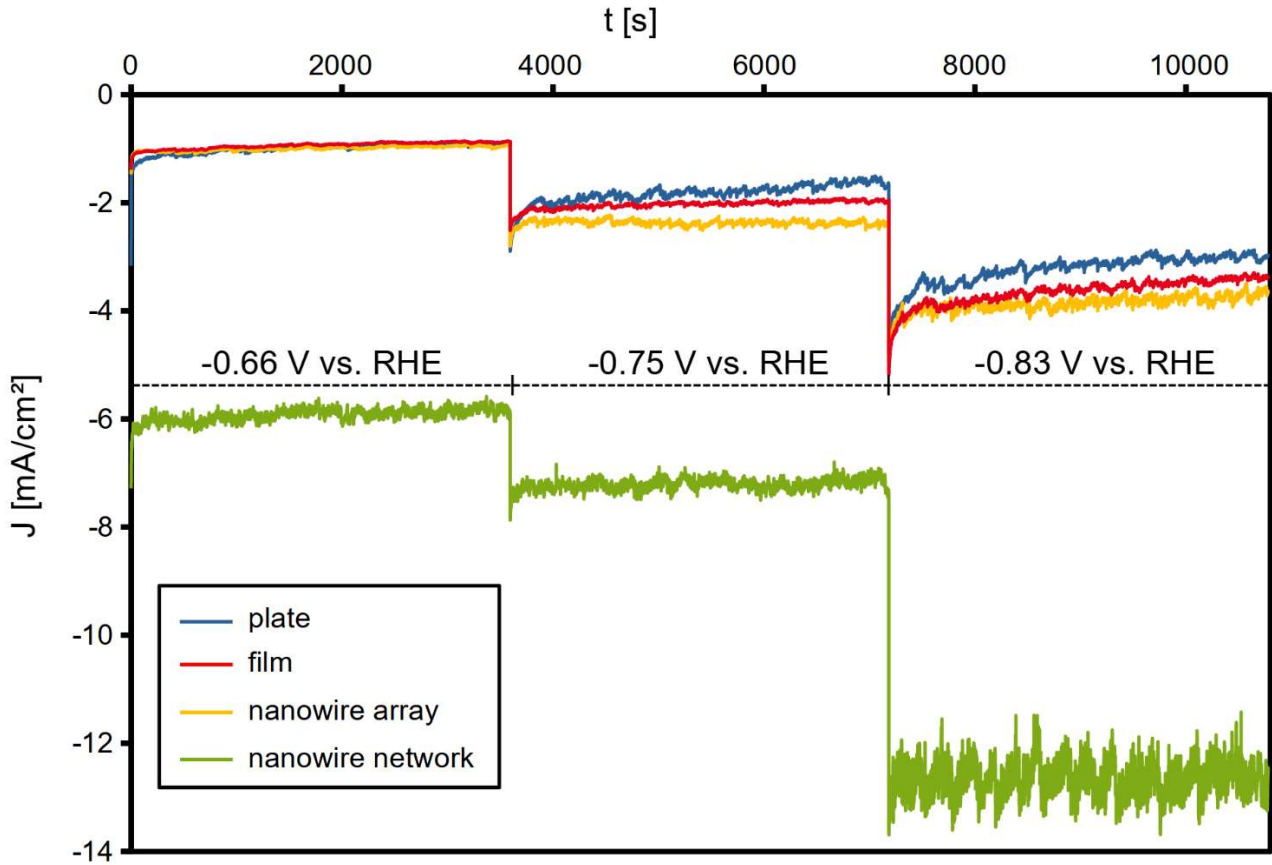


Figure 40: J - t curves for the CO_2 reduction reactions at an as-purchased Cu plate (blue), electrodeposited back-electrode film (red), parallel Cu nanowire array ($d = 150 \text{ nm}$, $F = 2 \times 10^9 \text{ cm}^2$, $h = 4 \text{ }\mu\text{m}$) (yellow), and Cu nanowire network ($d = 150 \text{ nm}$, $F = 8 \times 10^8 \text{ cm}^2$, $h = 30 \text{ }\mu\text{m}$) (green) at the three potentials of $U_{el} = -0.66 \text{ V vs. RHE}$, -0.75 V vs. RHE and -0.83 V vs. RHE , applied for 1 h each. The current density refers to the planar electrode area.

The potentials and current densities applied and recorded for each step are summarized in Table 4.

Table 4: Applied U_{appl} vs. Ag/AgCl , resulting U_{res} vs. RHE , compensated by the IR-drop, and J for the different structures used as electrode in the CO_2 reduction. All values are the median from measurements with three samples each.

	$U_{el} \text{ vs. RHE} = -0.66 \text{ V}$		$U_{el} \text{ vs. RHE} = -0.75 \text{ V}$		$U_{el} \text{ vs. RHE} = -0.83 \text{ V}$	
	$U_{appl} \text{ vs. Ag/AgCl [V]}$	$J \text{ [mA/cm}^2\text{]}$	$U_{appl} \text{ vs. Ag/AgCl [V]}$	$J \text{ [mA/cm}^2\text{]}$	$U_{appl} \text{ vs. Ag/AgCl [V]}$	$J \text{ [mA/cm}^2\text{]}$
As purchased Cu plate	-1.3	-1.0 ± 0.1	-1.5	-1.8 ± 0.2	-1.6	-3.2 ± 0.3
Electrodeposited Cu film	-1.3	-0.9 ± 0.1	-1.5	-2.0 ± 0.1	-1.6	-3.7 ± 0.2
Cu nanowire array	-1.4	-1.0 ± 0.0	-1.5	-2.4 ± 0.1	-1.7	-3.9 ± 0.1
Cu nanowire network	-1.5	-5.9 ± 0.1	-1.6	-7.2 ± 0.1	-2.0	-12.7 ± 0.3

Since the current density increases generally with increasing surface area from Cu-plate via Cu-film and nanowire array towards the nanowire network, the IR-drop, which is calculated by multiplying the current density J by the sample area of 1.8 cm^2 and the series resistance R_u , increases in the same manner. This is

due to the average resistance R_u determined for each sample before, after and in-between the different potential steps is equal within the error bars with values of $R_u = 27.3 \pm 1.7 \Omega$ for the Cu plates, $R_u = 29.5 \pm 2.4 \Omega$ for the electrodeposited Cu film, $R_u = 24.8 \pm 3.2 \Omega$ for the nanowire array and $R_u = 25.6 \pm 1.8 \Omega$. Thus, for reaching the same electrode potentials U_{el} vs. RHE, which are adjusted to differ only slightly for the different structures, the applied potential U_{appl} vs. Ag/AgCl also needs to be adjusted accordingly. The difference from plate to the film is only a factor of ~ 0.1 V for all potential steps due to the relatively small change in current density. In contrast, for a nanowire array, which has already twice the current density of the film, the applied potential needs to be between -0.3 to -0.6 V vs. Ag/AgCl higher, since the IR-drop that needs to be compensated is more significant. For the Cu nanowire network, the current density doubles again, leading to an even higher potential application that is necessary to achieve comparable IR-compensated U_{el} vs. RHE.

Thus, by adjusting the potential U_{appl} vs. Ag/AgCl, the CO₂ reduction reaction could be performed at the Cu-plate, the Cu-film, the Cu nanowire array and the Cu nanowire network at equal IR-compensated potentials U_{el} vs. RHE. Figure 41 displays the Faradaic efficiencies for the formation of a) all products, b) H₂, c) all gas phase CO₂ reduction products, d) the sum of the acids as products of the CO₂ reduction, namely HCOOH and CH₃COOH and e) the sum of the CO₂ reduction product alcohols, namely C₂H₆O, C₃H₈O, C₂H₆O₂. The CO₂ reduction displayed in these graphs was performed at potentials of $U_{el} = -0.66$ V vs. RHE, $U_{el} = -0.75$ V vs. RHE and $U_{el} = -0.83$ V vs. RHE.

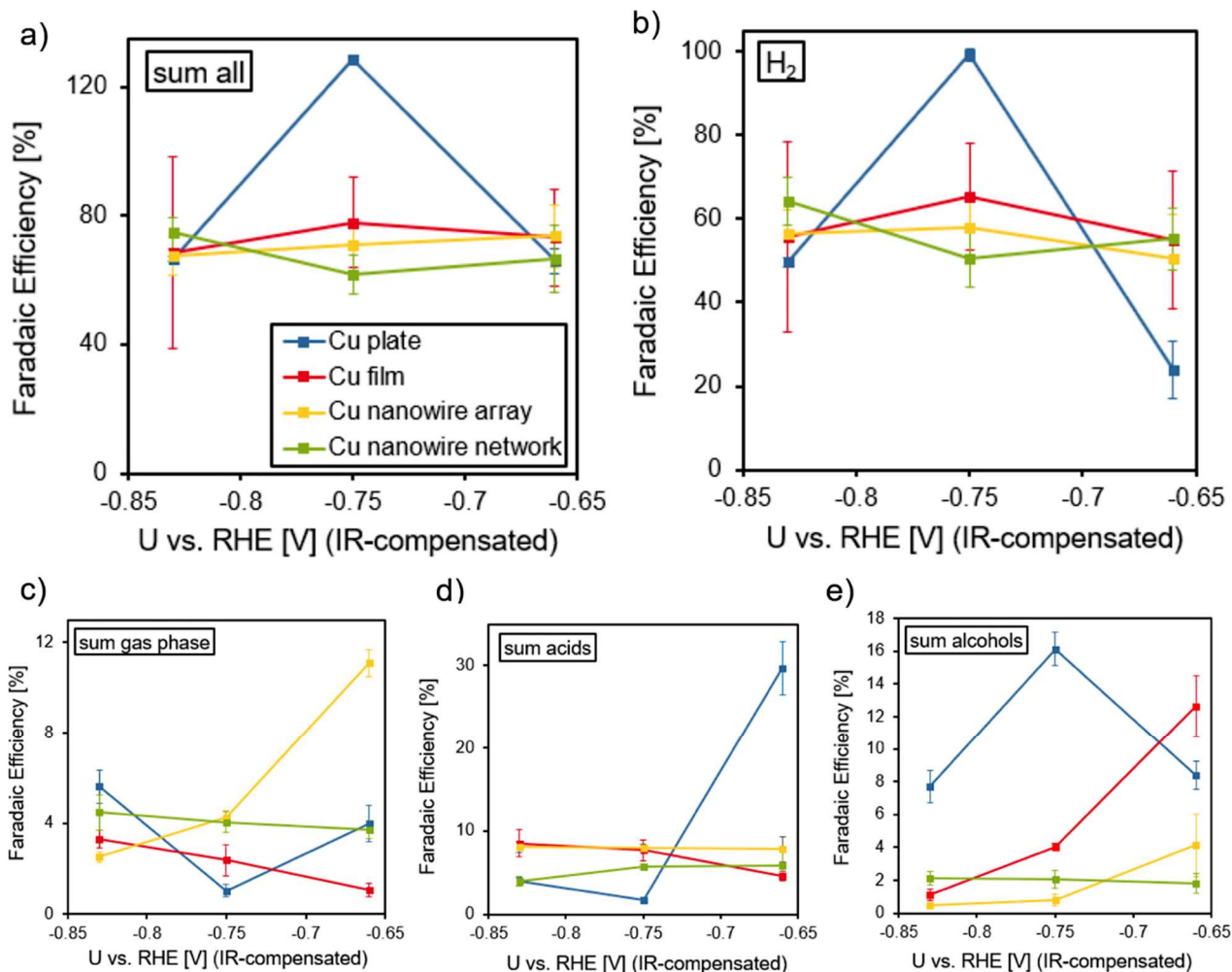


Figure 41: Faradaic efficiencies at different electrode potentials U_{el} of a) all reaction products, b) H₂, c) gas phase products (CO, CH₄, C₂H₄, C₂H₆), d) acidic liquid phase products (HCOOH, CH₃COOH) and e) alcohols (C₂H₆O, C₃H₈O, C₂H₆O₂) for the CO₂ reduction at a Cu-plate (blue), an electrodeposited Cu film (red) a Cu nanowire array (yellow) and a Cu nanowire network (green), i.e. the structures presented in Figure 39. The legend in a) is valid for all graphs.

As observable from Figure 41 a), the sum of the Faradaic efficiency for the formation of all products is below 80 % for all samples at all three potentials, except for the Cu-plate, which yielded more than 120 % at $U_{el} = -0.75$ V vs. RHE. As observable from Figure 41 b) this high value is triggered by a large Faradaic efficiency of almost 100 % for H₂ at this potential. This value does not seem reasonable, since more than 100 % total Faradaic efficiency is not possible. Thus, probably some imprecision in the gas chromatography hydrogen detection led to this inaccurate result. Except of this anomaly, the Cu-plate yielded the lowest total Faradaic efficiencies, which can be explained by its small surface area in comparison to the rougher and structured other samples. A comparison of Figure 41 a) and b) yields the conclusion that the most part of the reaction current is belonging to the hydrogen evolution, since the courses of the total Faradaic efficiency and the one of the H₂ evolution have the same shape at the different structures. Only at the low potential of -0.66 V vs. RHE, the H₂ evolution at the Cu-plate is with ~ 20 % relatively low. As observable from Figure 41 d) this is due to the preferred acid formation in this case. Except of this case, the Faradaic efficiencies for the gas phase CO₂ reduction products (Figure 41 c)) are relatively low and show no significant trends for the three

potentials. This is consistent with the relatively low Faradaic efficiencies for the acid and alcohol CO₂ reduction products and might be attributed to the relatively low potentials applied in these studies. Generally, the lack of trends can be attributed to the small potential region of only 0.17 V difference on which these tests were performed and the relatively low amount of CO₂ reduction reaction products that were produced, since the H₂ evolution always remained dominant.

For a closer look on the reaction, a more detailed analysis of the reaction products obtained after evaluation of the NMR and GC data is presented in Figure 42.

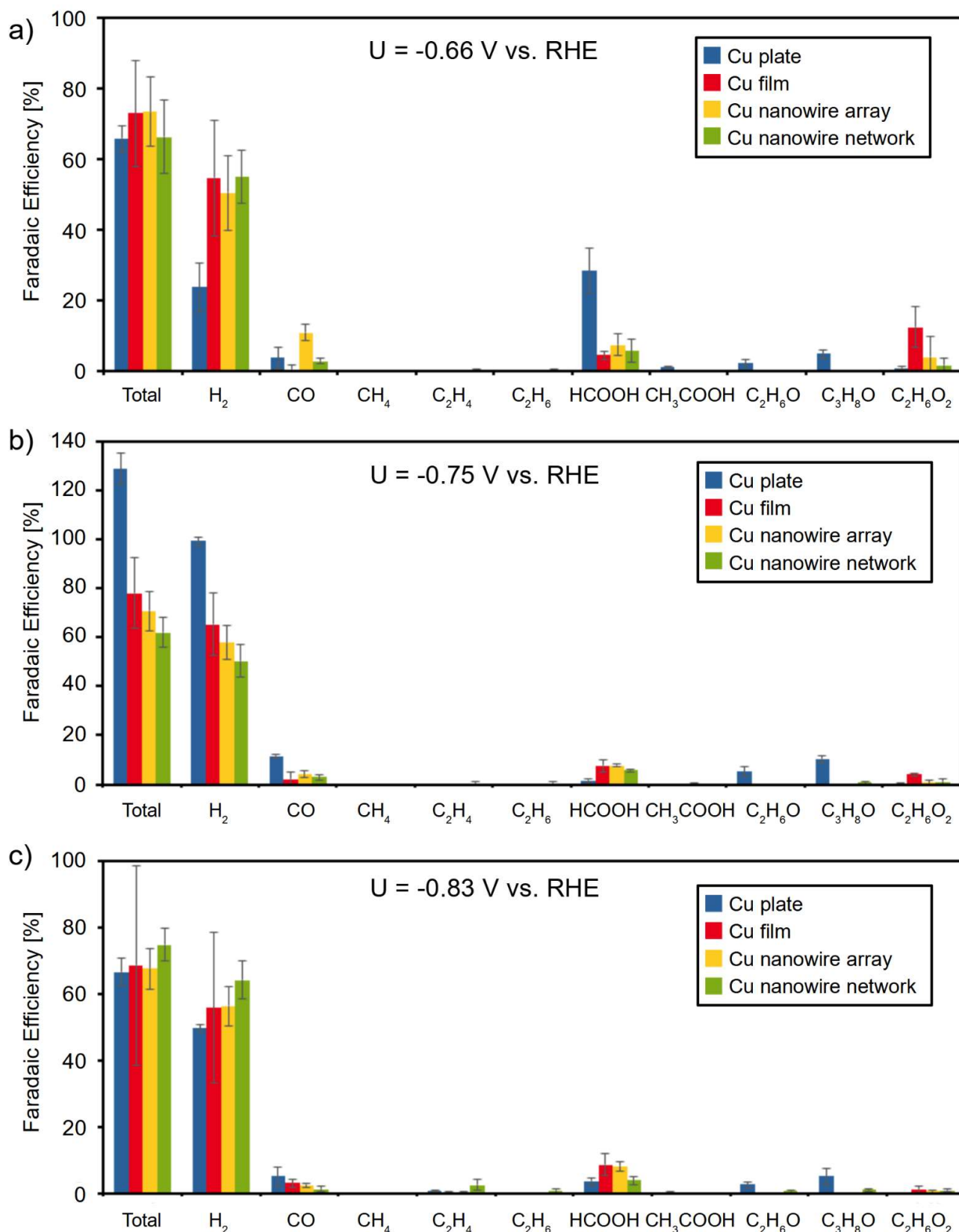


Figure 42: Faradaic efficiencies normalized on the planar sample area obtained for the different products after one hour CO₂ reduction at a) $U_{el} = -0.66 \text{ V vs. RHE}$, b) $U_{el} = -0.75 \text{ V vs. RHE}$ and c) $U_{el} = -0.83 \text{ V vs. RHE}$ for the as-purchased Cu plate (blue), electrodeposited back-electrode film (red), parallel Cu nanowire array ($d = 150 \text{ nm}$, $F = 2 \times 10^9 \text{ cm}^{-2}$, $h = 4 \text{ }\mu\text{m}$) (yellow), and Cu nanowire network ($d = 150 \text{ nm}$, $F = 8 \times 10^8 \text{ cm}^{-2}$, $h = 30 \text{ }\mu\text{m}$) (green).

For all of the electrode structures almost no CH_4 , C_2H_4 and C_2H_6 are produced regardless of the applied potentials with Faradaic efficiencies of these products below 1 %. Only at $U_{el} = -0.83$ V vs. RHE the nanowire networks show the production of C_2H_4 with a Faradaic efficiency of ~ 2.5 %. The competing H_2 evolution reaction is taking more than 50 % of the current efficiency for all structures, except the as-purchased Cu plate, where it has only an efficiency of ~ 25 % at $U_{el} = -0.66$ V vs. RHE. For this sample, the formation of HCOOH is predominant with a Faradaic efficiency of 29 %, while for the other structures this product has a very low efficiency value of less than 10 %. Synthesis of the C_2^+ products CH_3COOH , $\text{C}_2\text{H}_6\text{O}$ and $\text{C}_3\text{H}_8\text{O}$ is only detected at the as-purchased Cu plate as well. On the contrary, the Cu plate does not yield any $\text{C}_2\text{H}_6\text{O}_2$, whereas the Cu-film leads to efficiencies of more than 10 % for this product. At the nanowire array and nanowire network, $\text{C}_2\text{H}_6\text{O}_2$ formation is observed, but the respective efficiencies of 4 % and 1 %, are very low.

For all applied potentials, the production of C_2H_4 and C_2H_6 is almost negligible, however very small amounts could be detected for nanowire networks at more negative potentials. The HCOOH product efficiency has changed drastically for the Cu-plate, being relatively small at $U_{el} = -0.75$ V vs. RHE but ~ 30 % at $U_{el} = -0.66$ V vs. RHE, whereas the $\text{C}_2\text{H}_6\text{O}$ and $\text{C}_3\text{H}_8\text{O}$ synthesis which is occurring mainly at the Cu-plate reaches efficiency values that are double the values than at $U_{el} = -0.66$ V vs. RHE. $\text{C}_2\text{H}_6\text{O}_2$ is again mainly produced at the Cu-film. This time however, with a Faradaic efficiency of only 4 %, whereas it was produced with a Faradaic efficiency of ~ 13 % at the Cu-film at the lower potential of $U_{el} = -0.66$ V vs. RHE.

As shown in Figure 42 c) for $U_{el} = -0.83$ V vs. RHE, the faradaic efficiency for H_2 evolution levels off to values between ~ 50 % and ~ 65 % for the different electrode structures, however with slight changes in the relative values between the different structures. At this potential, the nanowire network produces detectable amounts of C_2H_4 and C_2H_6 up to charge efficiency values of 2.5 % and 0.8 %, respectively. The HCOOH efficiency is now between 5 and 10 % for all structures, slightly decreased in comparison to the lower potential step. $\text{C}_2\text{H}_6\text{O}$ and $\text{C}_3\text{H}_8\text{O}$ are again synthesized only at the Cu plate in significant amounts, but decreasing in efficiency, compared to the lower potential steps. The same decrease is observed for the $\text{C}_2\text{H}_6\text{O}_2$ product formation efficiency which is still observable predominantly at the Cu-film.

In summary, the reference Cu plate yields the highest current efficiencies for $\text{C}_2\text{H}_6\text{O}$ and $\text{C}_3\text{H}_8\text{O}$ formation at all potentials. When increasing the potential, the efficiency of these two products generally decreases.

At all measured potentials, the Cu nanowire network was the only catalyst to yield significant, although relatively low, efficiency for the formation of C_2H_4 and C_2H_6 . The efficiency for the HCOOH synthesis was lowest for the Cu nanowire network at all potentials in comparison to the other structures. This low formation of HCOOH , combined with the synthesis of C_2H_4 and C_2H_6 indicates that the HCOOH formed at the nanowire network in the first reduction steps may be trapped in the networks porous structure, continuing its reaction towards the more advanced C_2H_4 and C_2H_6 . This reaction pathway has been reported already for other catalyst structures in literature [50,204,220].

$C_2H_6O_2$ was formed at all four structures, with the Cu-film yielding the highest FE, especially at low voltages. At the as-purchased Cu-plate this formation was almost not happening, whereas at the Cu nanowire array and network structures, that are also placed on a Cu film, it is formed, although yielding lower FE values. This triggers the assumption, that the $C_2H_6O_2$ formation is promoted by the Cu sputter layer on top of the Cu film, or its rough topography.

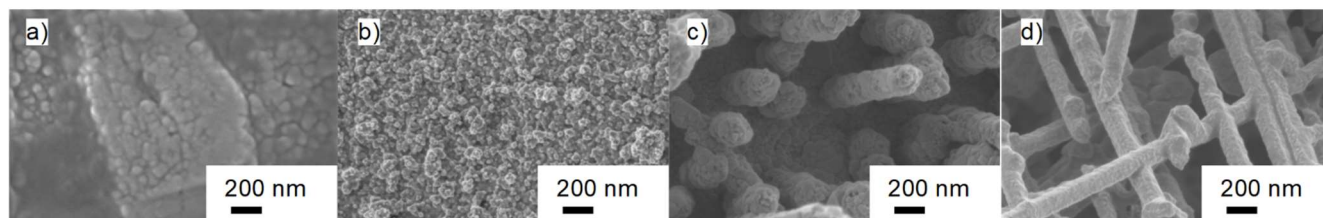


Figure 43: High magnification SEM images of the a) as purchased Cu plate, b) Cu film, c) Cu nanowire array and d) Cu nanowire network after the CO_2 reduction at the three different potentials of $U_{el} = -0.66$ V vs. RHE, -0.75 V vs. RHE and -0.83 V vs. RHE for 1 h each.

Figure 43 shows the SEM images of all four structures after the CO_2 reduction measurements. A comparison to the SEM images before the CO_2 reduction measurements (Figure 39) shows the Cu-surfaces getting a more granular surface with roughness increase, especially at the a) Cu-plate and c) nanowire array. This roughness increase is an indication of corrosion processes but does not yet lead to catalyst structure destruction. Thus, the stability of these structures as CO_2 reduction catalysts needs to be studied more extensively with long-term tests, as done for the Cu nanowire networks (chapter 4.9). Additionally accelerated stress tests with potential ramps would provide valuable information on the applicability of these structures as CO_2 reduction catalysts in industrial application.

4.3 Determining the suitable potential region for CO_2 reduction experiments at Cu nanowire networks

After these first CO_2 reduction studies of the three Cu structures at specific potentials, the suitable potential region for the CO_2 reduction experiments with Cu nanowire networks as catalysts was studied further to be able to perform CO_2 reduction studies over a broader potential region than already done in chapter 4.2. Thus, a nanowire network sample was inserted in the setup as described in section 4.1. and different current densities were applied and hold for 5 minutes each. The application of current densities allows to detect a limit for the electrode potentials U_{el} vs. RHE caused by the IR-drop. Thus, the electrode potentials for the potentiostatic CO_2 reduction at the Cu nanowire network can be evaluated. Before each current density step, EIS was performed to determine the resistance (R_u) of the cell including the network. This is required to determine the IR-drop of the setup in order to subsequently calculate the electrode potential U_{el} vs. RHE.

The measurements were carried out at room temperature, employing a CO_2 saturated 0.1 M $KHCO_3$ electrolyte (pH = 6.8) and an Ag/AgCl (3 M KCl) reference electrode ($E_0 = 0.207$ V). A 100% compensation

of the IR-drop, i.e. the series resistance R_u multiplied by the current I , is performed in all cases after the measurements, during the data analysis.

Figure 44 shows the uncompensated measured potentials U vs. $Ag/AgCl$ (blue), the resistance R_u determined between the potential steps (yellow), and the resulting IR-compensated electrode potentials U_{el} vs. RHE (red), calculated with equation (23 for the applied current densities displayed on the top of the graph. They result from the applied current I divided by the geometric sample area of 1.8 cm^2 . The pH value of the electrolyte remains constant throughout the whole measurement at a value of 6.8.

$$U_{el} \text{ vs. RHE} = U_{appl} \text{ vs. Ag/AgCl} + 0.059 * pH + E_{Ag/AgCl}^0 - I * R_u \quad (23)$$

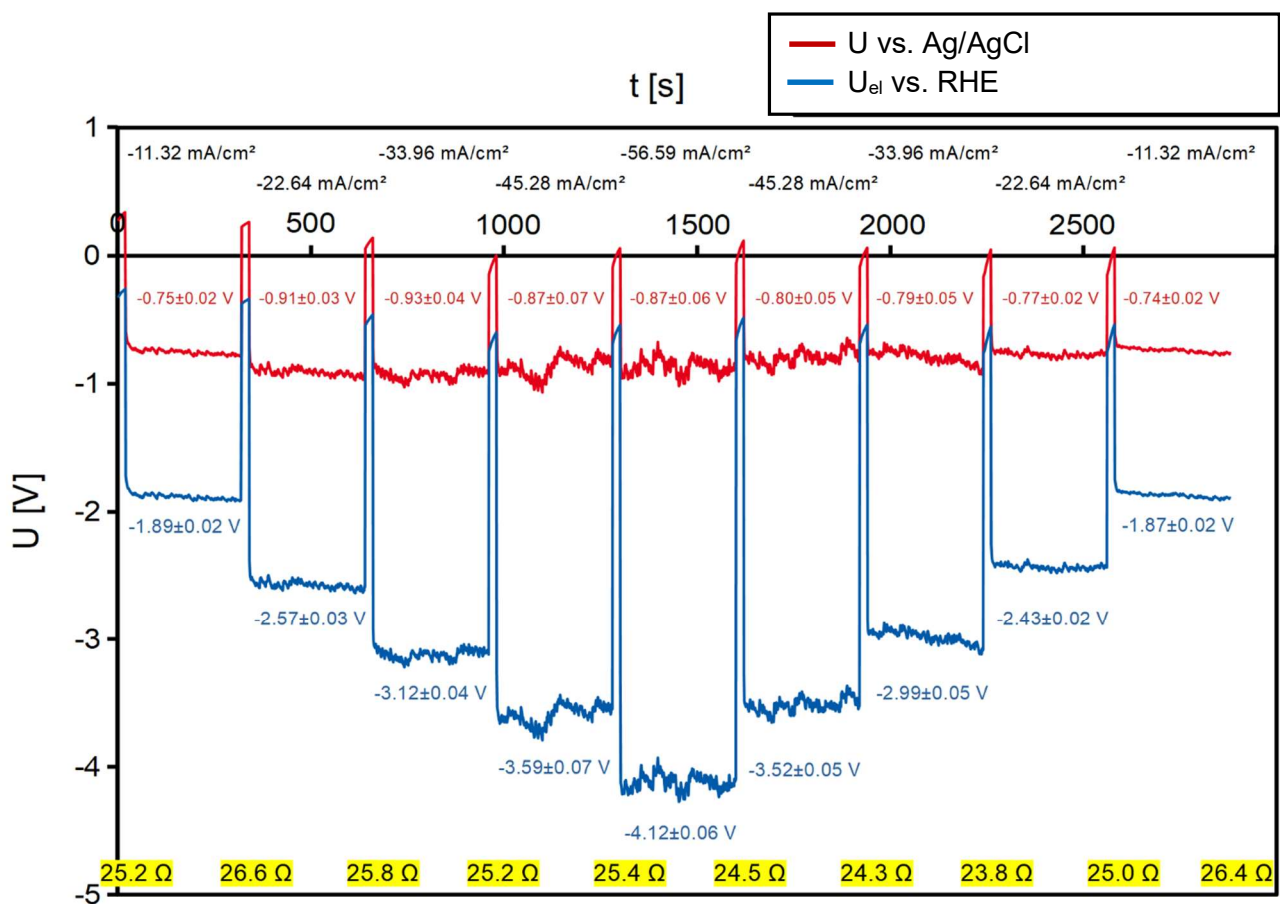


Figure 44: potentials U vs. $Ag/AgCl$ (blue) and resulting IR-compensated electrode potentials U_{el} vs. RHE (red) over time, with fixed current densities applied stepwise for 5 minutes each. In between the steps, R_u is determined by EIS (yellow).

The fluctuations of the potentials at given current densities increase with increasing potential due to stronger bubble formation, mainly caused by the water-splitting reaction. The values of the series resistance R_u of the cell, obtained from EIS measurements remain relatively constant over time in a region of $25.22 \pm 0.88 \Omega$. Thus, these studies indicate the possibility to perform stable CO_2 reduction at the

nanowire networks even at high applied potentials, at least when they are applied for a relatively short time. The networks stability for longer timeframes of high potential application will be analyzed later.

As shown in Figure 45, the potential U vs. $Ag/AgCl$ increases linearly with applied current density J . However, the electrode potential U_{el} vs. RHE only increases up to a maximum potential of -0.93 V vs. RHE due to an increasing IR-drop caused by the large current densities achieved by the generally large nanowire network surface area.

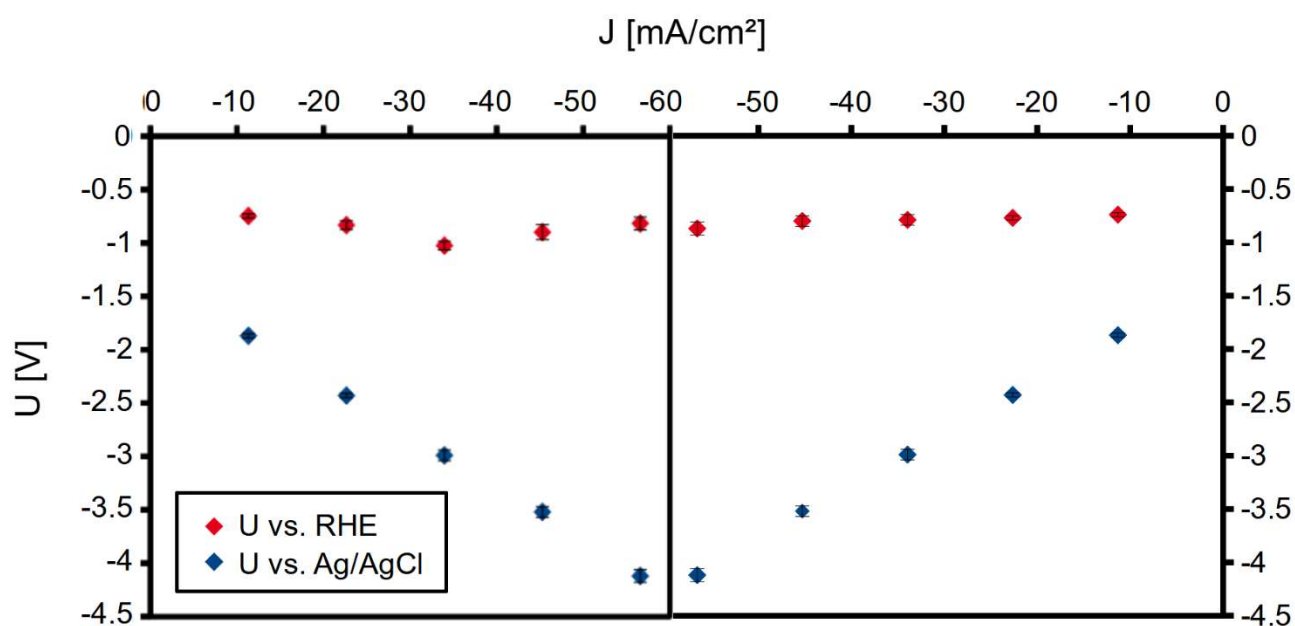


Figure 45: Potentials U vs. $Ag/AgCl$ and U_{el} vs. RHE over J curves for the measurements with increasing and decreasing galvanostatically applied current density steps. The error bars are hardly visible, since they are smaller than the symbols.

4.4 Product selectivity of the CO_2 reduction reaction at different potentials

The product selectivity of a CO_2 reduction catalyst can only be studied quantitatively, when the potential is applied potentiostatically, since the various reaction products need different electron transfers, when reduced out of CO_2 . For example, the reduction of CO_2 towards CO consumes two electrons, whereas the reduction towards $C_2H_6O_2$ consumes 10 electrons. Thus, the same measured current could be achieved by five times the amount of CO_2 reduced towards CO than to $C_2H_6O_2$. Therefore, it is not possible to provide comparable conditions for catalysts with different selectivities during galvanostatic operation, since this can only fix the total amount of reduced CO_2 . Thus, we investigate the potential-dependent product selectivity during the CO_2 reduction, on the applicable potential window in this setup, which is between $U_{el} = \sim -0.5$ V and $U_{el} = \sim -0.95$ V vs. RHE , using 15 Cu nanowire networks with identical geometrical parameters (height = $30 \mu m$, wire diameter ~ 150 nm, and nanowire number density = 8×10^8 cm⁻²). The CO_2 reduction reaction in 0.1 M $KHCO_3$ electrolyte was driven at 5 different electrode potentials between -0.5 and -0.82 V vs. RHE . For each potential, three independent measurements were performed to

test the reproducibility of the catalyst performance, using three different samples with the above-mentioned geometrical parameters and applying the preparation steps introduced in section 4.1. The charge efficiencies for the CO₂ reduction products at each potential were determined by averaging the Faradaic efficiencies of all three samples.

Table 5 shows U_{app} vs. $Ag/AgCl$, R_u , J , the IR-drop and the calculated U_{el} vs. RHE obtained as average of three samples measured at $U_{app} = -1.18, -1.31, -1.68, -1.66$ and -1.95 vs. $Ag/AgCl$.

Table 5: Average IR-drop of three samples each for the different potential steps at which CO₂ reduction was performed at Cu nanowire networks (height = 30 μm, wire diameter ~150 nm, and nanowire number density = 8×10⁸ cm⁻²). The current density is the average reduction current divided by the planar sample area of 1.8 cm².

U_{app} vs. $Ag/AgCl$ [V]	Series resistance R_u [Ω]	Average current density J [mA/cm ²]	IR drop [V]	U_{el} vs. RHE [V]
-1.18 ± 0.01	-25.87 ± 1.10	-1.62 ± 0.25	-0.07 ± 0.01	-0.50 ± 0.00
-1.31 ± 0.02	-25.57 ± 1.38	-2.36 ± 0.54	-0.11 ± 0.02	-0.60 ± 0.01
-1.68 ± 0.03	-27.02 ± 2.82	-7.42 ± 0.18	-0.35 ± 0.03	-0.72 ± 0.00
-1.66 ± 0.00	-26.39 ± 0.01	-6.71 ± 0.06	-0.31 ± 0.00	-0.75 ± 0.00
-1.95 ± 0.05	-26.70 ± 1.48	-11.96 ± 1.00	-0.56 ± 0.02	-0.82 ± 0.02

The values evidence the correspondence between U_{el} vs. RHE , j and R_u . An increase in current density causes a significant increase in IR-drop, which reaches values of 0.56 V at applied potentials around -1.95 V vs. $Ag/AgCl$. Thus, an even higher U_{app} vs. $Ag/AgCl$ needs to be applied here, for achieving a distinct electrode potential. The series resistance of the setup with the nanowire networks, which is not dependent on the applied potential, is always at comparable values.

A benefit of the Cu nanowire networks is the high current density achieved for low applied potentials. However, this causes a large IR-drop, which increases at larger potentials that correspond with higher currents, since the setup, i.e. the electrochemical cell, has a relatively high series resistance.

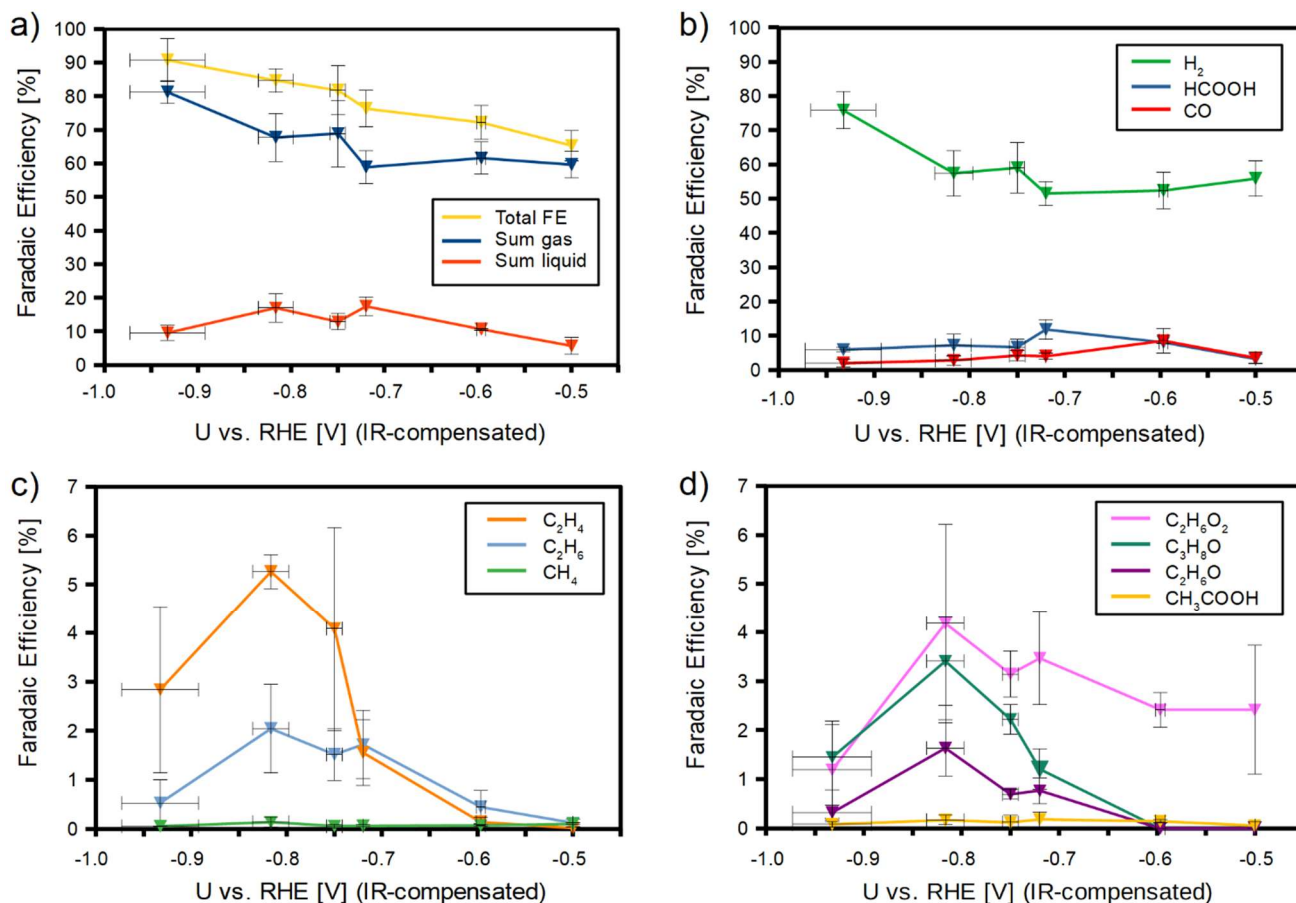


Figure 46: Faradaic efficiencies for the CO₂ reduction product synthesis with Cu-nanowire networks as catalyst at different potentials. The sums of the Faradaic efficiencies in total and for the sums of the gas- and liquid-phase products are shown in a). b) displays the formation efficiency of the unwanted side-product H₂ coming from the competing hydrogen evolution reaction as well as the efficiencies for HCOOH and CO formation. The current efficiencies for the carbohydrates C₂H₄, C₂H₆ and CH₄ are shown in c), while the ones for the alcohols are presented in d) with C₂H₆O, C₃H₈O, C₂H₆O₂ and CH₃COOH.

Figure 46 shows the Faradaic efficiencies (FE) as a function of the IR-compensated electrode potential. Figure 46 a) presents the total FE, which increases with increasing potential from ~65 % towards ~91 %. The contribution of the liquid phase products is small (10-15 %) and rather potential independent, whereas the gas phase products increase by ~20 % within the investigated potential range.

Figure 46 b) shows the FE of the products H₂ (green), HCOOH (blue), and CO (red). The FE of the concurring H₂ evolution reaction (HER) is around 50 – 60 % over the whole potential region, but increasing up to 80 % at -1.0 V vs. RHE, while HCOOH and CO exhibit lower FE values and peak around -0.7 V and -0.6 V vs RHE, respectively. CH₄ and CH₃COOH are minor reaction products, since they are only generated with FE < 1 % at every studied potential as it was also reported for the as purchased Cu-plate and the electrodeposited Cu film in section 4.2. This is in agreement with the studies of Kuhl et. al [50] at a Cu plate, where CH₃COOH was only produced in small quantities and CH₄ only at more negative potentials than -0.9 V vs. RHE. Ma et al. also did not observe these reaction products for their nanowire structures, even at more negative potentials [134]. The FE for HCOOH synthesis at our nanowire networks reached 11.8 ± 0.5 % at $U_{el} = -0.72$ V vs. RHE, which is comparable to FE values attained at a Cu-plate at this potential by Ma et al.

[50]. However, at higher potentials HCOOH formation efficiencies above 20 % were reported for CO₂ reduction at Cu plates [50], whereas for our nanowire networks it always remained slightly below 10 %, as it also did for the Cu plate and electrodeposited Cu film presented in section 4.2, where it was observed with ~4 % and 8 %, respectively. This clearly indicates that our Cu nanowire structures need to be tuned towards stability at higher reduction potentials, where significant CO₂ reduction towards HCOOH could probably be observed.

Figure 46 c) presents the FE attained for hydrocarbons. Whilst CH₄ is produced at our nanowire networks in minimal amounts with FE below 0.2 %, the hydrocarbons C₂H₄ and C₂H₆ show a maximum FE of 5.3 ± 0.4 % and 2.0 ± 0.9 % at $U_{el} = -0.83$ V vs. RHE, respectively, coinciding with the potential for most efficient C2 or C3 alcohol formation on this sample (Figure 46 d)), and leading to the conclusion that for the Cu nanowire networks C-C coupling is promoted at this potential value. For a Cu-plate, Kuhl et al reported a FE of ~5 % for C₂H₄ formation at this potential [50], which is much higher than for our commercial Cu plate and Cu film (see section 4.2). However, at higher potentials the efficiency of C₂H₄ production at the Cu plate increases, while for the nanowire networks it decreases. C₂H₆ was not reported as a product for the CO₂ reduction at the Cu plate by Kuhl et al [50] as well as for our Cu plate and Cu film in section 4.2, while the nanowire networks reach up to 2 %, which was also observed for Ma's nanowires at higher potentials [134].

Figure 46 d) shows the FE obtained for the alcohols. For C₂H₆O and C₃H₈O, FE of 1.6 ± 0.6 % and 3.4 ± 0.9 %, respectively, are attained at $U_{el} = -0.83$ V vs. RHE. At those potentials, Kuhl et al. reported no alcohol formation [50]. Our as purchased Cu plate (see section 4.2) showed corresponding FE of 2.5 ± 0.7 % and 5.0 ± 2.3 % for C₂H₆O and C₃H₈O, respectively, at this potential, whereas the Cu film did not produce alcohols. A special feature of the Cu nanowire networks is the formation of some amounts of C₂H₆O₂ with Faradaic efficiencies up to 4.2 ± 2 % also at -0.83V vs. RHE. This is by a factor of 20 higher than the maximum efficiency reported in literature for C₂H₆O₂ synthesis at a Cu-plate, even at higher potentials [50]. It is still higher than our studied Cu plate, where we observed minor C₂H₆O₂ formation with a maximum FE of 1.0 ± 0.5 % (see section 4.2). C₂H₆O₂ was also not yet observed as reaction product with such a Faradaic efficiency at any potential, for other Cu nanowire structures [134]. At dendritic sponge structures it has been synthesized with relatively high Faradaic efficiencies up to 25 % [53]. It has been hypothesized that the formation of C₂H₆O₂ occurs via a dimerization process of two adsorbed *CO molecules, since higher C₂H₆O₂ formation efficiencies have been observed at lower potentials, where dimerization is the predominant process [3,50]. Thus, our nanowire networks seem to promote the dimerization process by trapping and adsorbing CO molecules.

Due to the high IR values, CO₂ reduction reaction at Cu nanowire networks could not be investigated at reduction potentials more negative than -0.93 V vs. RHE. Although other Cu catalysts are reported to produce higher FE at more negative potentials, we think that our nanowire networks already have reached their maximum FE at -0.83 V, since their FE decrease again at $U_{el} = -0.9$ V vs. RHE. The results indicate that

Cu nanowire networks can perform CO₂ reduction, especially towards C₂⁺ products at lower electrode overpotentials than Cu plates. Given by the geometrical parameter of these samples, the interspace between individual wires can be regarded as an open cube with ~400 nm side length (see Figure 47). In these free volumes, intermediate products can be trapped promoting the C-C coupling for the C₂⁺ product formation.

In the potential region between -0.5 V and -0.93 V vs. RHE, the nanowire networks are stable without any surface or structural change as shown in the SEM images before and after CO₂ reduction (Figure 47 and Figure 48).

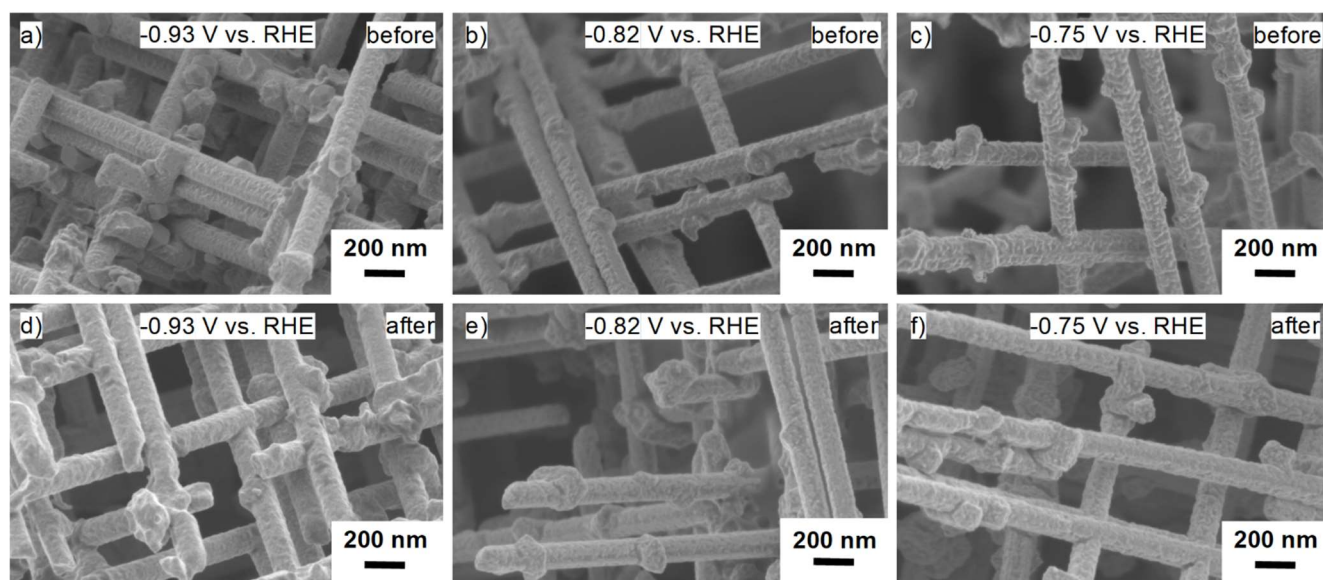


Figure 47: SEM images of the Cu nanowire networks before a)-c) and after d)-f) CO₂ reduction at potentials a,d) -0.93 ± 0.05 V, b,e) -0.82 ± 0.02 V, and c,f) -0.75 ± 0.00 V vs. RHE.

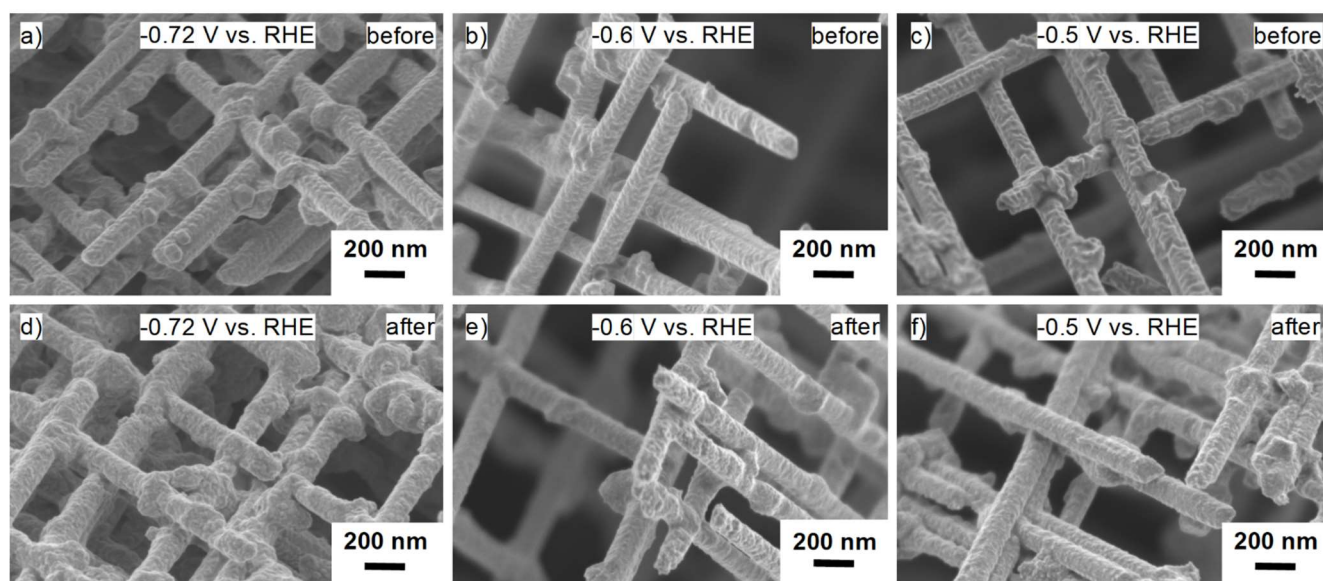


Figure 48: SEM images of the Cu nanowire networks before a)-c) and after (d)-f) CO₂ reduction at potentials a,d) -0.72 ± 0.00 V, b,e) -0.60 ± 0.01 V, and c,f) -0.5 ± 0.0 V vs. RHE.

All nanowire networks displayed in Figure 47 and Figure 48 have a slightly rough surface even before the CO₂ reduction originating from the acidic pre-cleaning and anodization process (see Figure 13 d)). It is outstanding that the surface roughness in the potential range between -0.5 V to -0.93 V vs. RHE does not change during the whole reaction process, consisting of surface reduction CV, EIS and the potentiostatic CO₂ reduction. Moreover, the general network structure, as well as the wire diameter remains constant. Thus, the nanowire networks are stable catalysts for electrochemical CO₂ reduction under these conditions. However, they possess the limitation that CO₂ reduction can be only performed in a relatively limited potential region when applying the electrochemical cell setup used in this thesis.

This limitation should be addressed in future studies by applying an electrochemical cell with a smaller gap between nanowire network, membrane and counter electrode, which would lead to a smaller series resistance reducing the IR-drop and thus allowing higher electrode potentials U_{el} vs. RHE. Another possibility, although not for application of the nanowire network as CO₂ reduction catalyst in industrial application, but for scientific studies of its catalyst performance, would be to reduce the sample size and thus decreasing the absolute current, lowering the IR-drop as well, which leads to higher achievable electrode potentials. In this way, scientific model studies of CO₂ reduction at Cu nanowire networks with variations in geometrical parameters like nanowire number density and nanowire diameter can be performed, allowing conclusions on the influence of the free space between the wires, i.e. the catalyst porosity, on the product selectivity. This could be a helpful tool to clarify reaction pathways towards the products, especially towards C₂H₆O₂, which is produced in a relatively large amount at relatively low potentials, when applying the nanowire networks as catalyst.

4.4.1 Structural characterization of the nanowire networks by XRD before and after the CO₂ reduction

Since the crystallographic orientation of a material is directly influencing the catalytic reactions at its surface [3,51,273], the structural properties of the nanowires were investigated by XRD.

The crystallinity of an electrodeposited material depends on the electrodeposition potential and type of potential application (i.e. constant, pulsed, reverse pulsed,...) [274]. Especially for Cu-nanowires it has been shown that it can be varied between a fine polycrystalline and single crystalline structure by adjusting the electrodeposition parameters [111,112,143]. Since the crystallinity, the surface, and the presence of grain boundaries affect the catalyst performance, the structure of a representative Cu nanowire network, electrodeposited into the etched ion-track template at a potential of $U = -20$ mV at $T = 60$ °C for 45 min out of 238 g/l CuSO₄ (99.995%, Sigma-Aldrich, Taufkirchen, Germany) + 21 g/l H₂SO₄ (99.999%, Sigma-Aldrich, Taufkirchen, Germany) + 0.5 ‰ DOWFAX 2A1 surfactant (chapter 2.3) was studied before and after the CO₂ reduction experiments (see experimental parameters and setup in chapter 4.1). Since the deposition

conditions change the Cu nanowire crystallographic orientation [275], all networks in this work were deposited at the same potential and deposition temperature as the specific network studied with XRD.

Knowing the wavelength of the applied X-rays, allows direct conclusions on parameters like lattice plane distance d_{hkl} and Miller Indices h, k and l , which classify the crystallographic structure [276]. With λ being the irradiation wavelength and d_{hkl} the lattice plane distance, the Bragg law describes the diffraction condition (equation (24)).

$$n * \lambda = 2d_{hkl} * \sin(\theta) \quad (24)$$

Equation (25) provides the distance d_{hkl} between given (hkl) planes with Miller indices h, k and l , when considering the specific cell constant a for a given material [277].

$$\frac{1}{d_{hkl}^2} = \frac{h^2 + k^2 + l^2}{a^2} \quad (25)$$

For the attribution of texture indices to the observed diffraction peaks, selection rules have to be applied. For a face centred cubic (fcc) structure like Cu [278], the hkl indices have to be either all odd or all even. For a fcc crystal structure, all other combinations of indices lead to destructive interference and thus no diffraction peak appears [276]. By taking into account the wavelength $\lambda = 1.5406 \text{ \AA}$ of the applied K_α X-rays and a lattice constant of $a = 3.597 \text{ \AA}$ [279], the 2θ values of different crystalline orientations for Cu are calculated using equation (26). The positions of the possible reflections are shown in Table 6.

$$2\theta = 2 * \sin^{-1}\left(\frac{\lambda}{2d_{hkl}}\right) \quad (26)$$

Table 6: Expected 2θ positions of the Cu XRD reflections for different crystallographic orientations.

h	k	l	2θ [°]
1	0	0	24.56
1	1	0	35.01
1	1	1	43.24
2	0	0	50.36
2	2	0	73.97
2	2	2	94.93
3	1	1	89.74

Comparing the diffraction peaks intensities $I(hkl)$ of a given sample with those of a standard powder diffractogram $I_o(hkl)$ of the same material with isotropic orientation provides information on a preferred

crystalline orientation. This can be quantified by the texture coefficient, calculated with equation (27), which is called the Harris method, with n being the number of considered reflections [280].

$$TC(hkl) = \frac{I(hkl)/I_0(hkl)}{n^{-1} \sum_n I(hkl)/I_0(hkl)} \quad (27)$$

A texture coefficient with a value larger than 1 indicates a preferred crystallographic orientation. The ratio between the different texture coefficients provides additional information on the crystal orientations present in a given sample.

In this work, X-ray diffractograms of Cu nanowire networks were recorded in reflection with a Seifert PTS 3003 diffractometer using a Cu anode and an X-ray mirror on the primary side of the aperture. On the secondary side a long soller slit and a graphite monochromator was used to separate the Cu K_α line ($\lambda = 1.5406 \text{ \AA}$). The device was operated by applying a generator voltage of 40 kV and a current of 40 mA. By using the Rayflex software, the scanning step size was set to 0.25° with an integration time of 0.4 s. By measuring in reflection on the free-standing Cu nanowire networks, the 2θ angle provides the criteria for constructive interference for the planes oriented in parallel to the sample base, i.e. in an angle of 45° towards the nanowire axis as sketched in the inset in Figure 49.

Figure 49 displays a representative diffractogram of a Cu nanowire network, with a wire diameter of $\sim 150 \text{ nm}$, electrodeposited under the same conditions indicated above ($T = 60^\circ \text{ C}$, $U = -20 \text{ mV vs. Ag/AgCl}$). The reflexes of the standard Cu powder diffractogram (JCPDS file No. 85-1326) [278] are marked by the black triangles.

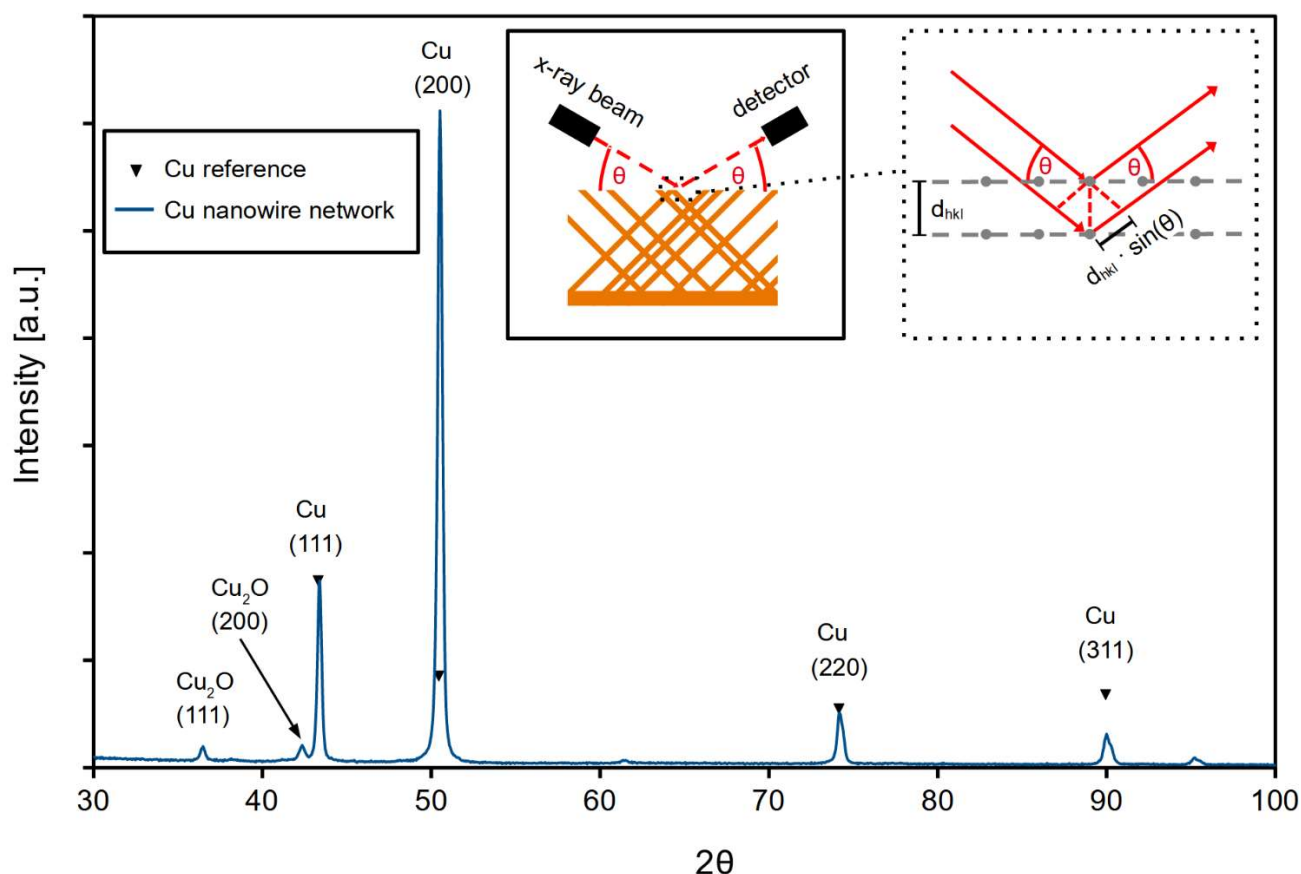


Figure 49: X-Ray diffractogram of a Cu nanowire network deposited at -20 mV vs. Ag/AgCl at 60 °C.

The diffractogram displays the reflections corresponding to the Cu (111), Cu (200), Cu (220) and Cu (311) planes. In addition, Cu₂O (111) and Cu₂O (200) reflections are observed with lower intensity, indicating the presence of Cu₂O, probably originating from the native Cu₂O surface layer, which is forming as soon as the nanowires are removed from the polymer template and in contact with air. The nanowire networks exhibit a strong (200) texture with a texture coefficient of 2.91, meaning that mainly the 200 planes are oriented parallel to the sample surface. This directly indicates that the 220 planes are preferentially oriented perpendicular to the nanowire axis due to the nanowire orientation and the measurement geometry as shown in the insets of Figure 49.

The crystallographic structures of Cu nanowire networks were analyzed by XRD before i.e. after pre-cleaning and anodization (blue line) and after CO₂ reduction for 1 h at different U_{el} vs. RHE (-0.6 V (red), -0.8 V (yellow) and -0.9 V (green)). The diffractograms are presented in Figure 50 together with the standard Cu powder diffractogram (JCPDS file No. 85-1326) [278] intensities, marked by the green triangles to evaluate preferred crystallographic orientations. For direct comparison all diffractograms are normalized to the (111) reflex of the Cu powder reference, which is its most prominent reflex indicating a (111) texture in standard Cu.

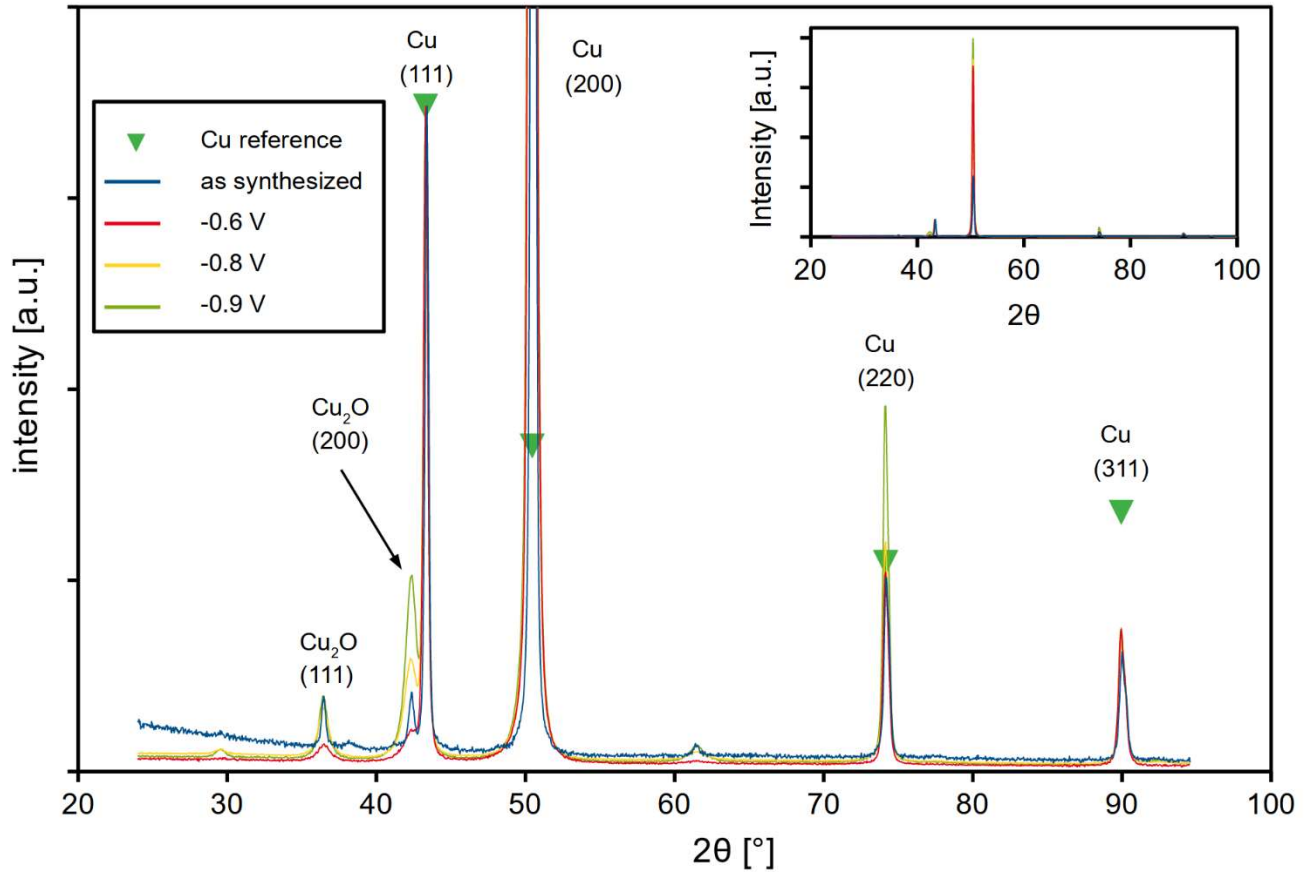


Figure 50: X-ray diffractograms of an as-synthesized Cu nanowire network (blue) and of nanowire networks after the application as catalyst for 1 h CO₂ reduction at potentials of -0.6 V vs. RHE (red), -0.8 V vs. RHE (green) and -0.9 V vs. RHE (yellow). The sample diffractograms are normalized to the Cu powder reference (111) reflection [278].

All diffractograms exhibit the expected Cu reflections. Additionally, they show small Cu₂O(111) and Cu₂O(200) peaks, which originate from the native surface oxide, formed as soon as the Cu nanowire network is exposed to air [281]. The texture coefficients (*TC*) are calculated by equation (28) and presented in Table 7. $I(hkl)$ denotes the intensity of the Cu reflection (*hkl*) of the sample belonging to a certain orientations peak *n* and $I_o(hkl)$ is the corresponding intensity of the standard powder diffractogram [278].

$$TC(hkl) = \frac{I(hkl)/I_o(hkl)}{n^{-1} \sum_n I(hkl)/I_o(hkl)} \quad (28)$$

Table 7: Texture coefficients of the different Cu nanowire networks with respect to the standard polycrystalline Cu powder diffractogram taken from the JCPDS data file [278]

	Cu (111)	Cu (200)	Cu (220)	Cu (311)
pristine	0.49	2.91	0.41	0.19
-0.6 V	0.18	3.56	0.17	0.10
-0.8 V	0.17	3.56	0.19	0.08
-0.9 V	0.15	3.50	0.26	0.08

All nanowire networks exhibit a strong (200) texture with respect to the sample surface because the TC values up to 3.56 are close to the maximal TC of 4 defined by the four considered reflections. Given the geometry of the XRD measurements (45° tilt of the wires), this means that the 220 planes are preferentially oriented perpendicular to the nanowire axis. This finding is in agreement with the preferred (220) texture of vertically oriented Cu nanowire arrays electrodeposited under similar conditions in earlier studies [112,282]. However, to prove this, the sample should be tilted by 45° for having the wires oriented to the X-ray beam in the same way as the parallel wires, and be rotated around the ϕ axis to evidence the 4-axis symmetry of the (220) reflections.

For the pristine nanowire network, the texture is even less than for the nanowire networks after CO_2 reduction. The texture coefficient of the (200) reflex is with 2.91 around 0.6 smaller than for the other networks. This difference is equalized by the slightly higher texture coefficients of the other peaks. The potential applied during CO_2 reduction does not have a significant influence on the texture coefficients. Only the (220) peak shows an increase at the highest reduction potential of -0.9 V vs. RHE, while the (111) and (200) peaks lose a bit of intensity. This could be an effect due to re-crystallization towards another structure at this potential, but needs to be confirmed by further studies. The texture changes of the (111) and (200) reflections could also be a first indication of cathodic corrosion, leaving the (220) crystals less attacked. But generally, the polycrystalline structure of the nanowires remains intact, which is supporting the network stability during the reaction. This observation is confirmed by SEM and STEM analysis.

4.4.2 Structural characterization of the nanowire networks by STEM before and after the CO_2 reduction

The Cu nanowire networks were also investigated by scanning transmission electron microscopy (STEM), which allows imaging and analysis of the crystallographic structure with atomic resolution.

For STEM imaging, small pieces of the Cu nanowire networks ($\sim 25 \text{ mm}^2$) were inserted in a glass test tube filled with 10 ml isopropanol (>99.5 %, Carl-Roth, Karlsruhe, Germany). The tube was then exposed to an ultrasonic bath (Elma Transonic 460/H) for 1 min so that the network pieces break apart into groups of ~ 3 -4 wires. A small amount of the isopropanol containing the nanowire network sections was drop-casted onto a Ni-TEM grid covered by a lacey carbon film (PLANO GmbH, Wetzlar, Germany).

Scanning transmission electron microscopy (STEM) of these nanowire networks was performed with a Titan Themis transmission electron microscope at an acceleration voltage of 300 kV at the Max Planck Institut für Eisenforschung, Düsseldorf, Germany. Three different imaging modes are available, providing different types of contrast, i.e., high angle annular dark field (HAADF), low angle annular dark field (LAADF) and annular bright field (ABF) imaging with three corresponding detectors, collecting scattered electrons under an angle of 8-16, 17-72, and 73-200 mrad, respectively. STEM analysis was performed on a synthesized, pre-cleaned, and anodized nanowire network with a nanowire diameter of only $\sim 85 \text{ nm}$ to provide transparency in the electron beam. The nanowire number density was $4 \times 10^9 \text{ cm}^{-2}$ which is higher

than for most of the samples used in this thesis, to facilitate STEM analysis. Figure 51 presents the high angle annular dark field (HAADF)-STEM images of a representative nanowire short section of an as-synthesized, pre-cleaned, and anodized Cu nanowire network.

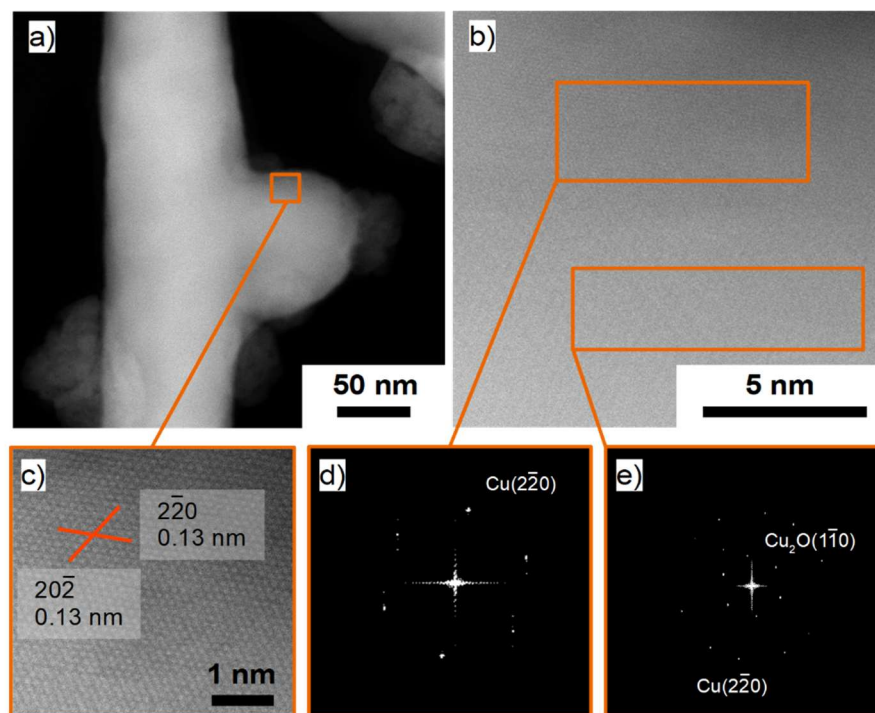


Figure 51: STEM images of an as-synthesized, pre-cleaned, and anodized Cu nanowire segment (diameter 85 nm). a) high angle annular dark field image of a Cu nanowire with a small part of an intersection, b) high-magnification STEM image close to the wire intersection revealing different crystalline structures, c) high-resolution STEM image providing an interatomic distance of 0.13 nm, and d,e) corresponding FFT images taken at the indicated positions at the Cu nanowire.

From the fast Fourier transform (FFT) pattern (Figure 51 d)) of the nanowire region shown in Figure 51 b), an interatomic distance of 0.13 nm can be deduced, consistent with the high-resolution STEM image (Figure 51 c)). This interatomic distance belongs to a face centered cubic (fcc) Cu crystal with the lattice constant $a = 3.597 \text{ \AA}$ [279]. The FFT pattern deduced at another nanowire position (Figure 51 e)) includes reflections with interatomic distances of 0.3 nm and 0.13 nm, which can be attributed to $\text{Cu}_2\text{O}(110)$ and $\text{Cu}(220)$ crystals, originating from the anodization pre-treatment as well as from the storage in air, respectively. The crystals are oriented along a [111] zone axis, indicating the presence of several crystals and partial oxidation. For the determination of the Cu_2O lattice planes, a lattice constant of $a = 4.27 \text{ \AA}$ was taken [283]. The Cu_2O layer at the surface is mainly resulting from the oxidative anodization process after the pre-cleaning. Thus, the STEM images reveal the expected polycrystalline nanowire structure with the oxide layer from the anodization that will be removed prior to the CO_2 reduction process, leading to an activated Cu surface.

Scanning transmission electron microscopy images on a pre-cleaned and anodized Cu nanowire network (height = 30 μm , wire diameter $\sim 80 \text{ nm}$, and nanowire number density = $8 \times 10^8 \text{ cm}^{-2}$) after CO_2 reduction at $U_{el} = -0.79 \pm 0.01 \text{ V vs. RHE}$ are presented in Figure 52. The network exhibited a thinner wire diameter

than the ones used for the other CO₂ reduction experiments in this thesis, to facilitate STEM analysis. As described in section 4.1, a surface reduction by 10 CV scans was applied prior to the CO₂ reduction reaction.

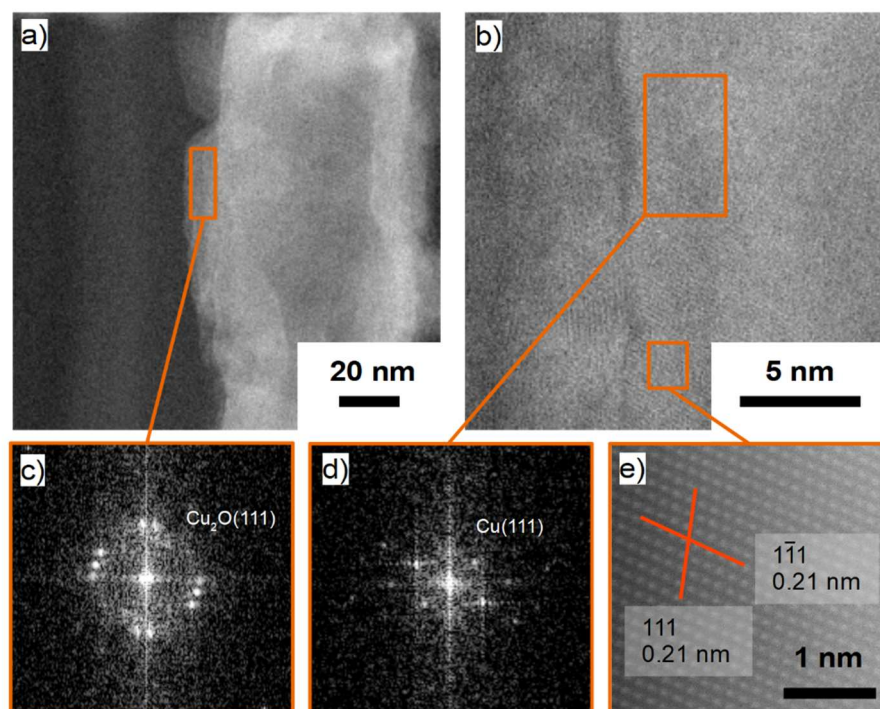


Figure 52: STEM images and analysis of a Cu nanowire after CO₂ reduction: a) HAADF image at the wire surface indicating a Cu₂O layer (c), b) high-magnification STEM image of a nanowire bulk region revealing a polycrystalline structure, c) and d) corresponding FFT images of the indicated positions, and e) high-resolution TEM image.

STEM analysis reveals that the Cu nanowires are composed of a larger Cu crystal core covered by small Cu₂O crystallites on the surface. They are Cu₂O(111) crystals with an interatomic distance of 0.25 nm as deduced from the FFT pattern presented in Figure 52 c). The FFT pattern of a bulk nanowire area (Figure 52 d)) shows reflections for the Cu(111) crystal structure with an interatomic distance of 0.21 nm, in agreement with the high-resolution STEM image of the nanowire part shown in Figure 52 e). The only information that can be concluded from the STEM analysis before and after the CO₂ reduction reaction is that the analyzed nanowire has a polycrystalline Cu₂O layer on the surface. This oxide layer cannot be formed during the CO₂ reduction reaction because of the applied reductive potential, but only afterwards. Thus, these results show no influence of the CO₂ reduction on the crystalline structure of the nanowires, which is consistent with the XRD observations presented in chapter 4.4.1. However, to get detailed insight into possible corrosion processes and the increase in texture, extended STEM studies along larger nanowire segments are necessary in future studies.

4.5 Effect of pre-cleaning and anodization of the Cu nanowire network on the product selectivity of the CO₂ reduction

An acidic pre-cleaning procedure was reported in literature by Lee and Min to improve electrochemical CO₂ reduction at Cu catalysts [166,167], and it was optimized for the NWNWs in this work, as explained above in chapter 2.4. In addition to the morphological studies discussed in section 2.4, we investigated the effect of the pre-cleaning and anodization process on the CO₂ reduction reaction efficiency and product selectivity at the Cu nanowire network catalysts. CO₂ reductions were performed at $U_{el} = -0.6, -0.7$ and -0.8 V vs. RHE on four Cu nanowire networks, two in the pristine state and two which were additionally pre-cleaned and anodized. Thus, all error bars in this section are the result of the averaging of both samples in each state. For the gas phase products, this error propagates with the statistic uncertainties resulting from the three injections into the gas chromatography during the 1 h reaction time. The corresponding current densities are displayed in Figure 53 in dark and light blue, respectively.

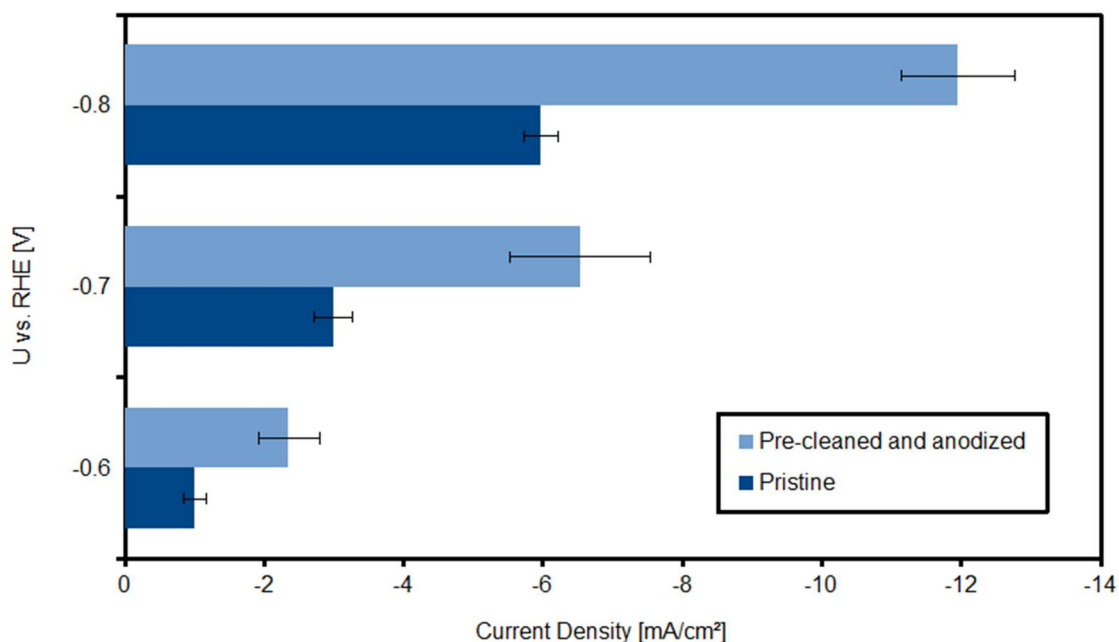


Figure 53: Current densities for the pre-cleaned and anodized Cu nanowire networks (light blue) in comparison to pristine Cu nanowire networks (blue).

For all three potentials, the current density for the CO₂ reduction reaction at the pre-cleaned and anodized samples is by a factor of ~ 2 higher than at the pristine Cu nanowire networks. This increase is, on the one hand, attributed to the larger surface roughness of the pre-cleaned samples, and on the other hand, to higher chemical reaction rates at the catalyst surface. In other words, the higher current densities are not only caused by larger surface areas being exposed to the electrolyte, but also by an increase in surface activity. Figure 54 shows the comparison of the Faradaic efficiencies of a) all reaction products, b) liquid phase products, and c) gas phase products for the CO₂ reduction at a pristine Cu nanowire network and a pre-cleaned one. The increased reaction efficiency is especially significant for the liquid phase products, as shown in Figure 54: Faradaic efficiencies of the CO₂ reduction reaction for pristine (dark blue) and pre-

cleaned and anodized (light blue) Cu nanowire networks for a) all products, b) liquid phase products, and c) gas phase products. Figure 54 b).

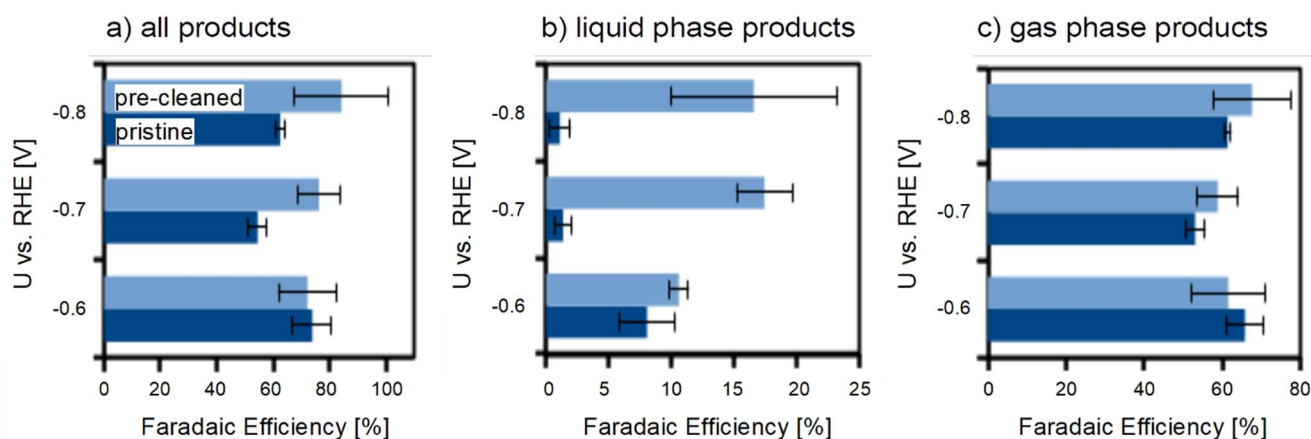


Figure 54: Faradaic efficiencies of the CO₂ reduction reaction for pristine (dark blue) and pre-cleaned and anodized (light blue) Cu nanowire networks for a) all products, b) liquid phase products, and c) gas phase products.

Except for the gas phase products at -0.6 V vs. RHE, the Faradaic efficiencies are higher for the pre-cleaned and anodized Cu nanowire networks. Especially for the generation of liquid phase products, the pre-cleaning and anodization process yields much higher Faradaic efficiencies. For the CO₂ reduction at the other potentials, the pre-cleaning and anodization is also slightly more beneficial for the gas-phase product efficiencies.

Figure 55 shows the Faradaic efficiencies of both, pristine (dark blue) and pre-cleaned and anodized Cu nanowire networks for the formation of the CO₂ reduction reaction intermediates H₂, CO and HCOOH, at $U = -0.6, -0.7$ and -0.8 V vs. RHE.

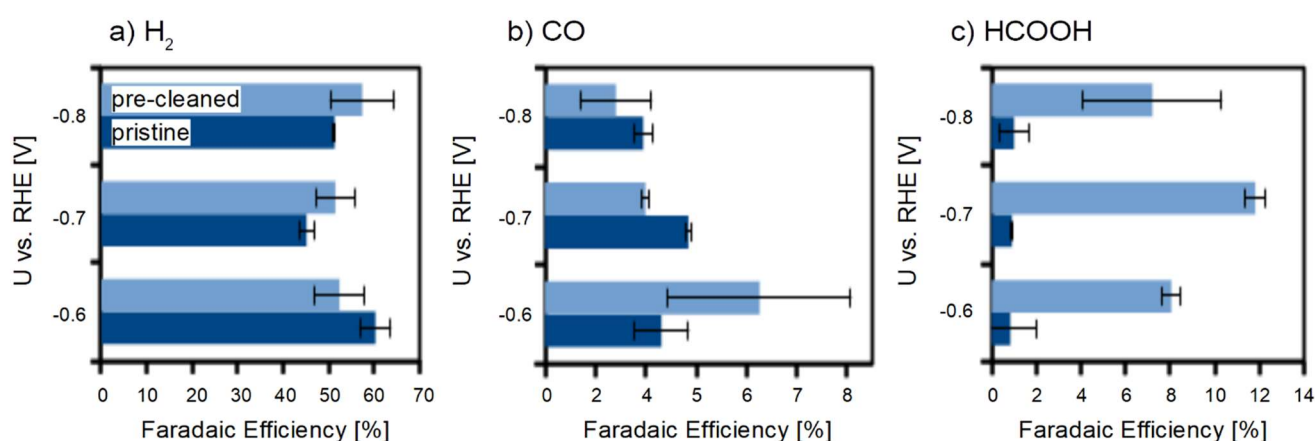


Figure 55: Faradaic efficiencies of a) H₂ evolution and the main reaction intermediates b) CO and c) HCOOH for pre-cleaned and anodized Cu nanowire networks (light blue) and pristine Cu nanowire networks (blue) at CO₂ reduction potentials of $U_{el} = -0.6, -0.7$ and -0.8 V vs. RHE.

For the hydrogen evolution reaction that is competing with the CO₂ reduction reaction, the Faradaic efficiency at $U_{el} = -0.8$ and -0.7 V vs. RHE is higher for the pre-cleaned and anodized samples. For the

reaction at -0.6 V $\sim 10\%$ more H_2 is produced at the pristine sample, which causes the higher Faradaic efficiency sum for gas phase products at this potential.

For CO_2 reduction towards CO , the Faradaic efficiency is higher at the pristine Cu nanowire networks, except for the reaction at -0.6 V vs. RHE. Since less CO is detected in the final reaction products, this confirms the advantage of the pre-treatment for the CO_2 reduction reaction, since more surface adsorbed CO reacts further to higher value products.

For HCOOH the product efficiencies at all potential steps are higher for the pre-cleaned and anodized Cu nanowire networks.

The comparison of the product evaluation efficiencies for the hydrocarbons CH_4 , C_2H_4 and C_2H_6 are compared in Figure 56 for the reaction at pristine as well as pre-cleaned and anodized Cu nanowire networks at the three different reduction potentials of $U_{el} = -0.6, -0.7$ and -0.8 V vs. RHE.

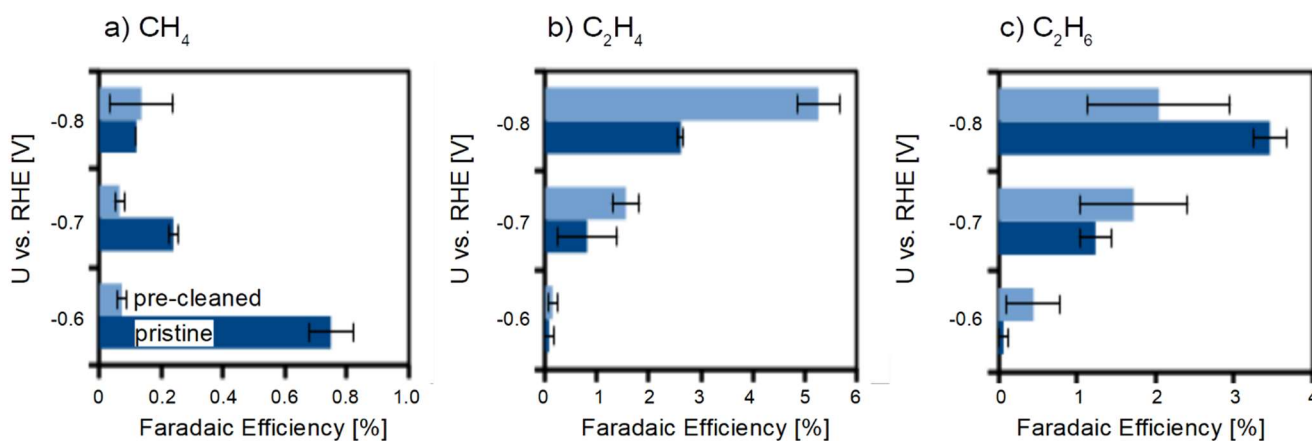


Figure 56: Faradaic efficiencies for the CO_2 reduction products a) CH_4 , b) C_2H_4 and c) C_2H_6 for pre-cleaned and anodized Cu nanowire networks (light blue) and pristine Cu nanowire networks (blue) at CO_2 reduction potentials of $U_{el} = -0.6, -0.7$ and -0.8 V vs. RHE.

The Faradaic efficiencies of CO_2 reduction towards CH_4 is extremely low ($<0.08\%$) with no clear trend for a promoted reaction at one of the two types of Cu nanowire networks. Thus, CH_4 is only a negligible side product of the CO_2 reduction reaction at Cu nanowire networks. For the formation of the desired reaction product C_2H_4 , the beneficiality of the acidic pre-cleaning and anodization process is stated again. At the low reaction potential of $U_{el} = -0.6\text{ V}$ vs. RHE, almost no C_2H_4 is produced, whereas for the other potentials, the Faradaic efficiency for the formation of C_2H_4 at the pre-cleaned and anodized Cu nanowire networks shows double the efficiency than on the pristine network, increasing the efficiency to a maximum of 5% for the pre-cleaned and anodized network at -0.8 V . For the formation of C_2H_6 , which is generally occurring at lower efficiencies than the C_2H_4 formation, the reactions at $U_{el} = -0.6$ and -0.7 V show higher Faradaic efficiencies at the pre-cleaned and anodized Cu nanowire network, whereas at -0.8 V vs. RHE, more C_2H_6 was produced at the pristine sample.

The comparison of the corresponding Faradaic efficiencies of other C2 and C3 reaction products is shown in Figure 57 for a) CH_3COOH , b) $\text{C}_2\text{H}_6\text{O}$, c) $\text{C}_3\text{H}_8\text{O}$ and d) $\text{C}_2\text{H}_6\text{O}_2$.

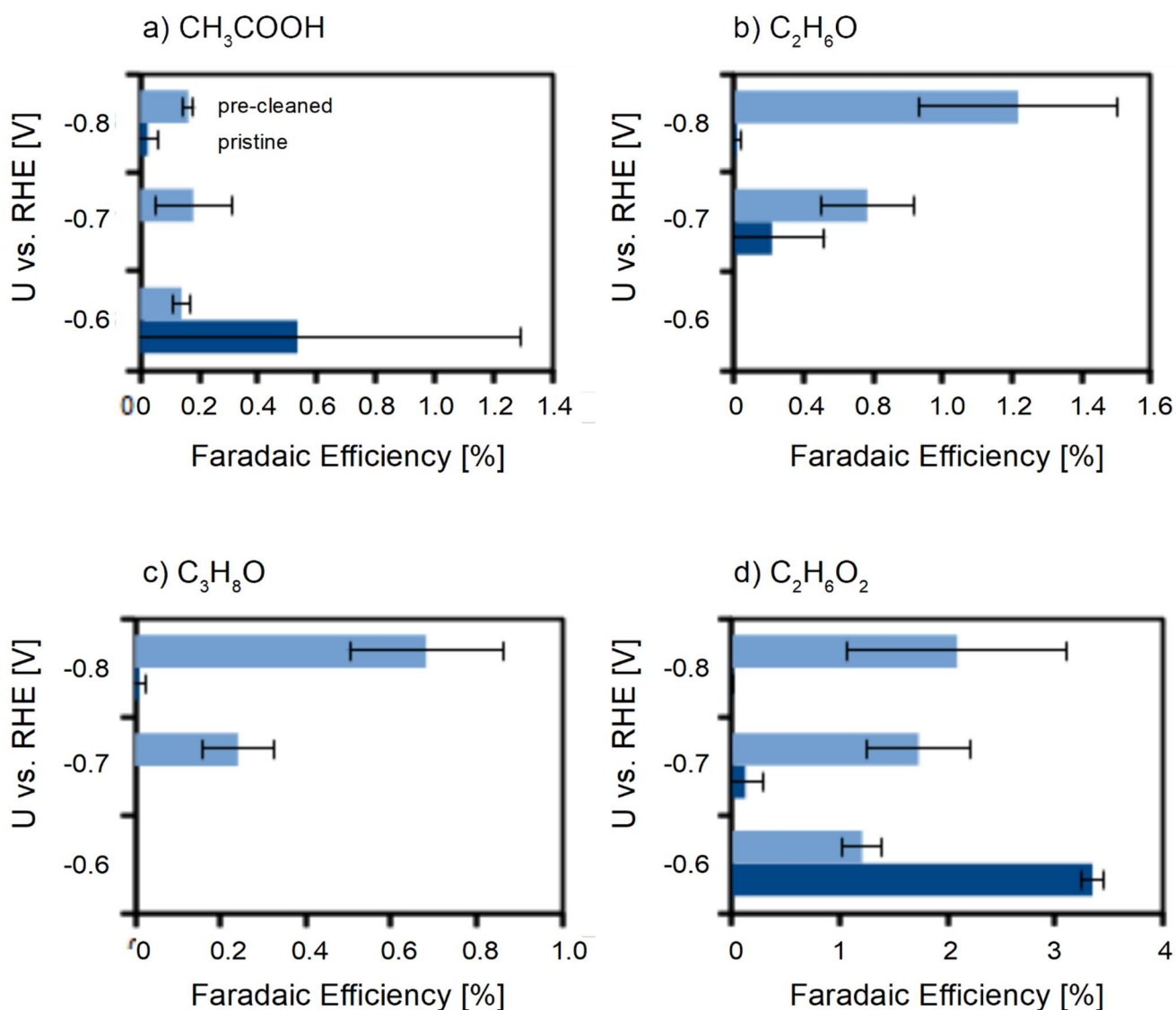


Figure 57: Faradaic efficiencies of the CO₂ reduction products a) CH₃COOH, b) C₂H₆O, c) C₃H₈O and d) C₂H₆O₂ at the three different potentials of $U_{el} = -0.6, -0.7$ and -0.8 V vs. RHE.

As clearly visible in Figure 57 a), CH₃COOH is synthesized at -0.6 V vs RHE to a larger amount on the pristine Cu nanowire network than on the pre-cleaned and anodized one, whereas at the other potentials the efficiency at the pre-treated network is slightly higher. However, for all potentials the Faradaic efficiency for CH₃COOH formation is below 0.6 %. Thus, it is a product only synthesized in negligibly small amounts.

For C₂H₆O also relatively low formation efficiencies are obtained as shown in b). At $U_{el} = -0.6$ V vs. RHE no ethanol is formed at all. This potential seems too low to transfer enough charge into the CO₂ reduction reaction for C₂H₆O formation. At the two higher potentials, C₂H₆O is formed mainly at the pre-cleaned and anodized Cu nanowire network with Faradaic efficiencies up to 1.2 %. The same behavior is visible for the formation of C₃H₈O c), which is not synthesized at all at the pristine Cu nanowire network, but up to an efficiency of 0.7 % at the pre-cleaned and anodized sample.

At $U_{el} = -0.6$ V vs. RHE the $C_2H_6O_2$ formation at the pristine Cu nanowire network is predominant with more than 3 % current efficiency, decreasing strongly and vanishing for increasing potentials, while the $C_2H_6O_2$ formation efficiency at the pre-cleaned and anodized Cu nanowire network is larger for higher potentials as shown in d).

Generally, it can be stated, that all C2+ products show higher formation efficiencies at the pre-cleaned and anodized Cu nanowire networks. The only two exceptions are CH_3COOH and $C_2H_6O_2$ at the low potential of $U_{el} = -0.6$ V vs. RHE. Thus, it can be concluded that the increased roughness and activation of the surface by the pre-cleaning and anodization process is beneficial for the C-C coupling of adsorbed CO molecules. It is assumed that CO reacts further to form advanced molecules, as the efficiency of unused CO as reaction product is opposite to the efficiency of the C2+ products.

Comparing the Faradaic efficiencies for the CO_2 reduction products at the pre-cleaned and anodized nanowire networks of this section to the ones of other networks with equal geometry, shown in chapter 4.4, one can state that the relation of the different products at each potential is basically the same. Only slight differences in the Faradaic efficiencies are observed, with those shown in chapter 4.4 being always a few percent smaller than those in chapter 4.5. Since each value is the average of two or three samples, this difference cannot come from sample effects. Especially, since the pre-cleaning and anodizing process, as well as the surface reduction process before the CO_2 reduction were the same. Since they cannot be traced back to either only liquid phase or only gas phase products, they must be caused by slight differences in the experimental setup, such as the calibration of the mass flow controllers, some plugging of the tubes or some leakages. A slightly different product crossover through the membrane might also be an explanation. To prove this, one always has to do in-situ product analysis in the anode compartment. This would shed light on the quality of different supplied membrane batches.

4.6 Failed CO_2 reduction at Cu nanowire networks with in-situ IR-drop correction

To perform the CO_2 reduction reaction in relation to the electrode potentials, the correction of the IR-drop across the cell needs to be performed. An in-situ correction procedure for the IR-drop was first tested on Cu nanowire networks by enabling the IR-compensation option of the potentiostat. To avoid overcompensation, only 85 % of the R_u gained by EIS were set to be compensated. This procedure had proven successful in CO_2 reduction at Cu-foams [53,168].

For the test measurement with enabled IR-correction, a desired electrode potential of $U_{el} = -1$ V vs. RHE was set as target in the potentiostat. This led to an application of more than -2.5 V vs. Ag/AgCl cell potential. During the chronoamperometric CO_2 reduction time of 1 h at this potential, the current did not remain constant, but increased and the system became unstable. A typical change in current density as a function of time is shown in Figure 58 where U_{appl} vs. Ag/AgCl is presented for CO_2 reduction at a Cu nanowire network without in-situ correction of the IR-drop (red) and with in-situ correction (blue). The yellow inset

numbers are the measured resistivity values R_u of the corresponding Cu nanowire networks before and after the potentiostatic measurement.

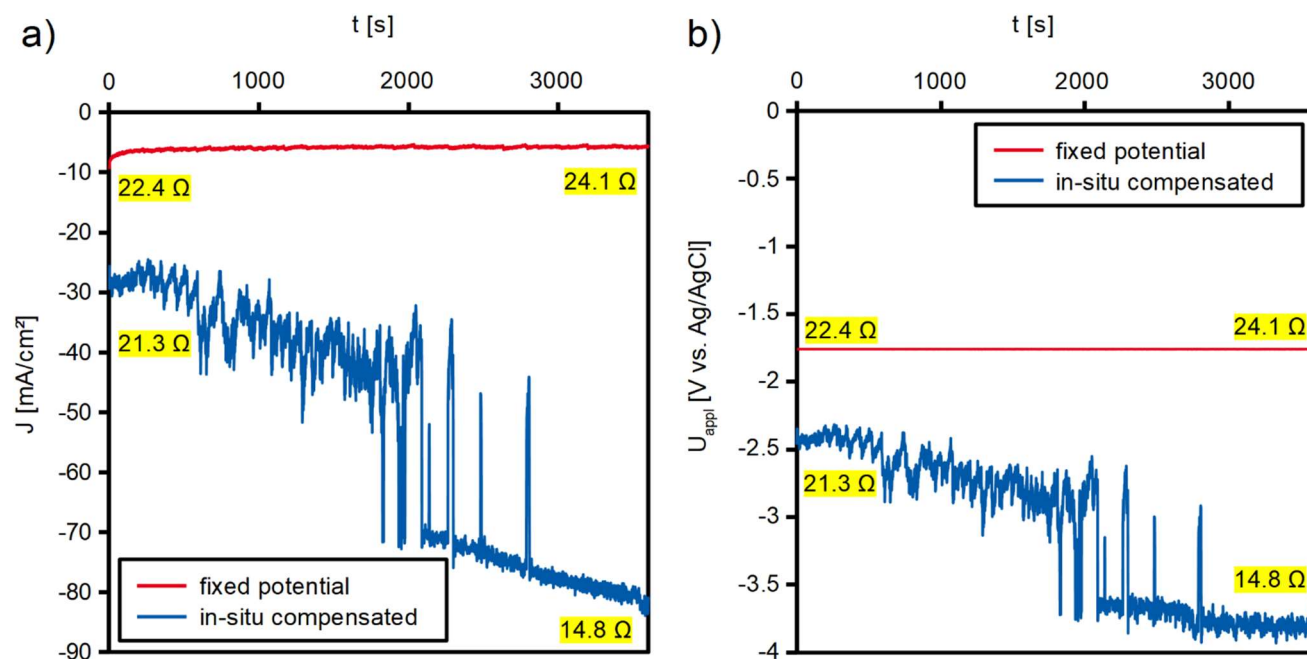


Figure 58: a) Current density J vs. t curve and b) U vs. t (right) for CO₂ reduction at two similar Cu nanowire networks, one without in-situ compensation of the IR-drop (red), and one with in-situ IR-compensation (blue).

For the CO₂ reduction reaction with in-situ IR-compensation, the potentiostat directly applied a potential of $U_{\text{appl}} = -2.5$ V vs. Ag/AgCl, for a desired electrode potential of -1.0 V vs. RHE. This automatically induced a current density of -30 mA/cm², which in the beginning remained constant, despite some fluctuations. Over time however, it increased towards -40 mA/cm² until after ~ 2000 s a critical point was reached, where the current density began to strongly fluctuate causing sharp peaks up to -70 mA/cm², and finally staying at these high values. The in-situ IR-compensation of the potentiostat reacted to these changes by assuming a higher IR-drop. Due to the increased current, it increased the applied potential even more, strengthening this effect. EIS showed that the resistance of the nanowire network had decreased drastically from 21.3 Ω to 14.8 Ω .

To get closer information on the origin of this resistance decrease, the Cu nanowire networks were analyzed by SEM before and after the CO₂ reduction measurements. The images of both Cu nanowire networks are shown in Figure 59.

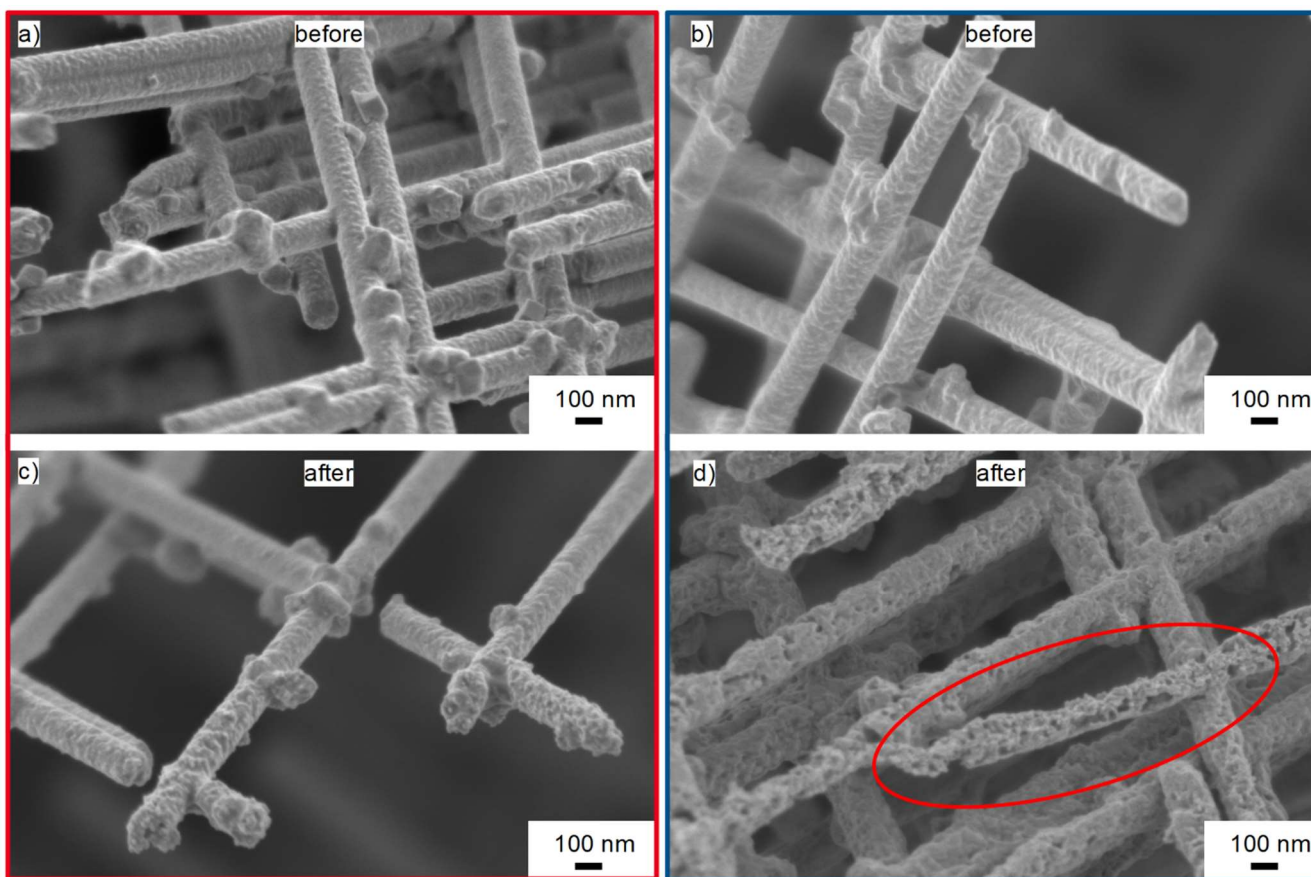


Figure 59: SEM images of the Cu nanowire network a) before and c) after CO₂ reduction at $U_{el} = -0.81$ V vs. RHE without in-situ IR-compensation with an applied potential of $U_{appl} = -1.8$ V vs. RHE and of the Cu-nanowire network b) before and d) after CO₂ reduction with in-situ compensation of the IR-drop.

The Cu nanowire network which was applied for CO₂ reduction at a fixed potential shows no changes in surface or structural properties. In contrast, the nanowire network measured with in-situ compensation of the IR-drop is severely corroded with porous features (highlighted in red in Figure 59 d)). These images demonstrate that the initial applied potential of -2.5 V vs Ag/AgCl, selected automatically by the potentiostat in the automatic IR-compensation mode results in severe nanowire degradation due to the increase of applied potential, caused by overcompensation.

Since a reductive potential is applied for the CO₂ reduction reaction, this degradation process is a matter of cathodic corrosion, which was already reported for CO₂ reduction in aqueous media at Cu surfaces at relatively mild cathodic potentials [284,285]. For the Cu nanowire network, this cathodic corrosion appearing at the applied potential of -2.5 V vs. Ag/AgCl caused an increase in surface area due to the degradation induced nanowire porosity, which is directly leading to a current increase.

The 0.1 M KHCO₃ electrolyte of this CO₂ reduction reaction was analyzed with inductively coupled plasma mass spectrometry (ICP-MS) to get a hint about the remains of the material, which degraded from the Cu nanowire networks during the cathodic corrosion. ICP-MS is a very precise analysis method, capable of detecting even traces of metals in liquids [286,287]. The detected amount of Cu was compared with a pristine 0.1 M KHCO₃ electrolyte that was not used for any CO₂ reduction before, thus containing only 0.05

μg of Cu as trace element. The Cu in the electrolyte after the reaction corresponds with $0.33 \mu\text{g}$ to 0.1% of the original mass of the Cu nanowire network of 2.7 mg which was determined by weighing the sample before the CO_2 reduction.

The amount of Cu in the electrolyte taken after the CO_2 reduction reaction with cathodic corrosion, is by a factor of ~ 7 higher than in the pristine solution. However, reviewing the SEM images, it seems that the corrosion of the wires involves much more material than the 0.1% deduced from the ICP-MS analysis. This suggests that some of the eroded material is redeposited onto the nanowire structure after its initial dissolution into the electrolyte. This dissolution-redeposition phenomenon is known for cathodic corrosion processes [288,289] and can play a beneficial role for the generation of advanced nanostructures [288]. According to SEM analysis of more than twenty nanowires (as illustrated in Figure 60), the wire diameter of our corroded network increased from $145.5 \pm 5.3 \text{ nm}$ to $172.7 \pm 19 \text{ nm}$. This substantial diameter growth indicates that the redeposition process probably also happens here.

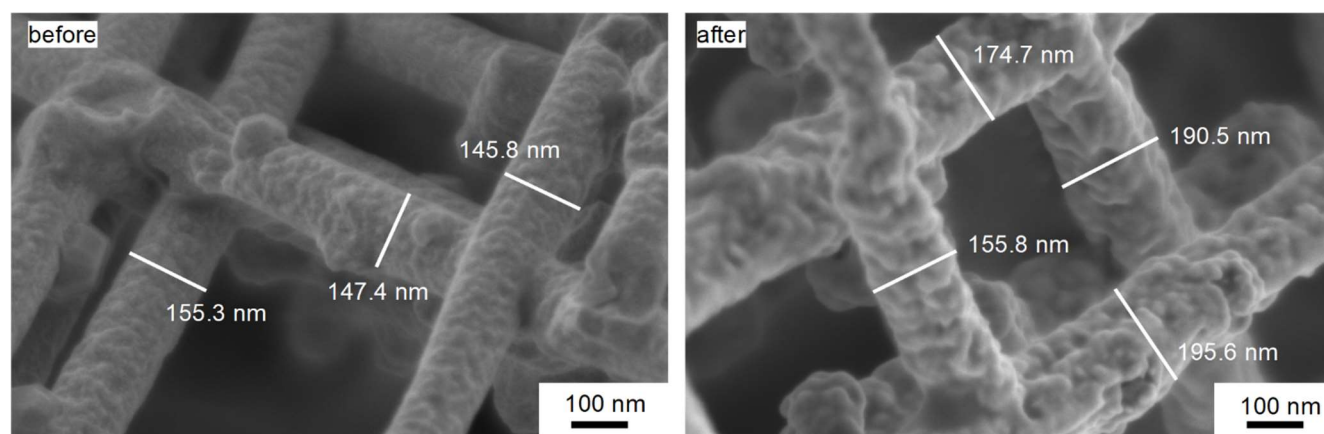


Figure 60: High-resolution SEM images of a corroded Cu nanowire network before and after CO_2 reduction, revealing a rougher surface and an increase of wire diameter from $145.5 \pm 5.3 \text{ nm}$ to $172.7 \pm 19 \text{ nm}$.

Given the results of these initial tests, in-situ IR-compensation is not recommended for CO_2 reduction measurements with Cu nanowire networks.

In turn, when the CO_2 reduction without in-situ IR-compensation was performed at a fixed $U_{\text{appl}} = -1.8 \text{ V}$ vs. Ag/AgCl, it led to an average current density of -6 mA/cm^2 . Thus, the resulting electrode potential, considering the IR-drop measured at the beginning, was $U_{\text{el}} = -0.81 \text{ V}$ vs. RHE. The changes in current density over time are minimal and R_u of the cell increases slightly from 22.4Ω at the beginning to 24.1Ω at the end of the measurement. These R_u values were obtained by EIS in the beginning and end of the measurement.

Therefore, all CO_2 reduction measurements in this work are carried out at constant applied potentials (U_{appl}) without the in-situ IR-compensation option. Instead, to guarantee comparability of the data, the IR-drop is corrected afterwards during data analysis by mathematical calculations using the raw data. Thus, the IR-compensated potential at the electrodes (U_{el}) during the CO_2 reduction is subsequently determined.

4.7 Studies on cathodic corrosion effects and timeframe at high applied potentials

Cathodic corrosion is a process that has been described first in the 19th century as particle clouds disappearing from metals by application of a cathodic potential [290–292]. In the first step of the cathodic corrosion mechanism, alkali ions of the electrolyte are reduced on the electrode surface, forming an alloy [290,291,293]. Subsequently, an exothermic leaching reaction transfers the alkali metal back into the electrolyte and the released metal from the cathode into metallic dust by hydrogen evolution. However, newer reports concluded that alloy formation and leaching mechanisms are insufficient to fully explain cathodic corrosion, since it is not only physical disintegration, but also involves a chemical reaction [294]. Furthermore, adsorbed hydrogen plays a role in accelerating the cathodic corrosion process [295]. Strong metal cations in an electrolyte were shown to be able to remove metal atoms from the electrode structure [288]. The anions of the electrolyte do not have an effect on the corrosion process at all and together with the strong reductive potential, any possibility of electrode oxidation in the cathodic corrosion process can be directly discarded [294].

Due to misfits of experimental results with a corrosion mechanism forming alloys from the electrode metal and the alkali ions of the electrolyte, a modified mechanism was proposed for cathodic corrosion. It is assuming the formation of a very high pH layer, rich in alkali cations and depleted of water, at the electrode surface due to HER. Thus, the cathodic polarization of the electrode induces a reduction of electrode metal to its anionic form at the surface. These anions are directly stabilized by the alkali cations in this layer of high pH value. Thus, at the interface, the metal electrode anions and the alkali cations form a Zintl complex [296]. This complex easily becomes solvated in the high pH layer and diffuses away from the electrode. Upon encountering free water, the metal anions are oxidized, forming hydrogen and charge-neutral metal atoms, which agglomerate and form metallic nanoparticles that are redeposited at the electrode structure due to the applied cathodic potential [294].

Focused studies on the cathodic corrosion processes on Cu electrodes delivered an explanation by the formation of metal hydrides that are released. They either evaporate or react with the electrolyte water to produce hydrogen gas and metallic particles, which can be redeposited back to the cathode surface [297,298]. Additionally, Cu has shown to be very prone to cathodic etching processes in aqueous solution that dissolve the electrode or can be used beneficially to synthesize Cu nanoparticles [292,299–301].

To specify the timeframe of cathodic corrosion during CO₂ reduction at high applied potentials and to rule out an effect induced by nanowire contaminations with molecules of the surfactant that is necessary for homogeneous nanowire deposition into the hydrophobic etched ion-track membrane [159], a Cu nanowire network and a Cu nanowire array, electrodeposited with and without surfactant addition, respectively, were placed in an electrochemical cell filled with 0.1 M KHCO₃. A potential $U_{appl} = -4$ V vs. Ag/AgCl was applied for 2 h. This potential was chosen, since previous experiments (see chapter 4.6) have shown $U_{appl} = -4$ V vs. Ag/AgCl to be the potential which ensues when corrosion of the nanowire network is happening.

The J - t curves of the nanowire network (electrodeposited with surfactant, blue) and the nanowire array (electrodeposited without surfactant, red) are presented in Figure 61. R_u was determined every 30 min by EIS and the values are written in the graph in the corresponding colours. Both nanowire structures exhibited similar geometric properties of $h = 30 \mu\text{m}$, $d = 150 \text{ nm}$ and $F = 2 \times 10^9 \text{ cm}^{-2}$ as well as a planar sample area of 1.8 cm^2 .

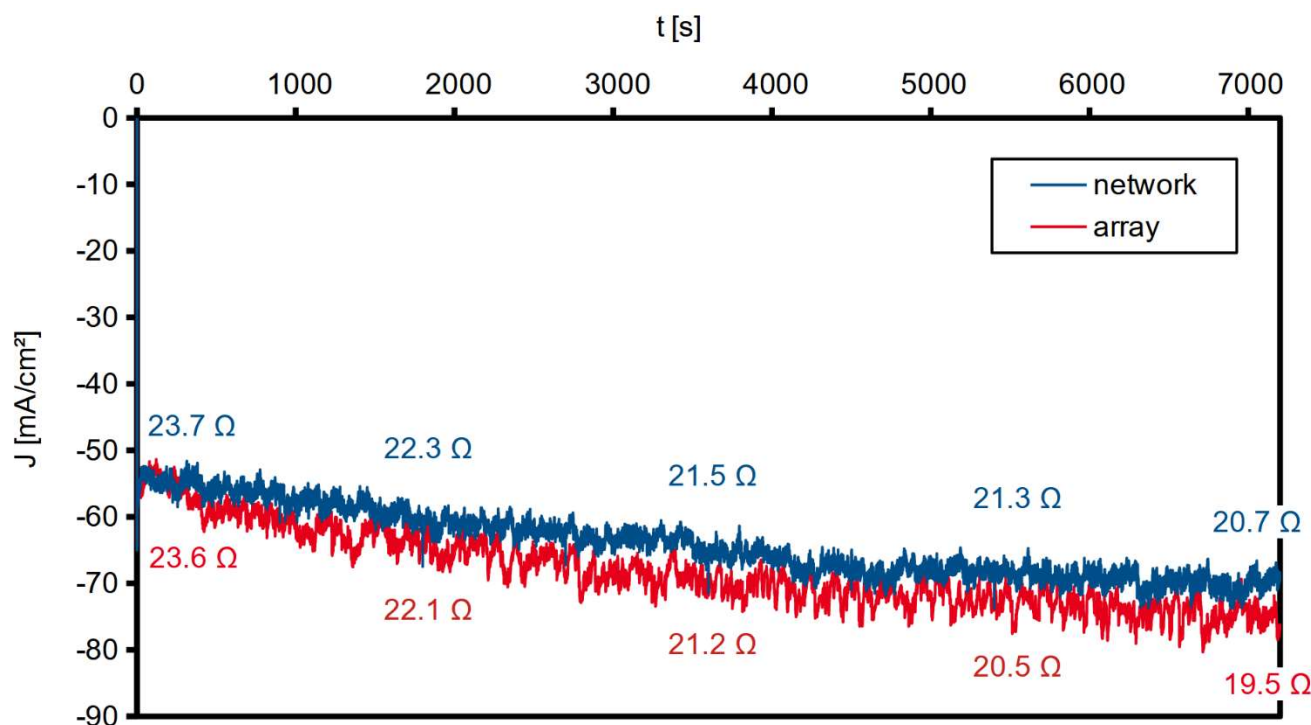


Figure 61: J - t curve for 2 h with an applied voltage of $U_{appl} = -4 \text{ V}$ vs. Ag/AgCl for a Cu nanowire network (blue) and a Cu nanowire array (red). The corresponding R_u values were determined by EIS in 30 min time steps. Both nanowire structures exhibited similar geometric properties of $h = 30 \mu\text{m}$, $d = 150 \text{ nm}$ and $F = 2 \times 10^9 \text{ cm}^{-2}$.

For the nanowire network, the current density linearly increases during the first hour from -54 mA/cm^2 to -64 mA/cm^2 . Within the second hour, this increase rate is a bit lower only from -64 mA/cm^2 towards -70 mA/cm^2 . Within the 2 hours, the resistance R_u decreases from 23.7Ω to 20.7Ω .

For the nanowire array, the evolution is quite similar, with the current density increasing from -54 mA/cm^2 to -67 mA/cm^2 within the first hour and to -77 mA/cm^2 after 2 hours. Thus, the current increase is a bit higher than for the nanowire network corresponding to a stronger R_u decrease from 23.6Ω to 19.5Ω .

These values are indicative for a continuous corrosion process over the 2 h of high potential application, which seems to be a bit stronger for the nanowire array, since higher current density that is normalizing the absolute current on the planar sample area, is indicating a larger ECSA, resulting from surface roughness increase by corrosion processes. The SEM analysis of the two structures, performed before and after the corrosion studies are presented in Figure 62.

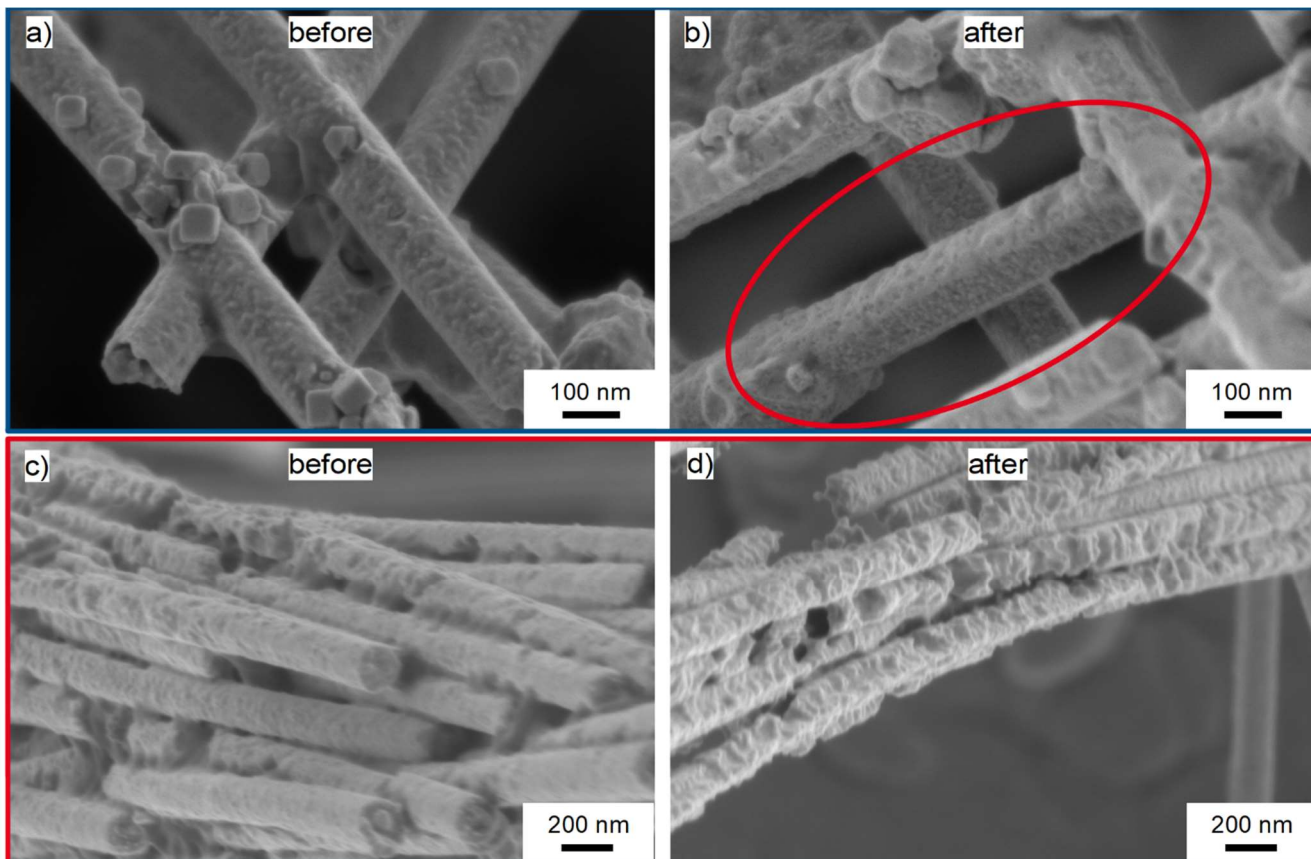


Figure 62: SEM images of a, b) the Cu nanowire network and c, d) the Cu nanowire array before and after the application of $U_{appl} = -4$ V vs. Ag/AgCl for 2 h. The red circle in b) marks a shape change of the nanowires of the network.

SEM analysis before and after the 2 h provides clear evidence of cathodic corrosion of the Cu nanowires in both structures that can manifest in material loss or a shape change from round towards a more faceted like outline of the Cu nanowires of the network due to surface restructuring during the corrosion [288,295,302] as marked with the red circle in Figure 62 b). The small cubes observable on the nanowire surface in Figure 62 a) before the CO_2 reduction reaction might be artefacts from slight recrystallisation during the surface reduction CVs. As already indicated by the current density curves and R_u values, the cathodic corrosion leading to porosity is even stronger for the nanowire array than for the network. This might be due to the fact that the applied potential is not homogeneously distributed along the nanowire-electrolyte interfaces. The tips of the wires are known to cause peaks in the electric field. Such field effects can possibly enhance corrosion of the Cu nanowire array. Generally, a surfactant contamination influencing the cathodic corrosion can be ruled out, since the wires appear even stronger corroded for the nanowire array deposited without surfactant.

Due to these corrosion effects at high U_{appl} and the IR-drop at the large current densities occurring during the CO_2 reduction at the Cu nanowire networks the applicable electrode potentials are limited. Thus, a cathodic potential of -0.93 V vs. RHE was the highest reachable potential for the CO_2 reduction (see chapter 4.4) without destroying the nanowire networks by cathodic corrosion. This is lower than the reported overpotentials in literature, being most efficient for CO_2 reduction at either Cu plates or Cu nanowire

structures synthesized by the reduction of CuO nanorods, which were between -1.05 V [50] and -1.1 V [134], respectively. For future studies this corrosion problem needs to be addressed on the one hand by changing the setup to lower resistance and thus less applied potential necessary for significant reaction currents due to a lower IR-drop. And on the other hand the nanowire networks could be improved in their stability against the cathodic corrosion by either a more single crystalline structure, achievable by lower electrodeposition potentials, or by slightly alloying it with more noble metals [298]. However, in this case the influence of the alloying element on the selectivity of the CO₂ reduction has to be kept in mind as well.

4.8 Test of long term stability of Cu nanowire networks during CO₂ reduction

To check the potential stability and nanowire network stability for a longer timeframe under CO₂ reduction conditions, three Cu nanowire networks were tested under cell potentials $U_{appl} = -2.4$ (blue), -3.1 (red) and -4.3 V (yellow) vs. Ag/AgCl for 5 h in the CO₂ reduction setup without gas flow. The recorded $J-t$ curves are presented in Figure 63 with the applied potentials U_{appl} vs. Ag/AgCl indicated in the corresponding colour on the right. The resulting electrode potentials U_{el} vs. RHE for the first and last 5 minutes are given in black above the curves at the left and right side, respectively.

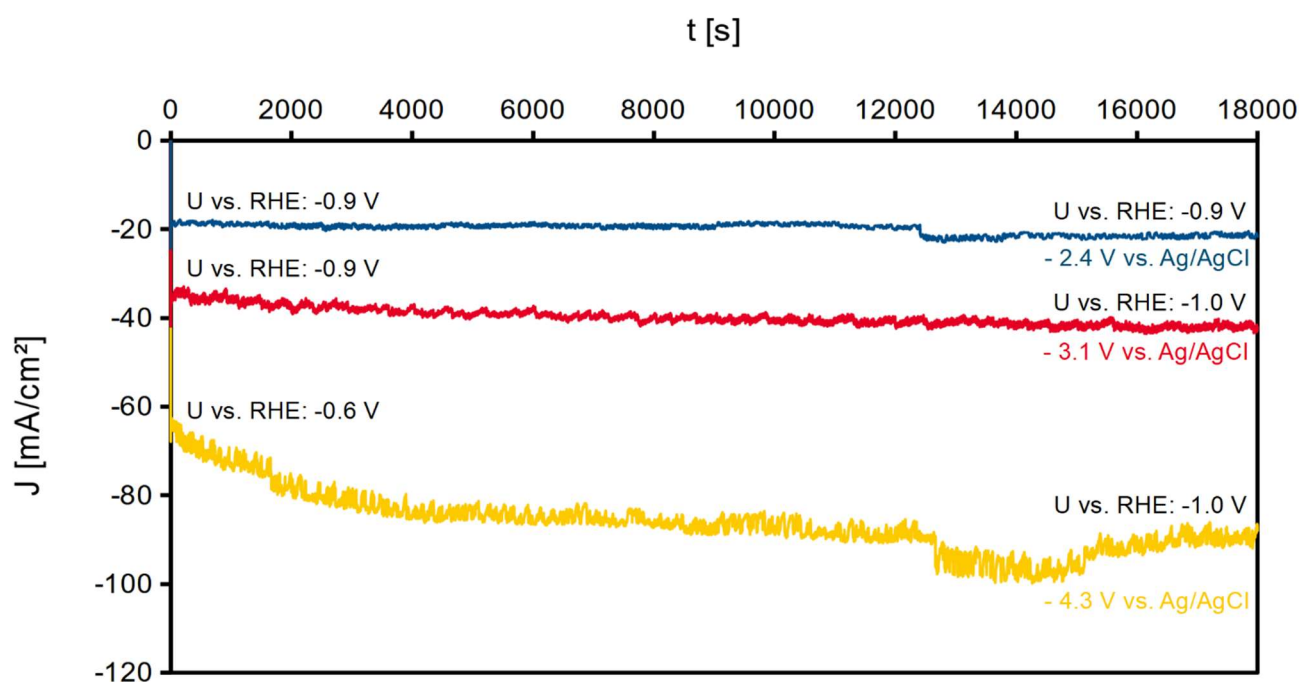


Figure 63: $J-t$ curves for 5 hours extinction of Cu nanowire networks to potentials of $U_{appl} = -2.4$ V vs. Ag/AgCl (blue), -3.1 V vs. Ag/AgCl (red) and -4.3 V vs. Ag/AgCl (yellow) in 0.1 M KHCO₃. The IR-compensated potentials U_{el} vs. RHE for the first and final 5 minutes of potential application are given in black above the curves on the left and right side, respectively.

R_u of the nanowire networks, which determines the IR-drop, was measured by EIS directly before the potential application and at the end after the 5 h test measurement. The values are listed in Table 8 and were used for the calculation of the IR-compensated electrode potentials at the beginning and end of the

process, taking the first and final average currents over 5 min as the other calculation factor for the IR-drop.

Table 8: Resistance of the different Cu nanowire networks before and after the application of $U_{appl} = -2.4, -3.1$ and -4.3 V vs. Ag/AgCl for 5 h each.

U_{appl} vs. Ag/AgCl [V]	R_u before [Ω]	R_u after [Ω]	ΔR_u [Ω]
-2.4	27.1	23.6	3.5
-3.1	24.9	20.5	4.4
-4.3	26.7	16.9	7.1

For the applied potential of $U_{appl} = -2.4$ V vs. Ag/AgCl, the resistance R_u drops over time by a value of 3.5Ω . Coupled to this, the current density increases slightly, shown by a jump after 3.3 h. However, the SEM images in Figure 64 do not show a strong change in surface roughness and structure. Thus, the origin of this resistance drop and sudden current increase remains unclear.

For the Cu nanowire network studied at $U_{appl} = -3.1$ V vs. Ag/AgCl, the resistance drops by a value of 4.4Ω from 24.9Ω to 20.5Ω . This drop occurs constantly with time, stated by a slight but constant increase in current density. Using these resistance values for the calculation of the IR-compensated potential leads to values of $U_{el} = -0.9$ V vs. RHE for the first 5 minutes and -1.0 V vs. RHE for the final 5 minutes. For this Cu nanowire network the resistance change can be directly attributed to roughness and thus surface area increase as deduced from the SEM images in Figure 64.

At $U_{appl} = -4.3$ V vs. Ag/AgCl the degradation of the Cu nanowire network is even more pronounced. A strong increase in surface roughness is directly visible in Figure 64. This is accompanied by a decrease in setup resistance (R_u) of 7.1Ω , represented by a strong current increase over time. This change especially occurs during the first hour of potential application by a value of 30 mA/cm^2 . After 3.3 h there is another jump in current density, similar as observed for the Cu nanowire network at $U_{appl} = -2.4$ V vs. Ag/AgCl. This leads to the conclusion that the cathodic corrosion, leading to the larger electrode surface and thus a strong current increase, occurs at this potential mainly during the first hour. The calculated electrode potentials for the first and final 5 minutes are $U_{el} = -0.6$ V and -1.0 V vs. RHE. The potential for the final 5 minutes corresponds to the desired potential of -1.0 V vs. RHE and represents the resistance drop and current density increase, since there are no large changes in current density during the last 5 minutes. However, for the first 5 minutes, the calculated, compensated potential value is probably incorrect, because the current density changes quite strongly within this time, representing an immediate resistance loss. This change in resistance can not be considered in the calculation of the compensated potential, since only the known R_u at the beginning of potential application can be applied.

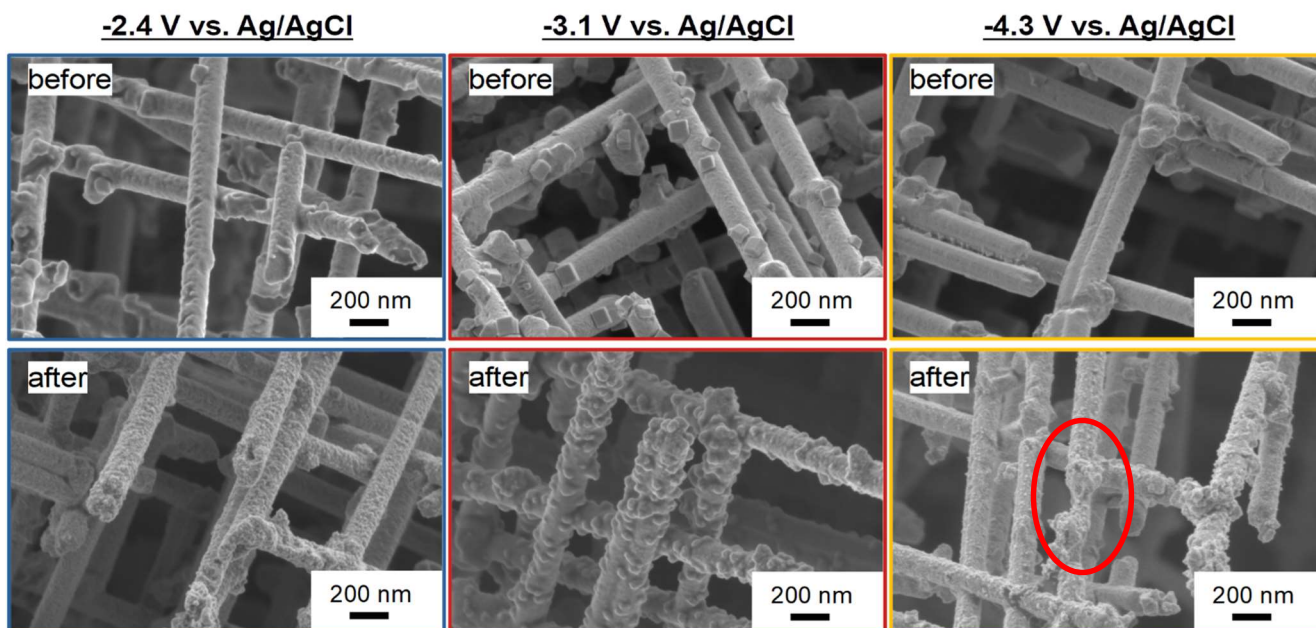


Figure 64: High resolution SEM images of the Cu nanowire networks applied to potentials of $U_{appl} = -2.4$ V vs. Ag/AgCl (blue), $U_{appl} = -3.1$ V vs. Ag/AgCl (red) and $U_{appl} = -4.3$ V vs. Ag/AgCl (yellow) for 5 h. The SEM images show the nanowire networks before (upper row) and after (lower row) the tests.

The control experiments show, that the degradation of the samples due to cathodic corrosion becomes more pronounced with increasing applied potential. This supports the explanation that cathodic corrosion takes place via dissolution of the metal atoms caused by electrolyte cations [288], which is more pronounced at higher potentials due to higher charge transfer in the structure. Moreover, due to the higher current, local heating may also enhance sample degradation [288]. Surface structure rearrangements, for Cu catalysts during CO₂ reduction at cathodic potentials, as we also observe at our Cu nanowire networks, have already been reported in literature. It was found that they are potential dependent, generating more step edges with increasing reduction potential [303], which is consistent with our observations as specifically observable in form of small surface crystallites and edges in Figure 65.

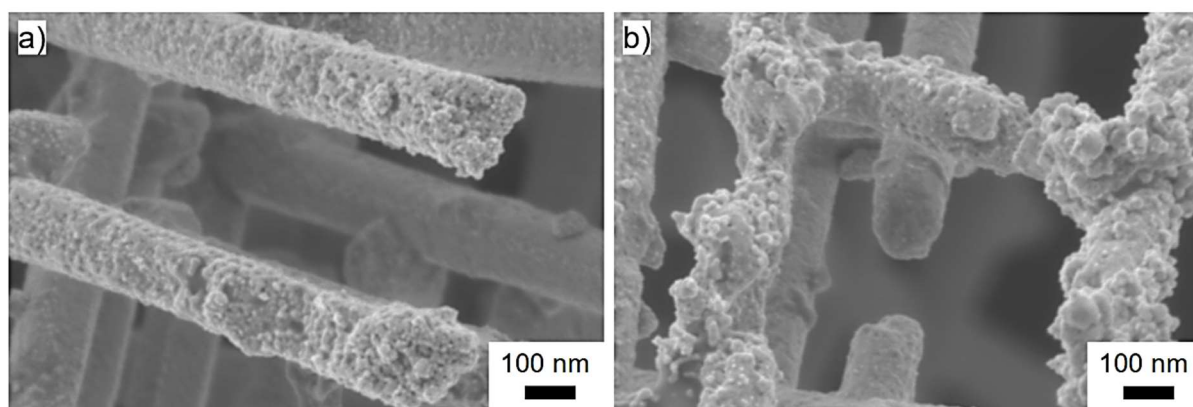


Figure 65: High magnification SEM images of the nanowire network surfaces applied to a) $U_{appl} = -3.1$ V vs. Ag/AgCl and b) $U_{appl} = -4.3$ V vs. Ag/AgCl for 5 h each, showing surface structuring with the formation of step edges in the shape of small crystallites.

This corrosion affects the resistance of the electrochemical cell with the nanowire network as cathode mainly by increasing the wire porosity and roughness, leading to a larger surface being exposed to the

electrolyte, which causes a decrease in charge transfer resistance. Thus, stronger corrosion leads to higher resistance losses of the setup as deducible from the current density curves. The data clearly indicate that the main corrosion process starts already in the first hour after potential application.

4.9 Evaluation of the product selectivity during long-term CO₂ reduction at Cu nanowire networks

To test the long-term stability and behavior of the Cu nanowire networks, potentiostatic CO₂ reduction applying them as catalyst was performed for 8 h (28800 s). We tested four different Cu nanowire networks at electrode potentials of $U_{el} = -0.6 \pm 0.0$, -0.64 ± 0.01 , -0.69 ± 0.01 and -0.83 ± 0.03 V vs. RHE, leading to the J - t curves presented in Figure 66. All networks exhibited the same geometric parameters, i.e. 1.8 cm² planar sample area, 30 μm network height, 150 nm nanowire diameter and a nanowire number density of 8×10^8 cm⁻². Each nanowire network was pre-cleaned, anodized and the surface reduced by 10 CV scans directly before the CO₂ reduction reaction in 0.1 M KHCO₃. The measurements were performed in the electrochemical two-compartment cell with the Selemion AMV anion exchange membrane. The gas phase reaction products were monitored continuously by injection into the GC every 28 minutes. The liquid phase reaction products were analyzed by NMR spectroscopy on the electrolyte after the reaction time. R_u of the setup was determined by EIS before and after the reaction.

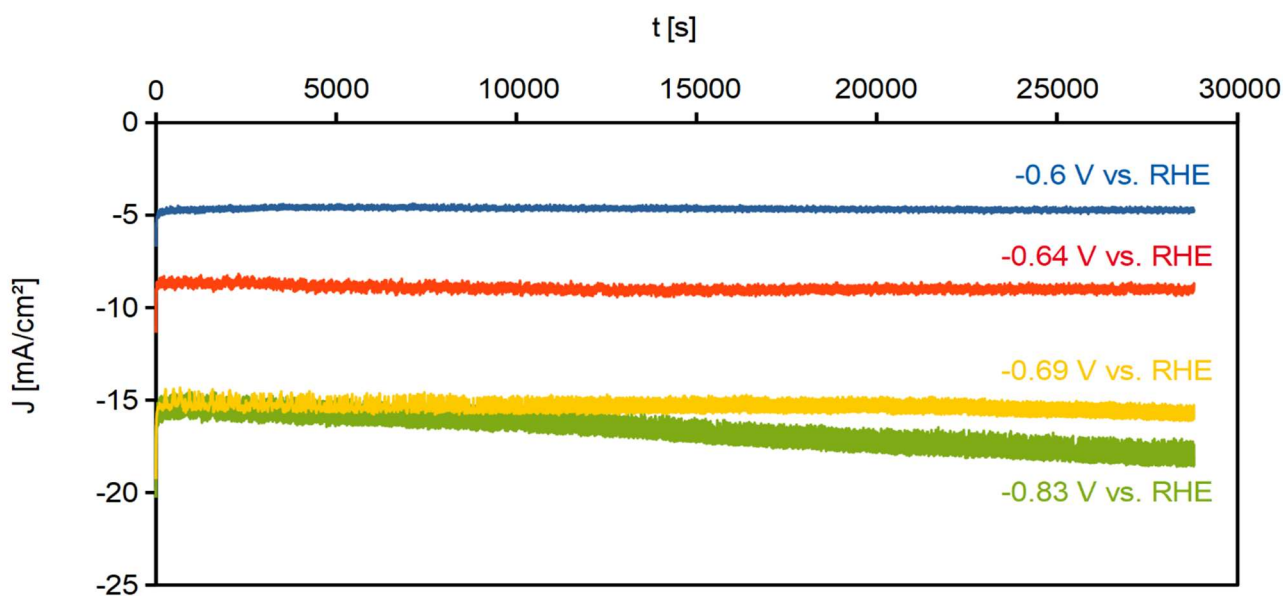


Figure 66: Current density J - t curves for electrochemical CO₂ reduction for 8 h at different Cu nanowire networks with identical geometrical parameters $h = 30$ μm, $d = 150$ nm and $F = 8 \times 10^8$ cm⁻² at different electrode potentials U_{el} vs. RHE.

During 8 h of CO₂ reduction at $U_{el} = -0.6 \pm 0.0$ V vs. RHE (blue) the current density remains constant for the whole time at ~ -4.8 mA/cm². Nonetheless, this sample encounters a resistance drop of 3.8 Ω from 25.2 Ω at the beginning to 21.4 Ω after the reaction. At $U_{el} = -0.64 \pm 0.01$ V vs. RHE a small current density increase from ~ -8.7 to ~ -9.1 mA/cm² happens, accompanied by a R_u drop of 4.5 Ω from 26.5 Ω to 22.0 Ω. At a

reduction potential of $U_{el} = -0.69 \pm 0.01$ V vs. RHE the current density increase is more pronounced from ~ 15.2 mA/cm² in the beginning to ~ 16 mA/cm² in the end. This current density increase is accompanied by a R_u drop of 3.6Ω from 23.0Ω to 19.4Ω . For the higher CO₂ reduction reaction potential at $U_{el} = -0.83 \pm 0.03$ V vs. RHE the current density increase is even more pronounced from ~ 15 mA/cm² towards ~ 18 mA/cm². The R_u drop is with 5.6Ω as difference from 22.2Ω before and 16.6Ω after the reaction the largest observed value. Thus, all Cu nanowire networks show a R_u drop of values between 3.6 and 5.8Ω , which increase, except for the sample applied at $U_{el} = -0.69 \pm 0.01$ V vs. RHE, with applied potential. The current density over time, which is a direct consequence of the R_u drop, increases with potential as well.

To check the origin of these resistance drops and to get information about the structural stability of the Cu nanowire networks during the long-term CO₂ reduction reactions, SEM imaging was performed before and after the reaction as shown in Figure 67.

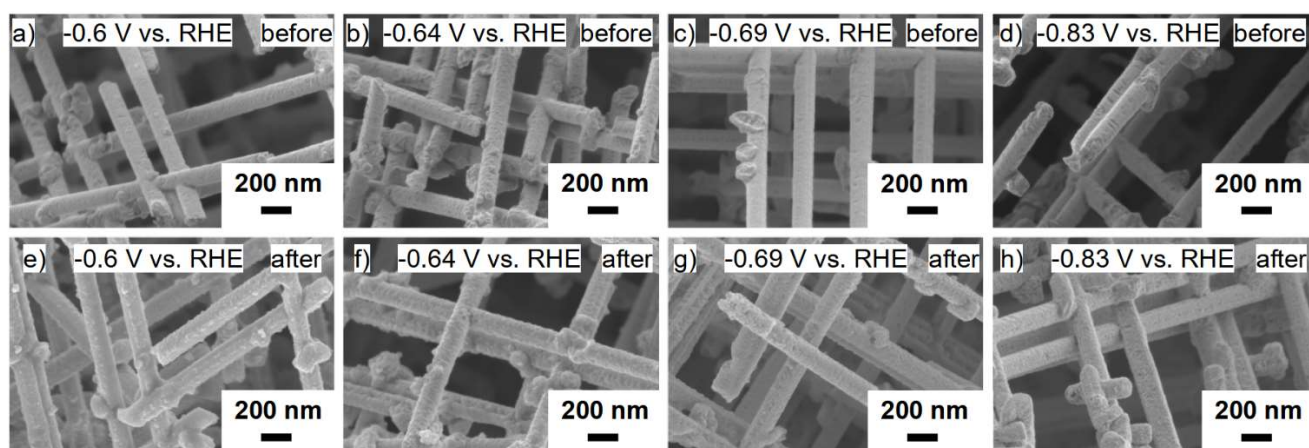


Figure 67: SEM images of the Cu nanowire networks before and after application as catalyst during 8 h of CO₂ reduction at potentials of a,e) $U_{el} = -0.6$ V vs. RHE, b,f) $U_{el} = -0.64$ V vs. RHE, c,g) $U_{el} = -0.69$ V vs. RHE and d,h) $U_{el} = -0.83$ V vs. RHE.

The SEM images in Figure 67 for the comparison of the nanowire networks before and after the 8 h of CO₂ reduction at different potentials, show no change of the general network structure, but a surface roughness increase (e)) as well as the formation of a few small pores in the nanowires (h)). A closer observation at larger magnification reveals degradation of the Cu nanowires and the formation of surface artifacts at different potentials as shown in Figure 68.

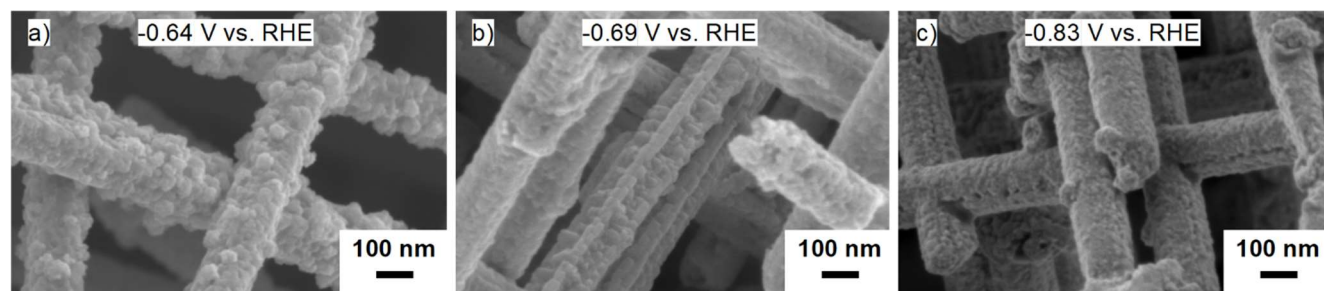


Figure 68: High magnification SEM images showing degradation of Cu nanowire networks during 8 h of CO₂ reduction at potentials of a) $U_{el} = -0.64$ V vs. RHE, b) $U_{el} = -0.69$ V vs. RHE and c) $U_{el} = -0.83$ V vs. RHE.

The high magnification images in Figure 68 clearly show a surface modification. This occurred for all nanowire networks, except for the one applied at $U_{el} = -0.6$ V vs. RHE, during the 8 h CO₂ reduction reaction. Already at $U_{el} = -0.64$ V vs. RHE (Figure 68 a)) small spherical nanoparticles, formed by dissolution and redeposition of material from the Cu nanowires, can be identified on the nanowire surface leading to a roughness increase. In literature this cathodic corrosion process is even applied for the synthesis of small nanoparticles [292,299]. When increasing the potential to $U_{el} = -0.69$ V vs. RHE (Figure 68 b)), the degradation by cathodic corrosion becomes more pronounced. Many nanowires along the whole sample area show a substantial material loss to the extent that only small solid webs remain along the nanowire axis. At an even higher reduction potential of $U_{el} = -0.83$ V vs. RHE (Figure 68 c)), the degradation seems not that prominent, but an increase in surface roughness is visible, and the nanowires are slightly porous. Overall, the long-term tests at different potentials reveal that degradation due to cathodic corrosion on the nanowire networks occurs to different degrees and in different ways. The roughness of the wire surface generally increases, which in turn leads to an increase in the surface area, as already mentioned several times. This surface change can be assumed as reason for the resistance loss leading to the current increase over time. Since this current does not increase abruptly, the degradation seems to happen gradually.

Figure 69 shows the time evolution of the Faradaic efficiencies of the gas phase products H₂ (green), CO (red), CH₄ (yellow), C₂H₄ (orange) and C₂H₆ (blue) for the CO₂ reduction reactions at potentials of a) $U_{el} = -0.6 \pm 0.0$ V vs. RHE, b) $U_{el} = -0.64 \pm 0.01$ V vs. RHE, c) $U_{el} = -0.69 \pm 0.01$ V vs. RHE and d) $U_{el} = -0.83 \pm 0.03$ V vs. RHE during the 8 h reaction process.

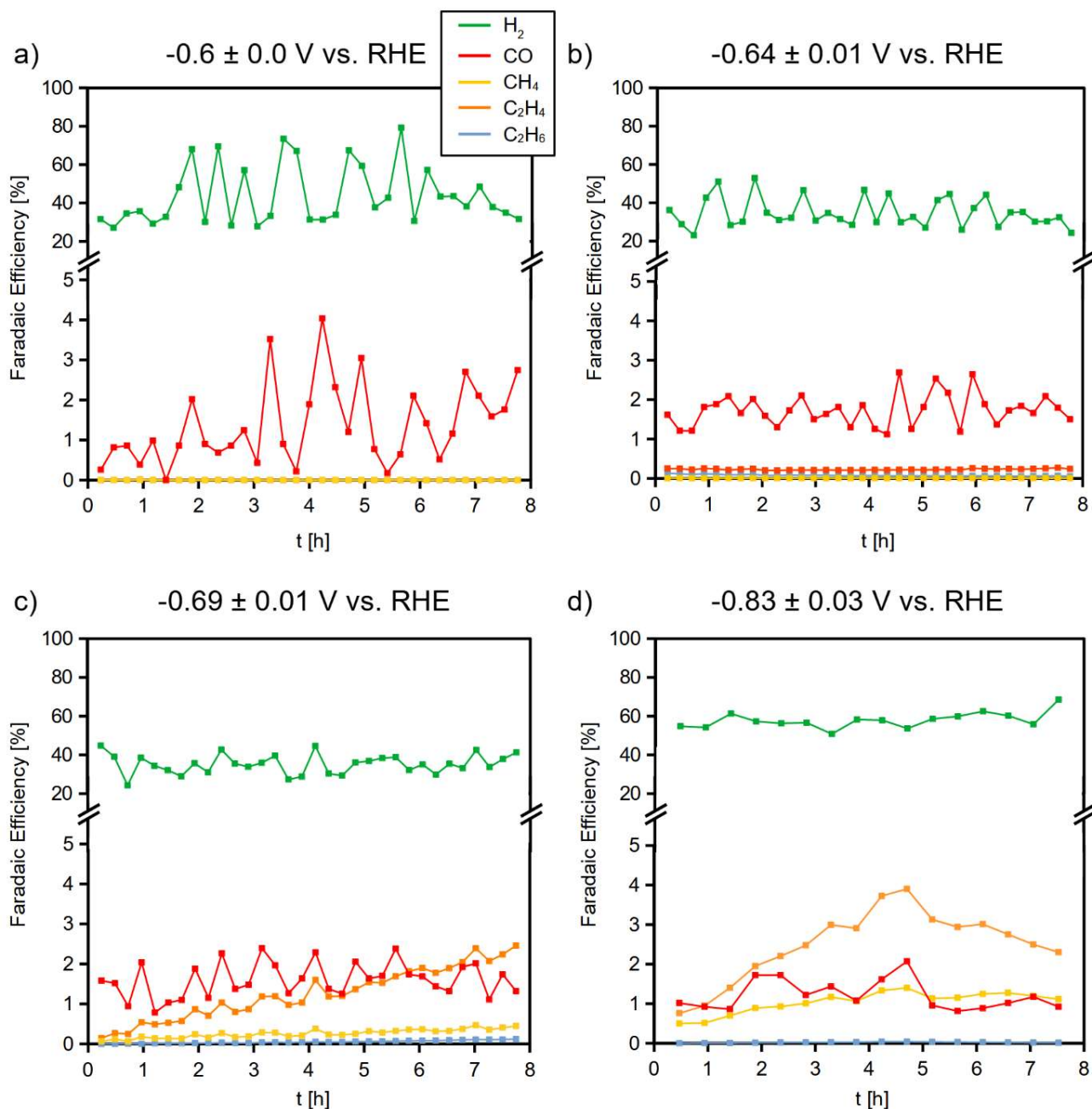


Figure 69: Faradaic efficiencies over time for the gas-phase products H₂ (green), CO (red), CH₄ (yellow), C₂H₄ (orange) and C₂H₆ (blue) during the 8 h CO₂ reduction reaction at potentials of a) $U_{el} = -0.6 \pm 0.0$ V vs. RHE, b) $U_{el} = -0.64 \pm 0.01$ V vs. RHE, c) $U_{el} = -0.69 \pm 0.01$ V vs. RHE and d) $U_{el} = -0.83 \pm 0.03$ V vs. RHE.

At the lowest electrode potential of a) $U_{el} = -0.6$ V vs. RHE, almost no gas-phase products CH₄, C₂H₄ and C₂H₆ are produced during the whole time with Faradaic efficiencies below 0.1 % for all of them. These Faradaic efficiencies are only slightly lower than the efficiencies for CO₂ reduction at Cu nanowire networks with similar geometric parameters that were performed for 1 h (see Figure 46), where these products were also only formed with negligible efficiencies below 0.5 %. For the 8 h reaction CO is produced with relatively constant efficiencies around 1.5 %. The FE of the hydrogen evolution varies strongly between 30 and 80 %. This variance can be attributed to the formation and trapping of H₂ bubbles leading to a higher product

amount, if they are released into the exhaust line before GC injection. The average value of H₂ efficiency is 52 ± 5 % which is in accordance with the H₂ evolution during 1 h of CO₂ reduction (FE = 42 ± 15 %) at the same potential. At $U_{el} = -0.6$ V vs. RHE, HCOOH was detected during the 8 h reaction with an efficiency of 1.8 %, which is already way lower than the formation efficiency of HCOOH of 8 % recorded during the 1 h measurement. All other liquid phase products were produced with very low Faradaic efficiencies (<0.4 %). At the higher CO₂ reduction potential of Figure 69 b) $U_{el} = -0.64 \pm 0.01$ V vs. RHE, the Faradaic efficiencies for the formation of the gas-phase products CH₄, C₂H₄ and C₂H₆ are still low (<0.3 %) and show no significant trends over time. The CO formation efficiency is again constant around 1.5 %. For the liquid phase products, only HCOOH shows a certain formation efficiency of 2.41 %. All other liquid phase products are detected by NMR with Faradaic efficiencies below 0.5 %.

At a potential of Figure 69 c) $U_{el} = -0.69 \pm 0.01$ V vs. RHE first trends over time are observed for the gas phase product formation along the 8 h CO₂ reduction reaction. CH₄ shows a minor efficiency increase from 0.07 % in the beginning to 0.47 % in the end. The same applies for C₂H₄ that increases from 0.14 to 2.46 %, while C₂H₆ remains constant with very low formation efficiencies around 0.12 %. Comparing those product formation efficiencies to those of the 1 h CO₂ reduction reaction, which are 0.1 % for CH₄ and 1.6 % for C₂H₄, respectively, they are in the same region. CO is formed with a constant efficiency of ~1.6 % during the 8 h reaction, whereas it reached 4 % during the comparable 1 h reaction. For liquid phase products, the Faradaic efficiencies for the 8 h CO₂ reduction reaction products are calculated to be below 1 % for all products, even for HCOOH. The H₂ evolution varies at a relatively low value of 35 ± 5 %.

The Faradaic efficiencies for the gas phase products during 8 h of CO₂ reduction reaction at Figure 69 d) $U_{el} = -0.83 \pm 0.03$ V vs. RHE show generally the highest values for all samples of this series. CH₄ increases over time from 0.5 to 1.4 % and C₂H₄ from 0.7 to 2.8 % reaching a higher level of around ~4 % after ~5 h. C₂H₆ is generated with formation efficiencies below 0.04% during the entire time. For the 8 h CO₂ reduction, the formation efficiency of CH₄ is higher than for the 1 h reaction (0.14 %), whereas the formation efficiencies of C₂H₄ and C₂H₆ are ~2 % higher. For the 8 h reaction at that potential the HER efficiency varies around 57 % ± 5 %. This observation is in accordance with the HER efficiency observed for the 1 h CO₂ reduction at $U_{el} = -0.83$ V vs. RHE, which is 57 ± 5 % as well. The Faradaic efficiencies of all liquid phase products reach only very low values for this sample, being below 0.6 %.

Generally, the CO₂ reduction reactions over 8 h show only slight trends for the gas phase reaction products with time, which is mainly based on the increase in Faradaic efficiency for C₂H₄ and CH₄. The efficiency of the H₂ evolution fluctuates quite strongly over time, but shows no significant trend in one direction. This can be attributed to bubble agglomeration, since the release of large hydrogen bubbles leads to a high product efficiency determined during the following GC injection. And then it takes some time, until large bubbles are formed again and thus, in the next injection, the amount of detected product is below the mean value.

Generally, the 8 h reactions showed less product formation efficiencies than the reactions at the same potential performed on different nanowire network samples with identical geometric parameters for 1 h, whose results were already presented in section 4.4. A comparison of the total Faradaic efficiencies as well as the ones for the gas- and liquid phase products for $U_{el} = -0.6, -0.7$ and -0.83 V vs. RHE is presented in Figure 70.

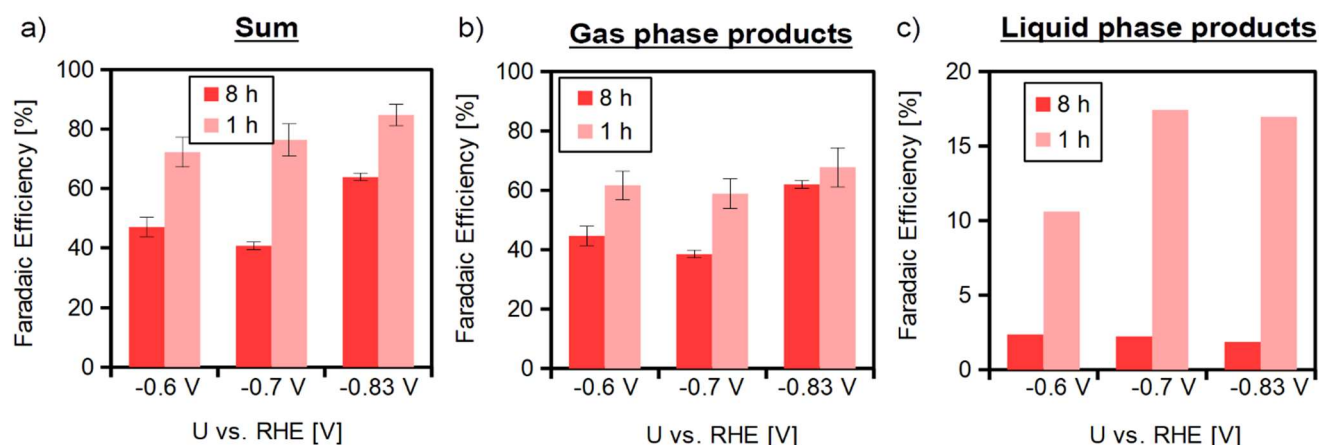


Figure 70: Comparisons of Faradaic efficiencies for CO₂ reduction with durations of 8 h and 1 h at potentials of $U_{el} = -0.6, -0.7$ and -0.83 V vs. RHE: a) total, b) gas phase and c) liquid phase product efficiencies.

The sum of the Faradaic efficiencies for the reaction products is at all potentials lower for the 8 h CO₂ reduction than for the respective 1 h reaction. The contribution of the gas phase products is a 17 % difference for $U_{el} = -0.6$ V vs. RHE, a 20 % difference for $U_{el} = -0.7$ V vs. RHE and a difference of only 6 % at $U_{el} = -0.83$ V vs. RHE. These differences are mainly caused by less H₂ evolution at the nanowire networks studied for 8 h and less release of the intermediate product CO, which is beneficial and indicating a higher formation of more advanced hydrocarbon CO₂ reduction products. However, these advanced gas phase hydrocarbons are not detected in a larger amount during the 8 h CO₂ reduction reaction than during the 1 h hour reaction. To sum it up, less activity for the CO₂ reaction overall for the nanowire networks studied at 8 h can be concluded. The origin of this activity loss is not very clear, but it could be originating from individual differences in the studied samples or surface passivation due to gas bubble trapping during the long-term electrolysis.

The NMR analysis of the electrolyte after the reaction shows very low Faradaic efficiencies for the liquid phase products of the 8 h CO₂ reduction reaction. Clear peaks for these products are visible in the NMR spectrum, but since the Faradaic efficiency normalizes the amount of formed product over the reaction time, the resulting efficiency values are very low. For the NMR analysis the electrolyte is taken out of the cell only after the full 8 h of reaction and is analyzed just then. It can be assumed, that the low number of liquid-phase products is due to ongoing reaction processes in the cathode compartment resulting in more advanced but not detectable molecules. It is also possible, that especially liquid phase products diffusing

through the anion exchange membrane into the anode compartment are oxidized back to CO₂, which has already been reported in literature [269,304,305].

Overall, the CO₂ reduction shows sums of total Faradaic efficiencies, i.e. the formation efficiency for all products, less than 100 %. This effect is pronounced for the samples studied for 8 h in comparison to the ones studied for 1 h. Since the presented experiments cannot correlate this effect to differences, e.g. in porosity or surface activity, between individual samples, or on the other hand to the suitability of the setup for long-term studies, more work in the future is needed to study and qualify the CO₂ reduction behavior of the Cu nanowires over long timeframes regarding product selectivity and overall reaction efficiency. Trends for the single products over time would then allow inferences on the surface modifications happening for example by cathodic corrosion processes.

For avoiding the problem of liquid phase product diffusion into the anode compartment, an advanced cell design with continuous product extraction is required and should be applied in further long-term studies [269].

4.10 Tests of reachable potentials during CO₂ reduction with different electrolyte concentrations

A strategy to reach higher electrode potentials for the CO₂ reduction at Cu nanowire networks and to decrease the amount of cathodic corrosion needs minimization of the IR-drop. A promising approach is to change the electrolyte concentration, since this influences the R_u value of the setup. The interplay between current density and resistance could be beneficial and yield higher IR-compensated electrode potentials. However, the change of electrolyte concentration has a direct impact on the local pH values at the surface of the Cu catalyst and thus changes the product selectivity of the CO₂ reduction reaction as well [49,306]. First tests for three different electrolyte concentrations with 0.1 M ($K = 0.0146$ S/cm) (as used for all other CO₂ reduction experiments in this thesis), 0.2 M ($K = 0.0292$ S/cm) and 1 M ($K = 0.146$ S/cm) KHCO₃ were performed by applying a potential of $U_{appl} = -1.3$ V vs. Ag/AgCl for 5 minutes and increasing it every 5 minutes in steps of -0.5 V from -1.5 V towards -4 V vs. Ag/AgCl. The R_u values of the setup were determined by EIS before and after completing the measurement. The electrolyte was saturated with CO₂ that was constantly bubbled through it with a gas flow rate of 30 ml/min, thus CO₂ reduction was performed at the catalyst but this time without product analysis.

The catalyst behavior of our Cu nanowire network (height = 30 μm, wire diameter ~150 nm, and nanowire number density = 8×10^8 cm⁻²) was compared with a high purity Cu plate. The current density over time ($J-t$) curves as well as the achieved, IR-compensated electrode potentials (U_{el}) are shown in Figure 71 for several electrolyte concentrations.

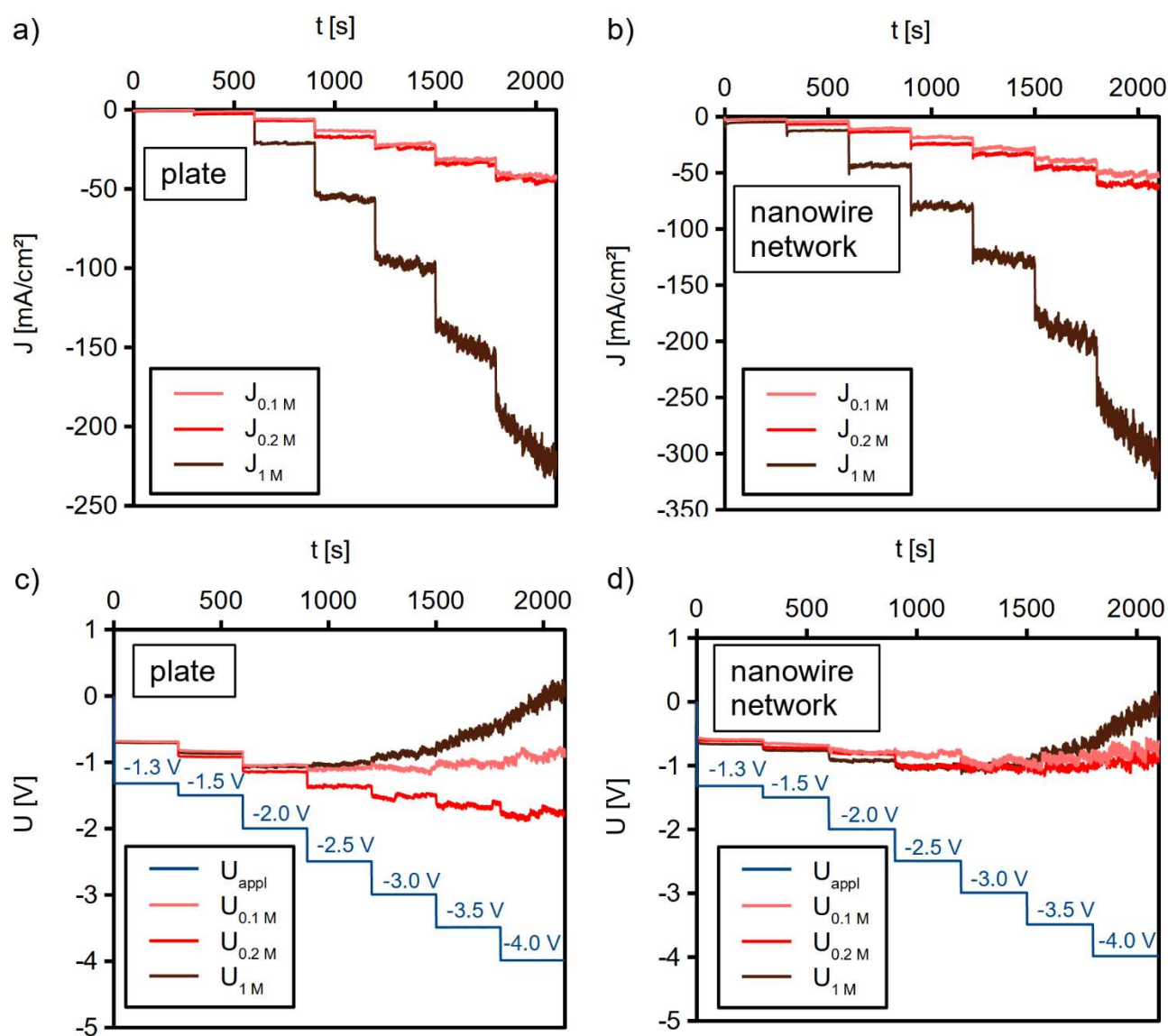


Figure 71: J - t curves (upper row) and resulting IR-compensated electrode potentials (U_{el}) (lower row) for the CO₂ reduction in differently concentrated electrolyte of 0.1, 0.2 and 1 M KHCO₃ saturated with CO₂ by constant gas flow. a) and b) at a Cu-plate and c) and d) for a Cu-nanowire network. The blue curves in the right graphs display the applied potential over time, which was increased every 5 minutes by -0.5 V up to a maximum value of -4.0 V vs. Ag/AgCl.

Generally, the current density becomes larger with increasing applied potential for all electrolyte concentrations. For higher electrolyte concentration, it is higher, reaching values above -200 mA/cm² for the 1 M KHCO₃ electrolyte. This is expected and supported by the resistances determined by EIS before the measurement. For the plate, for 0.1 M KHCO₃, the measured R_U is 33.7 Ω before the measurement, decreasing slightly towards 32.1 Ω afterwards. For 0.2 M KHCO₃ the initial resistance is already quite low with only 20.7 Ω and also shows a decrease of ~ 1 Ω to 19.2 Ω . 1 M KHCO₃ has a large conductivity, mirrored by a low resistance of only 8.7 Ω before and 7.7 Ω after the measurement. In all cases, the resistance only drops by 1 Ω over time, it thus can be stated that the Cu plate is resistant towards cathodic corrosion and the R_U values can be used for the calculation of the IR-compensated potential without generating large errors.

This increase in current density, forced by the higher applied potential, leads to an increase in IR-drop for the higher applied potentials. For applied potentials of $U_{appl} = -2.5 - -3.0$ V vs. Ag/AgCl, a saturation at an electrode potential value of -1.1 V vs. RHE is achieved for the 0.1 M KHCO_3 electrolyte. At this point, the electrode potentials decrease again, because the IR-drop increase is more pronounced than the increase of the applied potential. Especially for the 1 M KHCO_3 electrolyte, this decrease is strong, since the current density for this sample gets particularly high due to the low resistance of the setup.

On the other hand, for the 0.2 M KHCO_3 , the compensated potential steadily increases with increasing applied potential, up to a value of $U_{el} = -1.8$ V vs. RHE at an applied potential of $U_{appl} = -4.0$ V vs. Ag/AgCl. However, this value is close to saturation already at an applied potential of -3.0 V vs. Ag/AgCl. This higher reachable potential U vs. RHE in comparison to the setup with 0.1 M KHCO_3 is possible due to the lower electrolyte resistance leading to less IR-drop.

As shown in Figure 71 c) and d), our Cu nanowire networks in general show the same behavior as the Cu plates, but to a different extent. Due to the larger surface area and thus slightly lower R_u , the current density at the different steps is higher for the network than for the plate as expected. The resistance values measured by EIS before the measurement are close to the Cu plate, with 32.9Ω for the Cu nanowire network in 0.1 M KHCO_3 , 25.1Ω in 0.2 M KHCO_3 and 6.1Ω in 1 M KHCO_3 electrolyte.

In this case, the current density increases relatively similar for the 0.1 and 0.2 M KHCO_3 electrolytes, up to final values of -50 mA/cm^2 . For 1 M KHCO_3 the current density increase is quite strong reaching values of -230 mA/cm^2 for an applied potential of $U_{appl} = -4$ V vs. Ag/AgCl.

For the Cu nanowire network in 0.1 M KHCO_3 , the electrode potential reaches a maximum of $U_{el} = -1.0$ V vs. RHE at an applied potential of -2.5 and -3.0 V, decreasing slightly when increasing the applied potential. For the 0.2 M KHCO_3 electrolyte this behavior is similar approaching saturation at -1.0 V vs. RHE. Especially for the 1 M KHCO_3 electrolyte, the decrease after saturation is strong, since the current density for this sample gets very high due to the low resistance of the setup. It is important to note that the strong decrease of the IR-compensated potential at high applied potentials at the Cu nanowire networks as well as at the Cu-plate can only be interpreted as trend. The absolute values are not available, as the calculation for the IR-compensation for all values is based on R_u determined by EIS before the CO_2 reduction measurement. At applied potentials above $U_{appl} = -3$ V vs. Ag/AgCl, cathodic corrosion of the Cu nanowire networks leads to a change in the resistance and thus to a falsification of the plotted electrode potential. The appearance of cathodic corrosion in this potential region can also be seen in the $J-t$ curves for the Cu nanowire network, especially at 1 M KHCO_3 concentration, where the current density already increases during the 5 minutes of a single potential step. Moreover, EIS on the Cu nanowire network performed after the measurement procedure reveals a resistance decrease due to cathodic corrosion. For the nanowire network used at 0.1 M KHCO_3 , R_u dropped from 32.9Ω to 25.2Ω . At 0.2 and 1 M KHCO_3 concentration, the R_u drop was not as strong in absolute values, but still significant with 20.6Ω from 25.1Ω and 4.2Ω from

6.1 Ω , respectively. For the nanowire networks used in 0.1 and 0.2 M KHCO_3 , R_u dropped by $\sim 20\%$, whereas for the one used in 1 M KHCO_3 this drop was with $\sim 31\%$ even stronger.

Cathodic corrosion was also observed in SEM images of the nanowire networks taken before and after the test measurements as presented in Figure 72. A surface increase by roughening was already detected for the network used in 0.1 M KHCO_3 and even more for the network tested two times for CO_2 reduction, first in 0.2 and then in 1 M KHCO_3 . However, this roughness increase was smaller than for the nanowire networks applied to $U_{\text{appl}} = -4.3$ V vs. Ag/AgCl for 5 h (see chapter 4.8), probably due to the shorter time for the application of the high potential. And additionally, the high potential of ~ -4 V vs Ag/AgCl was applied directly for the 5 h test, whereas in these tests here, it was applied by increasing potential steps, giving the surface the chance to adjust a bit to this rough conditions.

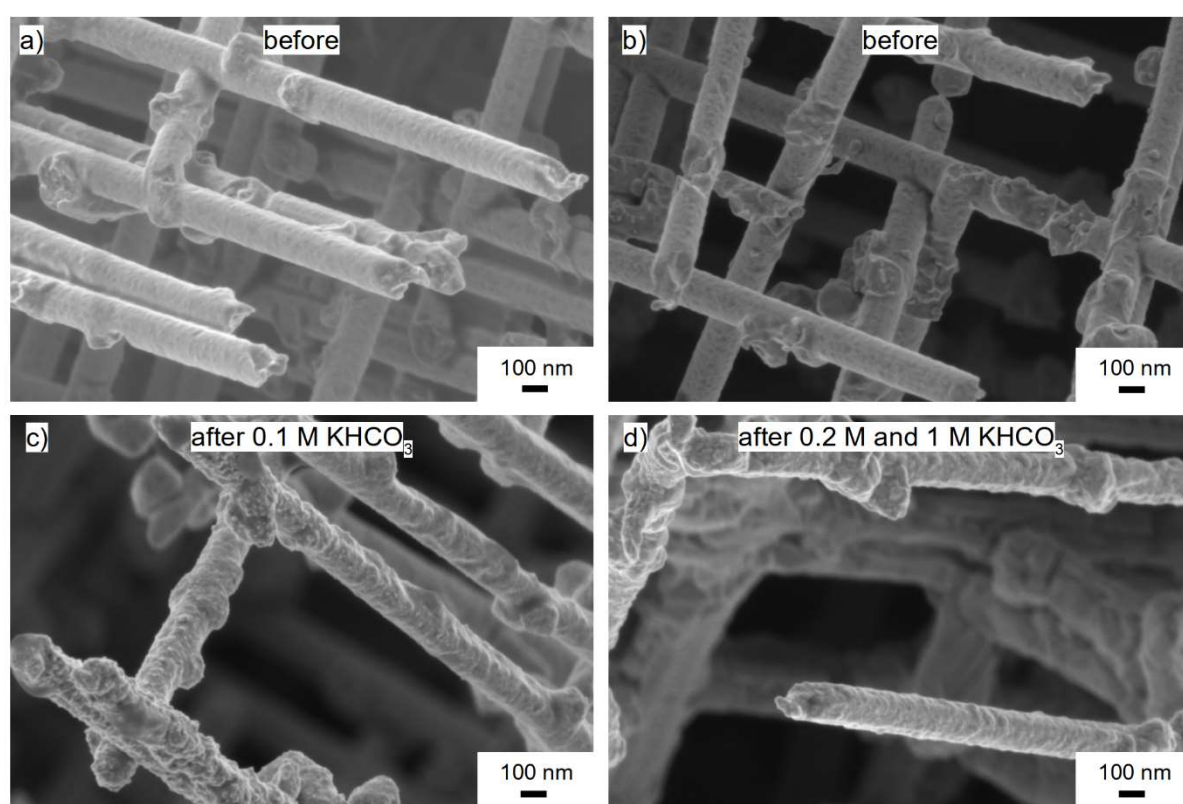


Figure 72: a) and b) SEM images of the Cu nanowire networks before (i.e. after pre-cleaning and anodization) and c) after the potential tests in 0.1 M KHCO_3 , and d) first in 0.2 M and then 1 M KHCO_3 with a duration of 2100 s.

The relation of U_{appl} vs. Ag/AgCl and the IR-compensated U_{el} vs. RHE for the Cu plate and Cu nanowire network in different electrolyte concentrations is shown in Figure 73.

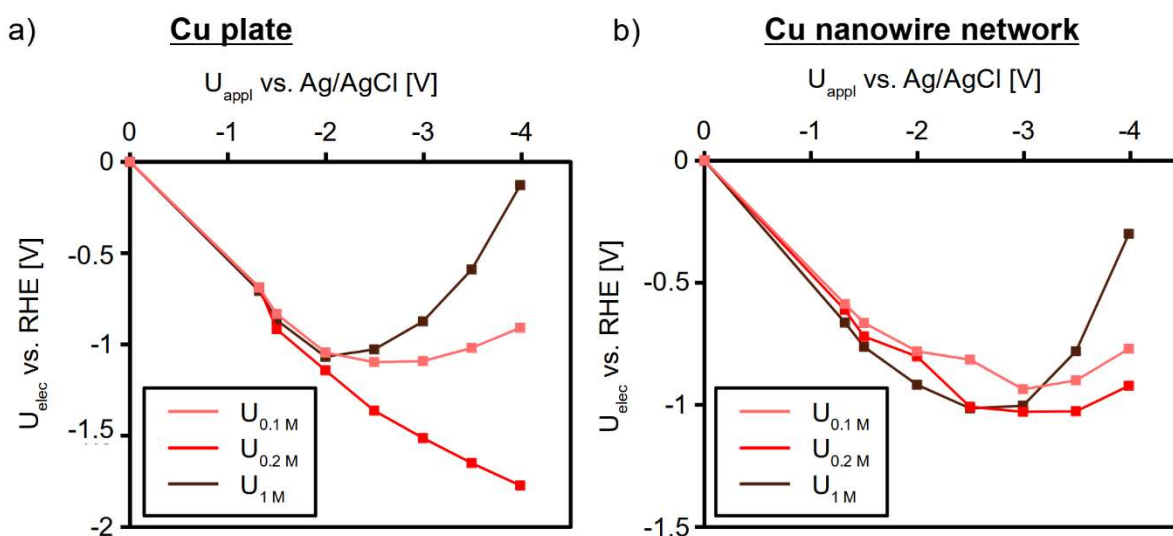


Figure 73: Comparison of the IR-compensated electrode potentials U_{el} vs. RHE resulting from the applied potentials U_{appl} vs. Ag/AgCl on a) a Cu-plate and b) a Cu nanowire network.

Figure 73 shows the reachable potential U_{el} vs. RHE to increase linearly up to -1.5 V at both structures. At higher applied potentials U_{appl} vs. Ag/AgCl, the further course depends on the electrolyte concentration. For the 0.1 M KHCO_3 electrolyte a maximum value of $U_{el} = -1.1$ V vs. RHE at an applied potential of -2.5 and -3.0 V vs. Ag/AgCl is reached before it decreases again. The nanowire network in this case reaches a maximum electrode potential of only -1.0 V at an applied potential of -3.0 V vs. Ag/AgCl, also decreasing at more negative potentials due to the increasing strength of the IR-drop effect.

In the 0.2 M KHCO_3 electrolyte, the IR-compensated electrode potential of the Cu plate increases constantly up to -1.8 V vs. RHE at an applied potential of -4 V vs. Ag/AgCl. However, the increase of the curve flattens with increasing applied potential. For the nanowire network, in this electrolyte concentration of 0.2 M, a maximum IR-compensated electrode potential of -1.1 V vs. RHE was reached at -3.0 and -3.5 V vs. Ag/AgCl and decreases afterwards, but the decrease is not as strong as for the test in 0.1 M KHCO_3 .

For the Cu plate tested in 1 M KHCO_3 , a maximum IR-compensated electrode potential of -1 V is already reached at -2 V vs. Ag/AgCl applied potential, and afterwards decreases quite strongly. Thus, with this high electrolyte concentration and the related high current densities, the IR-drop takes over quickly. For the Cu nanowire network, the same effect is observed by reaching a maximum electrode potential of -1 V vs. RHE at -2.5 vs Ag/AgCl applied potential.

From the variation of electrolyte concentration we conclude, that for CO_2 reduction at the Cu nanowire networks the achievable IR-compensated electrode potential vs. RHE reaches a saturation value at applied potential values of -2.5 V vs. Ag/AgCl. At higher applied potentials, the large IR-drop, caused by the high current densities due to the relatively large surface area, takes over and hinders higher electrode potentials. Moreover, cathodic corrosion has to be considered. Compared to a 0.1 M electrolyte concentration, 0.2 M attenuates this effect only slightly by leading to a 10 % higher electrode potential. At

the studied maximum electrolyte concentration of 1 M, the effect is not improved, because the reached maximum electrode potential is even slightly smaller due to the high current densities, caused by the low resistance of this highly concentrated electrolyte. Further tests need to clarify, whether an intermediate electrolyte concentration leads to a higher achievable IR-compensated potential. Further studies should also investigate, if the CO₂ reduction with a different electrolyte concentration leads to different results regarding the product selectivity.

5 Conclusions and Outlook

Homogeneous free-standing Cu nanowire networks with well-defined geometric properties were synthesized by electrodeposition in etched ion-track membranes. The nanowire networks were tailored regarding the nanowire parameters, including diameter ranging from 80 to 200 nm, network height from 5 to 30 μm and nanowire number density between 1×10^8 and $4 \times 10^9 \text{ cm}^{-2}$. The networks synthesized with these parameters provided a significantly larger geometrical area, of up to 300 cm^2 compared to the 1 cm^2 planar supporting area. These geometrical network parameters were selected to guarantee mechanical stability while offering free volume within the network for electrolyte access.

An acidic pre-cleaning and anodization procedure in H_2SO_4 and H_3PO_4 known to be beneficial for the efficiency of Cu catalysts in the CO_2 reduction reaction [166,167], was adjusted to guarantee proper surface preparation while preserving the nanowire network stability. For example, the acidic solutions were diluted and the immersion times were reduced. XRD analysis confirmed that the pre-cleaning, washing and anodizing protocol developed in this thesis did not affect the crystallinity of the sample significantly. SEM, TEM and EDX revealed that the surface of the pre-cleaned nanowire networks was free of contaminations and exhibited a rougher surface which enlarged the electrochemically active surface area compared to the as-deposited nanowires. Generally, the pre-cleaned and anodized nanowire networks exhibited higher activities in the CO_2 reduction reaction, leading to higher current density and higher formation efficiencies of the desired high value CO_2 reduction reaction products than for the as-grown networks. Especially for the C2+ products this trend was prominent, showing the beneficial effect of the adjusted pre-cleaning and activation procedure.

To evaluate the suitability of the Cu nanowire networks for catalysis, it is important to demonstrate that the entire geometrical surface can contribute to a given electrochemical reaction. For this, we synthesized nanowire networks with various geometrical surface areas and systematically determined the corresponding ECSA values. To account for the numerous interconnections, present in a highly interconnected free-standing nanowire network, a model was developed to calculate the geometrical surface area of Cu nanowire networks defined by the planar sample area, network height, nanowire diameter and number density. The ECSA of the nanowire networks with different geometrical parameters was determined experimentally by measuring their double-layer capacitance and comparing it to a lapped and polished Cu reference plate with a well-defined surface area. These measurements were performed by cyclic voltammetry in the same setup and electrolyte that was later used for CO_2 reduction. Thus, the surface area of a nanowire network can be directly determined with an additional measurement in the same setup before and after the CO_2 reduction reaction, providing direct information on surface changes. For future studies this approach has the great advantage that degradation of the nanowire networks can be quantified and related to the applied reduction potential and reaction time.

The performance of the Cu nanowire networks for CO₂ reduction was investigated by synthesizing a series of identical nanowire networks, i.e. same geometrical surface area, and measuring their CO₂ reduction efficiency and product selectivity at three different potentials. In addition, a high purity Cu-plate, and electrodeposited Cu film were also characterized. The obtained values were also compared to literature values reported for arrays of short parallel Cu nanowires. The CO₂ reduction efficiencies and product selectivity for a high purity Cu-plate, an electrodeposited planar Cu film, an array of short Cu nanowires and a Cu nanowire network of identical base area were compared at three different reduction potentials. At all potentials, the current density normalized on the planar sample area recorded during CO₂ reduction was highest for the nanowire network, followed in decreasing order by the nanowire array, the flat Cu film and Cu-plate electrode. This directly evidences the larger exposed surface area of the nanowire networks at which the reduction reaction takes place. The current density increase was not proportionally increasing with the measured surface area of the nanostructures. The carbon dioxide reduction product selectivity of the four samples was quite different. The Cu plate showed the highest current efficiencies for C₂H₆O and C₃H₈O formation at all potentials, whereas the Cu nanowire network was the only structure to form C₂H₄ and C₂H₆ at the studied potentials. C₂H₆O₂ formation was mainly observed at the electrodeposited planar Cu film and was attributed to the contribution of the sputtered Cu layer. None of the structures showed any significant changes in surface topography and structure during the 1h CO₂ reduction reaction at the applied potentials between -0.66 and -0.83 V vs. RHE.

These results highlighted that the Cu nanowire networks can be applied as catalyst for the CO₂ reduction, and are able to synthesize in particular C₂⁺ products that are not produced by planar Cu plates or other Cu structures reported in literature. The demonstrated C₂⁺ synthesis is tentatively ascribed to the effect of trapping gas phase reaction products in the free interspace between the nanowires. Due to the relatively low potentials applied to guarantee the stability of the networks, the current efficiencies of the different high value reduction products were low and the competing hydrogen evolution reaction always remained dominant. The electrode potential for the nanowire networks was limited to ~-0.9 V vs. RHE due to the large IR-drop caused by the relatively large cell resistance of the employed. It was possible to apply a higher potential of ~-1.0 V vs. RHE by increasing the electrolyte concentration to 0.2 M KHCO₃. The effect of the electrolyte concentration should be further explored in future experiments, as the electrolyte concentration may significantly change the product selectivity and reaction efficiency [49,306,307].

The CO₂ reduction reaction at the Cu nanowire networks showed no significant trends in gas-phase product selectivity within a reaction time of 8 h, but it did exhibit a gradual resistance loss leading to an increase of the current density. This resistance loss is attributed to cathodic corrosion and nanowire degradation combined with surface restructuring by material dissolution and redeposition as observed from SEM images.

The CO₂ reduction measurements at the high surface area nanowire networks can be improved in the future by improving the cell design. The reference electrode should be placed closer to the nanowire

networks surface, e.g. by a Haber-Luggin capillary. Additionally, the size of the electrochemical cell should be reduced to decrease the cell resistance by providing small distances between nanowire network, membrane and counter electrode. In addition, future studies should use a flow-cell, which is constantly fed with fresh electrolyte that is moving out constantly as well, including all the liquid phase products that could be then analyzed in-situ by e.g. Raman spectroscopy [308] or advanced local electrochemistry methods [309]. The evaluation of the liquid phase products should be also performed at shorter time intervals to avoid product loss over time by e.g. membrane crossover and oxidation. In the future, a more time-resolved product analysis can provide valuable information on the surface changes and their influence onto the CO₂ reduction reactions product selectivity.

Up to now, CO₂ reduction reactions had been reported only on arrays of parallel Cu nanowires synthesized by the reduction of CuO nanowires, which inherently exhibit a large size distribution. These nanowire arrays mainly reduced CO₂ towards CO and less to C₂+ products [244, 245]. On the contrary, our nanowire networks exhibit well defined geometrical parameters and thus, once the setup is optimized, a systematic investigation of their influence on the performance of the CO₂ reduction will provide exciting insights into the importance of precise geometric catalyst design for tailoring the selectivity of the CO₂ reduction reaction. This might help to design copper nanocatalysts that are specifically tuned towards high selectivity for a certain reaction product. Such experiments should systematically vary one geometrical parameter of the nanowire networks, e.g. the nanowire number density, by keeping the others constant. Analysis of the product selectivity in dependence on the nanowire number density and thus the pore size between the wires will provide valuable insights on the reaction mechanisms of Cu nanostructured and porous catalysis towards certain products.

Additionally, electrodeposition enables the fabrication of both poly- and single-crystalline nanowires. Thus, future studies can potentially investigate the influence of the crystallographic properties as well of the Cu nanowire networks on their performance and their stability against cathodic corrosion procedures. This will be done, e.g. by measuring of the ECSA before and after the CO₂ reduction experiments as well as by XRD, SEM imaging, and by directly analyzing the *J-t* curves during the reduction process. For owing the nanowire networks the chance to serve industrial standards for application as catalyst for the CO₂ electrolysis, accelerated stress tests with pulsed electrode potentials and ramped potential curves should be performed and would provide the final information on catalyst stability and degradation for application.

In summary, this thesis demonstrates the application of interconnected, tailored Cu nanowire networks as catalysts for CO₂ reduction reactions and provides valuable information on how to further improve the cell design and the measurement protocol to achieve reduction potentials larger than – 1 V vs. RHE, which have been shown to be beneficial for CO₂ reduction towards ethylene on Cu plates and other Cu nanostructures [52,53,134,257]. This higher reduction potentials could be achieved on other nanostructures due to their smaller surface area leading to less IR-drop.

Bibliography

1. Friedlingstein, P.; O'Sullivan, M.; Jones, M.W.; Andrew, R.M.; Hauck, J.; Olsen, A.; Peters, G.P.; Peters, W.; Pongratz, J.; Sitch, S.; et al. Global Carbon Budget 2020. *Earth Syst. Sci. Data* **2020**, *12*, 3269–3340, doi:10.5194/essd-12-3269-2020.
2. Merkel, A. The Role of Science in Sustainable Development. *Science* **1998**, *281*, 336–337, doi:10.1126/science.281.5375.336.
3. Nitopi, S.; Bertheussen, E.; Scott, S.B.; Liu, X.; Engstfeld, A.K.; Horch, S.; Seger, B.; Stephens, I.E.L.; Chan, K.; Hahn, C.; et al. Progress and Perspectives of Electrochemical CO₂ Reduction on Copper in Aqueous Electrolyte. *Chem. Rev.* **2019**, *119*, 7610–7672, doi:10.1021/acs.chemrev.8b00705.
4. Arrhenius, S. On the Influence of Carbonic Acid in the Air upon the Temperature of the Ground. *Philos. Mag. J. Sci.* **1896**, *5*, 237–276, doi:10.12987/9780300188479-028.
5. Callendar, G.S. The Artificial Production of Carbon Dioxide and Its Influence on Temperature. *Q. J. R. Meteorol. Soc.* **1938**, *64*, 223–240, doi:10.1002/qj.49706427503.
6. Manabe, S.; Wetherald, R.T. Thermal Equilibrium of the Atmosphere with a Given Distribution of Relative Humidity. *J. Atmospheric Sci.* **1967**, *24*, 241–259, doi:10.1175/1520-0469.
7. Keeling, C.D.; Bacastow, R.B.; Bainbridge, A.E.; Ekdahl, C.A.; Guenther, P.R.; Waterman, L.S.; Chin, J.F.S. Atmospheric Carbon Dioxide Variations at Mauna Loa Observatory, Hawaii. *Tellus* **1976**, *28*, 538–551, doi:10.1111/j.2153-3490.1976.tb00701.x.
8. Keeling, C.D.; Piper, S.C.; Bacastow, R.B.; Wahlen, M.; Whorf, T.P.; Heimann, M.; Meijer, H.A. *Exchanges of Atmospheric CO₂ and 13CO₂ with the Terrestrial Biosphere and Oceans from 1978 to 2000*; I. Global aspects, SIO Reference Series; Scripps Institution of Oceanography: San Diego, 2001;
9. Rohde, R.A.; Hausfather, Z. The Berkeley Earth Land/Ocean Temperature Record. *Earth Syst. Sci. Data* **2020**, *12*, 3469–3479, doi:10.5194/essd-12-3469-2020.
10. Lynas, M.; Houlton, B.Z.; Perry, S. Greater than 99% Consensus on Human Caused Climate Change in the Peer-Reviewed Scientific Literature. *Environ. Res. Lett.* **2021**, *16*, 114005, doi:10.1088/1748-9326/ac2966.
11. Lau, L.C.; Lee, K.T.; Mohamed, A.R. Global Warming Mitigation and Renewable Energy Policy Development from the Kyoto Protocol to the Copenhagen Accord—A Comment. *Renew. Sustain. Energy Rev.* **2012**, *16*, 5280–5284, doi:10.1016/j.rser.2012.04.006.
12. Hoad, D. The 2015 Paris Climate Agreement: Outcomes and Their Impacts on Small Island States. *Isl. Stud. J.* **2016**, *11*, 315–320, doi:10.24043/isj.351.
13. Bernardo, C.; Wang, L.; Vasca, F.; Hong, Y.; Shi, G.; Altafini, C. Achieving Consensus in Multilateral International Negotiations: The Case Study of the 2015 Paris Agreement on Climate Change. *Sci. Adv.* **2021**, *7*, eabg8068, doi:10.1126/sciadv.abg8068.
14. Eby, M.; Zickfeld, K.; Montenegro, A.; Archer, D.; Meissner, K.J.; Weaver, A.J. Lifetime of Anthropogenic Climate Change: Millennial Time Scales of Potential CO₂ and Surface Temperature Perturbations. *J. Clim.* **2009**, *22*, 2501–2511, doi:10.1175/2008JCLI2554.1.
15. Solomon, S.; Plattner, G.-K.; Knutti, R.; Friedlingstein, P. Irreversible Climate Change Due to Carbon Dioxide Emissions. *Proc. Natl. Acad. Sci.* **2009**, *106*, 1704–1709, doi:10.1073/pnas.0812721106.
16. Held, I.M.; Soden, B.J. Robust Responses of the Hydrological Cycle to Global Warming. *J. Clim.* **2006**, *19*, 5686–5699, doi:10.1175/JCLI3990.1.
17. Allen, M.R.; Ingram, W.J. Constraints on Future Changes in Climate and the Hydrologic Cycle. *Nature* **2002**, *419*, 228–232, doi:10.1038/nature01092.

18. Trenberth, K.E.; Jones, P.D.; Ambenje, P.; Bojariu, R.; Easterling, D.; Tank, A.K.; Parker, D.; Renwick, J.A.; Adler, R.; Alexander, L.; et al. Observations: Surface and Atmospheric Climate Change. In *Climate Change 2007: The Physical Science Basis*; Cambridge University Press: Cambridge, **2007**; pp. 747–845.
19. Seager, R.; Ting, M.; Held, I.; Kushnir, Y.; Lu, J.; Vecchi, G.; Huang, H.-P.; Harnik, N.; Leetmaa, A.; Lau, N.-C.; et al. Model Projections of an Imminent Transition to a More Arid Climate in Southwestern North America. *Science* **2007**, *316*, 1181–1184, doi:10.1126/science.1139601.
20. Zhang, X.; Zwiers, F.W.; Hegerl, G.C.; Lambert, F.H.; Gillett, N.P.; Solomon, S.; Stott, P.A.; Nozawa, T. Detection of Human Influence on Twentieth-Century Precipitation Trends. *Nature* **2007**, *448*, 461–465, doi:10.1038/nature06025.
21. Gao, X.; Giorgi, F. Increased Aridity in the Mediterranean Region under Greenhouse Gas Forcing Estimated from High Resolution Simulations with a Regional Climate Model. *Glob. Planet. Change* **2008**, *62*, 195–209, doi:10.1016/j.gloplacha.2008.02.002.
22. Burke, E.J.; Brown, S.J.; Christidis, N. Modeling the Recent Evolution of Global Drought and Projections for the Twenty-First Century with the Hadley Centre Climate Model. *J. Hydrometeorol.* **2006**, *7*, 1113–1125, doi:10.1175/JHM544.1.
23. Fischlin, A.; Midgley, G.F.; Price, J.; Leemans, R.; Dube, P.; Tarazona, J.; Velichko, A.; Athhopheng, J.; Beniston, M.; Bond, W.J.; et al. Ecosystems, Their Properties, Goods and Services. In *Climate Change 2007: Impacts, Adaptation, and Vulnerability*; Cambridge University Press: Cambridge **2007**; pp. 211–272.
24. Williams, J.W.; Jackson, S.T.; Kutzbach, J.E. Projected Distributions of Novel and Disappearing Climates by 2100 AD. *Proc. Natl. Acad. Sci.* **2007**, *104*, 5738–5742, doi:10.1073/pnas.0606292104.
25. Scholze, M.; Knorr, W.; Arnell, N.W.; Prentice, I.C. A Climate-Change Risk Analysis for World Ecosystems. *Proc. Natl. Acad. Sci.* **2006**, *103*, 13116–13120, doi:10.1073/pnas.0601816103.
26. Bindoff, N.L.; Willebrand, J.; Artale, V.; Cazenave, A.; Gregory, J.M.; Gulev, S.; Quéré, C.L.; Levitus, S.; Nojiri, Y.; Shum, C.K.; et al. Observations: Oceanic Climate Change and Sea Level. In *Climate Change 2007: The Physical Science Basis*; Cambridge University Press: Cambridge **2007**; pp. 747–845.
27. Pfeffer, W.T.; Harper, J.T.; O’Neel, S. Kinematic Constraints on Glacier Contributions to 21st-Century Sea-Level Rise. *Science* **2008**, *321*, 1340–1343, doi:10.1126/science.1159099.
28. Tol, R.S.J. The Economic Effects of Climate Change. *J. Econ. Perspect.* **2009**, *23*, 29–51, doi:10.1257/jep.23.2.29.
29. Piguet, E.; Pecoud, A.; de Guchteneire, P. Migration and Climate Change: An Overview. *Refug. Surv. Q.* **2011**, *30*, 1–23, doi:10.1093/rsq/hdr006.
30. Wilcox, J. *Carbon Capture*; 1st ed.; Springer: New York, **2012**; ISBN 978-1-4614-2214-3.
31. Kleij, A.W.; North, M.; Urakawa, A. CO₂ Catalysis. *ChemSusChem* **2017**, *10*, 1036–1038, doi:10.1002/cssc.201700218.
32. Dessì, P.; Rovira-Alsina, L.; Sánchez, C.; Dinesh, G.K.; Tong, W.; Chatterjee, P.; Tedesco, M.; Farràs, P.; Hamelers, H.M.V.; Puig, S. Microbial Electrosynthesis: Towards Sustainable Biorefineries for Production of Green Chemicals from CO₂ Emissions. *Biotechnol. Adv.* **2021**, *46*, 107675, doi:10.1016/j.biotechadv.2020.107675.
33. Obama, B. The Irreversible Momentum of Clean Energy. *Science* **2017**, *355*, 126–129, doi:10.1126/science.aam6284.
34. Artz, J.; Müller, T.E.; Thenert, K.; Kleinekorte, J.; Meys, R.; Sternberg, A.; Bardow, A.; Leitner, W. Sustainable Conversion of Carbon Dioxide: An Integrated Review of Catalysis and Life Cycle Assessment. *Chem. Rev.* **2018**, *118*, 434–504, doi:10.1021/acs.chemrev.7b00435.

35. Martín, A.J.; Larrazábal, G.O.; Pérez-Ramírez, J. Towards Sustainable Fuels and Chemicals through the Electrochemical Reduction of CO₂: Lessons from Water Electrolysis. *Green Chem.* **2015**, *17*, 5114–5130, doi:10.1039/C5GC01893E.
36. Chu, S.; Majumdar, A. Opportunities and Challenges for a Sustainable Energy Future. *Nature* **2012**, *488*, 294–303, doi:10.1038/nature11475.
37. Seh, Z.W.; Kibsgaard, J.; Dickens, C.F.; Chorkendorff, I.; Nørskov, J.K.; Jaramillo, T.F. Combining Theory and Experiment in Electrocatalysis: Insights into Materials Design. *Science* **2017**, *355*, 4998, doi:10.1126/science.aad4998.
38. Pei, Y.; Zhong, H.; Jin, F. A Brief Review of Electrocatalytic Reduction of CO₂—Materials, Reaction Conditions, and Devices. *Energy Sci. Eng.* **2021**, *9*, 1012–1032, doi:10.1002/ese3.935.
39. Zhu, W.; Michalsky, R.; Metin, Ö.; Lv, H.; Guo, S.; Wright, C.J.; Sun, X.; Peterson, A.A.; Sun, S. Monodisperse Au Nanoparticles for Selective Electrocatalytic Reduction of CO₂ to CO. *J. Am. Chem. Soc.* **2013**, *135*, 16833–16836, doi:10.1021/ja409445p.
40. Rahaman, M.; Dutta, A.; Broekmann, P. Size-Dependent Activity of Palladium Nanoparticles: Efficient Conversion of CO₂ into Formate at Low Overpotentials. *ChemSusChem* **2017**, *10*, 1733–1741, doi:10.1002/cssc.201601778.
41. Lu, Q.; Rosen, J.; Zhou, Y.; Hutchings, G.S.; Kimmel, Y.C.; Chen, J.G.; Jiao, F. A Selective and Efficient Electrocatalyst for Carbon Dioxide Reduction. *Nat. Commun.* **2014**, *5*, 3242, doi:10.1038/ncomms4242.
42. Ma, M.; Trzeźniewski, B.J.; Xie, J.; Smith, W.A. Selective and Efficient Reduction of Carbon Dioxide to Carbon Monoxide on Oxide-Derived Nanostructured Silver Electrocatalysts. *Angew. Chem. Int. Ed.* **2016**, *55*, 9748–9752, doi:10.1002/anie.201604654.
43. Back, S.; Yeom, M.S.; Jung, Y. Active Sites of Au and Ag Nanoparticle Catalysts for CO₂ Electroreduction to CO. *ACS Catal.* **2015**, *5*, 5089–5096, doi:10.1021/acscatal.5b00462.
44. Hori, Y.; Murata, A.; Kikuchi, K.; Suzuki, S. Electrochemical Reduction of Carbon Dioxide to Carbon Monoxide at a Gold Electrode in Aqueous Potassium Hydrogen Carbonate. *J. Chem. Soc. Chem. Commun.* **1987**, 728–729.
45. Hori, Y.; Murata, A.; Takahashi, R. Formation of Hydrocarbons in the Electrochemical Reduction of Carbon Dioxide at a Copper Electrode in Aqueous Solution. *J. Chem. Soc. Faraday Trans. 1 Phys. Chem. Condens. Phases* **1989**, *85*, 2309, doi:10.1039/f19898502309.
46. Agarwal, A.S.; Zhai, Y.; Hill, D.; Sridhar, N. The Electrochemical Reduction of Carbon Dioxide to Formate/Formic Acid: Engineering and Economic Feasibility. *ChemSusChem* **2011**, *4*, 1301–1310, doi:10.1002/cssc.201100220.
47. Spurgeon, J.M.; Kumar, B. A Comparative Technoeconomic Analysis of Pathways for Commercial Electrochemical CO₂ Reduction to Liquid Products. *Energy Environ. Sci.* **2018**, *11*, 1536–1551, doi:10.1039/C8EE00097B.
48. Verma, S.; Kim, B.; Jhong, H.-R. “Molly”; Ma, S.; Kenis, P.J.A. A Gross-Margin Model for Defining Technoeconomic Benchmarks in the Electroreduction of CO₂. *ChemSusChem* **2016**, *9*, 1972–1979, doi:10.1002/cssc.201600394.
49. Varela, A.S.; Kroschel, M.; Reier, T.; Strasser, P. Controlling the Selectivity of CO₂ Electroreduction on Copper: The Effect of the Electrolyte Concentration and the Importance of the Local pH. *Catal. Today* **2016**, *260*, 8–13, doi:10.1016/j.cattod.2015.06.009.
50. Kuhl, K.P.; Cave, E.R.; Abram, D.N.; Jaramillo, T.F. New Insights into the Electrochemical Reduction of Carbon Dioxide on Metallic Copper Surfaces. *Energy Environ. Sci.* **2012**, *5*, 7050–7059, doi:10.1039/c2ee21234j.

51. Takahashi, I.; Koga, O.; Hoshi, N.; Hori, Y. Electrochemical Reduction of CO₂ at Copper Single Crystal Cu(S)-[n(111)×(111)] and Cu(S)-[n(110)×(100)] Electrodes. *J. Electroanal. Chem.* **2002**, *533*, 135–143, doi:10.1016/S0022-0728(02)01081-1.
52. Etzold, B.J.M.; Krewer, U.; Thiele, S.; Dreizler, A.; Klemm, E.; Turek, T. Understanding the Activity Transport Nexus in Water and CO₂ Electrolysis: State of the Art, Challenges and Perspectives. *Chem. Eng. J.* **2021**, *424*, 130501, doi:10.1016/j.cej.2021.130501.
53. Zhang, G.-R.; Straub, S.-D.; Shen, L.-L.; Hermans, Y.; Schmatz, P.; Reichert, A.M.; Hofmann, J.P.; Katsounaros, I.; Etzold, B.J.M. Probing CO₂ Reduction Pathways in Copper Catalysts Using Ionic Liquid as a Chemical Trapping Agent. *Angew. Chem. Int. Ed.* **2020**, anie.202009498, doi:10.1002/anie.202009498.
54. Dutta, A.; Rahaman, M.; Mohos, M.; Zanetti, A.; Broekmann, P. Electrochemical CO₂ Conversion Using Skeleton (Sponge) Type of Cu Catalysts. *ACS Catal.* **2017**, *7*, 5431–5437, doi:10.1021/acscatal.7b01548.
55. Rahaman, M.; Dutta, A.; Zanetti, A.; Broekmann, P. Electrochemical Reduction of CO₂ into Multicarbon Alcohols on Activated Cu Mesh Catalysts: An Identical Location (IL) Study. *ACS Catal.* **2017**, *7*, 7946–7956, doi:10.1021/acscatal.7b02234.
56. Bagger, A.; Ju, W.; Varela, A.S.; Strasser, P.; Rossmeisl, J. Electrochemical CO₂ Reduction: A Classification Problem. *ChemPhysChem* **2017**, *18*, 3266–3273, doi:10.1002/cphc.201700736.
57. Schouten, K.J.P.; Pérez Gallent, E.; Koper, M.T.M. The Influence of pH on the Reduction of CO and CO₂ to Hydrocarbons on Copper Electrodes. *J. Electroanal. Chem.* **2014**, *716*, 53–57, doi:10.1016/j.jelechem.2013.08.033.
58. Calle-Vallejo, F.; Koper, M.T.M. Accounting for Bifurcating Pathways in the Screening for CO₂ Reduction Catalysts. *ACS Catal.* **2017**, *7*, 7346–7351, doi:10.1021/acscatal.7b02917.
59. Xiao, H.; Cheng, T.; Goddard, W.A. Atomistic Mechanisms Underlying Selectivities in C₁ and C₂ Products from Electrochemical Reduction of CO on Cu(111). *J. Am. Chem. Soc.* **2017**, *139*, 130–136, doi:10.1021/jacs.6b06846.
60. Liu, Y.; Goebel, J.; Yin, Y. Templated Synthesis of Nanostructured Materials. *Chem Soc Rev* **2013**, *42*, 2610–2653, doi:10.1039/C2CS35369E.
61. Lee, W.; Park, S.-J. Porous Anodic Aluminum Oxide: Anodization and Templated Synthesis of Functional Nanostructures. *Chem. Rev.* **2014**, *114*, 7487–7556, doi:10.1021/cr500002z.
62. Md Jani, A.M.; Losic, D.; Voelcker, N.H. Nanoporous Anodic Aluminium Oxide: Advances in Surface Engineering and Emerging Applications. *Prog. Mater. Sci.* **2013**, *58*, 636–704, doi:10.1016/j.pmatsci.2013.01.002.
63. Huang, X.; Mutlu, H.; Théato, P. The Toolbox of Porous Anodic Aluminum Oxide-Based Nanocomposites: From Preparation to Application. *Colloid Polym. Sci.* **2021**, *299*, 325–341, doi:10.1007/s00396-020-04734-0.
64. Fink, D.; Petrov, A.V.; Hoppe, K.; Fahrner, W.R.; Papaleo, R.M.; Berdinsky, A.S.; Chandra, A.; Chemseddine, A.; Zrineh, A.; Biswas, A.; et al. Etched Ion Tracks in Silicon Oxide and Silicon Oxynitride as Charge Injection or Extraction Channels for Novel Electronic Structures. *Nucl. Instrum. Methods Phys. Res. Sect. B Beam Interact. Mater. At.* **2004**, *218*, 355–361, doi:10.1016/j.nimb.2003.12.083.
65. Musket, R.G.; Yoshiyama, J.M.; Contolini, R.J.; Porter, J.D. Vapor Etching of Ion Tracks in Fused Silica. *J. Appl. Phys.* **2002**, *91*, 5760–5764, doi:10.1063/1.1467402.
66. Lang, M.; Glasmacher, U.A.; Moine, B.; Neumann, R.; Wagner, G.A. Etch-Pit Morphology of Tracks Caused by Swift Heavy Ions in Natural Dark Mica. *Nucl. Instrum. Methods Phys. Res. Sect. B Beam Interact. Mater. At.* **2004**, *218*, 466–471, doi:10.1016/j.nimb.2004.01.009.

67. Coleman, R.V.; Xue, Q.; Gong, Y.; Price, P.B. Atomic Force Microscope Study of Etched Tracks of Low-Energy Heavy Ions in Mica. *Surf. Sci.* **1993**, *297*, 359–370, doi:10.1016/0039-6028(93)90224-8.
68. Trautmann, C. Micro- and Nanoengineering with Ion Tracks. In *Ion Beams in Nanoscience and Technology*; Particle Acceleration and Detection; Springer Berlin Heidelberg: Berlin, Heidelberg, **2010** ISBN 978-3-642-00622-7.
69. Trautmann, C. Observation and Chemical Treatment of Heavy-Ion Tracks in Polymers. *Nucl. Instrum. Methods Phys. Res. Sect. B Beam Interact. Mater. At.* **1995**, *105*, 81–85, doi:10.1016/0168-583X(95)00555-2.
70. Fink, D. Ion Tracks in Polymers. In *Fundamentals of Ion-Irradiated Polymers*; Fink, D., Ed.; Springer Berlin Heidelberg: Berlin, Heidelberg, **2004**; pp. 171–206 ISBN 978-3-662-07326-1.
71. Furneaux, R.C.; Rigby, W.R.; Davidson, A.P. The Formation of Controlled-Porosity Membranes from Anodically Oxidized Aluminium. *Nature* **1989**, *337*, 147–149, doi:10.1038/337147a0.
72. Masuda, H.; Fukuda, K. Ordered Metal Nanohole Arrays Made by a Two-Step Replication of Honeycomb Structures of Anodic Alumina. *Science* **1995**, *268*, 1466–1468, doi:10.1126/science.268.5216.1466.
73. Nielsch, K.; Choi, J.; Schwirn, K.; Wehrspohn, R.B.; Gösele, U. Self-Ordering Regimes of Porous Alumina: The 10 Porosity Rule. *Nano Lett.* **2002**, *2*, 677–680, doi:10.1021/nl025537k.
74. Poinern, G.E.J.; Ali, N.; Fawcett, D. Progress in Nano-Engineered Anodic Aluminum Oxide Membrane Development. *Materials* **2011**, *4*, 487–526, doi:10.3390/ma4030487.
75. Martín, J.; Martín-González, M.; Francisco Fernández, J.; Caballero-Calero, O. Ordered Three-Dimensional Interconnected Nanoarchitectures in Anodic Porous Alumina. *Nat. Commun.* **2014**, *5*, 5130, doi:10.1038/ncomms6130.
76. Fleischer, R.L. *Nuclear Tracks in Solids: Principles and Applications*; 1st ed.; University of California Press: Berkeley, **1975**; ISBN 0-520-02665-9.
77. Spohr, R. *Ion Tracks and Microtechnology: Principles and Applications*; Bethge, K., Ed.; 1st ed.; Vieweg+Teubner: Wiesbaden, **1990**; ISBN 978-3-322-83103-3.
78. Apel, P.Y.; Dmitriev, S.N. Micro- and Nanoporous Materials Produced Using Accelerated Heavy Ion Beams. *Adv. Nat. Sci. Nanosci. Nanotechnol.* **2011**, *2*, 013002, doi:10.1088/2043-6262/2/1/013002.
79. Cornelius, T.W.; Apel, P.Y.; Schiedt, B.; Trautmann, C.; Toimil-Molares, M.E.; Karim, S.; Neumann, R. Investigation of Nanopore Evolution in Ion Track-Etched Polycarbonate Membranes. *Nucl. Instrum. Methods Phys. Res. Sect. B Beam Interact. Mater. At.* **2007**, *265*, 553–557, doi:10.1016/j.nimb.2007.10.004.
80. Toulemonde, M.; Trautmann, C.; Balanzat, E.; Hjort, K.; Weidinger, A. Track Formation and Fabrication of Nanostructures with MeV-Ion Beams. In *Proceedings of the Nuclear Instruments and Methods in Physics Research, Section B: Beam Interactions with Materials and Atoms*; **2004**; Vol. 216, pp. 1–8.
81. Dehaye, F.; Balanzat, E.; Ferain, E.; Legras, R. Chemical Modifications Induced in Bisphenol A Polycarbonate by Swift Heavy Ions. *Nucl. Instrum. Methods Phys. Res. Sect. B Beam Interact. Mater. At.* **2003**, *209*, 103–112, doi:10.1016/S0168-583X(02)02048-7.
82. Steckenreiter, T.; Balanzat, E.; Fuess, H.; Trautmann, C. Pyrolytic Effects Induced by Energetic Ions in Polymers. *Nucl. Instrum. Methods Phys. Res. Sect. B Beam Interact. Mater. At.* **1999**, *151*, 161–168, doi:10.1016/S0168-583X(99)00093-2.
83. Chakarvarti, S.K.; Vetter, J. Template Synthesis—a Membrane Based Technology for Generation of Nano-/Micro Materials: A Review. *Radiat. Meas.* **1998**, *29*, 149–159, doi:10.1016/S1350-4487(98)00009-2.

-
84. Possin, G.E. A Method for Forming Very Small Diameter Wires. *Rev. Sci. Instrum.* **1970**, *41*, 772–774, doi:10.1063/1.1684640.
 85. Spohr, R. Status of Ion Track Technology - Prospects of Single Tracks. In Proceedings of the Radiation Measurements; **2005**; Vol. 40, pp. 191–202.
 86. Toimil-Molares, M.E. Characterization and Properties of Micro- and Nanowires of Controlled Size, Composition, and Geometry Fabricated by Electrodeposition and Ion-Track Technology. *Beilstein J. Nanotechnol.* **2012**, *3*, 860–883, doi:10.3762/bjnano.3.97.
 87. Fischer, B.E.; Heiß, M.; Cholewa, M. About the Art to Shoot with Single Ions. *Nucl. Instrum. Methods Phys. Res. Sect. B Beam Interact. Mater. At.* **2003**, *210*, 285–291, doi:10.1016/S0168-583X(03)01038-3.
 88. Spohr, R.; Zet, C.; Fischer, B.E.; Kiesewetter, H.; Apel, P.; Gunko, I.; Ohgai, T.; Westerberg, L. Controlled Fabrication of Ion Track Nanowires and Channels. *Nucl. Instrum. Methods Phys. Res. Sect. B Beam Interact. Mater. At.* **2010**, *268*, 676–686, doi:10.1016/j.nimb.2009.12.017.
 89. Fischer, B.E. The Heavy-Ion Microprobe at GSI - Used for Single Ion Micromechanics. *Nucl. Instrum. Methods Phys. Res. Sect. B Beam Interact. Mater. At.* **1988**, *30*, 284–288, doi:https://doi.org/10.1016/0168-583X(88)90012-2.
 90. Rauber, M.; Alber, I.; Müller, S.; Neumann, R.; Picht, O.; Roth, C.; Schökel, A.; Toimil-Molares, M.E.; Ensinger, W. Highly-Ordered Supportless Three-Dimensional Nanowire Networks with Tunable Complexity and Interwire Connectivity for Device Integration. *Nano Lett.* **2011**, *11*, 2304–2310, doi:10.1021/nl2005516.
 91. Pérez-Mitta, G.; Trautmann, C.; Toimil-Molares, M.E.; Azzaroni, O. Single Ion Track-Etched Nanochannels for Analytical Applications. In *Chemically Modified Nanopores and Nanochannels*; Tagliacucchi, M., Szleifer, I., Eds.; William Andrew Publishing: Boston, 2017; pp. 61–83 ISBN 978-0-323-40182-1.
 92. Lee, P.L.J.; Thangavel, V.; Guery, C.; Trautmann, C.; Toimil-Molares, M.E.; Morcrette, M. Etched Ion-Track Membranes as Tailored Separators in Li-S Batteries. *Nanotechnology* **2021**, *32*, 365401, doi:10.1088/1361-6528/ac04a3.
 93. Siwy, Z.; Apel, P.; Baur, D.; Dobrev, D.D.; Korchev, Y.E.; Neumann, R.; Spohr, R.; Trautmann, C.; Voss, K.O. Preparation of Synthetic Nanopores with Transport Properties Analogous to Biological Channels. In Proceedings of the Surface Science; **2003**; Vol. 532–535, pp. 1061–1066.
 94. Schiedt, B.; Healy, K.; Morrison, A.P.; Neumann, R.; Siwy, Z. Transport of Ions and Biomolecules through Single Asymmetric Nanopores in Polymer Films. In Proceedings of the Nuclear Instruments and Methods in Physics Research, Section B: Beam Interactions with Materials and Atoms; **2005**; Vol. 236, pp. 109–116.
 95. Davenport, M.; Rodriguez, A.; Shea, K.J.; Siwy, Z.S. Squeezing Ionic Liquids through Nanopores. *Nano Lett.* **2009**, *9*, 2125–2128, doi:10.1021/nl900630z.
 96. Pérez-Mitta, G.; Toimil-Molares, M.E.; Trautmann, C.; Marmisollé, W.A.; Azzaroni, O. Molecular Design of Solid-State Nanopores: Fundamental Concepts and Applications. *Adv. Mater.* **2019**, *31*, 1901483, doi:10.1002/adma.201901483.
 97. Mara, A.; Siwy, Z.; Trautmann, C.; Wan, J.; Kamme, F. An Asymmetric Polymer Nanopore for Single Molecule Detection. *Nano Lett.* **2004**, *4*, 497–501, doi:10.1021/nl035141o.
 98. Harrell, C.C.; Choi, Y.; Horne, L.P.; Baker, L.A.; Siwy, Z.S.; Martin, C.R. Resistive-Pulse DNA Detection with a Conical Nanopore Sensor. *Langmuir* **2006**, *22*, 10837–10843, doi:10.1021/la061234k.
 99. Healy, K. Nanopore-Based Single-Molecule DNA Analysis. *Nanomed.* **2007**, *2*, 459–481, doi:10.2217/17435889.2.4.459.
 100. Xiao, K.; Wen, L.; Jiang, L. Biomimetic Solid-State Nanochannels: From Fundamental Research to Practical Applications. *Small* **2016**, *12*, 2810–2831, doi:10.1002/smll.201600359.

101. Laucirica, G.; Albesa, A.G.; Toimil-Molares, M.E.; Trautmann, C.; Marmisollé, W.A.; Azzaroni, O. Shape Matters: Enhanced Osmotic Energy Harvesting in Bullet-Shaped Nanochannels. *Nano Energy* **2020**, *71*, 104612, doi:10.1016/j.nanoen.2020.104612.
102. Pérez-Mitta, G.; Peinetti, A.S.; Cortez, M.L.; Toimil-Molares, M.E.; Trautmann, C.; Azzaroni, O. Highly Sensitive Biosensing with Solid-State Nanopores Displaying Enzymatically Reconfigurable Rectification Properties. *Nano Lett.* **2018**, *18*, 3303–3310, doi:10.1021/acs.nanolett.8b01281.
103. Wang, C.; Fu, Q.; Wang, X.; Kong, D.; Sheng, Q.; Wang, Y.; Chen, Q.; Xue, J. Atomic Layer Deposition Modified Track-Etched Conical Nanochannels for Protein Sensing. *Anal. Chem.* **2015**, *87*, 8227–8233, doi:10.1021/acs.analchem.5b01501.
104. Ulrich, N.; Spende, A.; Burr, L.; Sobel, N.; Schubert, I.; Hess, C.; Trautmann, C.; Toimil-Molares, M.E. Conical Nanotubes Synthesized by Atomic Layer Deposition of Al₂O₃, TiO₂, and SiO₂ in Etched Ion-Track Nanochannels. *Nanomaterials* **2021**, *11*, 1874, doi:10.3390/nano11081874.
105. Sobel, N.; Hess, C.; Lukas, M.; Spende, A.; Stühn, B.; Toimil-Molares, M.E.; Trautmann, C. Conformal SiO₂ Coating of Sub-100 Nm Diameter Channels of Polycarbonate Etched Ion-Track Channels by Atomic Layer Deposition. *Beilstein J. Nanotechnol.* **2015**, *6*, 472–479, doi:10.3762/bjnano.6.48.
106. Spende, A.; Sobel, N.; Lukas, M.; Zierold, R.; Riedl, J.C.; Gura, L.; Schubert, I.; Moreno, J.M.M.; Nielsch, K.; Stühn, B.; et al. TiO₂, SiO₂, and Al₂O₃ Coated Nanopores and Nanotubes Produced by ALD in Etched Ion-Track Membranes for Transport Measurements. *Nanotechnology* **2015**, *26*, doi:10.1088/0957-4484/26/33/335301.
107. Muench, F.; Oezaslan, M.; Seidl, T.; Lauterbach, S.; Strasser, P.; Kleebe, H.-J.; Ensinger, W. Multiple Activation of Ion Track Etched Polycarbonate for the Electroless Synthesis of Metal Nanotubes. *Appl. Phys. A* **2011**, *105*, 847–854, doi:10.1007/s00339-011-6646-z.
108. Jirage, K.B.; Hulteen, J.C.; Martin, C.R. Nanotubule-Based Molecular-Filtration Membranes. *Science* **1997**, *278*, 655–658, doi:10.1126/science.278.5338.655.109. Müller, S.; Schötz, C.; Picht, O.; Sigle, W.; Kopold, P.; Rauber, M.; Alber, I.; Neumann, R.; Toimil-Molares, M.E. Electrochemical Synthesis of Bi_{1-x}Sb_x Nanowires with Simultaneous Control on Size, Composition, and Surface Roughness. *Cryst. Growth Des.* **2012**, *12*, 615–621, doi:10.1021/cg200685c.
110. Movsesyan, L.; Schubert, I.; Yeranyan, L.; Trautmann, C.; Eugenia Toimil-Molares, M. Influence of Electrodeposition Parameters on the Structure and Morphology of ZnO Nanowire Arrays and Networks Synthesized in Etched Ion-Track Membranes. *Semicond. Sci. Technol.* **2016**, *31*, 014006, doi:10.1088/0268-1242/31/1/014006.
111. Toimil Molares, M.E.; Brötz, J.; Buschmann, V.; Dobrev, D.; Neumann, R.; Scholz, R.; Schuchert, I.U.; Trautmann, C.; Vetter, J. Etched Heavy Ion Tracks in Polycarbonate as Template for Copper Nanowires. *Nucl. Instrum. Methods Phys. Res. Sect. B Beam Interact. Mater. At.* **2001**, *185*, 192–197, doi:10.1016/S0168-583X(01)00755-8.
112. Toimil Molares, M.E.; Buschmann, V.; Dobrev, D.; Neumann, R.; Scholz, R.; Schuchert, I.U.; Vetter, J. Single-Crystalline Copper Nanowires Produced by Electrochemical Deposition in Polymeric Ion Track Membranes. *Adv. Mater.* **2001**, *13*, 62–65, doi:10.1002/1521-4095(200101)13.
113. Burr, L.; Schubert, I.; Sigle, W.; Trautmann, C.; Toimil-Molares, M.E. Surface Enrichment in Au–Ag Alloy Nanowires and Investigation of the Dealloying Process. *J. Phys. Chem. C* **2015**, *119*, 20949–20956, doi:10.1021/acs.jpcc.5b05596.
114. Picht, O.; Müller, S.; Alber, I.; Rauber, M.; Lensch-Falk, J.; Medlin, D.L.; Neumann, R.; Toimil-Molares, M.E. Tuning the Geometrical and Crystallographic Characteristics of Bi₂Te₃ Nanowires by Electrodeposition in Ion-Track Membranes. *J. Phys. Chem. C* **2012**, *116*, 5367–5375, doi:10.1021/jp210491g.
115. Daub, M.; Enculescu, I.; Neumann, R.; Spohr, R. Ni Nanowires Electrodeposited in Single Ion Track Templates. *J. Optoelectron. Adv. Mater.* **2005**, *2*, 865–870.

-
116. Dangwal, A.; Müller, G.; Maurer, F.; Brötz, J.; Fuess, H. Field Emission Properties of Bare and Gold-Coated Nickel Nanowires Grown in Polymer Ion-Track Membranes. *J. Vac. Sci. Technol. B Microelectron. Nanometer Struct. Process. Meas. Phenom.* **2007**, *25*, 586–589, doi:10.1116/1.2709888.
 117. Ohgai, T.; Enculescu, I.; Zet, C.; Westerberg, L.; Hjort, K.; Spohr, R.; Neumann, R. Magneto-Sensitive Nickel Nanowires Fabricated by Electrodeposition into Multi- and Single-Ion Track Templates. *J. Appl. Electrochem.* **2006**, *36*, 1157–1162, doi:10.1007/s10800-006-9200-5.
 118. Li, M.; Ulrich, N.; Schubert, I.; Sigle, W.; Peter Wagner, M.F.; Trautmann, C.; Toimil-Molares, M.E. Three-Dimensional Free-Standing Gold Nanowire Networks as a Platform for Catalytic Applications. *RSC Adv.* **2023**, *13*, 4721–4728, doi:10.1039/D2RA08035D.
 119. Rauber, M.; Cornelius, T.W.; Ensinger, W.; Huzel, D.; Mă, S. Controlled Synthesis of Nanowire Networks by Ion Track Template Electrodeposition. *GSI Scientific Report* **2008**, 357
 120. Naderi, N.; Hashim, M.R.; Rouhi, J. Synthesis and Characterization of Pt Nanowires Electrodeposited into the Cylindrical Pores of Polycarbonate Membranes. *Int. J. Electrochem. Sci.* **2012**, *7*, 8481–8486, doi:10.1016/S1452-3981(23)18010-2.
 121. Stegmann, C.; Muench, F.; Rauber, M.; Hottes, M.; Brötz, J.; Kunz, U.; Lauterbach, S.; Kleebe, H.-J.; Ensinger, W. Platinum Nanowires with Pronounced Texture, Controlled Crystallite Size and Excellent Growth Homogeneity Fabricated by Optimized Pulsed Electrodeposition. *RSC Adv.* **2014**, *4*, 4804, doi:10.1039/c3ra46204h.
 122. Wagner, M.F.P.; Paulus, A.S.; Brötz, J.; Sigle, W.; Trautmann, C.; Voss, K.; Völklein, F.; Toimil-Molares, M.E. Effects of Size Reduction on the Electrical Transport Properties of 3D Bi Nanowire Networks. *Adv. Electron. Mater.* **2021**, *7*, 2001069, doi:10.1002/aelm.202001069.
 123. Wagner, M.F.P. Bi and Sb Nanowire Assemblies for Thermoelectric Applications. PhD Thesis, Technische Universität Darmstadt: Darmstadt, **2018**.
 124. Cassinelli, M.; Müller, S.; Aabdin, Z.; Peranio, N.; Eibl, O.; Trautmann, C.; Toimil-Molares, M.E. Structural and Compositional Characterization of Bi_{1-x}Sb_x Nanowire Arrays Grown by Pulsed Deposition to Improve Growth Uniformity. *Nucl. Instrum. Methods Phys. Res. Sect. B Beam Interact. Mater. At.* **2015**, *365*, 668–674, doi:10.1016/j.nimb.2015.07.107.
 125. Yang, F.; Schröck, C.; Kugelstadt, J.; Zhang, S.; Scheu, C.; Trautmann, C.; Maijenburg, A.W.; Toimil-Molares, M.E. Cu₂O/TiO₂ Nanowire Assemblies as Photocathodes for Solar Hydrogen Evolution: Influence of Diameter, Length and Number Density of Wires. *Z. Für Phys. Chem.* **2020**, *234*, 1205–1221, doi:10.1515/zpch-2019-1529.
 126. Caddeo, F.; Himmelstein, F.; Mahmoudi, B.; Araújo-Cordero, A.M.; Eberhart, D.; Zhang, H.; Lindenberg, T.; Hähnel, A.; Hagendorf, C.; Maijenburg, A.W. Coating the Surface of Interconnected Cu₂O Nanowire Arrays with HKUST-1 Nanocrystals via Electrochemical Oxidation. *Sci. Rep.* **2023**, *13*, 13858, doi:10.1038/s41598-023-39982-x.
 127. Movsesyan, L.; Maijenburg, A.; Goethals, N.; Sigle, W.; Spende, A.; Yang, F.; Kaiser, B.; Jaegermann, W.; Park, S.-Y.; Mul, G.; et al. ZnO Nanowire Networks as Photoanode Model Systems for Photoelectrochemical Applications. *Nanomaterials* **2018**, *8*, 693, doi:10.3390/nano8090693.
 128. Luo, J.; Lan, M.; Wagner, M.; Ulrich, N.; Kopold, P.; Tzifas, I.; Wang, H.; Trautmann, C.; Toimil-Molares, M.E. Electrochemical Conversion of Cu Nanowire Arrays into Metal-Organic Frameworks HKUST-1. *J. Electrochem. Soc.* **2023**, *170*, 022506, doi:10.1149/1945-7111/acbba4.
 129. Hori, Y.; Takahashi, I.; Koga, O.; Hoshi, N. Electrochemical Reduction of Carbon Dioxide at Various Series of Copper Single Crystal Electrodes. *J. Mol. Catal. Chem.* **2003**, *199*, 39–47, doi:10.1016/S1381-1169(03)00016-5.

-
130. Hahn, C.; Hatsukade, T.; Kim, Y.-G.; Vailionis, A.; Baricuatro, J.H.; Higgins, D.C.; Nitopi, S.A.; Soriaga, M.P.; Jaramillo, T.F. Engineering Cu Surfaces for the Electrocatalytic Conversion of CO₂: Controlling Selectivity toward Oxygenates and Hydrocarbons. *Proc. Natl. Acad. Sci.* **2017**, *114*, 5918–5923, doi:10.1073/pnas.1618935114.
131. Reske, R.; Mistry, H.; Behafarid, F.; Roldan Cuenya, B.; Strasser, P. Particle Size Effects in the Catalytic Electroreduction of CO₂ on Cu Nanoparticles. *J. Am. Chem. Soc.* **2014**, *136*, 6978–6986, doi:10.1021/ja500328k.
132. Baturina, O.A.; Lu, Q.; Padilla, M.A.; Xin, L.; Li, W.; Serov, A.; Artyushkova, K.; Atanassov, P.; Xu, F.; Epshteyn, A.; et al. CO₂ Electroreduction to Hydrocarbons on Carbon-Supported Cu Nanoparticles. *ACS Catal.* **2014**, *4*, 3682–3695, doi:10.1021/cs500537y.
133. Mistry, H.; Behafarid, F.; Reske, R.; Varela, A.S.; Strasser, P.; Roldan Cuenya, B. Tuning Catalytic Selectivity at the Mesoscale via Interparticle Interactions. *ACS Catal.* **2016**, *6*, 1075–1080, doi:10.1021/acscatal.5b02202.
134. Ma, M.; Djanashvili, K.; Smith, W.A. Controllable Hydrocarbon Formation from the Electrochemical Reduction of CO₂ over Cu Nanowire Arrays. *Angew. Chem. Int. Ed.* **2016**, *55*, 6680–6684, doi:10.1002/anie.201601282.
135. Raciti, D.; Livi, K.J.; Wang, C. Highly Dense Cu Nanowires for Low-Overpotential CO₂ Reduction. *Nano Lett* **2015**, *7*, doi:10.1021/acs.nanolett.5b03298.
136. Sigmund, P. *Stopping of Heavy Ions a Theoretical Approach*; 1st ed.; Springer: Berlin, Heidelberg, **2004**; ISBN 978-3-642-06084-7.
137. Jackson, J.D. *Klassische Elektrodynamik*; Witte, C., Diestelhorst, M., Eds.; 5th ed.; Walter de Gruyter: Berlin, New York, **2013**; ISBN 3-11-033446-1.
138. Bethe, H. Zur Theorie des Durchgangs schneller Korpuskularstrahlen durch Materie. *Ann. Phys.* **1930**, *397*, 325–400, doi:10.1002/andp.19303970303.
139. Bloch, F. Zur Bremsung rasch bewegter Teilchen beim Durchgang durch Materie. *Ann. Phys.* **1933**, *408*, 285–320, doi:10.1002/andp.19334080303.
140. Fleischer, R.L.; Price, P.B.; Walker, R.M. Ion Explosion Spike Mechanism for Formation of Charged-Particle Tracks in Solids. *J. Appl. Phys.* **1965**, *36*, 3645–3652, doi:10.1063/1.1703059.
141. Wang, Z.G.; Dufourtt, C.; Paumierrt, E.; Toulemonde, M. The Sensitivity of Metals under Swift-Heavy-Ion Irradiation: A Transient Thermal Process. *J. Phys. Condens. Matter* **2004**, *6*, 6733–6750, doi:https://doi.org/10.1088/0953-8984/6/34/006.
142. Toulemonde, M.; Dufour, Ch.; Meftah, A.; Paumier, E. Transient Thermal Processes in Heavy Ion Irradiation of Crystalline Inorganic Insulators. *Nucl. Instrum. Methods Phys. Res. Sect. B Beam Interact. Mater. At.* **2000**, *166–167*, 903–912, doi:10.1016/S0168-583X(99)00799-5.
143. Toimil-Molares, M.E. Characterization and Properties of Micro- and Nanowires of Controlled Size, Composition, and Geometry Fabricated by Electrodeposition and Ion-Track Technology. *Beilstein J. Nanotechnol.* **2012**, *3*, 860–883, doi:10.3762/bjnano.3.97.
144. Petersen, F.; Enge, W. Energy Loss Dependent Transversal Etching Rates of Heavy Ion Tracks in Plastic. *Radiat. Meas.* **1995**, *25*, 43–46, doi:10.1016/1350-4487(95)00028-D.
145. Nastasi, M.; Mayer, J.; Hirvonen, J.K. *Ion-Solid Interactions: Fundamentals and Applications*; Cambridge Solid State Science Series; 1st ed.; Cambridge University Press: Cambridge, **1996**; ISBN 978-0521373760.
146. Ziegler, J.F. SRIM-2003. *Nucl. Instrum. Methods Phys. Res. Sect. B Beam Interact. Mater. At.* **2004**, *219–220*, 1027–1036, doi:10.1016/j.nimb.2004.01.208.
147. DeSorbo, W. Ultraviolet Effects and Aging Effects on Etching Characteristics of Fission Tracks in Polycarbonate Film. *Nucl. Tracks* **1979**, *3*, 13–32, doi:10.1016/0191-278X(79)90026-X.

-
148. Ferain, E.; Legras, R. Heavy Ion Tracks in Polycarbonate. Comparison with a Heavy Ion Irradiated Model Compound (Diphenyl Carbonate). *Nucl. Instrum. Methods Phys. Res. Sect. B Beam Interact. Mater. At.* **1993**, *82*, 539–548, doi:10.1016/0168-583X(93)96008-Z.
 149. Pépy, G.; Boesecke, P.; Kuklin, A.; Manceau, E.; Schiedt, B.; Siwy, Z.; Toulemonde, M.; Trautmann, C. Cylindrical Nanochannels in Ion-Track Polycarbonate Membranes Studied by Small-Angle X-Ray Scattering. *J. Appl. Crystallogr.* **2007**, *40*, s388–s392, doi:10.1107/S0021889807000088.
 150. Ditlov, V.A.; Gatchegov, A.U.; Enge, W.; Petersen, F.; Danziger, M.; Schulz, A.; Trofimov, V. The Radial Etching Velocity for Tracks in Polymer Film. *Radiat. Meas.* **1997**, *28*, 137–144, doi:10.1016/S1350-4487(97)00055-3.
 151. Fischer, B.E.; Spohr, R. Production and Use of Nuclear Tracks: Imprinting Structure on Solids. *Rev. Mod. Phys.* **1983**, *55*, 907–948, doi:10.1103/RevModPhys.55.907.
 152. Apel, P.; Blonskaya, I.; Dmitriev, S.; Orelovitch, O.; Sartowska, B. Structure of Polycarbonate Track-Etch Membranes: Origin of the “Paradoxical” Pore Shape. *J. Membr. Sci.* **2006**, *282*, 393–400, doi:10.1016/j.memsci.2006.05.045.
 153. Cornelius, T.W.; Schiedt, B.; Severin, D.; Pépy, G.; Toulemonde, M.; Apel, P.Y.; Boesecke, P.; Trautmann, C. Nanopores in Track-Etched Polymer Membranes Characterized by Small-Angle x-Ray Scattering. *Nanotechnology* **2010**, *21*, 155702, doi:10.1088/0957-4484/21/15/155702.
 154. Kiy, A.; Notthoff, C.; Dutt, S.; Grigg, M.; Hadley, A.; Mota-Santiago, P.; Kirby, N.; Trautmann, C.; Toimil-Molares, M.E.; Kluth, P. Ion Track Etching of Polycarbonate Membranes Monitored by *in Situ* Small Angle X-Ray Scattering. *Phys. Chem. Chem. Phys.* **2021**, *23*, 14231–14241, doi:10.1039/D1CP02063C.
 155. Guillot, G.; Rondelez, F. Characteristics of Submicron Pores Obtained by Chemical Etching of Nuclear Tracks in Polycarbonate Films. *J. Appl. Phys.* **1981**, *52*, 7155–7164, doi:10.1063/1.328690.
 156. Bard, A.; Faulkner, L. *Electrochemical Methods, Fundamentals and Applications*; Harris, D., Ed.; 2nd ed.; John Wiley & Sons: New York, **2001**; ISBN 978-0-471-04372-0.
 157. Hansal, Wolfgang E.G.; Sudipta, Roy *Pulse Plating*; 1st ed.; Eugen G. Leuze Verlag: Bad Saulgau, **2012**; ISBN 978-3-87480-265-9.
 158. Wang, Z.; Chen, Y.; Sun, X.; Duddu, R.; Lin, S. Mechanism of Pore Wetting in Membrane Distillation with Alcohol vs. Surfactant. *J. Membr. Sci.* **2018**, *559*, 183–195, doi:10.1016/j.memsci.2018.04.045.
 159. Ulrich, N. Copper Nanowire Networks as Electrocatalyst for Electrochemical CO₂ Reduction. Master Thesis, Technische Universität Darmstadt: Darmstadt, **2018**.
 160. Bell, D.C.; Garratt-Reed, A.J. *Energy Dispersive X-Ray Analysis in the Electron Microscope*; 1st ed.; Garland Science: London, **2003**;
 161. Russ, J.C. *Fundamentals of Energy Dispersive X-Ray Analysis*; 1st ed.; Butterworths & Co Ltd.: London, **1984**;
 162. Kortlever, R.; Shen, J.; Schouten, K.J.P.; Calle-Vallejo, F.; Koper, M.T.M. Catalysts and Reaction Pathways for the Electrochemical Reduction of Carbon Dioxide. *J. Phys. Chem. Lett.* **2015**, *6*, 4073–4082, doi:10.1021/acs.jpcclett.5b01559.
 163. Costentin, C.; Robert, M.; Savéant, J.-M. Catalysis of the Electrochemical Reduction of Carbon Dioxide. *Chem Soc Rev* **2013**, *42*, 2423–2436, doi:10.1039/C2CS35360A.
 164. Qiao, J.; Liu, Y.; Hong, F.; Zhang, J. A Review of Catalysts for the Electroreduction of Carbon Dioxide to Produce Low-Carbon Fuels. *Chem Soc Rev* **2014**, *43*, 631–675, doi:10.1039/C3CS60323G.
 165. Gattrell, M.; Gupta, N.; Co, A. A Review of the Aqueous Electrochemical Reduction of CO₂ to Hydrocarbons at Copper. *J. Electroanal. Chem.* **2006**, *594*, 1–19, doi:10.1016/j.jelechem.2006.05.013.
 166. Lee, S.Y.; Jung, H.; Kim, N.-K.; Oh, H.-S.; Min, B.K.; Hwang, Y.J. Mixed Copper States in Anodized Cu Electrocatalyst for Stable and Selective Ethylene Production from CO₂ Reduction. *J. Am. Chem. Soc.* **2018**, *140*, 8681–8689, doi:10.1021/jacs.8b02173.

-
167. Min, S.; Yang, X.; Lu, A.-Y.; Tseng, C.-C.; Hedhili, M.N.; Lai, Z.; Li, L.-J.; Huang, K.-W. Surface-Reconstructed Cu Electrode via a Facile Electrochemical Anodization-Reduction Process for Low Overpotential CO₂ Reduction. *J. Saudi Chem. Soc.* **2017**, *21*, 708–712, doi:10.1016/j.jscs.2017.03.003.
168. Straub, S.-D. Copper Foam Catalysts in CO₂ Electroreduction. PhD Thesis, Technische Universität Darmstadt: Darmstadt, **2021**.
169. Aksu, S. Electrochemical Equilibria of Copper in Aqueous Phosphoric Acid Solutions. *J. Electrochem. Soc.* **2009**, *156*, C387, doi:10.1149/1.3215996.
170. Glarum, S.H.; Marshall, J.H. The Anodic Dissolution of Copper into Phosphoric Acid. *J. Electrochem Soc.* **1985**, *132*, 7, doi:10.1149/1.2113686.
171. Bearden, J.A. X-Ray Wavelengths. *Rev. Mod. Phys.* **1967**, *39*, 78–124, doi:10.1103/RevModPhys.39.78.
172. Clark, E.L.; Resasco, J.; Landers, A.; Lin, J.; Chung, L.-T.; Walton, A.; Hahn, C.; Jaramillo, T.F.; Bell, A.T. Standards and Protocols for Data Acquisition and Reporting for Studies of the Electrochemical Reduction of Carbon Dioxide. *ACS Catal.* **2018**, *8*, 6560–6570, doi:10.1021/acscatal.8b01340.
173. Trasatti, S.; Petrii, O.A. Real Surface Area Measurements in Electrochemistry. *J. Electroanal. Chem.* **1992**, *327*, 353–376, doi:10.1351/pac19916305071.
174. Connor, P.; Schuch, J.; Kaiser, B.; Jaegermann, W. The Determination of Electrochemical Active Surface Area and Specific Capacity Revisited for the System MnO_x as an Oxygen Evolution Catalyst. *Z. Für Phys. Chem.* **2020**, *234*, 979–994, doi:10.1515/zpch-2019-1514.
175. Wei, C.; Sun, S.; Mandler, D.; Wang, X.; Qiao, S.Z.; Xu, Z.J. Approaches for Measuring the Surface Areas of Metal Oxide Electrocatalysts for Determining Their Intrinsic Electrocatalytic Activity. *Chem. Soc. Rev.* **2019**, *48*, 2518–2534, doi:10.1039/C8CS00848E.
176. Chinchén, G. The Measurement of Copper Surface Areas by Reactive Frontal Chromatography*1. *J. Catal.* **1987**, *103*, 79–86, doi:10.1016/0021-9517(87)90094-7.
177. Łukaszewski, M.; Soszko, M.; Czerwinski, A. Electrochemical Methods of Real Surface Area Determination of Noble Metal Electrodes – an Overview. *Int. J. Electrochem. Sci.* **2016**, 4442–4469, doi:10.20964/2016.06.71.
178. Hamann, C.H.; Vielstich, W. *Elektrochemie*; 4th ed.; Wiley-VCH: Weinheim, **2005**; ISBN 978-3-527-31068-5.
179. Hunter, R.J.; Wright, H.J.L. The Dependence of Electrokinetic Potential on Concentration of Electrolyte. *J. Colloid Interface Sci.* **1971**, *37*, doi:10.1016/0021-9797(71)90334-1.
180. Davis, J.A.; James, R.O.; Leckie, J.O. Surface Ionization and Complexation at the Oxide/Water Interface. *J. Colloid Interface Sci.* **1978**, *63*, 480–499, doi:10.1016/S0021-9797(78)80009-5.
181. Kruyt, H.R.; Jonker, G.H.; Overbeek, J.Th.G. *Colloid Science, Volume 1*; 1st ed.; Elsevier: Amsterdam, **1952**; ISBN 1-4443-2019-X.
182. Schoch, R.B.; Han, J.; Renaud, P. Transport Phenomena in Nanofluidics. *Rev. Mod. Phys.* **2008**, *80*, 839–883, doi:10.1103/RevModPhys.80.839.
183. Eijkel, J.C.T.; Berg, A. van den Nanofluidics: What Is It and What Can We Expect from It? *Microfluid. Nanofluidics* **2005**, *1*, 249–267, doi:10.1007/s10404-004-0012-9.
184. Abgrall, P.; Nguyen, N.T. Nanofluidic Devices and Their Applications. *Anal. Chem.* **2008**, *80*, 2326–2341, doi:10.1021/ac702296u.
185. Lyklema, J.; Overbeek, J.Th.G. On the Interpretation of Electrokinetic Potentials. *J. Colloid Sci.* **1961**, *16*, 501–512, doi:10.1016/0095-8522(61)90029-0.
186. Hunter, R.J. *Zeta Potential in Colloid Science: Principles and Applications*; 1st ed.; Academic Press: London, New York, **1981**; ISBN 978-0-12-361961-7.

-
187. Bagotsky, V.S. *Fundamentals of Electrochemistry*; 2nd ed.; Wiley & Sons: Pennington, **2006**; ISBN 978-0-471-70058-6.
 188. Bard, A.J.; Abruna, H.D.; Chidsey, C.E.; Faulkner, L.R.; Feldberg, S.W.; Itaya, K.; Majda, M.; Melroy, O.; Murray, R.W. The Electrode/Electrolyte Interface - a Status Report. *J. Phys. Chem.* **1993**, *97*, 7147–7173, doi:10.1021/j100130a007.
 189. Diao, K.K.; Xiao, Z.; Zhao, Y.Y. Specific Surface Areas of Porous Cu Manufactured by Lost Carbonate Sintering: Measurements by Quantitative Stereology and Cyclic Voltammetry. *Mater. Chem. Phys.* **2015**, *162*, 571–579, doi:10.1016/j.matchemphys.2015.06.031.
 190. Omae, I. Recent Developments in Carbon Dioxide Utilization for the Production of Organic Chemicals. *Coord. Chem. Rev.* **2012**, *256*, 1384–1405, doi:10.1016/j.ccr.2012.03.017.
 191. Federsel, C.; Jackstell, R.; Beller, M. State-of-the-Art Catalysts for Hydrogenation of Carbon Dioxide. *Angew. Chem. Int. Ed.* **2010**, *49*, 6254–6257, doi:10.1002/anie.201000533.
 192. Martín, C.; Fiorani, G.; Kleij, A.W. Recent Advances in the Catalytic Preparation of Cyclic Organic Carbonates. *ACS Catal.* **2015**, *5*, 1353–1370, doi:10.1021/cs5018997.
 193. Comerford, J.W.; Ingram, I.D.V.; North, M.; Wu, X. Sustainable Metal-Based Catalysts for the Synthesis of Cyclic Carbonates Containing Five-Membered Rings. *Green Chem.* **2015**, *17*, 1966–1987, doi:10.1039/C4GC01719F.
 194. Langanke, J.; Wolf, A.; Hofmann, J.; Böhm, K.; Subhani, M.A.; Müller, T.E.; Leitner, W.; Gürtler, C. Carbon Dioxide (CO₂) as Sustainable Feedstock for Polyurethane Production. *Green Chem* **2014**, *16*, 1865–1870, doi:10.1039/C3GC41788C.
 195. Alberico, E.; Nielsen, M. Towards a Methanol Economy Based on Homogeneous Catalysis: Methanol to H₂ and CO₂ to Methanol. *Chem. Commun.* **2015**, *51*, 6714–6725, doi:10.1039/C4CC09471A.
 196. Behrens, M. Promoting the Synthesis of Methanol: Understanding the Requirements for an Industrial Catalyst for the Conversion of CO₂. *Angew. Chem. Int. Ed.* **2016**, *55*, 14906–14908, doi:10.1002/anie.201607600.
 197. Gao, J.; Liu, Q.; Gu, F.; Liu, B.; Zhong, Z.; Su, F. Recent Advances in Methanation Catalysts for the Production of Synthetic Natural Gas. *RSC Adv.* **2015**, *5*, 22759–22776, doi:10.1039/C4RA16114A.
 198. Takeda, H.; Cometto, C.; Ishitani, O.; Robert, M. Electrons, Photons, Protons and Earth-Abundant Metal Complexes for Molecular Catalysis of CO₂ Reduction. *ACS Catal.* **2017**, *7*, 70–88, doi:10.1021/acscatal.6b02181.
 199. Miao, B.; Ma, S.S.K.; Wang, X.; Su, H.; Chan, S.H. Catalysis Mechanisms of CO₂ and CO Methanation. *Catal. Sci. Technol.* **2016**, *6*, 4048–4058, doi:10.1039/C6CY00478D.
 200. Aziz, M.A.A.; Jalil, A.A.; Triwahyono, S.; Ahmad, A. CO₂ Methanation over Heterogeneous Catalysts: Recent Progress and Future Prospects. *Green Chem.* **2015**, *17*, 2647–2663, doi:10.1039/C5GC00119F.
 201. Porosoff, M.D.; Yan, B.; Chen, J.G. Catalytic Reduction of CO₂ by H₂ for Synthesis of CO, Methanol and Hydrocarbons: Challenges and Opportunities. *Energy Environ. Sci.* **2016**, *9*, 62–73, doi:10.1039/C5EE02657A.
 202. Bansode, A.; Urakawa, A. Towards Full One-Pass Conversion of Carbon Dioxide to Methanol and Methanol-Derived Products. *J. Catal.* **2014**, *309*, 66–70, doi:10.1016/j.jcat.2013.09.005.
 203. Jin, S.; Hao, Z.; Zhang, K.; Yan, Z.; Chen, J. Advances and Challenges for the Electrochemical Reduction of CO₂ to CO: From Fundamentals to Industrialization. *Angew. Chem. Int. Ed.* **2021**, *60*, 20627–20648, doi:10.1002/anie.202101818.
 204. Garza, A.J.; Bell, A.T.; Head-Gordon, M. Mechanism of CO₂ Reduction at Copper Surfaces: Pathways to C₂ Products. *ACS Catal.* **2018**, *8*, 1490–1499, doi:10.1021/acscatal.7b03477.

205. Keszei, E. *Chemical Thermodynamics*; Springer: Berlin, Heidelberg, **2012**; Vol. 1; ISBN 978-3-642-19864-9.
206. Zhang, W.; Hu, Y.; Ma, L.; Zhu, G.; Wang, Y.; Xue, X.; Chen, R.; Yang, S.; Jin, Z. Progress and Perspective of Electrocatalytic CO₂ Reduction for Renewable Carbonaceous Fuels and Chemicals. *Adv. Sci.* **2018**, *5*, 1700275, doi:10.1002/advs.201700275.
207. Ren, D.; Wong, N.T.; Handoko, A.D.; Huang, Y.; Yeo, B.S. Mechanistic Insights into the Enhanced Activity and Stability of Agglomerated Cu Nanocrystals for the Electrochemical Reduction of Carbon Dioxide to *n*-Propanol. *J. Phys. Chem. Lett.* **2016**, *7*, 20–24, doi:10.1021/acs.jpcclett.5b02554.
208. Koper, M.T.M. Thermodynamic Theory of Multi-Electron Transfer Reactions: Implications for Electrocatalysis. *J. Electroanal. Chem.* **2011**, *660*, 254–260, doi:10.1016/j.jelechem.2010.10.004.
209. Goyal, A.; Marcandalli, G.; Mints, V.A.; Koper, M.T.M. Competition between CO₂ Reduction and Hydrogen Evolution on a Gold Electrode under Well-Defined Mass Transport Conditions. *J. Am. Chem. Soc.* **2020**, *142*, 4154–4161, doi:10.1021/jacs.9b10061.
210. Liu, X.; Xiao, J.; Peng, H.; Hong, X.; Chan, K.; Nørskov, J.K. Understanding Trends in Electrochemical Carbon Dioxide Reduction Rates. *Nat. Commun.* **2017**, *8*, 15438, doi:10.1038/ncomms15438.
211. Kibria, M.G.; Dinh, C.-T.; Seifitokaldani, A.; De Luna, P.; Burdyny, T.; Quintero-Bermudez, R.; Ross, M.B.; Bushuyev, O.S.; García de Arquer, F.P.; Yang, P.; et al. A Surface Reconstruction Route to High Productivity and Selectivity in CO₂ Electroreduction toward C₂₊ Hydrocarbons. *Adv. Mater.* **2018**, *30*, 1804867, doi:10.1002/adma.201804867.
212. Mistry, H.; Varela, A.S.; Bonifacio, C.S.; Zegkinoglou, I.; Sinev, I.; Choi, Y.-W.; Kisslinger, K.; Stach, E.A.; Yang, J.C.; Strasser, P.; et al. Highly Selective Plasma-Activated Copper Catalysts for Carbon Dioxide Reduction to Ethylene. *Nat. Commun.* **2016**, *7*, 12123, doi:10.1038/ncomms12123.
213. Monteiro, M.C.O.; Philips, M.F.; Schouten, K.J.P.; Koper, M.T.M. Efficiency and Selectivity of CO₂ Reduction to CO on Gold Gas Diffusion Electrodes in Acidic Media. *Nat. Commun.* **2021**, *12*, 4943, doi:10.1038/s41467-021-24936-6.
214. Birdja, Y.Y.; Pérez-Gallent, E.; Figueiredo, M.C.; Göttle, A.J.; Calle-Vallejo, F.; Koper, M.T.M. Advances and Challenges in Understanding the Electrocatalytic Conversion of Carbon Dioxide to Fuels. *Nat. Energy* **2019**, *4*, 732–745, doi:10.1038/s41560-019-0450-y.
215. Setterfield-Price, B.M.; Dryfe, R.A.W. The Influence of Electrolyte Identity upon the Electroreduction of CO₂. *J. Electroanal. Chem.* **2014**, *730*, 48–58, doi:10.1016/j.jelechem.2014.07.009.
216. De Gregorio, G.L.; Burdyny, T.; Loiudice, A.; Iyengar, P.; Smith, W.A.; Buonsanti, R. Facet-Dependent Selectivity of Cu Catalysts in Electrochemical CO₂ Reduction at Commercially Viable Current Densities. *ACS Catal.* **2020**, *10*, 4854–4862, doi:10.1021/acscatal.0c00297.
217. Kuo, T.-C.; Chou, J.-W.; Shen, M.-H.; Hong, Z.-S.; Chao, T.-H.; Lu, Q.; Cheng, M.-J. First-Principles Study of C–C Coupling Pathways for CO₂ Electrochemical Reduction Catalyzed by Cu(110). *J. Phys. Chem. C* **2021**, *125*, 2464–2476, doi:10.1021/acs.jpcc.0c10736.
218. Schneider, J.; Jia, H.; Muckerman, J.T.; Fujita, E. Thermodynamics and Kinetics of CO₂, CO, and H⁺ Binding to the Metal Centre of CO₂ Reduction Catalysts. *Chem Soc Rev* **2012**, *41*, 2036–2051, doi:10.1039/C1CS15278E.
219. Schouten, K.J.P.; Kwon, Y.; van der Ham, C.J.M.; Qin, Z.; Koper, M.T.M. A New Mechanism for the Selectivity to C1 and C2 Species in the Electrochemical Reduction of Carbon Dioxide on Copper Electrodes. *Chem. Sci.* **2011**, *2*, 1902, doi:10.1039/c1sc00277e.
220. Nie, X.; Wang, H.; Janik, M.J.; Chen, Y.; Guo, X.; Song, C. Mechanistic Insight into C–C Coupling over Fe–Cu Bimetallic Catalysts in CO₂ Hydrogenation. *J. Phys. Chem. C* **2017**, *121*, 13164–13174, doi:10.1021/acs.jpcc.7b02228.

-
221. Nie, X.; Luo, W.; Janik, M.J.; Asthagiri, A. Reaction Mechanisms of CO₂ Electrochemical Reduction on Cu(111) Determined with Density Functional Theory. *J. Catal.* **2014**, *312*, 108–122, doi:10.1016/j.jcat.2014.01.013.
222. Goodpaster, J.D.; Bell, A.T.; Head-Gordon, M. Identification of Possible Pathways for C–C Bond Formation during Electrochemical Reduction of CO₂: New Theoretical Insights from an Improved Electrochemical Model. *J. Phys. Chem. Lett.* **2016**, *7*, 1471–1477, doi:10.1021/acs.jpcllett.6b00358.
223. Sun, L.; Ramesha, G.K.; Kamat, P.V.; Brennecke, J.F. Switching the Reaction Course of Electrochemical CO₂ Reduction with Ionic Liquids. *Langmuir* **2014**, *30*, 6302–6308, doi:10.1021/la5009076.
224. Yang, K.D.; Ko, W.R.; Lee, J.H.; Kim, S.J.; Lee, H.; Lee, M.H.; Nam, K.T. Morphology-Directed Selective Production of Ethylene or Ethane from CO₂ on a Cu Mesopore Electrode. *Angew. Chem. Int. Ed.* **2017**, *56*, 796–800, doi:10.1002/ange.201610432.
225. Song, H.; Im, M.; Song, J.T.; Lim, J.-A.; Kim, B.-S.; Kwon, Y.; Ryu, S.; Oh, J. Effect of Mass Transfer and Kinetics in Ordered Cu-Mesostructures for Electrochemical CO₂ Reduction. *Appl. Catal. B Environ.* **2018**, *232*, 391–396, doi:10.1016/j.apcatb.2018.03.071.
226. Vasileff, A.; Zhu, Y.; Zhi, X.; Zhao, Y.; Ge, L.; Chen, H.M.; Zheng, Y.; Qiao, S. Electrochemical Reduction of CO₂ to Ethane through Stabilization of an Ethoxy Intermediate. *Angew. Chem. Int. Ed.* **2020**, *59*, 19649–19653, doi:10.1002/anie.202004846.
227. Hori, Y.; Takahashi, R.; Yoshinami, Y.; Murata, A. Electrochemical Reduction of CO at a Copper Electrode. *J. Phys. Chem. B* **1997**, *101*, 7075–7081, doi:10.1021/jp970284i.
228. Sun, Z.; Ma, T.; Tao, H.; Fan, Q.; Han, B. Fundamentals and Challenges of Electrochemical CO₂ Reduction Using Two-Dimensional Materials. *Chem* **2017**, *3*, 560–587, doi:10.1016/j.chempr.2017.09.009.
229. Kim, D.; Kley, C.S.; Li, Y.; Yang, P. Copper Nanoparticle Ensembles for Selective Electroreduction of CO₂ to C₂–C₃ Products. *Proc. Natl. Acad. Sci.* **2017**, *114*, 10560–10565, doi:10.1073/pnas.1711493114.
230. Nie, X.; Esopi, M.R.; Janik, M.J.; Asthagiri, A. Selectivity of CO₂ Reduction on Copper Electrodes: The Role of the Kinetics of Elementary Steps. *Angew. Chem. Int. Ed.* **2013**, *52*, 2459–2462, doi:10.1002/anie.201208320.
231. Zou, Q.Y.; Yang, G.N.; Wang, P.Y.; Zhang, Y.; Cui, C.Q.; Zhang, K. An Improved Pretreatment Method for the Fabrication of Cu–Ag Core-Shell Nanoparticles. *IOP Conf. Ser. Mater. Sci. Eng.* **2020**, *758*, 012035, doi:10.1088/1757-899X/758/1/012035.
232. Grosse, P.; Gao, D.; Scholten, F.; Sinev, I.; Mistry, H.; Roldan Cuenya, B. Dynamic Changes in the Structure, Chemical State and Catalytic Selectivity of Cu Nanocubes during CO₂ Electroreduction: Size and Support Effects. *Angew. Chem. Int. Ed.* **2018**, *57*, 6192–6197, doi:10.1002/anie.201802083.
233. Chen, C.S.; Wan, J.H.; Yeo, B.S. Electrochemical Reduction of Carbon Dioxide to Ethane Using Nanostructured Cu₂O-Derived Copper Catalyst and Palladium(II) Chloride. *J. Phys. Chem. C* **2015**, *119*, 26875–26882, doi:10.1021/acs.jpcc.5b09144.
234. Shin, H.-C.; Liu, M. Copper Foam Structures with Highly Porous Nanostructured Walls. *Chem. Mater.* **2004**, *16*, 5460–5464, doi:10.1021/cm048887b.
235. Sen, S.; Liu, D.; Palmore, G.T.R. Electrochemical Reduction of CO₂ at Copper Nanofoams. *ACS Catal.* **2014**, *4*, 3091–3095, doi:10.1021/cs500522g.
236. De Luna, P.; Quintero-Bermudez, R.; Dinh, C.-T.; Ross, M.B.; Bushuyev, O.S.; Todorović, P.; Regier, T.; Kelley, S.O.; Yang, P.; Sargent, E.H. Catalyst Electro-Redeposition Controls Morphology and Oxidation State for Selective Carbon Dioxide Reduction. *Nat. Catal.* **2018**, *1*, 103–110, doi:10.1038/s41929-017-0018-9.

237. Huan, T.N.; Simon, P.; Rouse, G.; Génois, I.; Artero, V.; Fontecave, M. Porous Dendritic Copper: An Electrocatalyst for Highly Selective CO₂ Reduction to Formate in Water/Ionic Liquid Electrolyte. *Chem. Sci.* **2017**, *8*, 742–747, doi:10.1039/C6SC03194C.
238. Loiudice, A.; Lobaccaro, P.; Kamali, E.A.; Thao, T.; Huang, B.H.; Ager, J.W.; Buonsanti, R. Tailoring Copper Nanocrystals towards C₂ Products in Electrochemical CO₂ Reduction. *Angew. Chem. Int. Ed.* **2016**, *55*, 5789–5792, doi:10.1002/anie.201601582.
239. Kwon, Y.; Lum, Y.; Clark, E.L.; Ager, J.W.; Bell, A.T. CO₂ Electroreduction with Enhanced Ethylene and Ethanol Selectivity by Nanostructuring Polycrystalline Copper. *ChemElectroChem* **2016**, *3*, 1012–1019, doi:10.1002/celec.201600068.
240. Kuang, S.; Li, M.; Xia, R.; Xing, L.; Su, Y.; Fan, Q.; Liu, J.; Hensen, E.J.M.; Ma, X.; Zhang, S. Stable Surface-Anchored Cu Nanocubes for CO₂ Electroreduction to Ethylene. *ACS Appl. Nano Mater.* **2020**, *3*, 8328–8334, doi:10.1021/acsanm.0c01745.
241. Melchionna, M.; Fornasiero, P.; Prato, M.; Bonchio, M. Electrocatalytic CO₂ Reduction: Role of the Cross-Talk at Nano-Carbon Interfaces. *Energy Environ. Sci.* **2021**, *14*, 5816–5833, doi:10.1039/D1EE00228G.
242. Perry, S.C.; Leung, P.; Wang, L.; Ponce de León, C. Developments on Carbon Dioxide Reduction: Their Promise, Achievements, and Challenges. *Curr. Opin. Electrochem.* **2020**, *20*, 88–98, doi:10.1016/j.coelec.2020.04.014.
243. Dinh, C.-T.; Burdyny, T.; Kibria, M.G.; Seifitokaldani, A.; Gabardo, C.M.; García de Arquer, F.P.; Kiani, A.; Edwards, J.P.; De Luna, P.; Bushuyev, O.S.; et al. CO₂ Electroreduction to Ethylene via Hydroxide-Mediated Copper Catalysis at an Abrupt Interface. *Science* **2018**, *360*, 783–787, doi:10.1126/science.aas9100.
244. Ma, M.; Djanashvili, K.; Smith, W.A. Selective Electrochemical Reduction of CO₂ to CO on CuO-Derived Cu Nanowires. *Phys. Chem. Chem. Phys.* **2015**, *17*, 20861–20867, doi:10.1039/C5CP03559G.
245. Raciti, D.; Mao, M.; Park, J.H.; Wang, C. Mass Transfer Effects in CO₂ Reduction on Cu Nanowire Electrocatalysts. *Catal. Sci. Technol.* **2018**, *8*, 2364–2369, doi:10.1039/C8CY00372F.
246. Raciti, D.; Mao, M.; Wang, C. Mass Transport Modelling for the Electroreduction of CO₂ on Cu Nanowires. *Nanotechnology* **2018**, *29*, 044001, doi:10.1088/1361-6528/aa9bd7.
247. Chen, L.; Tang, C.; Davey, K.; Zheng, Y.; Jiao, Y.; Qiao, S.-Z. Spatial-Confinement Induced Electroreduction of CO and CO₂ to Diols on Densely-Arrayed Cu Nanopyramids. *Chem. Sci.* **2021**, *12*, 8079–8087, doi:10.1039/D1SC01694F.
248. Chen, L.; Tang, C.; Jiao, Y.; Qiao, S.Z. Anomalous C-C Coupling on Under-Coordinated Cu (111): A Case Study of Cu Nanopyramids for CO₂ Reduction Reaction by Molecular Modelling. *ChemSusChem* **2021**, *14*, 671–678, doi:doi.org/10.1002/cssc.202002036.
249. Schouten, K.J.P.; Qin, Z.; Pérez Gallent, E.; Koper, M.T.M. Two Pathways for the Formation of Ethylene in CO Reduction on Single-Crystal Copper Electrodes. *J. Am. Chem. Soc.* **2012**, *134*, 9864–9867, doi:10.1021/ja302668n.
250. Roberts, F.S.; Kuhl, K.P.; Nilsson, A. High Selectivity for Ethylene from Carbon Dioxide Reduction over Copper Nanocube Electrocatalysts. *Angew. Chem. Int. Ed.* **2015**, *54*, 5179–5182, doi:10.1002/anie.201412214.
251. Binniger, T.; Pribyl, B.; Pătru, A.; Ruettimann, P.; Bjelić, S.; Schmidt, T.J. Multivariate Calibration Method for Mass Spectrometry of Interfering Gases Such as Mixtures of CO, N₂, and CO₂. *J. Mass Spectrom.* **2018**, *53*, 1214–1221, doi:10.1002/jms.4299.
252. Pătru, A.; Binniger, T.; Pribyl, B.; Schmidt, T.J. Design Principles of Bipolar Electrochemical Co-Electrolysis Cells for Efficient Reduction of Carbon Dioxide from Gas Phase at Low Temperature. *J. Electrochem. Soc.* **2019**, *166*, F34–F43, doi:10.1149/2.1221816jes.

253. Ju, W.; Bagger, A.; Hao, G.-P.; Varela, A.S.; Sinev, I.; Bon, V.; Roldan Cuenya, B.; Kaskel, S.; Rossmeisl, J.; Strasser, P. Understanding Activity and Selectivity of Metal-Nitrogen-Doped Carbon Catalysts for Electrochemical Reduction of CO₂. *Nat. Commun.* **2017**, *8*, 944, doi:10.1038/s41467-017-01035-z.
254. Gao, D.; Zhou, H.; Cai, F.; Wang, D.; Hu, Y.; Jiang, B.; Cai, W.-B.; Chen, X.; Si, R.; Yang, F.; et al. Switchable CO₂ Electroreduction via Engineering Active Phases of Pd Nanoparticles. *Nano Res.* **2017**, *10*, 2181–2191, doi:10.1007/s12274-017-1514-6.
255. Varela, A.S.; Schlaup, C.; Jovanov, Z.P.; Malacrida, P.; Horch, S.; Stephens, I.E.L.; Chorkendorff, I. CO₂ Electroreduction on Well-Defined Bimetallic Surfaces: Cu Overlayers on Pt(111) and Pt(211). *J. Phys. Chem. C* **2013**, *117*, 20500–20508, doi:10.1021/jp406913f.
256. Vasilyev, D.; Shirzadi, E.; Rudnev, A.V.; Broekmann, P.; Dyson, P.J. Pyrazolium Ionic Liquid Co-Catalysts for the Electroreduction of CO₂. *ACS Appl. Energy Mater.* **2018**, *1*, 5124–5128, doi:10.1021/acsaem.8b01086.
257. Chen, Y.; Li, C.W.; Kanan, M.W. Aqueous CO₂ Reduction at Very Low Overpotential on Oxide-Derived Au Nanoparticles. *J. Am. Chem. Soc.* **2012**, *134*, 19969–19972, doi:10.1021/ja309317u.
258. Min, X.; Kanan, M.W. Pd-Catalyzed Electrohydrogenation of Carbon Dioxide to Formate: High Mass Activity at Low Overpotential and Identification of the Deactivation Pathway. *J. Am. Chem. Soc.* **2015**, *137*, 4701–4708, doi:10.1021/ja511890h.
259. Chatterjee, T.; Boutin, E.; Robert, M. Manifesto for the Routine Use of NMR for the Liquid Product Analysis of Aqueous CO₂ Reduction: From Comprehensive Chemical Shift Data to Formaldehyde Quantification in Water. *Dalton Trans.* **2020**, *49*, 4257–4265, doi:10.1039/C9DT04749B.
260. McNaught, A.D.; Wilkinson, A.; Chalk, S.J. *IUPAC. Compendium of Chemical Terminology*; 2nd ed.; Blackwell Scientific Publications: Oxford, **1997**; ISBN 0-9678550-9-8.
261. Lichtenfels, D.H.; Fleck, S.A.; Burow, F.H. Gas-Liquid Partition Chromatography. *Anal. Chem.* **1955**, *27*, 1510–1513, doi:10.1021/ac60106a001.
262. Vidal-Madjar, C.; Guiochon, G. Applications of Gas-Solid Chromatography. *Sep. Purif. Methods* **1973**, *2*, 1–125, doi:10.1080/03602547408068792.
263. Stauffer, E.; Dolan, J.A.; Newman, R. *Fire Debris Analysis, Chapter 8: Gas Chromatography and Gas Chromatography–Mass Spectrometry*; 1st ed.; Academic Press, 2007; ISBN 978-0-08-055626-0.
264. Hansen, A.R.E.; Enemark-Rasmussen, K.; Mulder, F.A.A.; Jensen, P.R.; Meier, S. Versatile Procedures for Reliable NMR Quantification of CO₂ Electroreduction Products. *J. Phys. Chem. C* **2022**, *126*, 11026–11032, doi:10.1021/acs.jpcc.2c03448.
265. Rabi, I.I.; Millman, S.; Kusch, P.; Zacharias, J.R. The Molecular Beam Resonance Method for Measuring Nuclear Magnetic Moments. The Magnetic Moments of ³Li⁶, ³Li⁷ and ⁹F¹⁹. *Phys. Rev.* **1939**, *55*, 526–535, doi:10.1103/PhysRev.55.526.
266. Purcell, E.M.; Torrey, H.C.; Pound, R.V. Resonance Absorption by Nuclear Magnetic Moments in a Solid. *Phys. Rev.* **1946**, *69*, 37–38, doi:10.1103/PhysRev.69.37.
267. Bloch, F. Nuclear Induction. *Phys. Rev.* **1946**, *70*, 460–474, doi:10.1103/PhysRev.70.460.
268. Keeler, J. *Understanding NMR Spectroscopy*; 2nd ed.; Wiley-VCH: Weinheim, **2010**; ISBN 978-0-470-74608-0.
269. Zhang, J.; Luo, W.; Züttel, A. Crossover of Liquid Products from Electrochemical CO₂ Reduction through Gas Diffusion Electrode and Anion Exchange Membrane. *J. Catal.* **2020**, *385*, 140–145, doi:10.1016/j.jcat.2020.03.013.
270. Salvatore, D.A.; Gabardo, C.M.; Reyes, A.; O'Brien, C.P.; Holdcroft, S.; Pintauro, P.; Bahar, B.; Hickner, M.; Bae, C.; Sinton, D.; et al. Designing Anion Exchange Membranes for CO₂ Electrolysers. *Nat. Energy* **2021**, *6*, 339–348, doi:10.1038/s41560-020-00761-x.

-
271. Henkensmeier, D.; Najibah, M.; Harms, C.; Žitka, J.; Hnát, J.; Bouzek, K. Overview: State-of-the Art Commercial Membranes for Anion Exchange Membrane Water Electrolysis. *J. Electrochem. Energy Convers. Storage* **2021**, *18*, 024001, doi:10.1115/1.4047963.
272. Hore, P.J. A New Method for Water Suppression in the Proton NMR Spectra of Aqueous Solution. *J. Magn. Reson.* **1983**, *54*, 539–542, doi:10.1016/0022-2364(83)90335-9.
273. Bagger, A.; Ju, W.; Varela, A.S.; Strasser, P.; Rossmeisl, J. Electrochemical CO₂ Reduction: Classifying Cu Facets. *ACS Catal.* **2019**, *9*, 7894–7899, doi:10.1021/acscatal.9b01899.
274. Walsh, F.C.; Herron, M.E. Electrocrystallization and Electrochemical Control of Crystal Growth: Fundamental Considerations and Electrodeposition of Metals. *J. Phys. Appl. Phys.* **1991**, *24*, 217–225, doi:10.1088/0022-3727/24/2/019.
275. Duan, J.; Liu, J.; Mo, D.; Yao, H.; Maaz, K.; Chen, Y.; Sun, Y.; Hou, M.; Qu, X.; Zhang, L.; et al. Controlled Crystallinity and Crystallographic Orientation of Cu Nanowires Fabricated in Ion-Track Templates. *Nanotechnology* **2010**, *21*, 365605, doi:10.1088/0957-4484/21/36/365605.
276. Waseda, Y.; Eiichiro, M.; Kozo, S. *X-Ray Diffraction Crystallography*; 1st ed.; Springer Berlin Heidelberg: Heidelberg, **2011**; ISBN 978-3-642-16634-1.
277. Bragg, W.H.; Bragg, W.L. The Reflection of X-Rays by Crystals. *Philosophical Transactions of the Royal Society* **1913**, *88*, 428–438, doi:10.1098/rspa.1913.0040.
278. Swanson, H.; Tatge, E. *Standard X-Ray Diffraction Powder Patterns*; National Bureau of Standards (U.S.), **1953**; Vol. 1;.
279. Davey, W.P. Precision Measurements of the Lattice Constants of Twelve Common Metals. *Phys. Rev.* **1925**, *25*, 753–761, doi:10.1103/PhysRev.25.753.
280. Harris, G.B. X. Quantitative Measurement of Preferred Orientation in Rolled Uranium Bars. *Lond. Edinb. Dublin Philos. Mag. J. Sci.* **1952**, *43*, 113–123, doi:10.1080/14786440108520972.
281. Suzuki, S.; Ishikawa, Y.; Isshiki, M.; Waseda, Y. Native Oxide Layers Formed on the Surface of Ultra High-Purity Iron and Copper Investigated by Angle Resolved XPS. *Mater. Trans.* **1997**, *38*, 1004–1009, doi:10.2320/matertrans1989.38.1004.
282. Maurer, F.; Brötz, J.; Karim, S.; Molares, M.E.T.; Trautmann, C.; Fuess, H. Preferred Growth Orientation of Metallic Fcc Nanowires under Direct and Alternating Electrodeposition Conditions. *Nanotechnology* **2007**, *18*, 135709, doi:10.1088/0957-4484/18/13/135709.
283. Ruiz, E.; Alvarez, S.; Alemany, P.; Evarestov, R.A. Electronic Structure and Properties of Cu₂O. *Phys. Rev. B* **1997**, *56*, 7189–7196, doi:10.1103/PhysRevB.56.7189.
284. Kim, Y.-G.; Baricuatro, J.H.; Javier, A.; Gregoire, J.M.; Soriaga, M.P. The Evolution of the Polycrystalline Copper Surface, First to Cu(111) and Then to Cu(100), at a Fixed CO₂ RR Potential: A Study by Operando EC-STM. *Langmuir* **2014**, *30*, 15053–15056, doi:10.1021/la504445g.
285. Kim, Y.-G.; Javier, A.; Baricuatro, J.H.; Torelli, D.; Cummins, K.D.; Tsang, C.F.; Hemminger, J.C.; Soriaga, M.P. Surface Reconstruction of Pure-Cu Single-Crystal Electrodes under CO-Reduction Potentials in Alkaline Solutions: A Study by Seriatim ECSTM-DEMS. *J. Electroanal. Chem.* **2016**, *780*, 290–295, doi:10.1016/j.jelechem.2016.09.029.
286. Jarvis, K.E. *Handbook of Inductively Coupled Plasma Mass Spectrometry*; 1st ed.; Springer Science+Business Media: New York, **1992**; ISBN 978-1-4051-0916-1.
287. Krupp, E.; Seby, F.; Rodríguez Martín-Doimeadios, R.; Holliday, A.; Moldovan, M.; Köllensperger, G.; Hann, S.; Donard, O. Trace Metal Speciation with ICP-MS Detection. In *Inductively Coupled Plasma Mass Spectrometry Handbook*; John Wiley & Sons, **2005**; Vol. 1, pp. 259–335 ISBN 978-1-4051-0916-1.
288. Hersbach, T.J.P.; Koper, M.T.M. Cathodic Corrosion: 21st Century Insights into a 19th Century Phenomenon. *Curr. Opin. Electrochem.* **2021**, *26*, 100653, doi:10.1016/j.coelec.2020.100653.

289. Vanrenterghem, B.; Bele, M.; Zepeda, F.R.; Šala, M.; Hodnik, N.; Breugelmans, T. Cutting the Gordian Knot of Electrodeposition via Controlled Cathodic Corrosion Enabling the Production of Supported Metal Nanoparticles below 5 Nm. *Appl. Catal. B Environ.* **2018**, *226*, 396–402, doi:10.1016/j.apcatb.2017.12.080.
290. Haber, F. Über Elektrolyse der Salzsäure nebst Mitteilungen über kathodische Formation von Blei. III. Mitteilung. *Z. Für Anorg. Chem.* **1898**, *16*, 438–449, doi:10.1002/zaac.18980160144.
291. Haber, F. The Phenomenon of the Formation of Metallic Dust from Cathodes. *Trans Am Electrochem Soc* **1902**, *2*:189–196. *Trans Am Electrochem Soc* **1902**, 189–196.
292. Yanson, A.I.; Rodriguez, P.; Garcia-Araez, N.; Mom, R.V.; Tichelaar, F.D.; Koper, M.T.M. Cathodic Corrosion: A Quick, Clean, and Versatile Method for the Synthesis of Metallic Nanoparticles. *Angew. Chem. Int. Ed.* **2011**, *50*, 6346–6350, doi:10.1002/anie.201100471.
293. Kabanov, B.N. Incorporation of Alkali Metals into Solid Cathodes. *Electrochimica Acta* **1968**, *13*, 19–25, doi:10.1016/0013-4686(68)80003-9.
294. Yanson, Yu.I.; Yanson, A.I. Cathodic Corrosion. I. Mechanism of Corrosion via Formation of Metal Anions in Aqueous Medium. *Low Temp. Phys.* **2013**, *39*, 304–311, doi:10.1063/1.4795002.
295. Hersbach, T.J.P.; McCrum, I.T.; Anastasiadou, D.; Wever, R.; Calle-Vallejo, F.; Koper, M.T.M. Alkali Metal Cation Effects in Structuring Pt, Rh, and Au Surfaces through Cathodic Corrosion. *ACS Appl. Mater. Interfaces* **2018**, *10*, 39363–39379, doi:10.1021/acsami.8b13883.
296. Westbrook, J.H.; Fleischer, R.L. *Intermetallic Compounds: Principles and Practice, Volume 3: Progress*; 1st ed.; Wiley & Sons: Cichester, **2002**; ISBN 0-471-49315-5.
297. Otsuka, R.; Uda, M. Short Communication: Cathodic Corrosion of Cu in H₂SO₄. *Corros. Sci.* **1969**, 703–705, doi:10.1016/S0010-938X(69)80101-0.
298. Wirtanen, T.; Prenzel, T.; Tessonier, J.-P.; Waldvogel, S.R. Cathodic Corrosion of Metal Electrodes—How to Prevent it in Electroorganic Synthesis. *Chem. Rev.* **2021**, *121*, 10241–10270, doi:10.1021/acs.chemrev.1c00148.
299. Yanson, A.I.; Yanson, Yu.I. Cathodic Corrosion. II. Properties of Nanoparticles Synthesized by Cathodic Corrosion. *Low Temp. Phys.* **2013**, *39*, 312–317, doi:10.1063/1.4795197.
300. Feng, J.; Chen, D.; Sediq, A.S.; Romeijn, S.; Tichelaar, F.D.; Jiskoot, W.; Yang, J.; Koper, M.T.M. Cathodic Corrosion of a Bulk Wire to Nonaggregated Functional Nanocrystals and Nanoalloys. *ACS Appl. Mater. Interfaces* **2018**, *10*, 9532–9540, doi:10.1021/acsami.7b18105.
301. Najdovski, I.; Selvakannan, P.; O’Mullane, A.P. Cathodic Corrosion of Cu Substrates as a Route to Nanostructured Cu/M (M=Ag, Au, Pd) Surfaces. *ChemElectroChem* **2015**, *2*, 106–111, doi:10.1002/celc.201402259.
302. Li, G.; Liu, H.; Yang, H.; Chen, X.; Ji, K.; Yang, D.; Zhang, S.; Ma, X. Tuning Product Distributions of CO₂ Electroreduction over Copper Foil through Cathodic Corrosion. *Chem. Eng. Sci.* **2022**, *263*, 118142, doi:10.1016/j.ces.2022.118142.
303. Simon, G.H.; Kley, C.S.; Roldan Cuenya, B. Potential-Dependent Morphology of Copper Catalysts During CO₂ Electroreduction Revealed by In Situ Atomic Force Microscopy. *Angew. Chem. Int. Ed.* **2021**, *60*, 2561–2568, doi:10.1002/anie.202010449.
304. McCallum, C.; Gabardo, C.M.; O’Brien, C.P.; Edwards, J.P.; Wicks, J.; Xu, Y.; Sargent, E.H.; Sinton, D. Reducing the Crossover of Carbonate and Liquid Products during Carbon Dioxide Electroreduction. *Cell Rep. Phys. Sci.* **2021**, *2*, 100522, doi:10.1016/j.xcrp.2021.100522.
305. Wang, N.; Miao, R.K.; Lee, G.; Vomiero, A.; Sinton, D.; Ip, A.H.; Liang, H.; Sargent, E.H. Suppressing the Liquid Product Crossover in Electrochemical CO₂ Reduction. *SmartMat* **2021**, *2*, 12–16, doi:10.1002/smm2.1018.

-
306. Moura de Salles Pupo, M.; Kortlever, R. Electrolyte Effects on the Electrochemical Reduction of CO₂. *ChemPhysChem* **2019**, *20*, 2926–2935, doi:10.1002/cphc.201900680.
307. Kas, R.; Kortlever, R.; Yilmaz, H.; Koper, M.T.M.; Mul, G. Manipulating the Hydrocarbon Selectivity of Copper Nanoparticles in CO₂ Electroreduction by Process Conditions. *ChemElectroChem* **2015**, *2*, 354–358, doi:10.1002/celec.201402373.
308. Jin, L.; Seifitokaldani, A. In Situ Spectroscopic Methods for Electrocatalytic CO₂ Reduction. *Catalysts* **2020**, *10*, 481, doi:10.3390/catal10050481.
309. Zhang, G.; Cui, Y.; Kucernak, A. Real-Time In Situ Monitoring of CO₂ Electroreduction in the Liquid and Gas Phases by Coupled Mass Spectrometry and Localized Electrochemistry. *ACS Catal.* **2022**, *12*, 6180–6190, doi:10.1021/acscatal.2c00609.

List of abbreviations

AAO – anodic aluminium oxide

ABF – annular bright field

ALD – atomic layer deposition

C_{DL} – double layer capacitance

DFT – density functional theory

ECSA – electrochemically active surface area

EDL – electrical double layer

EDX – energy dispersive X-ray spectroscopy

EIS – electrochemical impedance spectroscopy

fcc – face centered cubic

FFT – fast Fourier transform

GC – gas chromatography

HAADF – high angle annular dark field

HER – hydrogen evolution reaction

HRSEM – high resolution scanning electron microscopy

ICP-MS – inductively coupled plasma mass spectrometry

LAADF – low angle annular dark field

MFC – mass flow controller

NMR – nuclear magnetic resonance

PC – polycarbonate

PEEK- polyether ether ketone

PET – polyethylene terephthalate

PZC – point of zero charge

RDS – rate determining step

RHE – reference hydrogen electrode

SAED – selected area electron diffraction

SCE – saturated calomel electrode

SE – secondary electron

SEM – scanning electron microscopy

S_{Geo} – geometrical surface area

SHE- standard hydrogen electrode

SSA – specific surface area

STEM- scanning transmission electron microscopy

TC – texture coefficient

TEM – transmission electron microscopy

UV – ultraviolet

XRD – X-ray diffraction

List of figures

- Figure 1: a) Atmospheric CO₂ concentration from 1958-2022 observed at the Mauna Loa observatory in Hawaii, showing a strong increase of ~25 % over the past 60 years [8] and b) global average temperature on land and ocean recorded from 1850 on. Published with permission from Dr. Pieter Tans, NOAA/GML (gml.noaa.gov/ccgg/trends/) and Dr. Ralph Keeling, Scripps Institution of Oceanography (scrippsco2.ucsd.edu/).....7
- Figure 2: The electronic energy loss (dashed green line), the nuclear energy loss (dashed red line) and the resulting total energy loss as sum (blue line) as a function of the specific energy of Au ions a) and the projected range b) in polycarbonate according to simulations using the SRIM2003 code [146]. The ranges for the irradiation energies of 5.6 MeV/u, 8.3 MeV/u and 11.1 MeV/u used in this work are marked with dashed black lines. 13
- Figure 3: Schematics of the irradiation of polymer foils a) perpendicular to the polymer surface and b) under 45° tilt combined with a rotation of 90° around the surface normal between irradiation steps. 14
- Figure 4: a) Schematic of the initial stages of etching of the ion-track. The pore opening angle α depends on the ratio of the track etching rate v_t and bulk etching rate v_b . b) For $v_t \gg v_b$ cylindrical nanochannels are achieved as visible in the cross section of the nanopore network template that was sequentially irradiated from four directions under an angle of 45 ° to the surface normal..... 15
- Figure 5: Cross section of the thermostatic pot and the sample holders used for selective ion-track etching of the irradiated polymer foils. For etching, the pot temperature is controlled to 50 ± 2 °C and a magnetic stirrer is situated under the sample holder 16
- Figure 6: SEM images of polymer membranes with interconnected nanopores of 150 nm diameter. Both samples were irradiated under a tilting angle of 45° from four directions with fluences of a) 1×10^8 cm⁻² and b) 2.5×10^8 cm⁻², each. The frame marks the region of 20 x 15 μ m in which the pores are counted for fluence determination. 17
- Figure 7: Representative SEM images of etched ion-track membranes with interconnected nanopore network structure, a) top-view and b) cross-section view. 17
- Figure 8: Average pore radius as a function of etching time in 6 M NaOH solution at 50 °C. Each data point represents a mean value from all pores placed in a square region of 20 x 15 μ m on three independently etched membranes..... 18
- Figure 9: a) Scheme of the electrochemical two-electrode setup, applied for electrodeposition of the Cu backelectrode onto the Cu-sputtered rough side of the PC membrane. The arrows indicate the deposition direction of the Cu ions from anode to cathode. b) scheme of the electrochemical three-

electrode setup, applied for electrodeposition of Cu nanowires into the interconnected nanochannels of the PC membrane.	21
Figure 10: Representative $I-t$ curve recorded during the electrodeposition of Cu at an applied potential of $U = -20$ mV vs. Ag/AgCl into a track-etched membrane with interconnected nanochannels. As schematically indicated, three different regimes can be distinguished during the deposition process. The arrow is indicating the beginning of cap growth when the pores are completely filled.....	22
Figure 11: SEM images of a Cu nanowire network electrodeposited for 15 minutes at -20 mV vs. Ag/AgCl with a clearly visible network structure in a) top view and b) cross sectional view.....	24
Figure 12: Setup for the anodization of the Cu nanowire network with 0.1 M H_3PO_4 in an electrochemical cell. The network serves as working electrode and is contacted from the back side with a Cu plate, whereas a Pt wire serves as counter electrode for the potential application in a two-electrode setup.	25
Figure 13: SEM images of the Cu nanowire network before and after consecutive pre-cleaning and anodization steps. a) pristine state b) after immersion in 0.1 M H_2SO_4 , c) after immersion in 0.1 M H_3PO_4 and d) after anodization.....	25
Figure 14: EDX spectra of Cu nanowire networks, synthesized on a Cu backelectrode. a) before (pristine) and b) after pre-cleaning. The position of the copper signals are marked in red and the positions of possible contaminations of sulfur and phosphor are marked in green [171].....	26
Figure 15: a) Two-dimensional scheme of the nanowire network of height h , full wire length L_f , effective length L_e of wire segments with accessible surface, nanowire diameter d , total number of nanowires n and spacing x between adjacent wires. b) SEM image of a nanowire network with examples of intersecting nanowires marked by yellow circles	28
Figure 16: Model calculation of a) surface area, b) volume, c) mass and d) specific surface area as a function of network height for fixed nanowire diameter (150 nm) and number density (8×10^8 cm ⁻²) on a planar sample of 1.8 cm ² size.....	30
Figure 17: Model calculation for a) surface area A , b) volume V , c) mass m and d) <i>specific surface area</i> as a function of nanowire diameter for a nanowire network with a constant network height of 30 μ m and a fixed nanowire number density of 8×10^8 wires/cm ² on a planar area of 1.8 cm ²	31
Figure 18: Model calculation of the Cu nanowire networks a) surface area A , b) volume V , c) mass m and d) specific surface area as a function of nanowire number density with constant network height and nanowire diameter of 30 μ m and 150 nm, respectively, on a planar area of 1.8 cm ²	32
Figure 19: Gouy-Chapman-Stern model of the electrical double layer at the solid-electrolyte interface, with the corresponding potential distribution as a function of distance from the material [182].....	34

Figure 20: a) Schematics and b) photography of components of the PEEK electrochemical cell used for double layer capacitance measurements. The nanowire network mounted on a Cu stamp is inserted from the front side. Both front and rear cell parts are screwed together. The counter electrode is electrically contacted from the rear side with an Al foil.....	36
Figure 21: CV scans recorded for a lapped and polished Cu reference plate in 0.1 M KHCO ₃ . The blue box shows the non-Faradaic region between 0.2 and 0.4 V.....	38
Figure 22: CV scans performed on the 1.8 cm ² lapped and polished Cu plate with scan rates of 30 (blue), 40 (red) and 50 mV/s (red) at potentials of 280 ± 10 mV, 320 ± 10 mV and 360 ± 10 mV.....	38
Figure 23: Three CV scans for a representative Cu nanowire network (1.8 cm ² area, 30 μm height, 150 nm nanowire diameter, 2×10 ⁹ cm ⁻² nanowire number density) recorded between U = -0.5 V and U = 0.5 V (vs. Ag/AgCl) at a scan rate of 10 mV/s. The non-Faradaic region is highlighted in the light blue box.	39
Figure 24: CV scans with scan rates of 30 mV/s, 40 mV/s and 50 mV/s at potentials of -90 ± 10 mV, -70 ± 10 mV, -50 ± 10 mV and -20 ± 10 mV.....	40
Figure 25: Experimentally determined ECSA values (black squares) and calculated theoretical surface areas (red line) (shaded areas indicate uncertainties in the model due to the stochastic nanowire arrangement) of Cu nanowire networks with systematic variations of the network height <i>h</i> . The inset displays the fixed wire parameters of this series.....	41
Figure 26: Nanowire network a) before and b) after the acidic pre-cleaning process. The as-synthesized networks have a smooth surface while acidic cleaning obviously roughens the wire surface.....	42
Figure 27: Experimentally determined ECSA values (black squares) and calculated theoretical surface areas (red line) (shaded areas indicate uncertainties due to the stochastic nanowire arrangement) of Cu nanowire networks with systematic variations of the nanowire diameter <i>d</i> . The inset displays the fixed parameters for this series.	42
Figure 28: SEM images of Cu nanowire networks with different wire diameter used for ECSA determination. The images were taken after the acidic pre-cleaning, but before the ECSA measurement. The inset displays the average nanowire diameter calculated from 10-20 nanowires measured as shown exemplarily in the images.	43
Figure 29: Experimentally determined ECSA values (black squares) and calculated theoretical surface areas (red line) (shaded areas indicate uncertainties due to the stochastic nanowire arrangement) of Cu nanowire networks with systematic variations of the nanowire number density <i>F</i> . The inset displays the fixed parameters for this series.	44

Figure 30: Scheme of a sustainable carbon cycle based on the transfer of CO ₂ into synthetic fuels by electrochemical CO ₂ reduction reactions [203].	46
Figure 31: Proposed CO ₂ reduction reaction pathways for hydrocarbon products (black) via intermediates (grey) on Cu catalysts, as indicated by studies with dendritic Cu foam catalysts modified by ionic liquids. The carbene pathways are marked with yellow arrows, the dimerization pathways in green [53].	48
Figure 32: Examples of Cu nanostructures that are presented in literature as activity enhanced catalysts for CO ₂ reduction reactions, such as a) dendritic Cu foams [53], b) spherical nanoparticles [231], c) nanocubes [232], d) nanoparticles on a polycrystalline Cu film [233] and e) nanowire arrays derived by the reduction of CuO nanowires [134].	51
Figure 33: a) Schematics and b) photograph of the electrochemical cell used for CO ₂ reduction experiments. The nanowire network is inserted in the corresponding front opening of the cell by a Cu stamp, all cell parts are screwed together and the counter electrode is electrically contacted from the back side by an Al foil.	55
Figure 34: Exemplary CV scans from -0.5 V vs. Ag/AgCl to -1.8 V vs. Ag/AgCl recorded during the surface reduction of a Cu nanowire network with $d = 150$ nm, $h = 30$ μm, $F = 8 \times 10^8$ cm ⁻² .	56
Figure 35: Resistance R_u of a Cu nanowire network after a certain number of CV scans for surface reduction.	57
Figure 36: Electrochemical impedance spectroscopy measurement for a Cu nanowire network ($d = 150$ nm, $h = 30$ μm, $F = 8 \times 10^8$ cm ⁻²), performed after the electrochemical surface reduction.	58
Figure 37: Exemplary chronoamperometric current density over time ($J-t$) for one-hour potentiostatic CO ₂ reduction at a Cu nanowire network at an electrode potential U_{el} of -0.75 V vs. RHE.	59
Figure 38: EIS measurement for the same Cu nanowire network, measured after potentiostatic CO ₂ reduction for one hour at -0.75 V vs. RHE.	60
Figure 39: High magnification SEM images of the a) as purchased Cu plate, b) electrodeposited fine-grained Cu film, c) Cu nanowire array (cross-section image) and d) Cu nanowire network, all before the CO ₂ reduction experiments.	61
Figure 40: $J-t$ curves for the CO ₂ reduction reactions at an as-purchased Cu plate (blue), electrodeposited back-electrode film (red), parallel Cu nanowire array ($d = 150$ nm, $F = 2 \times 10^9$ cm ⁻² , $h = 4$ μm) (yellow), and Cu nanowire network ($d = 150$ nm, $F = 8 \times 10^8$ cm ⁻² , $h = 30$ μm) (green) at the three potentials of $U_{el} = -0.66$ V vs. RHE, -0.75 V vs. RHE and -0.83 V vs. RHE, applied for 1 h each. The current density refers to the planar electrode area.	62

Figure 41: Faradaic efficiencies at different electrode potentials U_{el} of a) all reaction products, b) H_2 , c) gas phase products (CO , CH_4 , C_2H_4 , C_2H_6), d) acidic liquid phase products ($HCOOH$, CH_3COOH) and e) alcohols (C_2H_6O , C_3H_8O , $C_2H_6O_2$) for the CO_2 reduction at a Cu-plate (blue), an electrodeposited Cu film (red) a Cu nanowire array (yellow) and a Cu nanowire network (green), i.e. the structures presented in Figure 39. The legend in a) is valid for all graphs.	64
Figure 42: Faradaic efficiencies normalized on the planar sample area obtained for the different products after one hour CO_2 reduction at a) $U_{el} = -0.66$ V vs. RHE, b) $U_{el} = -0.75$ V vs RHE and c) $U_{el} = -0.83$ V vs. RHE for the as-purchased Cu plate (blue), electrodeposited back-electrode film (red), parallel Cu nanowire array ($d = 150$ nm, $F = 2 \times 10^9$ cm ⁻² , $h = 4$ μ m) (yellow), and Cu nanowire network ($d = 150$ nm, $F = 8 \times 10^8$ cm ⁻² , $h = 30$ μ m) (green).	66
Figure 43: High magnification SEM images of the a) as purchased Cu plate, b) Cu film, c) Cu nanowire array and d) Cu nanowire network after the CO_2 reduction at the three different potentials of $U_{el} = -0.66$ V vs. RHE, -0.75 V vs. RHE and -0.83 V vs. RHE for 1 h each.	68
Figure 44: potentials U vs. $Ag/AgCl$ (blue) and resulting IR-compensated electrode potentials U_{el} vs. RHE (red) over time, with fixed current densities applied stepwise for 5 minutes each. In between the steps, R_u is determined by EIS (yellow).	69
Figure 45: Potentials U vs. $Ag/AgCl$ and U_{el} vs. RHE over J curves for the measurements with increasing and decreasing galvanostatically applied current density steps. The error bars are hardly visible, since they are smaller than the symbols.	70
Figure 46: Faradaic efficiencies for the CO_2 reduction product synthesis with Cu-nanowire networks as catalyst at different potentials. The sums of the Faradaic efficiencies in total and for the sums of the gas- and liquid-phase products are shown in a). b) displays the formation efficiency of the unwanted side-product H_2 coming from the competing hydrogen evolution reaction as well as the efficiencies for $HCOOH$ and CO formation. The current efficiencies for the carbohydrates C_2H_4 , C_2H_6 and CH_4 are shown in c), while the ones for the alcohols are presented in d) with C_2H_6O , C_3H_8O , $C_2H_6O_2$ and CH_3COOH . .	72
Figure 47: SEM images of the Cu nanowire networks before a)-c) and after d)-f) CO_2 reduction at potentials a,d) -0.93 ± 0.05 V, b,e) -0.82 ± 0.02 V, and c,f) -0.75 ± 0.00 V vs. RHE.	74
Figure 48: SEM images of the Cu nanowire networks before a)-c) and after (d)-f) CO_2 reduction at potentials a,d) -0.72 ± 0.00 V, b,e) -0.60 ± 0.01 V, and c,f) -0.5 ± 0.0 V vs. RHE.	74
Figure 49: X-Ray diffractogram of a Cu nanowire network deposited at -20 mV vs. $Ag/AgCl$ at 60 °C.	78
Figure 50: X-ray diffractograms of an as-synthesized Cu nanowire network (blue) and of nanowire networks after the application as catalyst for 1 h CO_2 reduction at potentials of -0.6 V vs. RHE (red), -0.8 V vs. RHE (green) and -0.9 V vs. RHE (yellow). The sample diffractograms are normalized to the Cu powder reference (111) reflection [278].	79

Figure 51: STEM images of an as-synthesized, pre-cleaned, and anodized Cu nanowire segment (diameter 85 nm). a) high angle annular dark field image of a Cu nanowire with a small part of an intersection, b) high-magnification STEM image close to the wire intersection revealing different crystalline structures, c) high-resolution STEM image providing an interatomic distance of 0.13 nm, and d,e) corresponding FFT images taken at the indicated positions at the Cu nanowire.....	81
Figure 52: STEM images and analysis of a Cu nanowire after CO ₂ reduction: a) HAADF image at the wire surface indicating a Cu ₂ O layer (c)), b) high-magnification STEM image of a nanowire bulk region revealing a polycrystalline structure, c) and d) corresponding FFT images of the indicated positions, and e) high-resolution TEM image.....	82
Figure 53: Current densities for the pre-cleaned and anodized Cu nanowire networks (light blue) in comparison to pristine Cu nanowire networks (blue).....	83
Figure 54: Faradaic efficiencies of the CO ₂ reduction reaction for pristine (dark blue) and pre-cleaned and anodized (light blue) Cu nanowire networks for a) all products, b) liquid phase products, and c) gas phase products.	84
Figure 55: Faradaic efficiencies of a) H ₂ evolution and the main reaction intermediates b) CO and c) HCOOH for pre-cleaned and anodized Cu nanowire networks (light blue) and pristine Cu nanowire networks (blue) at CO ₂ reduction potentials of $U_{el} = -0.6, -0.7$ and -0.8 V vs. RHE.....	84
Figure 56: Faradaic efficiencies for the CO ₂ reduction products a) CH ₄ , b) C ₂ H ₄ and c) C ₂ H ₆ for pre-cleaned and anodized Cu nanowire networks (light blue) and pristine Cu nanowire networks (blue) at CO ₂ reduction potentials of $U_{el} = -0.6, -0.7$ and -0.8 V vs. RHE.....	85
Figure 57: Faradaic efficiencies of the CO ₂ reduction products a) CH ₃ COOH, b) C ₂ H ₆ O, c) C ₃ H ₈ O and d) C ₂ H ₆ O ₂ at the three different potentials of $U_{el} = -0.6, -0.7$ and -0.8 V vs. RHE.....	86
Figure 58: a) Current density J vs. t curve and b) U vs. t (right) for CO ₂ reduction at two similar Cu nanowire networks, one without in-situ compensation of the IR-drop (red), and one with in-situ IR-compensation (blue).....	88
Figure 59: SEM images of the Cu nanowire network a) before and c) after CO ₂ reduction at $U_{el} = -0.81$ V vs. RHE without in-situ IR-compensation with an applied potential of $U_{appl} = -1.8$ V vs. RHE and of the Cu-nanowire network b) before and d) after CO ₂ reduction with in-situ compensation of the IR-drop...	89
Figure 60: High-resolution SEM images of a corroded Cu nanowire network before and after CO ₂ reduction, revealing a rougher surface and an increase of wire diameter from 145.5 ± 5.3 nm to 172.7 ± 19 nm.	90
Figure 61: J - t curve for 2 h with an applied voltage of $U_{appl} = -4$ V vs. Ag/AgCl for a Cu nanowire network (blue) and a Cu nanowire array (red). The corresponding R_u values were determined by EIS in 30 min	

time steps. Both nanowire structures exhibited similar geometric properties of $h = 30 \mu\text{m}$, $d = 150 \text{ nm}$ and $F = 2 \times 10^9 \text{ cm}^{-2}$	92
Figure 62: SEM images of a, b) the Cu nanowire network and c, d) the Cu nanowire array before and after the application of $U_{\text{appl}} = -4 \text{ V vs. Ag/AgCl}$ for 2 h. The red circle in b) marks a shape change of the nanowires of the network.....	93
Figure 63: $J-t$ curves for 5 hours extinction of Cu nanowire networks to potentials of $U_{\text{appl}} = -2.4 \text{ V vs. Ag/AgCl}$ (blue), $-3.1 \text{ V vs. Ag/AgCl}$ (red) and $-4.3 \text{ V vs. Ag/AgCl}$ (yellow) in 0.1 M KHCO_3 . The IR-compensated potentials U_{el} vs. RHE for the first and final 5 minutes of potential application are given in black above the curves on the left and right side, respectively.....	94
Figure 64: High resolution SEM images of the Cu nanowire networks applied to potentials of $U_{\text{appl}} = -2.4 \text{ V vs. Ag/AgCl}$ (blue), $U_{\text{appl}} = -3.1 \text{ V vs. Ag/AgCl}$ (red) and $U_{\text{appl}} = -4.3 \text{ V vs. Ag/AgCl}$ (yellow) for 5 h. The SEM images show the nanowire networks before (upper row) and after (lower row) the tests.....	96
Figure 65: High magnification SEM images of the nanowire network surfaces applied to a) $U_{\text{appl}} = -3.1 \text{ V vs. Ag/AgCl}$ and b) $U_{\text{appl}} = -4.3 \text{ V vs. Ag/AgCl}$ for 5 h each, showing surface structuring with the formation of step edges in the shape of small crystallites.....	96
Figure 66: Current density $J-t$ curves for electrochemical CO_2 reduction for 8 h at different Cu nanowire networks with identical geometrical parameters $h = 30 \mu\text{m}$, $d = 150 \text{ nm}$ and $F = 8 \times 10^8 \text{ cm}^{-2}$ at different electrode potentials U_{el} vs. RHE.....	97
Figure 67: SEM images of the Cu nanowire networks before and after application as catalyst during 8 h of CO_2 reduction at potentials of a,e) $U_{\text{el}} = -0.6 \text{ V vs. RHE}$, b,f) $U_{\text{el}} = -0.64 \text{ V vs. RHE}$, c,g) $U_{\text{el}} = -0.69 \text{ V vs. RHE}$ and d,h) $U_{\text{el}} = -0.83 \text{ V vs. RHE}$	98
Figure 68: High magnification SEM images showing degradation of Cu nanowire networks during 8 h of CO_2 reduction at potentials of a) $U_{\text{el}} = -0.64 \text{ V vs. RHE}$, b) $U_{\text{el}} = -0.69 \text{ V vs. RHE}$ and c) $U_{\text{el}} = -0.83 \text{ V vs. RHE}$	98
Figure 69: Faradaic efficiencies over time for the gas-phase products H_2 (green), CO (red), CH_4 (yellow), C_2H_4 (orange) and C_2H_6 (blue) during the 8 h CO_2 reduction reaction at potentials of a) $U_{\text{el}} = -0.6 \pm 0.0 \text{ V vs. RHE}$, b) $U_{\text{el}} = -0.64 \pm 0.01 \text{ V vs. RHE}$, c) $U_{\text{el}} = -0.69 \pm 0.01 \text{ V vs. RHE}$ and d) $U_{\text{el}} = -0.83 \pm 0.03 \text{ V vs. RHE}$	100
Figure 70: Comparisons of Faradaic efficiencies for CO_2 reduction with durations of 8 h and 1 h at potentials of $U_{\text{el}} = -0.6, -0.7$ and -0.83 V vs. RHE : a) total, b) gas phase and c) liquid phase product efficiencies.	102
Figure 71: $J-t$ curves (upper row) and resulting IR-compensated electrode potentials (U_{el}) (lower row) for the CO_2 reduction in differently concentrated electrolyte of $0.1, 0.2$ and 1 M KHCO_3 saturated with CO_2	

by constant gas flow. a) and b) at a Cu-plate and c) and d) for a Cu-nanowire network. The blue curves in the right graphs display the applied potential over time, which was increased every 5 minutes by -0.5 V up to a maximum value of -4.0 V vs. Ag/AgCl..... 104

Figure 72: a) and b) SEM images of the Cu nanowire networks before (i.e. after pre-cleaning and anodization) and c) after the potential tests in 0.1 M KHCO_3 , and d) first in 0.2 M and then 1 M KHCO_3 with a duration of 2100 s. 106

Figure 73: Comparison of the IR-compensated electrode potentials U_{el} vs. RHE resulting from the applied potentials U_{appl} vs. $Ag/AgCl$ on a) a Cu-plate and b) a Cu nanowire network..... 107

List of tables

Table 1: Geometrical surface areas and C_{DL} of the full Cu plate and the same plate with a surface area reduced with Kapton tape.....	37
Table 2: Double layer capacity C_{DL} and ECSA values for different samples with identical geometrical parameters (30 μm network height, 150 nm wire diameter and a nanowire number density of $8 \times 10^8 \text{ cm}^{-2}$ on a planar sample area of 1.8 cm^2) from independent ECSA determination measurements.....	45
Table 3: Half-cell reactions and standard equilibrium potentials for CO_2 reduction reactions to value added chemicals in aqueous solution at $\text{pH} = 7$ [50,206,207].	47
Table 4: Applied U_{appl} vs. Ag/AgCl , resulting U_{res} vs. RHE , compensated by the IR-drop, and J for the different structures used as electrode in the CO_2 reduction. All values are the median from measurements with three samples each.....	62
Table 5: Average IR-drop of three samples each for the different potential steps at which CO_2 reduction was performed at Cu nanowire networks (height = 30 μm , wire diameter $\sim 150 \text{ nm}$, and nanowire number density = $8 \times 10^8 \text{ cm}^{-2}$). The current density is the average reduction current divided by the planar sample area of 1.8 cm^2	71
Table 6: Expected 2θ positions of the Cu XRD reflections for different crystallographic orientations.....	76
Table 7: Texture coefficients of the different Cu nanowire networks with respect to the standard polycrystalline Cu powder diffractogram taken from the JCPDS data file [278].....	79
Table 8: Resistance of the different Cu nanowire networks before and after the application of $U_{appl} = -2.4, -3.1$ and -4.3 V vs. Ag/AgCl for 5 h each.....	95

Publications

Parts and results of this thesis were already published in the following publications and presented at the following international conferences.

Peer-Reviewed Publications

N. Ulrich, M. Schäfer, M. Römer, S. Straub, S. Zhang, J. Brötz, C. Trautmann, C. Scheu, B.J.M. Etzold, M.E. Toimil-Molares

Cu Nanowire Networks with Well-defined Geometrical Parameters for Catalytic Electrochemical CO₂ Reduction

ACS Appl. Nano Mater., **2023**, 6, 6, 4190-4200, <https://doi.org/10.1021/acsanm.2c05232>

N. Ulrich, A. Spende, L. Burr, N. Sobel, I. Schubert, C. Hess, C. Trautmann, M.E. Toimil-Molares

Conical Nanotubes Synthesized by Atomic Layer Deposition of Al₂O₃, TiO₂, and SiO₂ in Etched Ion-Track Nanochannels

Nanomaterials, **2021**, 11, 1874, <https://doi.org/10.3390/nano11081874>

J. Luo, M. Lan, M. Wagner, N. Ulrich, P. Kopold, I. Tzifas, H. Wang, C. Trautmann, M.E. Toimil-Molares

Electrochemical Conversion of Cu Nanowire Arrays into Metal-Organic Frameworks HKUST-1

Journal of The Electrochemical Society, **2023**, 170, 022506 <https://doi.org/10.1149/1945-7111/acbba4>.

M. Li, N. Ulrich, I. Schubert, W. Sigle, M. Wagner, C. Trautmann, M.E. Toimil-Molares

Three-dimensional free-standing gold nanowire networks as a platform for catalytic applications

RSC Adv., **2023**, 13, 4721-4728, <https://doi.org/10.1039/D2RA08035D>

Q. Chen, B. Sochor, A. Chumakov, M. Betker, N. Ulrich, M.E. Toimil-Molares, K. Gordeyeva, L.D. Söderberg, S. Roth

Cellulose-Reinforced Programmable and Stretch-Healable Actuators for Smart Packaging

Adv. Funct. Mater., **2022**, 32, 2208074, doi: <https://doi.org/10.1002/adfm.202208074>

Q. Chen, M. Betker, C. Harder, C.J. Brett, M. Schwartzkopf, N. Ulrich, M.E. Toimil-Molares, C. Trautmann, L.D. Söderberg, C.L. Weindl, V. Körstgens, P. Müller-Buschbaum, M. Ma, S. Roth

Biopolymer-Templated Deposition of Ordered and Polymorph Titanium Dioxide Thin Films for Improved Surface-Enhanced Raman Scattering Sensitivity

Adv. Funct. Mater., **2021**, 2108556, <https://doi.org/10.1002/adfm.202108556>

P. Ruff, M. Carrillo-Solano, N. Ulrich, A. Hadley, P. Kluth, M.E. Toimil-Molares, C. Trautmann, C. Hess

Nanoscale Structuring in Confined Geometries using Atomic Layer Deposition: Conformal Coating and Nanocavity Formation

Z. Phys. Chem., **2018**, 232(7–8), 1147–1171, <https://doi.org/10.1515/zpch-2017-1058>

Talks at Workshops and Conferences

N. Ulrich, M. Schäfer, M. Römer, S. Straub, C. Trautmann, B. Etzold, M.E. Toimil-Molares

Copper nanowire networks synthesized by electrodeposition in etched ion-track membranes as catalyst for electrochemical CO₂ reduction

Electrodeposition of nanostructures, EDNano e-seminar, **2022**, virtual conference room

N. Ulrich, M. Schäfer, M. Römer, S. Straub, S. Zhang, C. Trautmann, B. Etzold, C. Scheu, M.E. Toimil-Molares

Copper nanowire networks for electrochemical CO₂ reduction synthesized by ion-track nanotechnology

Ion-Beam Workshop, **2022**, Jena, Germany

N. Ulrich, M. Schäfer, M. Römer, S. Straub, J. Brötz, C. Trautmann, B. Etzold, M.E. Toimil-Molares

Cu nanowire networks as catalyst for electrochemical CO₂ reduction

Workshop of the Helmholtz society on matter materials and life, MML, **2021**, virtual conference room

Posters at Workshops and Conferences

N. Ulrich, J. Brötz, S. Zhang, M. Römer, S. Straub, C. Trautmann, B. Etzold, M.E. Toimil-Molares

Copper nanowire networks as catalyst for electrochemical CO₂ reduction

Workshop on CO₂ electroreduction of the Helmholtz society, **2021**, virtual conference room

N. Ulrich, J. Brötz, S. Zhang, C. Trautmann, B. Etzold, M.E. Toimil-Molares

Copper nanowire networks for electrocatalytic applications synthesized by ion-track technology

Ion-beam workshop, **2021**, virtual conference room

N. Ulrich, M. Breiner, C. Gütz, J. Brötz, C. Trautmann, S. Waldvogel, M.E. Toimil-Molares

Synthesis and Characterization of Three-Dimensional Copper Nanowire Networks for Electrocatalysis

International symposium on swift heavy ions in matter, SHIM, **2018**, Caen, France

N. Ulrich, S. Straub, J. Brötz, C. Trautmann, B. Etzold, M.E. Toimil-Molares

Synthesis and Characterization of Three-Dimensional Copper Nanowire Networks for CO₂ Reduction

International workshop on electrodeposition of nanostructures, EDNano, **2018**, Bristol, United Kingdom

N. Ulrich, M. Breiner, C. Gütz, J. Brötz, C. Trautmann, S. Waldvogel, M.E. Toimil-Molares

Synthesis and Characterization of Three-Dimensional Copper Nanowire Networks for Electrocatalysis

NanoGE Fall meeting, **2018**, Torremolinos, Spain

Bachelor Theses (co-supervised)

Michelle Schäfer

Bestimmung der elektrochemisch aktiven Oberfläche von Kupferanodrahtnetzwerken

Technische Universität Darmstadt, September 2021

Alexander Pascale

Elektrochemische CO₂ Reduktion an Kupferanodrahtnetzwerken hergestellt durch Ionenspurtechnologie und Elektrodeposition

Technische Universität Darmstadt, März 2020

Internship Reports (co-supervised)

Michelle Schäfer

Bestimmung der elektrochemisch aktiven Oberfläche von Kupferanodrahtnetzwerken

Technische Universität Darmstadt, Januar 2021

Alexander Pascale

Cu-Nanodrähte als Elektrokatalysator für elektrochemische CO₂ Reduktion

Technische Universität Darmstadt, August 2019

Acknowledgements

Here I would like to express my sincere gratitude to all people who contributed to the success of this work.

In particular I thank:

- Prof. Dr. Maria Eugenia Toimil-Molares for the supervision of this work, fruitful scientific discussions as well as proofreading of this thesis and all the publications, posters and contributions to conferences. I am thankful for all the support and the extensive introduction into scientific work.
- Prof. Dr. Christina Trautmann for giving me the chance to enter the materials research group of GSI, for sharing her deep knowledge about ion-matter interaction and ion-track technology. I am grateful for all the scientific discussions and for the constant support over all the years, especially for taking the time to proofread my thesis during her free time after retirement.
- Prof. Dr. Bastian J.M. Etzold for guiding my pathway into electrochemistry by providing the possibility to perform the CO₂ reduction experiments in his lab at TU Darmstadt as well as for agreeing to be the co-referee of this thesis and sharing all of his knowledge about electrochemical reactions during productive scientific discussion meetings.
- Prof. Dr. Jan Philipp Hofmann and Prof. Dr. Ulrike Kramm for being part of my examination committee.
- The GSI Target Lab especially Dr. Bettina Lommel and Dr. Birgit Kindler for sputtering a thin Cu layer on each etched ion-track membrane as well as for lapping and polishing the Cu plates for ECSA reference measurements
- Dr. Joachim Brötz (Materialwissenschaften, TU Darmstadt) for XRD analysis of the Cu nanowire networks.
- Dr. Siyuan Zhang alias «Spark» (MPIE, Düsseldorf) for the STEM analysis of the Cu nanowires as well as for detailed analysis and deep exchange of ideas.
- Michelle Schäfer and Alexander Pascale for contributing to this work with their bachelor theses. Supervising you was a great pleasure.
- Melina Römer and Nicolai Schmitt for helping me with the CO₂ reduction measurements in the Technische Chemie department at TU Darmstadt. Thank You a lot for coming early in the morning and staying until the evening at all the long measuring days.
- The NMR centre of TU Darmstadt, especially Dr. Jörg Fohrer and Christina Spanheimer for the NMR analysis of the electrolytes of the CO₂ reduction reactions for detecting even the tiniest amounts of liquid phase products.

-
- The whole team of the Etzoldlab for the nice working atmosphere and fruitful discussions about the magic of electrochemistry in the lab or during the daily walks after lunch.
 - The materials research group at GSI for the great working atmosphere, the discussions about science and all other daily topics as well as for all the cakes and the great team-spirit. With all the mutual support, this group felt like a family during work and all the other activities.
 - My friends and my family, especially my parents, for always being interested and believing in me and for the permanent encouragement and mental support in various ways.
 - My colleagues at Schlötter for the motivating words and understanding for the moods it generated writing the thesis in parallel to a fulltime job.
 - I acknowledge financial support by the HGS HiRe for FAIR graduate school. I am very thankful for the workshops and soft skill courses they provide, which offered the chance to gather widespread knowledge and personal development beyond the borders of this thesis.



Nils Ulrich

Fähigkeiten

- Nanotechnologie
- Elektrochemie
- Oberflächentechnik
- Galvanotechnik
- Projektmanagement

Programme

- Microsoft Office
- AutoCAD
- MestReNova
- VersaStudio

Sprachen

- Deutsch ●●●●●
- Englisch ●●●●○
- Französisch ●●○○○

Berufserfahrung

Project Manager Hydrogen Technologies

Dr.-Ing. Max Schlötter GmbH, Geislingen -10/2022 – heute
Abteilung R&D

- Entwicklung galvanischer Beschichtungen für Wasserelektrolyse
- Entwicklung galvanischer Beschichtungsverfahren
- Entwicklung von elektrochemischen Testverfahren
- Betreuung von Forschungs- und Kundenprojekten

Wissenschaftlicher Mitarbeiter

GSI Helmholtzzentrum, Darmstadt - 08/2018 – 10/2022
Abteilung Materialforschung

- Herstellung von ionenstrahlmodifizierten Polymermembranen
- Herstellung von Nanodrahtstrukturen für katalytische Anwendungen
- Betreuung und Wartung der ALD-Anlage
- Rasterelektronenmikroskopie

Bildungsweg

Promotion in Materialwissenschaft

Technische Universität Darmstadt - 08/2018 – 10/2024
Abschluss: Dr. rer. Nat.

Studium der Materialwissenschaft

Technische Universität Darmstadt - 10/2011 - 08/2018
Abschluss: Master of Science, Note 1,9

SCHULABSCHLUSS

Goetheschule Wetzlar - 08/2008 - 07/2011
Abschluss: Abitur, Note 1,8

Publikationen

- Cu Nanowire Networks with Well-defined Geometrical Parameters for Catalytic Electrochemical CO₂ Reduction – ACS Applied Nano Materials – 03/2023
- Three-dimensional free-standing gold nanowire networks as a platform for catalytic applications – RSC Advances – 02/2023
- Electrochemical Conversion of Cu Nanowire Arrays into Metal-Organic Frameworks HKUST-1 – Journal of the Electrochemical Society – 02/2023
- Cellulose-Reinforced Programmable and Stretch-Healable Actuators for Smart Packaging – Advanced Functional Materials – 10/2022
- Biopolymer-Templated Deposition of Ordered and Polymorph Titanium Dioxide Thin Films for Improved Surface-Enhanced Raman Scattering Sensitivity – Advanced Functional Materials – 10/2021
- Conical Nanotubes Synthesized by Atomic Layer Deposition of Al₂O₃, TiO₂ and SiO₂ in Etched Ion-Track Nanochannels – Nanomaterials - 07/2021
- Nanoscale Structuring in Confined Geometries using Atomic Layer Deposition: Conformal Coating and Nanocavity Formation – Zeitschrift für Physikalische Chemie – 07/2018

Weiterbildung

Erwerb der Fachkunde im Strahlenschutz

TÜV Süd - 11/2024

Erwerb der Fachkunde im Strahlenschutz gemäß Fachkunderichtlinie Technik für die Fachkundegruppe R3

Elektrochemie für Naturwissenschaftler, Ingenieure und Techniker

DECHEMA - 10/2023

ETOS Winter School 2022

Kursthema: Chemische und ingenieurstechnische Perspektiven der organischen Elektrosynthese - 02/2022

Grundlagen und Projektbearbeitung mit AutoCAD

Dipl. Ing. Marko Frass - 01/2022

AutoCAD: 3D-Modellierung, 2D-Schnitte

Dr. Oksana Zhebel - 01/2022

Soft Skill Course III

Helmholtz Graduiertenschule HGS-HIRe - 10/2021

Kursthema: Leadership and Career Development

Durchgeführt von Coaching4Careers

Soft Skill Course II

Helmholtz Graduiertenschule HGS-HIRe - 02/2021

Kursthema: Leading Teams in a Research Environment

Durchgeführt von Coaching4Careers

Soft Skill Course I

Helmholtz Graduiertenschule HGS-HIRe - 10/2020

Kursthema: Making an Impact as an Effective Researcher

Durchgeführt von Coaching4Careers

Ehrenamt

Juror Chemie bei Jugend forscht

Bewertung von Wettbewerbsbeiträgen - 2023 – heute

Fluglehrer Segelflug

Ausbildung von Segelflugpiloten - 2013 – heute